



**Development of a Linear Vernier Hybrid Machine for
Direct Drive Wave Energy Converters**

Ahmed Almoraya
B.Sc., M.Sc.

A thesis submitted for the degree of
Doctor of Philosophy

School of Engineering

Newcastle University
United Kingdom

June 2019

Abstract

The work presented in this thesis concerns the development of linear electric machines for use with wave energy converters. The machine topology selected, the Linear Vernier Hybrid Machine, is extensively investigated, specifically looking at alternative magnet configurations. Topologies are evaluated by their generation capabilities at low velocities, as demanded by Direct Drive Wave Energy Converters. Attention is mainly focused on improving the electromagnetic performance and reducing the magnet mass. A new topology of the Linear Vernier Hybrid Machine is proposed for these purposes, known later as Inset Magnet Consequent Pole machine. Tapered ferromagnetic poles are employed in this topology, which have shown a great impact on minimising the inherent pole-to-pole leakage flux as well as the unwanted cogging force.

Further investigation into the Inset Magnet Consequent Pole machine focuses on improving the power factor through modifications made to the machine structure with no increase in the mass magnet, steel or copper used. Two novel variants with the added benefit of flux concentration effect are proposed and described. Finite Element Analysis is used to optimize, analyse and compare the electromagnetic performances for the three investigated machines.

Considering the complexity of manufacturing and number of components, two selected topologies are built and tested in the laboratory, the Inset Magnet Consequent Pole machine and V-shape Consequent Pole machine. The experimental results are compared to the simulation results to validate the design. In general, a good agreement is shown between the predicted and measured results. Afterwards, the experimental results obtained from the two prototypes are compared with each other. These results verify that the proposed V-shape Consequent Pole topology is superior in terms of no-load back EMF, force and power factor, while it exhibits lower cogging force in comparison with the Inset Magnet Consequent Pole topology. It is therefore concluded that the V-shape Consequent Pole machine is the best compromise between power factor, efficiency and ease of manufacture. It has half the number of components per pole of the best machine design presented, yet delivers 91% of the force density and 93% of the power factor.

The last part of this thesis investigates the feasibility of using the proposed V-shape Consequent Pole machine as an alternative design for an existing wave energy device developed by Uppsala University to assess the effect of employing this sort of machine on

the overall machine size and costs. Five variants of the V-shape Consequent Pole machine are described and compared.

Acknowledgements

All praises and thanks to Allah, Almighty god, and peace upon his messenger Mohammed, Who said: “Whoever is not thankful to the people is not thankful to Allah”.

Thanks are due to my academic supervisors. Firstly to Dr. Nick Baker, who has tirelessly given advice, counsel and support throughout these past years and patiently read and commented on my work, I thank you. Next to Dr. Kristopher Smith, who has greatly helped and supported throughout this project, I thank you.

Financial support from the Technical and Vocational Training Corporation, Saudi Arabia, has made this research possible and is gratefully acknowledged.

I would also like to thank the technicians and support staff at Newcastle University for helping me build, put together and test the prototypes. Special thanks go to Chris Manning from the mechanical workshop and James Richardson and Gordon Marshall in the UG lab.

I am also indebted to my colleagues in the UG lab (Electrical Power Group). It has been an exciting and great pleasure to work with creative, dedicated and talented colleagues. In particular Mohammad Raihan who has generously shares his knowledge with me. We had many interesting discussions during the past years, and I will always remember the time we spent together and the friendship.

I would like to thank my close friends Abdullah Faqihi and Ahmed Althobaiti for all the great moments we had shared together in Newcastle during the past few years.

I would also like to take this opportunity to thank my brother-in-law, Mohammed Al-qahtani and all his family members for their support and encouragement.

I am deeply indebted to my parents who, throughout my life, have shown me unconditional love and support. I would like also to mention my brothers and sisters at this point, who have always encouraged me in my work and life choices.

I cannot find the words to express my appreciation to my wife, Eidah. Her beautiful heart and sincerity have kept me optimistic about life. She has continually encouraged me and has supported me at every turn. Without her endless love, help and care, I would have been unable to accomplish this thesis.

This thesis is dedicated to my son, Ghassan, born on 14th June 2018.

Table of Contents

Abstract	i
Acknowledgements	iii
Table of Contents.....	iv
List of Figures	x
List of Tables.....	xvi
Nomenclature	xviii
Chapter 1: Introduction.....	1
1.1 Problem Statement and Motivation.....	1
1.2 Aim and objectives	2
1.3 Contribution to knowledge.....	3
1.4 Thesis layout	3
1.5 Published work.....	5
Chapter 2. Literature Review.....	7
2.1 Introduction.....	7
2.2 A Brief History and Development	7
2.3 Potential of Wave Energy in the UK	8
2.4 Classifications of WECs	10
2.4.1 Classifications of WECs Based on Wave Direction.....	10
2.4.1.1 Attenuator	10
2.4.1.2 Point absorber	11
2.4.1.3 Terminator.....	11
2.4.2 Classifications of WECs Based on Their Operation Principle	12
2.4.2.1 Submerged Pressure Differential (SPD)	12
2.4.2.2 Oscillating Wave Surge Converter (OWSC)	12
2.4.2.3 Oscillating Water Column (OWC)	12
2.4.2.4 Overtopping Devices (ODs).....	13
2.5 Power Take-off Systems	13
2.5.1 Pneumatic Systems	13
2.5.2 Hydraulic Systems	14
2.5.3 Direct Drive Mechanical Systems	15
2.5.4 Direct Drive PTO Systems	16

Table of Contents

2.5.4.1	The Archimedes Wave Swing (AWS).....	17
2.5.4.2	Inter Project Service (IPS) Buoy	18
2.5.4.3	Floating Buoy	19
2.6	Linear Electrical Machines	20
2.6.1	Linear Conventional Machines.....	21
2.6.1.1	Linear Induction Machine (LIM).....	21
2.6.1.2	Linear Permanent Magnet Synchronous Machine (LPMSM)	22
2.6.2	Variable Reluctance Permanent Magnet Machines (VRPMMs).....	23
2.6.2.1	Linear Transverse Flux Machine (LTFM).....	24
2.6.2.1.1	Power factor	26
2.6.2.1.2	End windings.....	27
2.6.2.1.3	Cogging force	27
2.6.2.2	Linear Vernier Hybrid Machine (LVHM)	27
2.6.2.2.1	Power factor	29
2.6.2.2.2	Attraction force	30
2.6.2.3	Linear Flux Switching Machine (LFSM)	30
2.6.3	Linear Tubular Permanent Magnet Machine (LTPMM).....	32
2.7	Selection of Machine for Further Development	33
2.8	Conclusion	36
Chapter 3. Development of the Linear Vernier Hybrid Machine.....		37
3.1	Introduction.....	37
3.2	Description of C-core Inset Magnet Consequent Pole (IMCP) Machine	37
3.3	Consequent Pole (Ferromagnetic Pole)	39
3.4	Design methodology	41
3.5	Mesh Sensitivity	42
3.6	Investigation of the C-core IMCP Machine.....	43
3.6.1	PM thickness	43
3.6.2	Translator Tooth Tip.....	44
3.6.3	Ferromagnetic Pole Ratio	45
3.6.4	Thickness of the Translator Coreback.....	47
3.7	Performance Comparison between the C-core Baseline LVHM and the C-core IMCP Machine	48
3.7.1	Flux Linkage and Back EMF	48
3.7.2	Force Capablity	50

3.7.3	Cogging Force	52
3.7.4	Power Factor	53
3.8	Machine Layout Development.....	53
3.9	Comparison between C-core and E-core IMCP Machines	54
3.10	Final IMCP Machine.....	56
3.10.1	Impact of Number of PM Pole Pairs	57
3.10.2	Description of the Proposed Final IMCP Machine.....	59
3.10.3	Operation Principle.....	61
3.10.4	Investigation of the Final IMCP Machine	62
3.10.4.1	PM thickness	62
3.10.4.2	Ferromagnetic Pole Ratio	63
3.10.4.3	PM Width.....	65
3.10.4.4	Translator Tooth Width.....	67
3.10.4.5	Translator Tooth Tip	68
3.10.4.6	Airgap Length	69
3.10.5	Armature Winding.....	70
3.10.6	Initial Performance Analysis	71
3.10.6.1	No-load Flux Linkage	71
3.10.6.2	Force Capability.....	72
3.10.6.3	Cogging Force.....	73
3.11	Conclusion	74
Chapter 4. New Configurations of Linear Vernier Hybrid Machine with V-shape Magnets.....		76
4.1	Introduction.....	76
4.2	Power Factor Improvement in the VHMs.....	76
4.3	V-shape Consequent Pole (VCP) Topology	77
4.3.1	Machine Configuration	77
4.3.2	Modified V-shape PM Arrays	78
4.3.3	Design Investigation	79
4.3.4	Validation of the VCP Machine	82
4.4	V-shape Topology.....	84
4.4.1	Machine Configuration.....	84
4.4.2	Machine Investigation	85
4.5	Performance Comparison.....	87

Table of Contents

4.5.1	Airgap Flux Density and Flux Density Distribution	88
4.5.2	No-load Flux Linkage.....	90
4.5.3	No-load Back EMF.....	91
4.5.4	Force Production	93
4.5.5	Force Capability	94
4.5.6	Cogging Force	96
4.5.7	Inductance.....	97
4.5.8	Losses and Efficiency.....	100
4.5.9	Mass.....	102
4.5.10	Attraction Force.....	103
4.5.11	Power Factor.....	108
4.6	Selection of Prototype Machines	108
4.7	Conclusion	109
Chapter 5. Prototype Manufacturing and Assembly		110
5.1	Introduction.....	110
5.2	Parameters of Prototypes	110
5.3	Stator Construction	111
5.4	Stator Aluminum Support.....	111
5.5	Winding	112
5.6	The Permanent Magnets	114
5.7	Translator Construction	116
5.8	Translator Support	117
5.8.1	Translator Aluminium Support.....	117
5.8.2	Translator Tufnol Support	118
5.8.3	Carbon Fibre Rods.....	119
5.9	Machine Aluminum Housing.....	121
5.10	Attaching Linear Guide (Rail) to the Machine Aluminium Housing	123
5.11	Attaching Carriages to the Translator Support	123
5.12	The Shaft.....	124
5.13	General Assembly and the Test-rig	125
5.14	Conclusion	126
Chapter 6. Experimental Results and Evaluation		127
6.1	Introduction.....	127

Table of Contents

6.2	Phase Resistance and Inductance Measurements	127
6.2.1	Phase Resistance Measurement	127
6.2.1.1	IMCP machine	128
6.2.1.2	VCP Machine	129
6.2.2	Phase Inductance	130
6.2.2.1	IMCP Machine	130
6.2.2.2	VCP Machine	132
6.3	No-load back EMF	132
6.3.1	IMCP Machine	133
6.3.2	VCP Machine	137
6.4	Cogging Force	140
6.4.1	IMCP Machine	141
6.4.2	VCP Machine	143
6.5	Force Production	145
6.5.1	IMCP Machine	145
6.5.2	VCP Machine	147
6.6	Force Variation with Current	147
6.6.1	IMCP Machine	147
6.6.2	VCP Machine	148
6.7	Resistive Load Tests	149
6.7.1	IMCP Machine	149
6.7.2	VCP Machine	151
6.8	Thermal Performance	152
6.8.1	IMCP machine	152
6.8.2	VCP Machine	154
6.9	Comparison of the IMCP and VCP Prototype Machines	154
6.9.1	No-load Back EMF	155
6.9.2	Cogging Force	156
6.9.3	Force Production	156
6.9.4	Output Power	157
6.9.5	Power Factor	158
6.10	Conclusion	159
	Chapter 7. Proposed VCP Machine for a 30kW Wave Energy Device	161

Table of Contents

7.1	Introduction.....	161
7.2	Description of the Existing LPMG Developed by Uppsala University	161
7.3	Multiple-Side Structure.....	164
7.4	Potential Advantages of Using the VCP Machine as an Alternative Generator for UU-WEC	165
7.5	Description of the Proposed Variants	166
7.6	Comparison of Mass and Cost of Active Materials	175
7.7	Conclusion	177
Chapter 8. Conclusion and Future Work.....		179
8.1	Introduction.....	179
8.2	Chapter / Results Summary	179
8.3	Suggestions for Future Work.....	184
8.3.1	The V-shape Machine.....	184
8.3.2	The Inset Magnet Consequent Pole Machine	185
8.3.3	The V-shape Consequent Pole Machine.....	186
8.3.4	Case Study	186
References.....		187
Appendix A: CAD Drawings		196
Appendix B: Glue Datasheet		205
Appendix C: Tufnol Datasheet.....		207
Appendix D: Carbon Fibre Rod Datasheet.....		208
Appendix E: Linear Guideway Datasheet.....		209
Appendix F: IMCP Machine Integrated with a Full Test Rig		211

List of Figures

Figure 2. 1: Global average wave energy in kW/m of crest length panning 10 years period [19].....	9
Figure 2. 2: (a) Attenuator (b) point absorber (c) terminator [21, 22]	11
Figure 2. 3: (a) Oscillating wave surge converter (b) oscillating water column (c) Overtopping Device[21]	13
Figure 2. 4: Schematic of a hydraulic PTO	14
Figure 2. 5: Illustration of a direct drive mechanical PTO	16
Figure 2. 6: Alternative power take off schemes[29]	17
Figure 2. 7: (a) The Archimedes Wave Swing (b) cross-section (c) photo [31].....	18
Figure 2. 8: Cross-section of the IPS buoy	19
Figure 2. 9: Floating buoy system	19
Figure 2. 10: Concept of linear machine.....	20
Figure 2. 11: Main classification of linear machine (a) short stator (b) short translator	21
Figure 2. 12: Linear induction machine.....	22
Figure 2. 13: Linear PM machine [36]	23
Figure 2. 14: Magnetic gearing.....	24
Figure 2. 15: Transverse flux machine	26
Figure 2. 16: Single phase unit of the LVHM	29
Figure 2. 17: Linear flux switching machine (a) single-sided [52] and (b) double-sided [80]	32
Figure 2. 18: Ironless tubular linear PM machine[86].....	33
Figure 3. 1: Machine configuration (a) baseline LVHM (b) C-core IMCP machine	38
Figure 3. 2: Flux contour, (a) baseline LVHM machine (b) C-core IMCP machine (dotted lines represent the flux leakage and solid line is the main flux).....	40
Figure 3. 3: Flux lines predicted by FEA, (a) baseline LVHM, (b) C-core IMCP.....	41
Figure 3. 4: Generated mesh for the proposed IMCP machine	43
Figure 3. 5: The effect of PM thickness on the thrust force	44
Figure 3. 6: Module of translator	45
Figure 3. 7: The effect of C_{tip} ratio on the thrust force	45
Figure 3. 8: Module of stator tooth (a) straight teeth (b) tapered teeth.....	46

Figure 3. 9: Variation of the thrust and cogging forces with respect to F_{pr}	46
Figure 3. 10: Variation of the thrust and cogging forces with respect to the translator coreback	47
Figure 3. 11: Comparison of no-load flux linkage (a) baseline LVHM, (b) C-core IMCP machine.....	49
Figure 3. 12: Comparison of no-load back EMF (a) baseline LVHM, (b) C-core IMCP machine.....	49
Figure 3. 13: Comparison of thrust force (a) baseline LVHM, (b) C-core IMCP machine .	50
Figure 3. 14: Comparison of thrust force capability (a) baseline LVHM, (b) C-core IMCP machine.....	51
Figure 3. 15: Comparison of cogging force (a) baseline LVHM, (b) C-core IMCP machine	52
Figure 3. 16: C-core IMCP (a) configuration (b) flux distribution.....	55
Figure 3. 17: Integrated 3-phase E-core IMCP (a) configuration (b) flux distribution.....	55
Figure 3. 18: E-core IMCP (a) configuration (b) flux distribution.....	56
Figure 3. 19: The effect of varying the number of PM pole pairs on the flux distribution (a) 2 PM pole pairs (b) 4 PM pole pairs.....	59
Figure 3. 20: Configuration of the proposed IMCP machine	60
Figure 3. 21: Operation principle at different translator positions. (a) Position a. (b) Position b. (c) Position c. (d) Position d.	61
Figure 3. 22: No-load field distribution (a) $x=0$, (b) $x=8\text{mm}$	62
Figure 3. 23: Variation of thrust force with respect to the magnet thickness	63
Figure 3. 24: Module of stator and translator	64
Figure 3. 25: The effect of ferromagnetic pole ratio on the thrust force and cogging force	64
Figure 3. 26: Effect of PM width on the thrust force and cogging force.....	66
Figure 3. 27: Consequent pole (a) rectangular (b) tapered	66
Figure 3. 28: No-load back EMF waveform under different PM width	67
Figure 3. 29: Effect of translator tooth width on the thrust force and cogging force	68
Figure 3. 30: Variation of the thrust force and cogging force with respect to the C_{tip} ratio .	69
Figure 3. 31: The effect of the airgap length on the thrust force	70
Figure 3. 32: Schematic of armature winding for the upper stator	70
Figure 3. 33: Flux linkage waveforms	72
Figure 3. 34: Variation of the static force with applied DC current	73

Figure 3. 35: Cogging force waveform.....	74
Figure 4. 1: Machine configuration (a) IMCP machine (b) VCP machine.....	78
Figure 4. 2: V-shape PM array structure (a) with ribs (b) without ribs	79
Figure 4. 3: The effect of iron ribs in the linear Vernier machine proposed in [117]	79
Figure 4. 4: Geometrical parameters for VCP machine.....	80
Figure 4. 5: The effect of the magnet span ration on the thrust force.....	80
Figure 4. 6: Saturation effect (a) $M_{sr} = 0.18$ and (b) $M_{sr} = 0.24$	81
Figure 4. 7: Different designs with different PM dimensions and fixed PM volume for VCP machine.....	81
Figure 4. 8: Variation of the thrust force and cogging force with respect to the design type	82
Figure 4. 9: No-load flux linkage waveforms over an electrical cycle.....	83
Figure 4. 10: No-load flux linkage harmonic spectrum.....	83
Figure 4. 11: V-shape machine configuration	85
Figure 4. 12: Geometrical parameters for V-shape machine	86
Figure 4. 13: Different designs with different PM dimensions and fixed PM volume for V-shape machine.....	86
Figure 4. 14: Variation of the thrust and cogging forces with respect to the design type ...	87
Figure 4. 15: No-load airgap flux density under one stator tooth for the three machines ...	88
Figure 4. 16: No-load flux density plot (a) IMCP (b) VCP and (c) V-shape machines	90
Figure 4. 17: Effect of machine configuration on the leakage flux and flux linkage (a) IMCP (b) VCP and (C) V-shape machine	91
Figure 4. 18: No-load flux linkage waveforms for the three machines	91
Figure 4. 19: No-load back EMF waveforms for the three machines.....	92
Figure 4. 20: No-load back EMF harmonic spectrum	93
Figure 4. 21: Thrust force waveforms for the three machines.....	94
Figure 4. 22: Force capability for the three machines	96
Figure 4. 23: Cogging force waveforms for the three machines	97
Figure 4. 24: Self inductances (a) IMCP (b) VCP and (c) V-shape machine.....	99
Figure 4. 25: Losses in the three machines	101
Figure 4. 26: Efficiency for the three machines.....	102
Figure 4. 27: VCP with different airgap displacements.....	104

Figure 4. 28: Attraction force between stator and translator for the IMCP machine (a) 0.1 mm displacement, (b) 0.5 mm displacement and (c) 0.9 displacement.....	105
Figure 4. 29: Attraction force between stator and translator for the VCP machine (a) 0.1 mm displacement, (b) 0.5 mm displacement and (c) 0.9 displacement.....	106
Figure 4. 30: Attraction force between stator and translator for the V-shape machine (a) 0.1 mm displacement, (b) 0.5 mm displacement and (c) 0.9 displacement.....	107
Figure 5. 1: Laminated stators (a) IMCP (b) VCP.....	111
Figure 5. 2: Stator Aluminium Support	112
Figure 5. 3: Winding process(a) Tufnol sheet (b) Tufnol sheet assembly (c) coil (d) final winding connection (banana plugs).....	113
Figure 5. 4: Insulation test using Megger	114
Figure 5. 5: Un-assembled magnets after checking and marking their polarities (a) IMCP magnets (b) VCP magnets	115
Figure 5. 6: Magnet assembly (a) IMCP (b) VCP (c) Tufnol support for V-shape magnets	116
Figure 5. 7: Laminated translator.....	117
Figure 5. 8: Assembled aluminium I-beam	117
Figure 5. 9: Assembled I-beam and carriage	118
Figure 5. 10: Tufnol shape effect (a) rectangular-shaped Tufnol (b) T-shaped Tufnol	119
Figure 5. 11: Laminated translator and Tufnol bars before the assembly	120
Figure 5. 12: Laminated translator and Tufnol bars after the assembly	120
Figure 5. 13: Flux linkage contour plot (a) with carbon fibre rods (b) without carbon fibre rods	121
Figure 5. 14: Stationary aluminium housing with mounted linear guides (a) CAD drawing (b) photo	122
Figure 5. 15: Attachment of the carriages	124
Figure 5. 16: U-shaped aluminium support	124
Figure 5. 17: A complete assembled linear machine	125
Figure 5. 18: A complete assembled test rig.....	126
Figure 6. 1: Resistance measurement setup (a) method 1 and (b) method 2	128
Figure 6. 2: Inductance measurement scheme	130

List of Figures

Figure 6. 3: Inductance measurement setup (method 1).....	131
Figure 6. 4: Inductance measurement setup (method 2).....	131
Figure 6. 5: Comparison of predicted and measured no-load back EMF of the IMCP machine at 0.3m/s.....	134
Figure 6. 6: Comparison of predicted and measured harmonic spectra for the IMCP machine	135
Figure 6. 7: Measured no-load back EMF of the IMCP machine at constant speed of 0.3m/s for one stroke, 120mm	135
Figure 6. 8: Measured no-load back EMF of the IMCP machine under variable speed for one stroke, 120mm	136
Figure 6. 9: Voltage-speed characteristics at open circuit for the IMCP machine	136
Figure 6. 10: Comparison of predicted and measured no-load back EMF of the VCP machine at 0.3m/s.....	138
Figure 6. 11: Comparison of predicted and measured harmonic spectra for the VCP machine	139
Figure 6. 12: Measured no-load back EMF of the VCP machine under variable speed for one stroke, 120mm	139
Figure 6. 13: Voltage-speed characteristics at open circuit for the VCP machine	140
Figure 6. 14: Complete test rig	141
Figure 6. 15: Variation of the measured cogging force of the IMCP machine with translator displacement over two pole pitches with offset.....	142
Figure 6. 16: Comparison of predicted and measured cogging force of the IMCP machine after removing the offset.....	143
Figure 6. 17: Comparison of predicted and measured cogging force of the VCP machine after removing the offset	144
Figure 6. 18: Static DC force measurement setup	145
Figure 6. 19: Winding connection diagram used for static DC force measurement.....	146
Figure 6. 20: Comparison of predicted and measured static DC force of the IMCP machine	146
Figure 6. 21: Comparison of predicted and measured static DC force of the VCP machine	147
Figure 6. 22: Comparison of predicted and measured static DC force of the IMCP machine under different excitation currents.....	148

Figure 6. 23: Comparison of predicted and measured static DC force of the IMCP machine under different excitation currents.....	149
Figure 6. 24: Resistive load tests measurement setup	150
Figure 6. 25: Generator equivalent circuit connected to a 3-phase resistive load	150
Figure 6. 26: Variation of the output power of the IMCP machine under different resistive loads.....	151
Figure 6. 27: Variation of the output power of the VCP machine under different resistive loads.....	152
Figure 6. 28: Thermal test measurement setup	153
Figure 6. 29: Thermal behaviour of the IMCP machine.....	153
Figure 6. 30: Thermal behaviour of the VCP machine.....	154
Figure 6. 31: Comparison of the measured no-load back EMF at 0.3m/s for IMCP and VCP machines	155
Figure 6. 32: Comparison of the measured cogging force for IMCP and VCP machines .	156
Figure 6. 33: Comparison of the measured static DC force for IMCP and VCP machines	157
Figure 6. 34: Comparison of the resistive load test for IMCP and VCP machines	158
Figure 7. 1: (a) buoy (b) hull (c) UU-WEC (d) system layout (e) Translator with PM mounted on (f) top view of stator (g) laminated single side of the stator [123, 125, 126].....	164
Figure 7. 2: Possible winding configuration for multiple-sided machine [35].....	165
Figure 7. 3: Design A structure.....	167
Figure 7. 4: Multiple double-sided structure developed in [130]	168
Figure 7. 5: Design B structure (a) top view (b) 3D rendered view and (c) side view.....	169
Figure 7. 6: Design C structure (a) top view (b) 3D rendered view	171
Figure 7. 7: Design D structure (a) top view (b) 3D rendered view (c) side view (d) winding configuration described in section 8.3	173
Figure 7. 8: Design E structure (a) top view (b) 3D rendered view	175
Figure 7. 9: Mass and cost comparison	177

List of Tables

Table 2. 1: Comparison of linear machines for low speed applications	35
Table 3. 1: Key parameters for both baseline LVHM and C-core IMCP machine	39
Table 3. 2: Materials assigned in FEA model.....	42
Table 3. 3: Performance comparison of baseline LVHM and C-core IMCP machine.....	56
Table 3. 4: Specifications of the proposed IMCP machine	60
Table 3. 5: Slot and coil parameters	71
Table 3. 6: No-load flux linkage.....	72
Table 4. 1: PM dimensions and V-angle for the six designs	82
Table 4. 2: Flux linkage for the VCP machine	84
Table 4. 3: PM dimensions and V-angle for the four designs	86
Table 4. 4: Comparison of Peak and RMS values of the back EMF	92
Table 4. 5: Comparison of the average thrust force and force ripple	94
Table 4. 6: Comparison of force density and shear stress	95
Table 4. 7: Comparison of cogging force and cogging force/ thrust force ration.....	97
Table 4. 8: Comparison of self and mutual inductances.....	100
Table 4. 9: Mass comparison	103
Table 5. 1: Key parameters for both prototypes	110
Table 5. 2: Magnet dimensions.....	114
Table 6. 1: Comparison of predicted and measured resistance values of the IMCP machine	129
Table 6. 2: Comparison of predicted and measured resistance values of the VCP machine	129
Table 6. 3: Comparison of predicted and measured inductance values of the IMCP machine	132
Table 6. 4: Comparison of predicted and measured inductance values of the VCP machine	132

List of Tables

Table 6. 5: Variation of the no-load back EMF with different airgap length for IMCP machine	137
Table 6. 6: Variation of the no-load back EMF with different airgap length for VCP machine	140
Table 6. 7: Variation of the cogging force with different airgap length for IMCP machine	143
Table 6. 8: Variation of the cogging force with different airgap length for VCP machine	144
Table 6. 9: Comparison of the measured magnitude of the back EMF for IMCP and VCP machines	155
Table 6. 10: Comparison of the measured DC static force for IMCP and VCP machines.	157
Table 6. 11: Summary of the performance comparison for IMCP and VCP machines	160
Table 7. 1: Main specifications for the LPMG developed by UU.....	162
Table 7. 2: Mass of design A	167
Table 7. 3: Mass of design B	170
Table 7. 4: Mass of design C	171
Table 7. 5: Mass of design D	173
Table 7. 6: Mass of design E	175
Table 7. 7: Comparison between five configurations	176
Table 7. 8: Material prices used in cost analysis	177
Table 8. 1: Summary of the performance comparison for IMCP and VCP machines	183

Nomenclature

A	Conductor area
A_{ag}	Airgap area
AWS	Archimedes Wave Swing
α	V-angle
β	Flux density
CO ₂	Carbon Dioxide
CE	European Commission
DD	Direct Drive
DECC	Department of Energy and Climate Change
DDMSs	Direct Drive Mechanical System
DC	Direct current
D_{mt}	Displacement between C-core modules
D_{st}	Displacement between adjacent stator teeth
FEA	Finite element analysis
F	Number of Ferromagnetic poles
f	Frequency
F_{pr}	Ferromagnetic pole ratio
F_{max}	Maximum force
F_{min}	Minimum force
$F_{average}$	Average force
F_d	Force density
I	Current
IMCP	Inset magnet consequent pole
IPS	Inter Project Service
Ke	Current coefficient
K _h	Hysteresis coefficient
L	Self-inductance

Nomenclature

l	Conductor length
LCR	Inductance-capacitance-resistance
LFSM	Linear flux switching machine
LIM	Linear induction machine
LPMSM	Linear permanent magnet synchronous machine
LTPMM	Linear tubular permanent magnet machine
LVHM	Linear Vernier hybrid machine
m	Number of phases
m_s	Magnet span
m_{sr}	Magnet span ratio
n	Positive integer
N_{coil}	Number of coils
ODs	Overtopping Devices
OWC	Oscillating Water Column
OWSC	Oscillating Wave Surge Converter
P_{cu}	Copper loss
PF	Power factor
P_{eddy}	Eddy current loss
P_{iron}	Iron loss
PM	Permanent magnet
PMLG	Permanent Magnet Linear Generator
POT	Power take-off
P_{out}	Output power
R	Phase resistance
R_g	Airgap reluctance
R_m	Permeant magnet reluctance
R&D	Research & Development
SPD	Submerged Pressure Differential
THD	Total harmonic distortion
VCP	V-shape consequent pole

Nomenclature

v	Velocity
VRPMM	Variable reluctance permanent magnet machine
ω	Angular velocity
WEC	Wave Energy Converter
W_{ut}	Displacement between C-core stator tooth
w_{PM}	Width of the permanent magnet
W_{ut}	Mechanical displacement between two C-core teeth
W_{tip}	Width of the translator tooth tip
W_{root}	Width of the translator tooth root
W_{tip}	Ratio of the width of the translator tooth tip to the translator tooth pitch
W_{root}	Ratio of the translator tooth root to the translator tooth pitch
W_{sts}	Width of the stator tooth shoe
x	Translator displacement
η	Efficiency
ρ	Electrical resistivity
σ	Shear stress
Ψ_m	Flux produce by permanent magnet
τ_t	Translator tooth pitch

Chapter 1: Introduction

1.1 Problem Statement and Motivation

A large fraction of the world's population relies upon fossil fuel for their energy, due to this the planet is facing a global challenge for the future. The enormous growth of human population, and with it the parallel rise in energy consumption, will surely lead to the inevitable extinguishing of already depleted supplies of fossil fuel. Furthermore, going ever deeper into the Earth's crust is problematic.

Mankind must reduce dependency upon fossil fuel, focusing upon global issues that pertain to both CO₂ levels, and resulting climate change - electricity needs to be generated from natural, renewable, resources – such as wind, wave and solar power. Limitations to wind and solar power are that they are small supplementary additions to the grid, they have irregular supply and lower power density[1]. Wave energy, however, has a large power density and a huge supply - this in turn allows huge possibilities that could input globally, and thus further power demand [1].

In the 1970's, research started to look at extracting energy from ocean waves. Hydraulic and air turbines have been proposed to interface wave energy devices with a conventional high speed rotary electrical generator. However, using these interfaces means the system becomes more complex, and this presents issues of reliability and maintenance, and these are particularly important in an offshore context. Moreover, the air turbines and hydraulics create energy loss - this in turn means issues of efficiency.

Direct Drive Wave Energy Converters (DD-WECs) offer a solution to these problems by connecting the translator of a linear generator directly to a floating device - for example a buoy - which moves with the motion of the waves, while the stator is fixed on the seabed. The result is an elimination of interconnected moving parts as used in non-direct drive WECs, creating a robust system with improved efficiency. The linear generator adopted in this system must generate high thrust force at low speed, which can be achieved by employing a variable reluctance machine such as the Linear Vernier Hybrid Machine (LVHM) proposed in [2]. However, the downside is this machine needs high quantities of magnet material and suffers from low power factor and high cogging force.

To sum up this thesis is concerned with the development of the LVHM capable of supplying the required power at low velocities demanded by wave energy converters.

Research into such machines simplifies the use of direct drive power take-off, whereby the electrical machine is coupled directly to the moving part of the device.

1.2 Aim and objectives

The main aim of this research is to investigate an alternative linear electrical machine topologies for improved performance in direct drive wave energy converters.

The specific objectives of this research are as follows:

- To design, optimise and analyse the LVHM with consequent pole for the purpose of magnet mass reduction.
- To investigate the effect of implementing tapered ferromagnetic poles on the machine electromagnetic performance.
- To examine the influence of varying the translator tooth tip on flux behaviour.
- To reduce the thickness of the translator coreback.
- To improve the power factor by replacing the rectangular Permanent Magnet (PM) with a V-shape PM arrangement.
- To improve the power factor further by burring the V-shaped PM with adjacent alternating polarity to provide flux concentration effect in both polarities.
- To explore the structural and mechanical aspects of an unconventional permanent magnet machine topology.
- To perform a comparative study on different machine topologies when all machines have the same PM mass, overall active volume and current density.
- To examine the feasibility of implementing proposed Inset Magnet Consequent Pole (IMCP) machine in a real direct drive wave energy converter developed by Uppsala University.
- To build and test two selected lab-scale prototypes
- To validate results by performing an experimental set-up for assessing the agreement between the simulated and measured results.

Based on the problem statement defined above, research question of the thesis is formulated as:

- How should the Linear Vernier Hybrid Machine be designed in order to maximise its utility/performance for a direct drive wave energy applications?

1.3 Contribution to knowledge

The research in this thesis contributes toward the linear version of VHMs modelling, design optimisation, reduction of the magnet and translator mass. The significant contributions are discussed in detail in Chapters 3, 4 and 6 and can be summarised as:

- 1) The LVHM topology which improves on some of the problems associated with pole-to-pole leakage flux is developed and evaluated. The tapered ferromagnetic poles are utilised and analysed in this design, which can reduce the leakage flux circulating between neighbouring PMs in the baseline VHM [2]. Reshaping the consequent poles would also result in a noticeable reduction of the undesirable harmonics. Therefore, the developed design is capable of producing higher no-load back EMF and thrust force, while it exhibits lower cogging force and force ripple compared to its counterpart.
- 2) A novel configuration of consequent pole LVHM incorporated with V-shape magnet arrays, which provide flux concentration effect, is proposed and designed in line with the aim of power factor improvement. In addition, this machine can offer higher force density compared to the IMCP machine.
- 3) A developed topology of the LVHM with the feature of flux concentration and rib-less V-shape magnet arrays with alternating polarity is proposed to further improve the power factor without increasing the magnet mass.
- 4) A new translator assembly is proposed to keep the translator core back as minimal as possible offering a significant reduction in the translator mass.
- 5) A case study on integrating the V-shape consequent pole machine into an existing wave energy device has been carried out in this research. A number of designs with different assembly structure has been studied. The material consumption and associated costs of the scaled up machines have been investigated and evaluated. The results imply that the proposed machine can offer a significant reduction in the PM mass. The optimal structure can save the translator mass.

1.4 Thesis layout

The layout and contents of the thesis is briefly described here:

Chapter 2: This Chapter gives literature review on wave energy converters and linear electrical machines. It starts with an introduction to wave energy, followed by the potential of extracting this sort of energy. The most common existing wave energy converters used to extract the energy from the waves are described as based on their classifications. An

overview of power take-off systems is also presented, in which the direct drive power take-off is covered in significant details, supported with some available examples. The Chapter ends with a survey on a number of topologies of linear electrical machines that have been proposed for DD-WECs. The operation principles, advantages and disadvantages of each topology are also discussed. Based on one favoured topology, different magnet configurations are identified and investigated.

Chapter 3: This Chapter begins with a description of the development of the C-core Inset Magnet Consequent Pole machine. The focus is, however, on the influence of employing the ferromagnetic poles on the machine performance. The effect of adopting these reshaped poles on cogging force minimisation are illustrated and analysed. A deep analysis of the electromagnetic performance of the C-core IMCP machine is compared to that of the baseline LVHM [2]. Further investigations on E-core IMCP machine is also covered in detail.

Chapter 4: This Chapter introduces a novel structure of consequent pole LVHM by integrating V-shape magnet arrays with iron poles, providing a flux concentration effect. This feature would result in an increase in the airgap flux density and hence the power factor. Further investigation on the LVHM with buried magnets is performed later, in which a new V-shaped machine with adjacent alternating polarity is analysed and compared to the former one. One topology was selected to be built considering the manufacturing complexity.

Chapter 5: This Chapter gives a detailed description of manufacturing process for the two selected laboratory prototypes machines covered in Chapters 3 and 4. Practical assembly techniques are proposed for translator and stator assembly, where the minimum possible thickness of the translator core back can be achieved, and the mechanical airgaps can be flexibly adjusted. A complete test rig used in validation tests, which includes the prototype machine, ball screw drive and force transducer is discussed.

Chapter 6: This Chapter presents details of the experimental evaluations and compares them with the simulation results in order to validate predictions.

Chapter 7: This Chapter presents a case study focusing on the replacement of the existing large-scale linear generator developed by Uppsala University with the proposed V-shape

Consequent pole. A number of designs are investigated in terms of the active material consumption and associated costs.

Chapter 8: This Chapter identifies the key conclusions derived from this research along with author's recommendations for further work.

1.5 Published work

Journals

1. Almoraya AA, Baker NJ, Smith KJ, Raihan MAH. *Design and analysis of a flux concentrated Linear Vernier Hybrid Machine with Consequent Poles*, IEEE Transactions Industry Applications Society, 2019.
2. Baker, N.J., Raihan, M.A., Almoraya, A.A., Burchell, J.W. and Mueller, M.A., *Evaluating Alternative Linear Vernier Hybrid Machine Topologies for Integration into Wave Energy Converter*, IEEE Transactions on Energy Conversion, 33(4), pp.2007-2017,2018.
3. B. McGilton, A.A. Almoraya, M. A. H. Raihan, R. Crozier, N.J. Baker, M. Mueller; *An Investigation into Linear Generators with Integrated Magnetic Gear for Wave Energy Power Take-Off*, In: *The Journal of Engineering: IET*.
4. Almoraya AA, Baker NJ, Smith KJ, Raihan MAH. *Flux Concentrated Doubly Salient Linear Permanent Magnet Machine*, In: *The Journal of Engineering: IET*.

Conferences

1. Baker N.J., Raihan M.A.H., Almoraya A., McDonald S.; *Electric drive train design for wave energy converter*, In *The 12th International Symposium on Linear Drives for Industry Applications (LDIA2019, Neuchâtel, Switzerland*.
2. Almoraya, A.A., Baker, N.J., Smith, K.J. and Raihan, M.A.H., 2018, September. *A New Configuration of a Consequent Pole Linear Vernier Hybrid Machine with V-shape Magnets*, In 2018 XIII International Conference on Electrical Machines (ICEM) (pp. 2002-2008). IEEE.
3. Almoraya, A.A., Baker, N.J., Smith, K.J. and Raihan, M.A.H., 2017, August. *An investigation of a linear flux switching machine with tapered ferromagnetic poles*, In

Electrical Machines and Systems (ICEMS), 2017 20th International Conference on (pp. 1-5). IEEE.

4. Baker, N.J., Raihan, M.A.H., Almoraya, A.A. and Wang, J., 2017. *Electric Machine Design for Wave Energy Converters*, in. In European Wave and Tidal Energy Conference-EWTEC.
5. Almoraya, A.A., Baker, N.J., Smith, K.J. and Raihan, M.A.H., 2017, May. *Development of a double-sided consequent pole linear Vernier hybrid permanent-magnet machine for wave energy converters*, In Electric Machines and Drives Conference (IEMDC), 2017 IEEE International (pp. 1-7). IEEE.

Chapter 2. Literature Review

2.1 Introduction

The aim of this Chapter is to explore why DD-WECs require the development of new electrical machines. The Chapter also gives the reader a brief history on the development of wave energy and its potential as a renewable energy resource in the UK. The classifications of WECs based on wave direction and operation principle are introduced. As such, an overview of the most common existing technologies of the WECs, which are driven through mechanical intermediates such as pneumatic or hydraulic systems, or can be directly driven by a linear generator are provided. Different power take-off (PTO) systems of WECs are introduced and described. In particular a direct drive system is discussed in some depth, highlighting the required electrical machine for of such a system.

The last part of the Chapter presents an overview of small-scale linear electrical machines that have been proposed for DD-WECs, and briefly outlines both the operation principles and constructional features on which they are based. The main characteristics of the linear machines are given in order to highlight their key advantages and disadvantages. Considering primarily the mechanical and electrical point of view, one machine topology is selected for further investigation and is developed in the next two Chapters.

2.2 A Brief History and Development

The extraction and utilisation of the ocean waves as a source of energy was first recognised in Paris in 1799, when Girard and his son proposed and designed a machine for capturing the wave's motion to move large wooden beams for driving pumps and mills [3]. After more than ten years Bochaux-Praceique constructed the first wave energy converter using an oscillating water column to supply his house with electricity [4]. In the late 1940s, the Japanese pioneer of modern wave energy developed and tested several concepts of floating buoys driven by wave energy, one of which later became known as oscillating water column [5].

In 1973, due to the oil crisis a renewed concern about alternative energy such as wave, wind and solar energy was motivated in many affected countries including the UK. During this time the UK government funded academic institutions and industries to prepare plans

for how wave energy could be exploited. A famous milestone in wave energy was the invention of the Salter Duck by Stephen Salter from the University of Edinburgh [6]. In the 1980s, with the recovery of oil prices, the UK government dropped wave energy funding in favour of high rated generating systems including coal and nuclear power plants, [7]. Nevertheless, some researchers continued working in this area and a few prototypes were tested in the sea.

Over the next decade, with the increase in global temperature and fuel prices, the government funding and hence research in the field of wave energy was rekindled once again, leading to an increased level of R&D projects. During this period the European Commission (EC) played a significant role in boosting innovation and cooperation between countries by supporting conferences affiliated with ocean technology and marine science. Also as a result of that support, the European Wave Energy Thematic Network and the Coordinated Action of Ocean Energy were established in 2000 and 2004 respectively [8]. Since 2008, ocean energy devices have been contributing small amounts to power generation in the UK by more than 11,000 MWh of electricity [9]. There are many different concepts that developers have devised to convert the energy of ocean waves into electricity. These include devices with different principles of operation and PTO mechanisms and there is yet to be an agreement on one particular device configuration.

A large amount of research has been conducted by industry in the progress of WECs; as discussed in detail in section 2.6. A comprehensive review on the history of ocean energy is not covered in depth in this thesis. However, more information about the major existing gaps, barriers and challenges to the progress of this sector can be found in [7, 10-13]

2.3 Potential of Wave Energy in the UK

Among all renewable energy resources wave energy is one of the most promising resources that has drawn tremendous attention in the last decade due to the most distinguishing features from other renewable energy resources [14]. Wave energy has higher power density than that of wind and solar power, i.e. 15-20 times higher and is capable of generating electricity up to 90% of the time with the aid of WECs [14]. Figure 2.1 illustrates the average power density in different locations around the world. It can be observed that in some European countries including the UK, wave power could be harnessed very effectively to produce electricity. The global wave power resource is estimated to have a potential of 2TW [14, 15]. A calculation of a wave traveling over a line around the coast has been widely

applied to estimate the potential of wave energy in the UK [9], which represents nearly 27GW. In the UK, considering the fishing, shipping and other environmental constraints the offshore and nearshore regions are estimated to provide 70 TWh/year and 5.7 TWh/year respectively [16]. To put this Figure into perspectives, the annual UK's energy consumption is 360 TWh/year, meaning that over 10% of the expected 2050 electricity demand could be met by utilising these resources [16]. This potential has attracted the wave energy developers' attention along with more than 250 wave energy companies and 100 tidal developers [16].

According to the Department of Energy and Climate Change (DECC) in 2011, 27 GW of wave power and tidal stream could be established by 2050 [17]. However, reference [18] has reported that 960 kW of the existing installed wave power and 2100 kW of the installed tidal in the UK have not met the expectations of DECC. Progress in the UK is less than expected, and some developers have had to stop working as all the challenges of ocean energy are recognised.

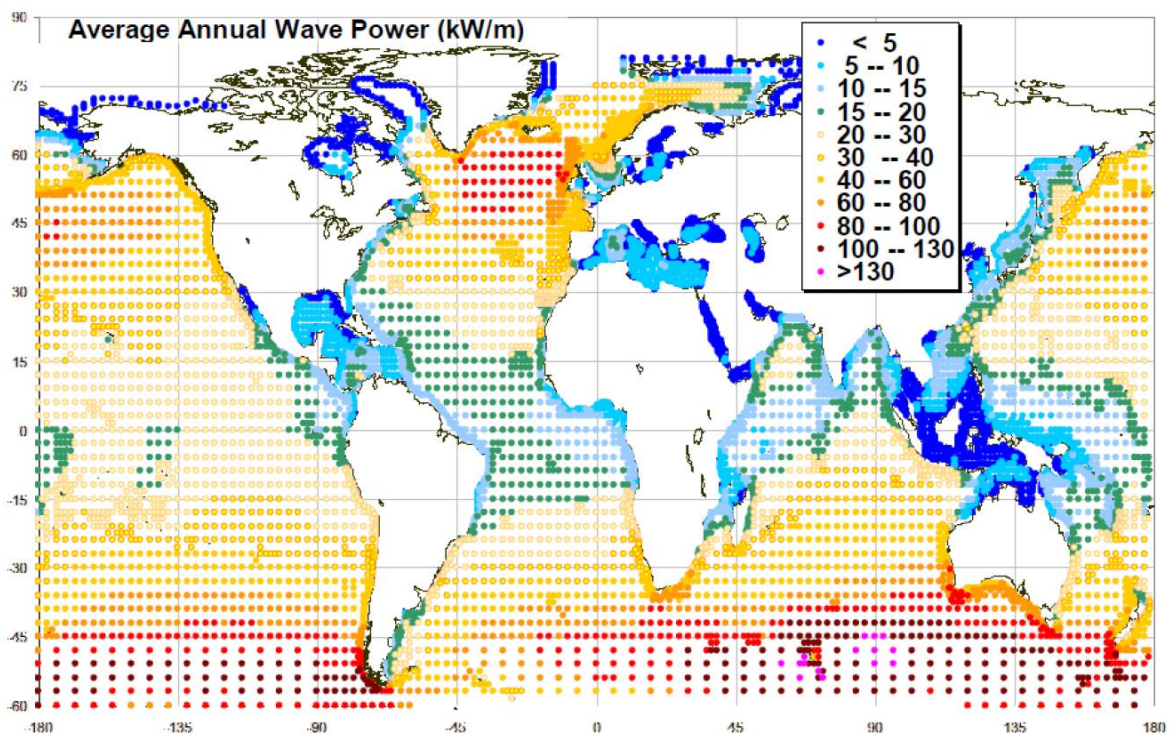


Figure 2. 1: Global average wave energy in kW/m of crest length panning 10 years period [19]

2.4 Classifications of WECs

There are a lot of challenges and issues associated with WECs especially when designing and constructing these devices. Authors [20] have reported the key technical challenges which include:

- Irregular motion of waves
- More efficient resources are available for offshore in which regular maintenance is problematic
- The difficulty of performing the long-term sea trial measurements due to the lack of robustness in rough seas
- The importance of making predictions of the storms and other extreme wave conditions when power levels can exceed 2000kW/m².
- The conversion of low frequency (nearly 0.1 Hz), and high force oscillating movement into beneficial motion to drive an electrical generator with an output quality satisfying the grid requirements.
- As waves vary in height and period, their respective power levels vary accordingly. While gross average power levels can be predicted in advance, this variable input has to be converted into a smooth electrical output and hence usually necessitates some type of energy storage system, or other means of compensation such as an array of devices.

Presently, there are many WECs being developed. These devices can be classified based on their location; shoreline, nearshore or offshore, and the way of capturing energy from the waves. An extensive review of wave energy converter technologies are available in [8, 21, 22].

2.4.1 Classifications of WECs Based on Wave Direction

2.4.1.1 Attenuator

An attenuator WEC is a long floating device which is designed with a short length relative to the wavelength. When the instant waves travel in parallel to the device, bodies ride the waves. These bodies are generally jointed units so they flex and bend as waves pass along their length, and the relative motion between the segments is used to produce power. The Pelamis became the first offshore WEC to produce electricity into the grid in Portugal,

at the Aguadoura Wave Park in 2008[23]. An example of this technology is the Pelamis device shown in Figure 2.2 (a) developed by Ocean Power Delivery Ltd.

2.4.1.2 Point absorber

A point absorber is a device that extracts energy from waves. With its small dimensions of the floater in comparison with the dominant wavelength, this system can offer high extracted wave power to mass ratio [21]. It is a floating body that can move up and down on the surface of the water or flooded under the water depending on the pressure differential as shown in Figure 2.2 (b). This device possesses the merit of capturing energy from a wave's motion in any direction either a vertical or horizontal direction. It also has the advantage of being able to withstand strong storms. There are many examples of point absorbers, one of which is the heaving point absorber proposed by Vantorre et al. in 2004. Another example is the Ocean Power Technology's Powerbuoy [24].

2.4.1.3 Terminator

Terminators are semi-submerged devices which spread perpendicular to the predominant direction of the wave, while their main axis is parallel to the incoming wave. The oscillating water column is a form of terminator, in which the waves force water to enter through the input port underneath the surface and is hence stored in the enclosed chamber. As the water pressure increases, the top of the structure forces the air out to drive the turbine for generating electricity. Figure 2.2 (c) shows an example of this type of terminator known as Oceanlinx Moored Oscillating Water Column Terminator, off the Coast of Australia.

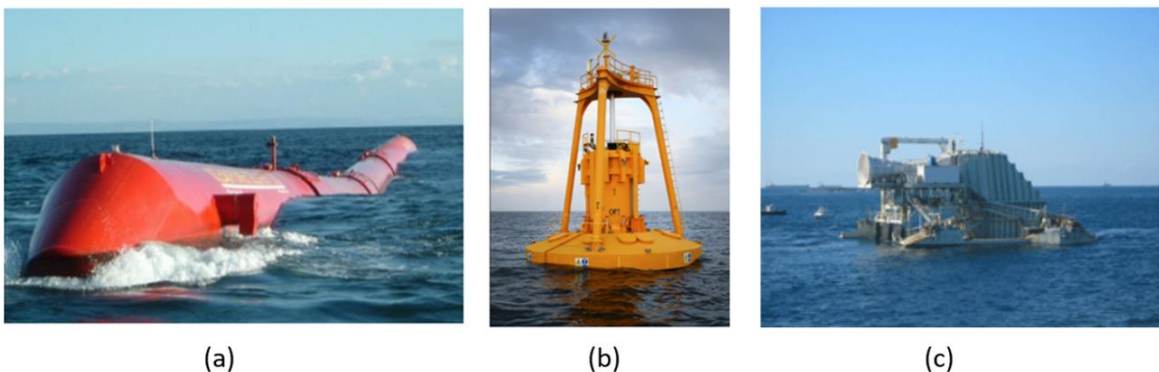


Figure 2. 2: (a) Attenuator (b) point absorber (c) terminator [21, 22]

2.4.2 Classifications of WECs Based on Their Operation Principle

WECs have been categorized in several ways , [25], [3], [21] based on their approach of extracting the energy or operation principle. The classifications described in [21, 22] are presented in this section. According to the literature, the most promising type has not been nominated yet. The basic operating principles of the three main classifications are described below.

2.4.2.1 Submerged Pressure Differential (SPD)

This concept operates based on the utilisation of the dynamic pressure alteration above the submerged point absorber between wave crests and neighbouring troughs. It is situated near shore and basically consists of two major parts: a seabed-mounted tubular chamber and moveable tube on the top. A well-known example of this category is the Archimedes Wave Swing, which will be described in detail in section 2.5.4.1.

2.4.2.2 Oscillating Wave Surge Converter (OWSC)

The OWSC is a near-shore version of wave power technology that is designed to extract ocean wave energy. It has a bottom-hinged flap placed perpendicular to the seabed as shown in Figure 2.3 (a), in which the flap swings back and forth with the aid of the boosted horizontal particle waves' motion. Since this system is capable of working with a large variety of wave ranges, the efficiency of electricity production from waves is improved as a result. The Aquamarine Power Oyster [26] is a developed OWSC that was established in Edinburgh in 2005. A large-scale prototype has been designed and built by European Marine Energy Centre (EMEC).

2.4.2.3 Oscillating Water Column (OWC)

The OWC is a shoreline device which comprises of a large concrete chamber with an opening submerged under the waterline as shown in Figure 2.3 (b). As waves move a large amount of water is collected and forced into the chamber, acting as a piston by compressing the air within the chamber. This pressurized air is then released to drive the turbine which is connected to the generator for power production. It has been reported that the concept of the OWC device possesses the advantage of having a simple and rigid structure [5]. This technology can be installed at the shoreline as Wavegen Limpet, which was mounted in the

Isle of Islay, Scotland. Another example of the OWC device is Oceanlinx, proposed by Australian wave energy developer with two versions: one for the surface and the other for deep water [5].

2.4.2.4 Overtopping Devices (ODs)

The design structure of overtopping devices demonstrated in Figure 2.3 (c) allows sea water captured from incident waves to flow passing through slopes towards storage reservoirs above sea level. Then, the contained water returns to the sea passing through a conventional hydro-turbine located below the reservoir, which is coupled to a generator to produce power. An example of the overtopping device is the Wave Dragon [21]

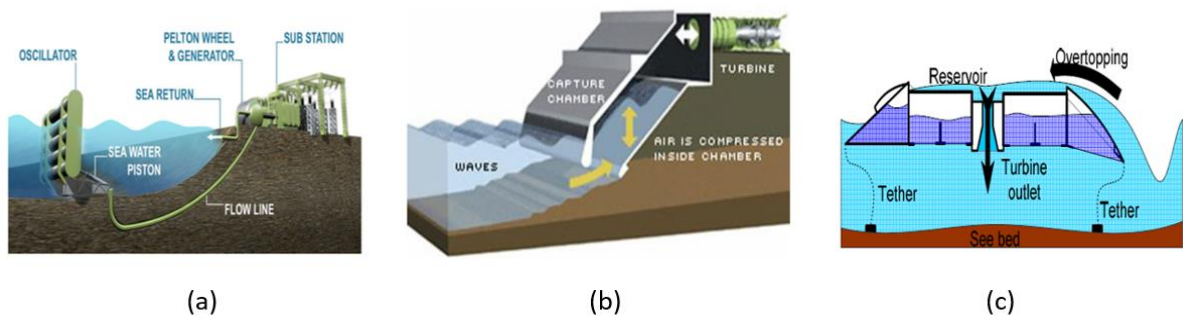


Figure 2. 3: (a) Oscillating wave surge converter (b) oscillating water column (c) Overtopping Device[21]

2.5 Power Take-off Systems

The power take-off system can be defined as the mechanism that is used to convert mechanical motion into useable electricity. In these systems, the conversion processes basically requires either a direct-drive linear generator or a conventional rotary generator coupled to a mechanical interface to generate electrical power by transferring the alternative motion into continuous unidirectional motion. The mechanical interface can be a pneumatic or hydraulic turbine, or a mechanical gearbox. General descriptions for the most common PTO systems as follows:

2.5.1 Pneumatic Systems

In wave energy devices such as an Oscillating Water Column, air turbines are commonly used to convert wave energy into mechanical energy. The concept was to use the

oscillating water level produced by the ocean waves to drive a turbine. The key challenge facing this device is the bidirectional nature of the airflow. Rectifying the air flow combined with a conventional turbine through non-returning valves is one solution. However, this configuration is complex, has high maintenance costs and for prototype size the valves become too large to be a viable option [13]. Therefore, a self-rectifying air turbine can be used to obtain a unidirectional rotation converted from an alternating air flow as another solution.

In the last 40 years, many kinds of self-rectifying turbines have been proposed, such as Wells turbines, Impulse turbines and Denniss-Auld turbines. The Wells air turbine is the most common air turbine in WECs [21] due to its capacity to rotate continuously in the same direction independent of the airflow direction, and the merits of a relatively high velocity ratio of rotational blade to airflow and has low manufacturing cost. However, several drawbacks have been reported such as low torque at small flow rates; low efficiency (<65%); poor starting; high noise; and a relatively large diameter for its power [21].

2.5.2 Hydraulic Systems

Large forces on oscillating bodies can be extracted from waves in low frequencies. This characteristic of the waves allows high pressure oil hydraulic systems to be employed in WECs. The following diagram describes the basic structure of the hydraulic PTO systems adopted in WECs.

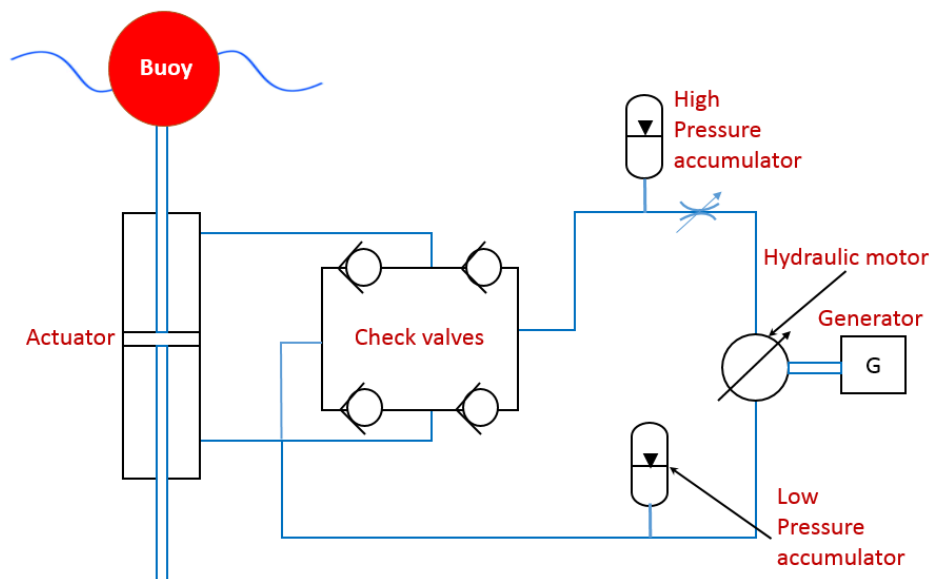


Figure 2. 4: Schematic of a hydraulic PTO

The extracted forces produced by the waves allow the body or buoy of the WEC to activate a hydraulic arm or piston, leading to high pressurised hydraulic oil. The fluid flows in the circuit passing through check valves, which in turn allow the oil to flow in only one direction. In other words, these valves can rectify the hydraulic fluid to flow in one direction regardless of the direction of the piston motion. Then, the hydraulic fluid is collected in a high-pressure accumulator. The absence of the accumulator would lead to an imbalanced flow rate, which can influence the hydraulic motor output and thus create an irregular generator output as a consequence. The electrical generator is derived by the hydraulic motor to generate the electricity. The energy output and the overall efficiency of the system can be determined by controlling the flow into the hydraulic motor. Though the flow is smoothed by the accumulator and a flow control valve in this circuit, further advanced control strategies are employed in PTO systems to maximize the output power in a wide range of sea states [21]. Finally, the low-pressure accumulator provides a definite level of low pressure in return line so as to prevent cavitation.

These systems have the feature of strong large quantities with a smooth output power. However, there are a number of challenges associated with their design and operation: the containment of the hydraulic fluid, the wear of the seals, the efficiency of the PTO, the maintenance of the system under real sea conditions, the possibility of excess motion of the piston and the need for end-stops and energy storage are among those which are discussed in detail in [21]

2.5.3 Direct Drive Mechanical Systems

Direct mechanical drive systems (DDMSs) are mechanical intermediates that are used to link the WEC directly to the electrical generator, which in turn can reduce the number of moving parts as illustrated in Figure 2.5. These mechanical intermediates can be a step up gear box, pulley, simple mooring line and belt in which they are usually used in point absorber WECs. Either rotary or linear electrical machines can be used to generate electricity. In both cases storage and frequency converter systems are required to compensate the velocity variations. For this type of PTO the available storage system can be a battery, electrochemical cells, ultra-capacitor and flywheel. All of which have advantages and disadvantages, e.g. the battery can offer high energy density but a short life span and is environmental unfriendly, whereas the ultra-capacitor has a longer life span but a higher price. The most common example of a point absorber using DDMS is that

developed by Uppsala University [27], which basically comprises of a buoy coupled through a connection line to a linear generator positioned on the seabed.

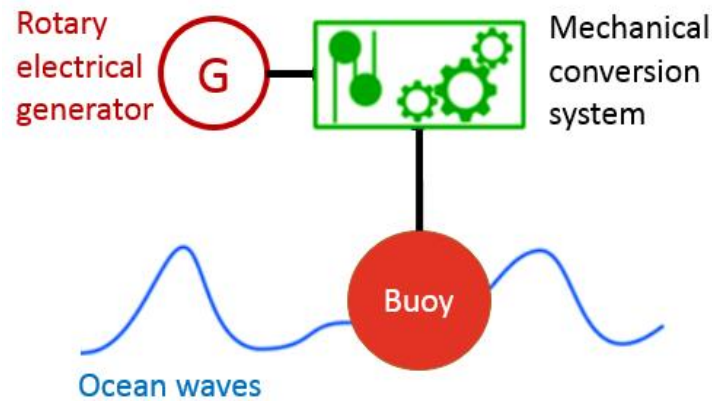


Figure 2. 5: Illustration of a direct drive mechanical PTO

2.5.4 Direct Drive PTO Systems

Direct-drive PTO systems are systems where the moving part of the converter, such as a buoy or wave swing, is directly coupled to the moving part of the linear generator, the translator. The speed of the electrical machine now, however, has to match the speed of the buoy, (0.5 to 2 m/s). Which means, direct drive mechanisms can reduce the number of energy conversion steps of the conventional systems as shown in Figure 2.6. In other words, the mechanical interfaces such as gearbox, hydraulic and pneumatic systems, which are often used to link the prime mover to the high-speed electrical generator can be eliminated. Consequently, maintenance requirements are reduced plus the efficiency and reliability of the overall system can be significantly improved [28]. Though this leads to a simple system with few components, it calls for the design of an unconventional electrical machine that must be capable of producing electricity efficiently with a low-speed and high thrust force input.

The work in this thesis will focus on linear PM machines suitable for DD-WECs.

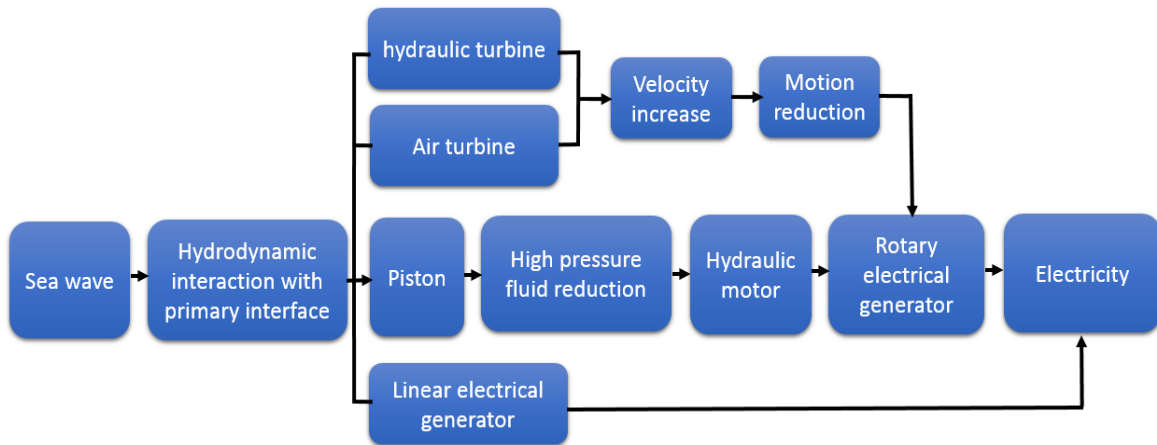


Figure 2. 6: Alternative power take off schemes[29]

2.5.4.1 The Archimedes Wave Swing (AWS)

The Archimedes Wave Swing (AWS) was the first original DD-WEC integrated with a large Permanent Magnet Linear Generator (PMLG)[30]. It was developed in the Netherlands and the 2MW full-scale submerged prototype was tested offshore in Portugal in 2004 [31]. However, a floating buoy is not employed in the AWS. It is a completely flooded cylindrical device which comprises of two main parts: One is the top floater part which oscillates vertically and the other part is a cylinder fixed to the seabed as shown in Figure 2.7 (a). As waves pass over the AWS the air is compressed, forcing the floater against the stationary structure. When the waves move away the pressure is released allowing the floater to go back to its original position. This vertical oscillation is converted into mechanical energy to drive the translator of the PMLG, which is directly coupled to the movable part of the AWS. The PMLG is a double-sided flat machine in which the windings are mounted within the inner stator, while the magnets are located on the outer translator as shown in Figure 2.7 (b). Archimedes Wave Swing Ocean Energy has taken further steps to develop the AWS by introducing two point absorber concepts. One such is an improved version of the initial AWS known as MK-II. The other device is the recent AWS-III with 2.5 MW rated output power [32], which consists of a multi- interconnected air chambers to convert wave power to pneumatic power through pressurised air within each chamber. The pneumatic power is hence converted to electrical power by turbine-generator sets. The AWS-III offers a significant feature of eliminating the end-stop issues owed to the use of the air as a transmission medium.

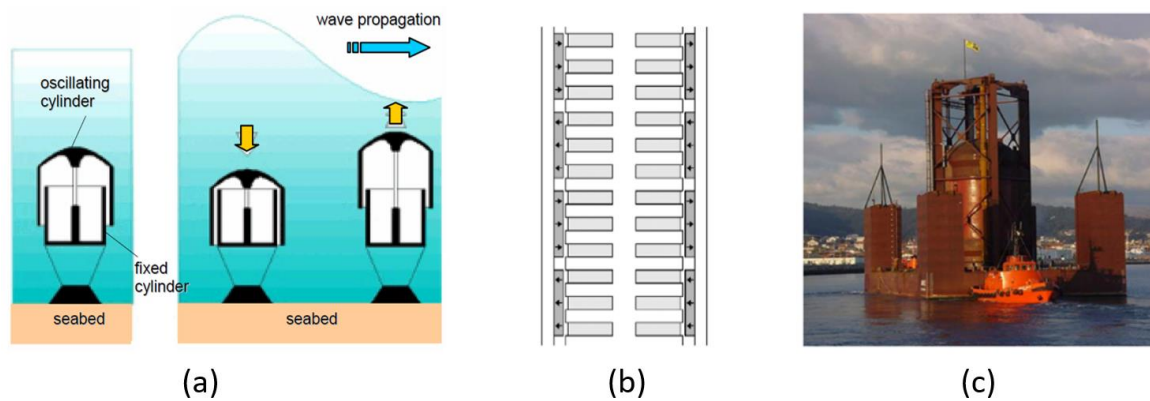


Figure 2. 7: (a) The Archimedes Wave Swing (b) cross-section (c) photo [31]

2.5.4.2 Inter Project Service (IPS) Buoy

The IPS Buoy is a semi-submerged system which was initiated by a Swedish company in 1980s. This device is a circular buoy, fixed by a flexible rope allowing its vertical movement, with a long vertical fully submerged acceleration tube with open top and bottom ends to the sea as shown in Figure 2.8. As waves pass under the buoy the acceleration tube moves up and down based on the mass of damping water contained in the acceleration tube which acts as the reference body of the movement. The relative motion of the piston and floater tube system can be used for the power take-off. When the oscillation amplitude exceeds a critical value, the piston is detached from the mass of the surrounding water and comes out of the cylinder, thus allowing it to follow the oscillation of the tube. This feature offers an extra level of protection against the PTO being damaged. This device also has a further benefit of being able to oscillate in an inclined direction, which changes the buoyancy force and thus frequency response. It has been shown that by employing the IPS buoy the instant wave power can be converted to electricity with an efficiency of 30–35% [33]. The sloped IPS buoy has drawn interest from research field on the target of limiting the drive stroke and improving the overload protection [33].

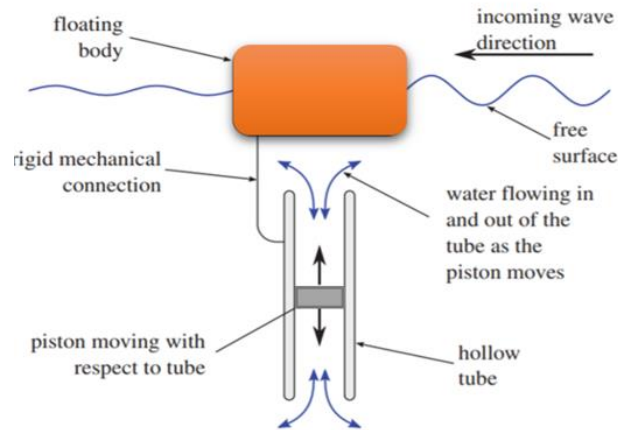


Figure 2. 8: Cross-section of the IPS buoy

2.5.4.3 Floating Buoy

A heaving buoy is a floating device that can be cylindrical or spherical, oscillating vertically with the motion of the ocean waves and reacting against a common reference frame as shown in Figure 2.9. It can be installed nearshore or offshore, be floating or submerged. Due to the restriction of the motion direction of this device only 50% can be extracted as a maximum portion of the energy available in its absorption width.

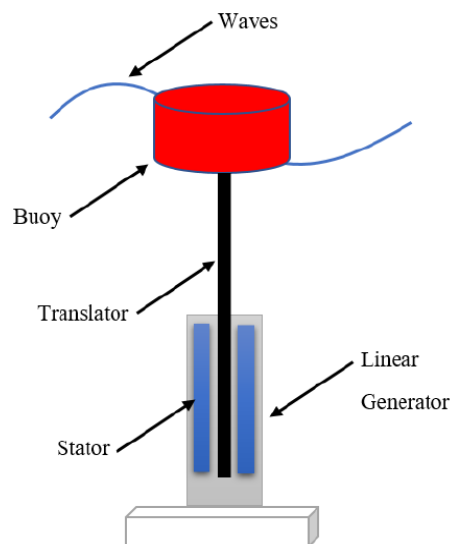


Figure 2. 9: Floating buoy system

2.6 Linear Electrical Machines

In general, electrical machines play a significant role in facilitating any kind of mechanical work. They have been extensively used in industrial and domestic applications in which the majority of them are rotary. However, a linear motion is required in many applications, e.g. transportation, automation systems, and direct drive renewable energy applications. The concept of the linear machine is a rotary machine cut along radial plane and unwrapped, as shown in Figure 2.10, so that a traveling magnetic field is produced by the three phase windings[34]. The general operation principles of this category of machines is the same as that of the equivalent rotary machine: the interaction of the stationary track (stator) and the translator fields causes a conversion of magnetic energy into a force and hence motion. The linear machine can be either a motor or generator, and in both cases magnetic forces are directly developed between stator and translator.

Figure 2.10 also shows the cross-section of the linear machine derived from rotary machine configuration. It consists of two main parts: the stator which is the stationary and the translator which represents the movable part. The relative length between the stator and translator is different depending on the specific application, meaning that either the stator or translator needs to be longer than the other for a constant active area. If the stator and translator have the same length, and the motion is applied on the moving part of the machine, a portion of one side of the translator loses the interaction with the stator, while a part of the translator appears beyond the airgap and hangs free from the other side. Consequently, the linear machines can be classified into two main groups as illustrated in Figure 2.11:

- Linear machines with short stator and extended translator;
- Linear machines with short translator and extended stator.

In addition, the translator, can accommodate either the armature windings [35], permanent magnets [36], or both [37].

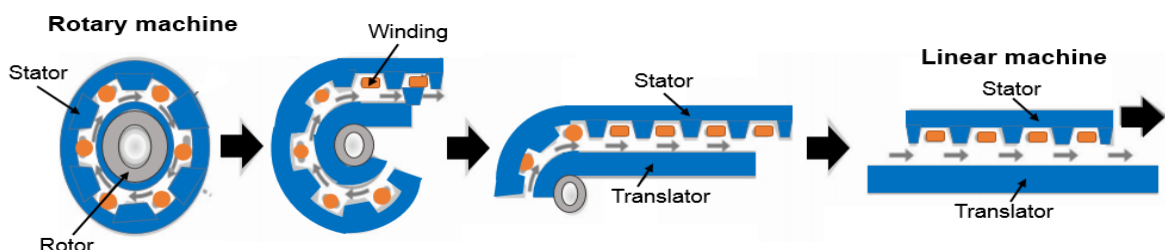


Figure 2. 10: Concept of linear machine

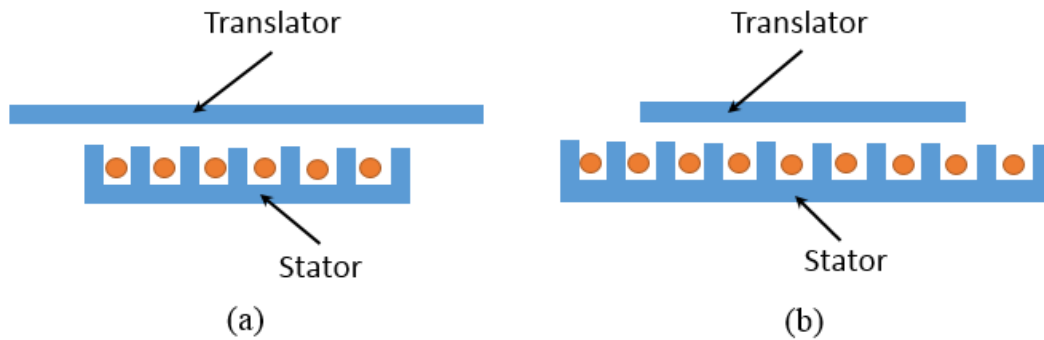


Figure 2. 11: Main classification of linear machine (a) short stator (b) short translator

2.6.1 Linear Conventional Machines

2.6.1.1 Linear Induction Machine (LIM)

The linear induction machine (LIM) is a flat version of the conventional rotary induction machine. It has three-phase stator windings in its primary, while the secondary houses the squirrel cage that derived from its rotary counterpart in which brushes or slip rings can be eliminated as shown in Figure 2.12. Due to its simple structure and low initial cost this machine is used in a wide variety of applications such as railway transit and automotive suspension systems[38], or wave energy conversion [39].

In the LIM, when the stator windings are fed by a three-phase AC current supply, a travelling magnetic field is produced which travels at synchronous speed in the airgap region. As a consequence, the translator speed will not reach the synchronous speed of the travelling magnetic field in the stator resulting in an induced back EMF in the translator. The difference between the two speeds is known as ‘slip’, which causes the force and hence the translation motion. If the slip is zero, no EMF would be induced in the translator, no current will flow and thus no force would be produced. If the translator speed exceeds the synchronous speed of the magnetic field, the machine acts as a generator. By connecting the armature windings to a controllable converter, any slip speed can be obtained at any translator velocity. Thus, the output power can be easily controlled for a variable input speed as such the rotary counterpart is normally employed in wind turbine.

When the LIM operates as a generator, it delivers an active power to the electrical supply and draws reactive magnetization current from the supply, thus requiring a bi-directional grid connection. If the mechanical airgap is larger than its equivalent of the rotary version, the inductance and thus the reactance of the winding is small, leading to an increase in the excitation current and hence a reduction of the total efficiency of the machine.

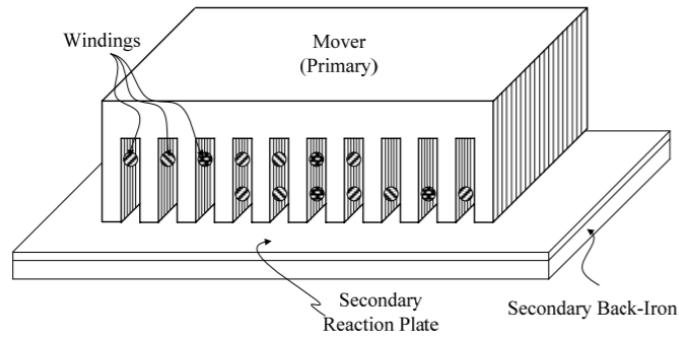


Figure 2. 12: Linear induction machine

2.6.1.2 Linear Permanent Magnet Synchronous Machine (LPMSM)

Since the development of the soft and hard magnetic materials had begun, the Linear Permanent Magnet Synchronous Machines contributed to facilitate the transmission of the linear motion in direct-drive applications [40]. The LPMSMs have been extensively employed in several applications such as trains, industrial equipment, military and other fields [36, 40-42]. The use of the PM in linear synchronous machines has shown that higher thrust force, fast response and lower losses can be achieved compared to other types of synchronous machines. In addition, the absence of the translator windings influences its mass and size and requires little to no maintenance. However, the cost of the PM materials, the existence of stray magnet fields, and the cogging force caused by slotted structure and end effect are considered as severe drawbacks, which have restricted their use in some applications [36, 43].

The LPMSM has a simple structure stator core with inherently low synchronous reactance, while the translator has PMs located on its surface as shown in Figure 2.13. The PMs can be placed on the translator surface or inset in the translator structure. The stator also offers a wide range of winding arrangements: single phase, multiple phase, different ratio of slot/pole/phase, distributed or concentrated windings. The PMs act as the excitation source to generate the excitation field in the translator, which in turn interacts with the travelling magnetic field produced by the armature windings[42]. The working principle of the LPMSM is the same as that of the Wound-field Synchronous Linear Machine, in which the excitation field is provided by the installed PMs rather than the excitation windings.

When the translator is driven, the flux generated by the PMs cut the fixed stator windings in a sequence manner, resulting in an induced EMF.

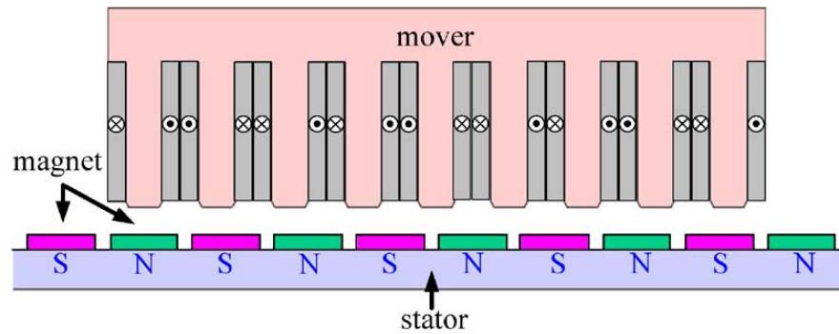


Figure 2. 13: Linear PM machine [36]

2.6.2 Variable Reluctance Permanent Magnet Machines (VRPMMs)

The Variable Reluctance Permanent Magnet machines are superior to the conventional machines in terms of their high shear stress [36, 44]. A member of this family known as the Transverse Flux Machine (TFM) can achieve an airgap shear stress of 100 kN/m^2 compared to only $20\text{-}30 \text{ kN/m}^2$ achieved by its conventional counterpart [45]. This implies that by employing the VRPM machines the airgap area can be reduced by a factor of five, resulting in a small machine for direct drive applications.

The adoption of the magnetic gearing allows this kind of machine to produce a rapid flux change with only a small physical displacement. The concept of magnetic gearing is demonstrated in Figure 2.14, in which an individual stator tooth is split into three flux modulated poles interacting with five PMs mounted on the translator surface. As the translator travels by one pole pitch the flux will be reserved following the orientation of those magnets aligned with the split teeth, as illustrated in Figure 2.14 (a and b). On the other hand, in the toothless structure the rotor should move five times of this distance as shown in Figure 2.14 (c) and Figure 2.14 (d). Which means, the rate of change of flux has been increased five times by employing the split teeth design. However, there are only three active magnets producing the main flux at any time, resulting in a reduction of the maximum flux by a factor of $3/5$ compared to 'c' and 'e'. Hence, the net magnetic gearing of the split translator and stator poles is threefold. Various types of these machines have been proposed and are in use [37, 46-52], all of them have the same basic principle of operation. The three most common topologies will be presented in the next three sub-sections.

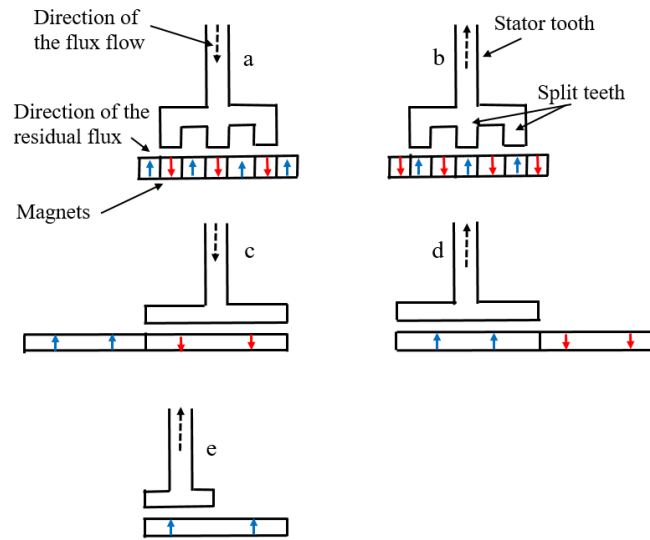


Figure 2. 14: Magnetic gearing

2.6.2.1 Linear Transverse Flux Machine (LTFM)

Authors [46], have reported that LTFMs are capable of producing much higher force densities than other types machines with a factor of three to five times. This indicates that the LTFMs might be the most suitable candidate for those applications where high force density is required. This class of machine possesses some advantages distinguished from other machines. Most significantly, the space required for the armature windings can be maximized without sacrificing the space allocated for carrying the main magnetic flux, which therefore increases the design flexibility [53]. Another benefit of the LTFMs is that the force density can be simply increased by reducing the pole pitch for a given overall dimensions or increasing the number of poles. Thus, by employing the linear transverse flux generators both the active volume and mass can be reduced compared to the longitudinal flux permanent magnet generators. On the other hand, the LTFMs suffer from a number of disadvantages such as force ripple, low power factor, poor overloading capability and the complexity of the manufacturing process [54] resulting in a limitation of their use in some applications. However, optimizing the shape of the current waveform can sufficiently reduce the force ripple as proposed in [55].

Figure 2.15 shows the geometry of a single-sided LTFM where the flux travels perpendicular to the direction of motion. It has a translator with surface-mounted PMs in a specific arrangement that allows the flux to flow parallel and perpendicular to the airgap. The stator coils are individually wound around each side of a series of U-shaped iron cores directing the flux in a manner that alternate translator poles energize the same conductor [56,

57]. The outcome is an inherently 3-D flux path, and the flux generated by each pole pair links the winding.

In the conventional PM machine configuration, the electric and magnetic loadings are sharing the same space. Hence, the influence of increasing the number of poles of this machine, for example by duplicating the number of poles both number of turns per coil and the associated induced voltage will be halved as a result. Moreover, the flux will be halved resulting in halving the induced voltage once more. However, both voltage drops will be compensated by the duplication of the number of coils and the magnitude of the frequency. Which implies that the induced voltage in the windings is not affected and thus the VA rating of the machine is still the same as before. However, in the LTFM magnetic loading and electric loading lie in different planes, i.e. the magnetic loading is set by the axial pole length, while the electric loading is set by the side width [58]. As shown in Figure 2.15 the number of poles in the bottom design is double of that of the top design in which the pole pitch has been minimized by 50% of its initial value. This obviously demonstrates that the magnetic loading of the machine has not been affected. The magnitude of the flux that surrounds the winding has not been also changed, while the current loading is kept constant. However, the rate of change of the flux is duplicated due to a duplication of the number of poles, which in turn results in doubling the induced EMF. Therefore, increasing the number poles by reducing the pole pitch using the same quantity of iron, copper and current will not influence the electrical loading of the machine leading to a double increase of the machine VA rating.

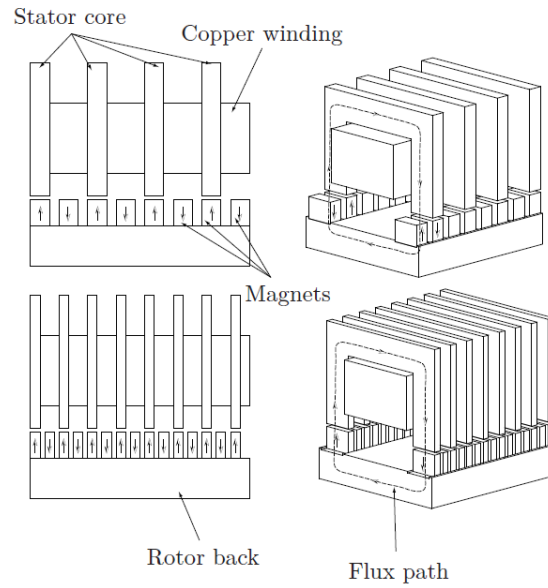


Figure 2. 15: Transverse flux machine

2.6.2.1.1 POWER FACTOR

The LTFMs suffer from low power factor which is considered as one of the most common drawbacks of this category of machine, where the typical achievable values within the range of 0.35-0.55, as reported in [59]. As well known, for a fixed real power output, the capacity and relative cost of the converter is inversely proportional to the power factor of the electrical machine, which leads to a considerable rise in the VA rating of the converter [48, 60, 61]. This indicates that the costs of the required drive circuit for the LTFMs are anticipated to be higher than the equivalent drive circuit for the conventional machines. In addition, as stated by [59], the advancement in this field has a very limited scope, and the poor power factor is something inherent in this machine. The existence of the large leakage flux in the LTFMs significantly contributes to the reduction of the power factor, where nearly 50% of the magnets leakage flux and 70% of the armature leakage flux have been reported [59]. In theory, the leakage of the machine is presumed to be negligible. However, in practice if the machine length is kept constant and the number of poles is increased, the pole pitch then is reduced which allows the pole-to-pole leakage flux to increase resulting in poor utilisation of magnets. Furthermore, by increasing the number of poles, the operating frequency of the machine will be increased consequently and thus the value of the reactance.

2.6.2.1.2 END WINDINGS

The rotary version TFMs has an attractive advantage of the non-appearance of physical end winding, where the additional space is not required in this case. However, in a conventional TFM only half of the winding is active at any particular time. As the U-shaped laminated cores are spaced by air, and not by iron which allows the air to surround the winding, the result is inefficient cooling of the machine. Moreover, since these portions of the winding are exposed to the air, their impacts will be similar to that caused by the end windings which lead to active material waste and contributing in increased mass, leakage and copper losses in the machine [62]. In the configuration of a LTFM an extra portion of end winding is required to wrap the stator teeth as existing in its rotary counterpart.

2.6.2.1.3 COGGING FORCE

Cogging force is a significant problem in the LTFMs due to the equality of the stator tooth span to that of the pole span. Hence, this phenomenon cannot be suppressed by employing the conventional techniques such as skewing, and the short-pitch winding is not applicable. The possible method for the cogging force reduction in this kind of machines is to design the machine with a small magnetic loading and large electrical loading. However, since the amount of the armature leakage flux is highly depends on the electrical loading the power factor will be reduced as a result.

2.6.2.2 Linear Vernier Hybrid Machine (LVHM)

The Linear Vernier Hybrid Machine is a derived topology of the variable reluctance machine, which can provide high force density [63]. The origin of the term hybrid is from the incorporation of facets of the flux-switching machine and flux reversal machine. For over four decades, the development of the brushless PM machines has shown the impending limits to their characteristic performances growth, while there is still a great need for new machines with higher power densities[60]. Therefore, the VHM has been extensively studied as an alternative choice for the conventional machine to meet this requirement [44, 64-67]. This class of machine exclusively exploits an extra flux so-called modulation flux due to the magnetic modulation effects plus the regular PM flux. Thanks to this effects, the VHMs are capable of generating considerable higher no-load back EMF and higher power density compared to the conventional PM machines. As well known in the field of PM machines design, specific combinations of slots/magnets are required to create the modulation effects.

In this case, the required PM poles in VHM are usually more than that of the conventional PM machine. If the number of winding poles are the same in both machines, the VHM with its large number of PM poles would operate with higher frequency than the conventional one leading to a significant increase in the reactance and hence a drop in the power factor and concerns about an increase in the eddy-current and hysteresis losses in the iron core[60]. Therefore, the VHMs are nominated as suitable candidate for low speed and high torque applications [44, 49, 66-70]. However, reference [60] stated that this evaluation is unfair as the comparison has been made considering both machine topologies have the same number of winding poles rather than the same number of PM poles. Hence, the dependable assessment of competitiveness of the PM Vernier machine is essential. However, so far a small number of studies with a fair comparison of the two topologies has been reported.

Muller and Baker proposed and built the first linear version of the VHM for direct-drive wave energy applications with a shear stress of 143.9kN/m^2 [71]. This machine has a simple structure of double-sided stators with six C-shaped iron cores facing each other symmetrically. Both PMs and windings are mounted on the stator, while the toothed translator is sandwiched between the stator sides. Each stator pole is wound with a single coil in which these four coils are connected in series to form one phase. There is also a set of multiple magnets with an adjacent alternating polarity placed on each individual stator tooth. The pitch of both translator's slot and tooth is similar to that of the magnet pole pitch. Figure 2.16 shows a single phase unit with two identical C-shaped iron cores, in which a three modules of these with a displacement of 120 electrical degrees are required to form the complete three phase machine. The basic operation principle of the machine relies on the magnetic gearing effect: short pitch PMs (say $<50\text{mm}$) travel with respect to the slotted translator with similar pitch. The variation of the reluctance is provided by the slotted translator and hence a rapid flux is produced as a result leading to a large rate of change of the energy in the airgap shear stress. The initial development of this machines is covered in detail in Chapter 3.

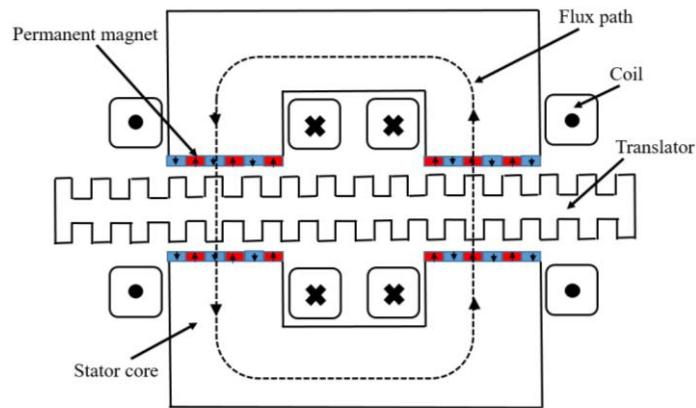


Figure 2. 16: Single phase unit of the LVHM

2.6.2.2.1 POWER FACTOR

As with other members of the family of the VRPM machines, the internal reactance of the VHM is very high contributing to one of the limitations associated with this type of machine, the undesirable poor power factor. Thus, an over-rated power electronic converter is required to overcome the drop in the power factor [48, 60, 61]. As known, the VHM is incapable of achieving the same value of the flux density produced by the conventional PM machine when both machines have the same PM volume. This is due to the fact that the PM arrangement corresponding one stator winding pole in the VHM produces a heteropolar field, in which half of the PMs under one winding pole generate the main flux at any instant, while the remaining PMs produce the leakage flux. Consequently, a higher reactive effect or a higher number of turns is required for a given design, leading to low power factor. If the stator winding of VHM are designed to be same as that of the conventional PM machine, the phase inductance in the two machines can be supposed to be the same in a sensible design. In this case, the VHM has lower flux linkage and hence lower power factor. These points implies that the high phase inductance is not the main reason of the poor power factor in the VHM[60]. Which means, by increasing the main flux produced by PMs the poor power factor can be improved [48, 60, 61, 72], which is the desired technique adopted in this research. Two new topologies are proposed with aim to improve the power factor which will be discussed in detail in Chapter 4.

Different topologies have been proposed to improve the power factor of the VHMs, for example, the use of an auxiliary DC winding [61]. The implementation of this winding would enable the magnetization level of the PMs to be controlled, resulting in a controllable no-load airgap flux density [61]. The feature of the flux- control capability can contribute to the

power factor improvement. However, an unavoidable side effect of this is an increase in the copper loss and converter losses plus an increase in winding material consumption. Therefore, the machine efficiency and initial cost can be influenced, albeit partially offset by a de-rated power converter. In addition, in [61], the PMs are placed on the translator resulting in insufficient magnet utilization for large amplitude applications. In [48], the authors proposed an effective topology of a rotary Vernier machine with an improved power factor using flux concentration rotor structure and double-sided stators. However, again converting this machine into a linear version requires a large amount of PM material since the PMs are located in the translator, which will considerably increase the initial cost especially for long stroke applications.

2.6.2.2.2 ATTRACTION FORCE

The existence of the iron-core in linear machines causes a strong magnetic force between the translator and stator [28]. The attraction force or airgap closing force acts to close the airgap influencing the bearings deterioration. Since the VHM shown in Figure 2.16 has double-sided stators, the two magnetic forces produced by both stators react against each other, which theoretically cancel out. The asymmetric airgap resulting from the manufacturing tolerances is the leading cause of this force. According to [73], the value of the attraction force can be 5 to 10 times of the tangential shear stress. If the airgaps are non-identical, the result is a large net force between the primary and secondary parts as verified in [74]. In a large-scale generator such as the AWS, the length of the translator is approximately 8m, hence it is improbable to maintain the airgap uniform along this length. Therefore, a rigid structural support is needed to keep the airgap. It should be indicated that by increasing the number of stator sides, the performance of VHM approaches that of the tubular one, but the manufacturing cost will be increased as a consequence. Chapter 7 introduces a full-scale eight-sided VHM in attempt to obtain a design with less attraction force as stated in [75].

2.6.2.3 Linear Flux Switching Machine (LFSM)

Flux switching PM machine is a member of the family of VRPM machines with a doubly salient structure which was first proposed in 1955 [52]. The linear version of this kind of machines are attractive for long stroke applications since both PMs and armature winding are placed on the short part of machine (can be stator or translator), which in turn reduces

the required amount of PMs and copper in comparison to the conventional long-stroke linear PM machines, leading to a significant reduction in the initial cost. The machine consists of a translator and stator and can be constructed as single-sided [76], multi-sided [37, 52] or tubular [77]. The stator has six U-shaped cores, each phase comprises of a PM sandwiched between two adjacent U-shaped cores, while the phase coil is wound around the teeth adjacent to the magnet. Non-magnetic spacers are located between phases. Figure 2.17 (a) shows the configuration of a single-sided FSLG. When the mover travels from the initial alignment position to the next alignment position, the flux produced by PM links the corresponding coil and varies from peak negative to peak positive. Consequently, the rate of change in this flux caused an induced back EMF in the winding.

Although this machine exhibits high force and power density, it normally consumes a larger amount of PMs than the conventional PM machine [76]. However, it can offer high PM utilisation due to the absence of the leakage flux [78]. The machine also has the merits of high power factor and a simple and robust structure [37, 79]. In addition, the fault tolerance capability under one phase fault condition of this class of machines is one of the most attractive features for industry applications where the requirement of the system reliability can be increased. The LFSMs have been widely used in a wide range of applications which require long secondary, particularly in traction systems [76]. They have been also investigated for high thrust low speed applications such as direct drive wave energy converters [52, 80]. Another linear flux switching generator for the same application was proposed in [80], where an additional DC excitation was employed, as shown in Figure 2.17 (b). The results of these prototypes have shown that the LFSM is suitable to use as a low speed direct-driven generator. However, due to the doubly salience structure for both stator and translator plus the end effect, it exhibits extensive cogging force which leads to periodic ripples in thrust force, and hence degrades the machine performance [81].

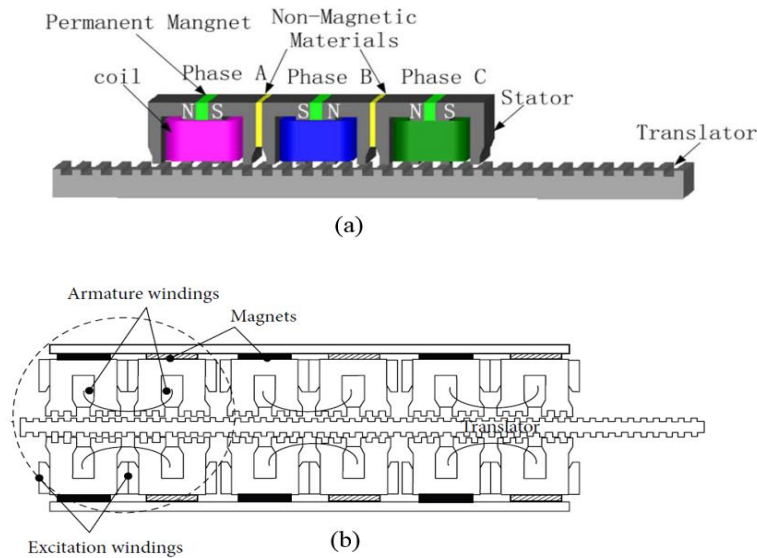


Figure 2. 17: Linear flux switching machine (a) single-sided [52] and (b) double-sided [80]

2.6.3 Linear Tubular Permanent Magnet Machine (LTPMM)

Linear tubular permanent magnet machine is another form of linear machines where the primary stationary part is wrapped around the secondary one in parallel to the motion, in which these two parts are separated circumferentially by the mechanical airgap. The active part of the mover comprises of a combination of ring-shaped iron and magnet poles. The magnets are axially magnetised in which the flux is concentrated in the iron pieces which act as north and south poles. The term tubular refers to the cross-sectional shape of the machine and hence covers a wide range of possible topologies. Of the various linear machine topologies, the linear tubular machines with PM excitation possess the distinctive merits of a high force density, high ratio of PM utilisation, which make them more attractive choice for applications where dynamic performance and reliability are crucial [82]. In addition, the non-appearance of the end windings in their configuration can reduce the copper consumption [83]. Different PM arrangements can be adopted in the LTPMMs since the PMs may have different orientation of magnetisation [84], size and location (inner or outer PM [85]).

Recently, the synchronous LTPMMs with magnets on the translator are the common linear generators used in the direct drive wave energy conversion systems [86, 87]. However, the complexity of the translator structure and the implementation of the laminated core are undesirable drawbacks of this class of linear machines[88]. Besides, the heavy translator of the LTPMMs increases the heavy shifting mechanical tensions the heaving buoys, which is one of the main challenges in the development of wave power technology[14]. The problem

of the translator structure can be avoided by employing different topology where the magnets can be mounted on in the stationary part of the machine, the stator, such as the linear VHM [89] and linear flux switching machine [77]. The developed Soft Magnetic Composite (SMC) can overcome the problem associated with the core lamination[90].

The ironless LTPMM is another configuration of this topology where the iron core is removed resulting in a significant saving of the core material and the associated structural parts. The ironless structure shown in Figure 2.18 can significantly reduce the undesirable magnetic attraction force which may increase the radial load on the bearings [91]. The translator comprises of a non-magnetic shaft surrounded by a set of ring-shaped PMs with alternating polarity arrangement separated by magnetic steel spacers. However, this configuration has a negative impact on the generator performance [73, 92], in which high magnetic losses occur in the stator due to the high variation of the flux ratio, requiring a laminated stator. Furthermore, a shear stress about 10kN/m^2 of this configuration caused by infinite airgap has been reported [73, 93], which is regarded as a poor shear stress for direct drive wave energy converters.

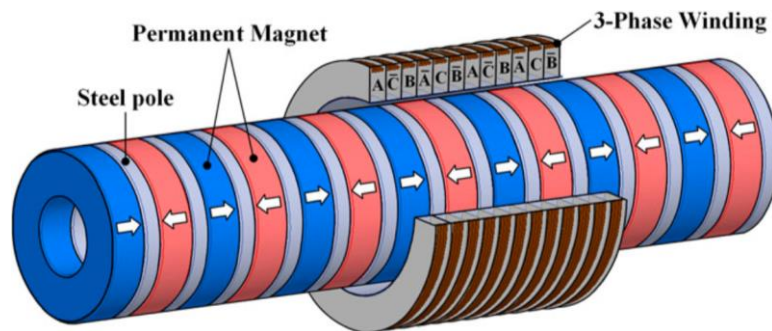


Figure 2. 18: Ironless tubular linear PM machine[86]

2.7 Selection of Machine for Further Development

Electrical machines with PM excitation can offer higher shear stress compared to those with electrical excitation. According to the above review which is summarised in Table 2.1, the need for regular maintenance resulted from the brushes required in the conventional linear machines make this category of machines undesirable for direct-drive wave energy converter, offshore devices in particular. The low shear stress and high copper consumption are other disadvantages of the conventional machines, in which their use in low speed high thrust applications might be limited. Among all VRPM machines the LTFM offers the highest shear stress where the smallest machine would be required to react a given force.

However, the complexity of manufacturing resulted from the configuration of stator and translator, the reported high cogging force and poor power factor, and inherently 3D flux pattern, plus translator mounted magnets are major drawbacks that are persuasive reasons to make this kind of machine out of the scope of the present research.

Though the LFSM has shown a great magnet utilisation, it requires a large amount of PMs which can increase the initial cost of the direct drive generator owing to its bulky size. In addition, the stator iron teeth can be easily saturated which may limit the electric loading. Cogging force produced by the LFSM and the potential noise and vibration resulting from harmonics are serious disadvantages.

The majority of the proposed linear tubular machines for DD-WECs have PMs mounted on the translator contributing to the level of complexity of manufacturing. Furthermore, a large amount of PMs are required, in which half of the translator length must be covered by PMs, which would increase the initial cost, especially in long stroke applications. Even in tubular versions of VRPM machines where the PMs are mounted on the short stator, the cost of the ring-shaped PMs are more expensive compared to the bar PMs, so this topology is out of our interest.

A comprehensive review on linear generators for DD-WECs considering the cost and operational aspects has been performed in [94], in which the VHM and LFSM were the most promising topologies. It has been reported that the existing Vernier machines suffer from relatively low power factor, namely less than 0.4 [61], meaning that the converter must be overrated by a factor of 4. This is not yet a reason to stop research in this direction, because the converter is much cheaper than the low speed direct-drive generator [46], so that it might be sensible to use a more expensive converter if the generator cost can be reduced.

The outcomes of the above discussion and the advantages listed in Table 2.1 make it worthwhile to investigate the LVHM for further development and analysis. A thorough optimization of this topology might improve the magnet utilisation and power factor significantly. Therefore, the LVHM was selected as the most promising topology for further research.

The outline of this option will be deeply presented and discussed in the next Chapters.

Table 2. 1: Comparison of linear machines for low speed applications

Topology	Advantages	Disadvantages
LIM	<ul style="list-style-type: none"> • simple structure • low initial cost 	<ul style="list-style-type: none"> • requires high excitation current • low efficiency • low shear stress
LPMSM	<ul style="list-style-type: none"> • high power factor • high efficiency 	<ul style="list-style-type: none"> • requires a large amount of PM • low shear stress • high translator mass • PMs on the translator
LTFM	<ul style="list-style-type: none"> • very high shear stress • high force and power densities 	<ul style="list-style-type: none"> • high copper consumption • high copper loss • complex structure • high cogging force • PMs on the translator
LVHM	<ul style="list-style-type: none"> • high shear stress • high force and power densities • simple structure • robust translator structure • low translator mass • low PM mass • high efficiency • Shares the advantages of TFM and flux reversal machine • PMs in the stator 	<ul style="list-style-type: none"> • poor magnet utilisation • attraction force is an issue • low power factor
LFSM	<ul style="list-style-type: none"> • simple structure • high shear stress • great magnet utilisation • high power factor • robust translator structure • PMs in the stator 	<ul style="list-style-type: none"> • requires a large amount of PM mass • high cogging force • attraction force is an issue • stator iron teeth are easy to saturate
LTPMM	<ul style="list-style-type: none"> • high force density • low attraction force • absence of the end-windings • can have ironless stator 	<ul style="list-style-type: none"> • the ironless topology suffers from poor shear stress about 10kN/m^2 • expensive ring PMs • requires a large amount of PMs • most topologies have PM on the translator • complex structure especially for large-scale • high cogging force

2.8 Conclusion

Within this Chapter the idea, need and history of utilising energy from ocean waves have been introduced. The classifications of the WECs based on direction and operation principle have been discussed. Furthermore, different PTO systems have been presented and described, in which the features of the direct-drive PTO systems over the mechanical direct drive, pneumatic and hydrologic systems have been highlighted. It is shown that development of linear machines to facilitate direct drive power take-off could be advantageous.

Different topologies of linear machines have been also surveyed and described in this Chapter. Details have been given of conventional linear induction machines, linear PM synchronous machines, linear variable reluctance PM machines and linear tubular PM machines. A discussion outlining their benefits and drawbacks has also taken place. The linear variable reluctance PM machines have high shear stress allowing these machines to be built in compact size compared to the conventional linear permanent magnet synchronous machines. Despite the intense competition between the members of the family of the linear variable reluctance PM machines, the double-sided linear Vernier hybrid machine has simple structure where both magnets and windings are mounted in the stator, while the robust translator consists of iron. Although this machine suffers from low power factor, the converter appears to be much cheaper than the low speed direct-drive machine. The flux concentration effect can be exploit to improve the no-load airgap flux density. Hence, this method has been shown to improve the power factor without increasing the PM mass, i.e by adopting a topology that is capable of providing a flux concentration effect. Therefore, it is worthwhile to investigate this topology further. The proceeding Chapters investigate this type of electrical machine for the purposes of improving the magnet utilisation and operating power factor.

Chapter 3. Development of the Linear Vernier Hybrid Machine

3.1 Introduction

The main work of this PhD develops the Linear Vernier Hybrid Machine (LVHM), introduced in the previous Chapter into a new design for the purpose of improving the machine electromagnetic performance, while reducing magnet use. This Chapter commences with a description of modifying an existing design to give a simple stator structure and introducing tapered ferromagnetic poles. Using Finite Element Analysis (FEA), the developed design has been optimised and analysed in order to achieve the optimal thrust force and minimum cogging force. The Chapter concludes by evaluating the performance of the final design, which will be known later as Inset Magnet Consequent Pole (IMCP) machine. This machine has been constructed in the laboratory, in which the manufacturing and assembly processes will be described in more detail in Chapter 5. The verification and validation of the FEA model are then investigated by comparison to experimental results obtained from the prototype machine, which will be discussed in Chapter 6.

3.2 Description of C-core Inset Magnet Consequent Pole (IMCP) Machine

The linear Vernier hybrid machine proposed in [95], and developed in [68, 96], shown in Figure 3.1 (a) was investigated to improve the electromagnetic performance while reducing the magnet mass. Figure 3.1 (b) shows the structure of the three-phase C-core IMCP machine in which the stator is formed of modular C-shaped laminated iron cores with a coil wound around each C-shaped tooth, while the PMs and consequent poles are placed on the surface of each stator tooth. The consequent poles, which will be described in detail in the next section are adopted in the C-core IMCP machine where one polarity of PM is missing and replaced with a piece of lamination, which means that this configuration has the same polarity either S or N as shown in the above-mentioned Figure, whereas alternating adjacent magnets are used in the baseline, meaning that in the C-core IMCP machine the magnetization directions of all PMs are the same. The specifications of the C-core baseline LVHM and IMCP machine are listed in Table 3.1.

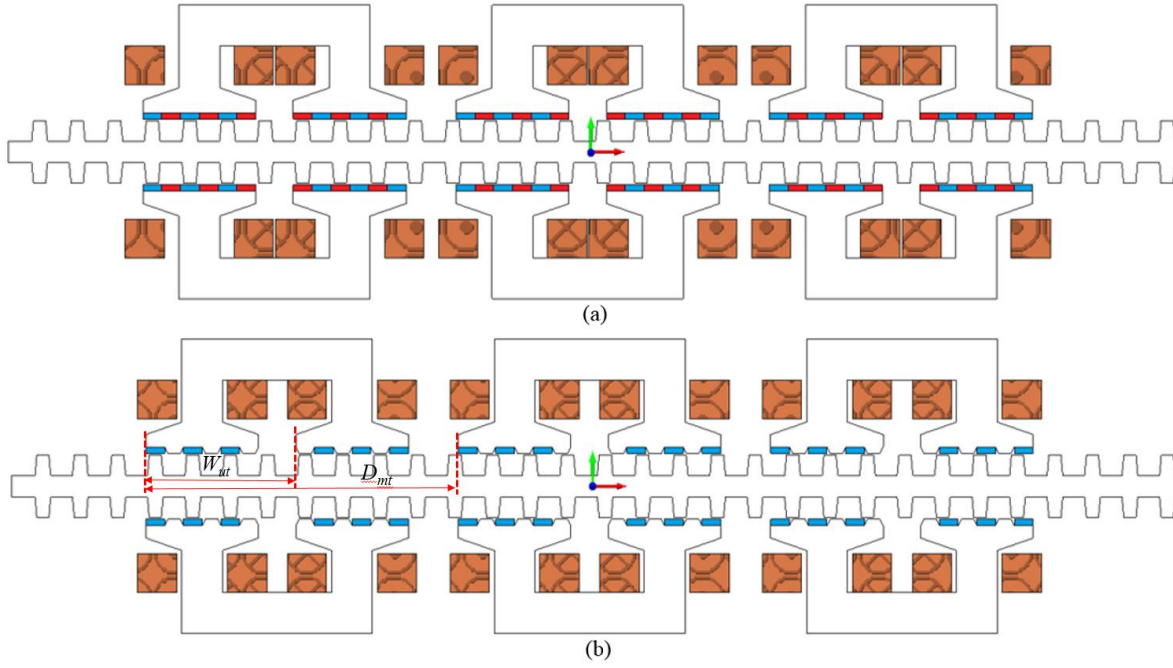


Figure 3. 1: Machine configuration (a) baseline LVHM (b) C-core IMCP machine

Since the C-core IMCP design possess almost the same structure of the baseline LVHM, the magnet width is equal to half of the translator tooth pitch. The relative displacement between the teeth of the C-shaped module is 360 electrical degrees, given by

$$W_{ut} = (m+F+2n) w_{PM} \quad (3.1)$$

where, W_{ut} is the space between the teeth of the C-shaped module, W_{pm} is the width of the PM, m is the number of PMs, F is the number of ferromagnetic poles and n is a positive integer. Moreover, in order to obtain the three phase machine, the mechanical displacement D_{mt} between adjacent C-shaped modules should satisfy

$$D_{mt} = (n \pm 1/3)\tau_t \quad \text{or} \quad (n \pm 1/6)\tau_t \quad (3.2)$$

Where n is a positive integer and τ_t is the translator tooth pitch.

Table 3. 1: Key parameters for both baseline LVHM and C-core IMCP machine

Item	Unit	Baseline	C-core IMCP
Rated speed	m/s	1.2	1.2
Number of PMs	mm	72	36
Airgap length	mm	1	1
PM width	mm	12	12
Ferromagnetic pole width	mm	12	12
Stack length	mm	100	100
Mover tooth height	mm	10	10
PM volume	cm ³	129.6	259.2

3.3 Consequent Pole (Ferromagnetic Pole)

A consequent pole structure can be employed in Vernier machines for the purpose of minimising the magnet use [97]. It has been proven that the Vernier machines with only half the magnet volume can achieve higher back EMF amplitude and capability of torque/ force density than conventional Vernier machines [97-100].

For wave energy applications, Vernier machines with consequent pole structure have been proposed in [61, 101, 102]. However, the PMs are mounted on the translator, where a large quantity of PMs is still required to form a translator, which can be suitable for long stroke applications. Therefore, to tackle this problem, it is desirable to employ the consequent pole structure in the Vernier machine with PMs mounted in the stator. Which will be investigated in this research.

The proposed C-core IMCP machine offers distinctive advantages compared to baseline LVHM. These advantages can be summarised as follows:

- Since the stator structure adopts the consequent pole, mass of magnets can be halved.
- Consequent pole structure in either stator or mover causes a reduction in the fringing flux and thus increases the main flux [99, 103].
- Since the number of PMs is halved, the interaction between the PMs and translator teeth would be influenced leading to lower cogging force compared to its baseline counterpart.

- Reduction in the quantity of PMs eases the assembly process.

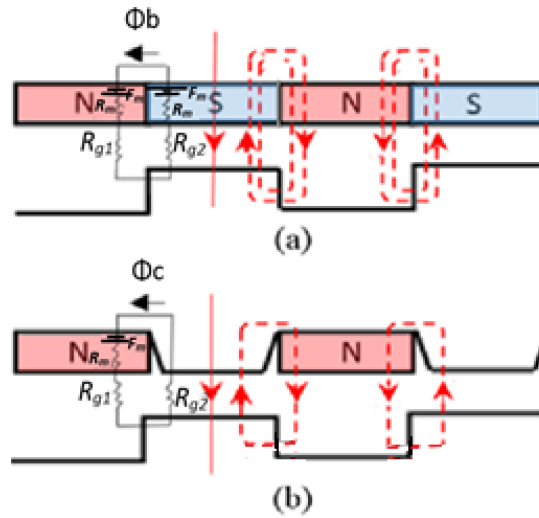


Figure 3. 2: Flux contour, (a) baseline LVHM machine (b) C-core IMCP machine (dotted lines represent the flux leakage and solid line is the main flux).

Figure 3.2 shows the PM and slot structure of the baseline LVHM and C-core IMCP machine. It can be seen that half the PMs produce the main flux, while the remaining PMs produce leakage flux. In other words, south poles generate the effective flux, while north poles generate the leakage flux. Viz, some of the flux lines produced by the south poles pass the airgap towards the translator teeth and then go through tooth edges to the north poles rather than linking the armature winding. Based on a simple reluctance network the leakage flux of the baseline LVHM and proposed IMCP machine can be expressed as:

$$\Phi_b = \frac{F_m}{\frac{R_{g1}+R_{g2}}{2} + R_m} \quad (3.3)$$

$$\Phi_c = \frac{F_m}{R_{g1}+R_{g2}+R_m} \quad (3.4)$$

Where R_{g1} is the slot airgap reluctance, R_{g2} is the tooth airgap reluctance, R_m is the PM reluctance, and Φ_b and Φ_c are the flux leakages of the baseline LVHM and C-core IMCP machine respectively. According to (3.3) and (3.4) it can be observed that the baseline LVHM machine produces higher leakage flux compared with that of the C-core IMCP machine, allowing the main flux of the later machine to be significantly improved with 50%

less PM material. Therefore, the C-core IMCP machine is capable of generating higher no-load back EMF and thrust force.

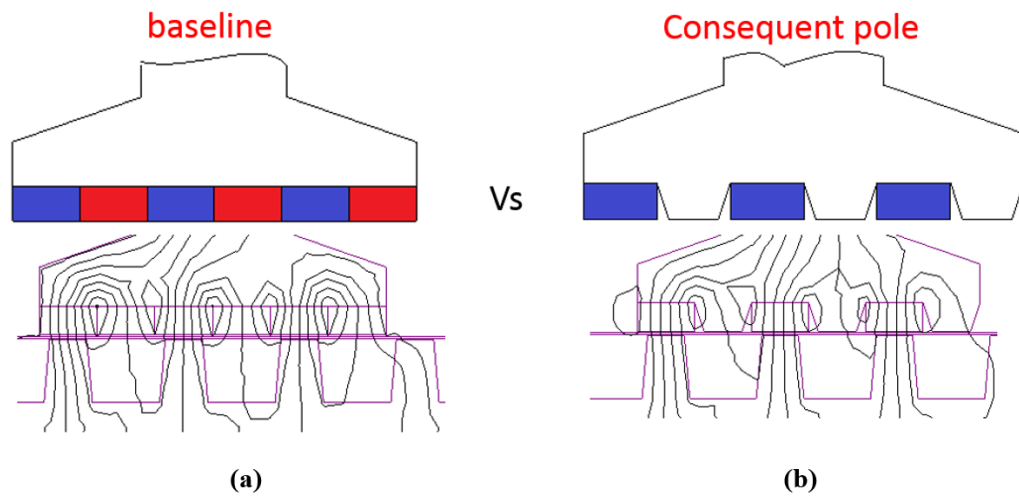


Figure 3. 3: Flux lines predicted by FEA, (a) baseline LVHM, (b) C-core IMCP

Figure 3.3 illustrates the flux plot from 2-D FEA for both the baseline LVHM and the developed C-core IMCP machine. It can be seen that the C-core IMCP machine possess a greater main flux and lesser flux leakage compared with the baseline LVHM. It should be mentioned that the equivalent analyses for a rotary version was conducted in [99].

3.4 Design methodology

This thesis is conducted by multi-dimensional approaches in order to achieve its aims and objectives. The research methods are based on an in-house finite element simulation package called Infolytica MagNet, though which simulations of existing and new LVHM are implemented.

Furthermore, 2D-FEA (Infolytica MagNet software) was employed to implement transient simulation of the LVHM, while 2D static FEA was used to predict the cogging force using the same intervals that would be employed in the equivalent static experimental test discussed later in section 6.4, allowing a fair comparison to be made between these results. The greatest benefit of FEA is that it solves the magnetic and the electrical circuits simultaneously, evaluating electrical variables such as currents, voltages and powers, as well as magnetic forces and flux distribution. Therefore, the effect of small design changes on the overall performance can be observed with high accuracy. The materials selected within the software are listed in Table 3.2

Table 3. 2: Materials assigned in FEA model

Item	Material
Permanent magnet	Neodymium Iron Boron: 38/15
coil	Copper: 92% IACS
Lamination steel	M270-35A

3.5 Mesh Sensitivity

Prior to using FEA for detailed design, it is necessary to verify the sensitivity of the solution to the mesh size. FEA splits the model into a fine mesh of elements. These elements are usually of first or second order tetrahedrons with their specific set of equations that once solved provide the solution of the magnetic fields in the model.

In this thesis, the initial analysis are performed based on FEA solutions, the accuracy of which can be affected by the mesh size, particularly within regions where flux lines change direction rapidly, such as in the airgap of the machine. This is due to the rapid changes in the magnetic field and stored energies. However, a fine mesh comes at the cost of longer computation time. Consequently, the mesh of the FEA solution should be within sensible limits to give a valid solution.

A mesh sensitivity analysis was carried out in which the mesh size was minimised until very small alteration in d-axis flux or peak force occurred because of finer mesh i.e. less than 1%. A further reduction in the mesh size can lead to a significant increase in the computation time with a negligible improvement in accuracy of the results.

The airgap of the machine is considered as the crucial region where mesh refinement would have the major impact as most energy is stored there and field alters orientation the most. For this reason, the mesh of the airgap was considerably denser than other regions in the machine. The maximum element size in the airgap was limited to 0.5mm, compared to 3mm in other parts of the model.

The airgap was divided into four segments as conducted in [49] and shown in Figure 3.4. These were called stator air box, stator remesh, translator air box and translator remesh. The translator and stator air boxes extend into the airgap by 0.25mm, corresponding to $\frac{1}{4}$ of the airgap length to make sure that they clear any stator or rotor components that have acute angled edges. This is important as very high errors in the field are more likely to be occurred in these areas.

The force calculated in MagNet™ based on the Maxwell Stress method along a surface with such field irregularities would lead to an extremely inexact calculation [104]. Therefore, by expanding the translator and stator air boxes into the airgap and allocating a material called virtual air in MagNet™, the problem caused by the field errors at component edges can be removed. This is known as a virtual air shell [104].

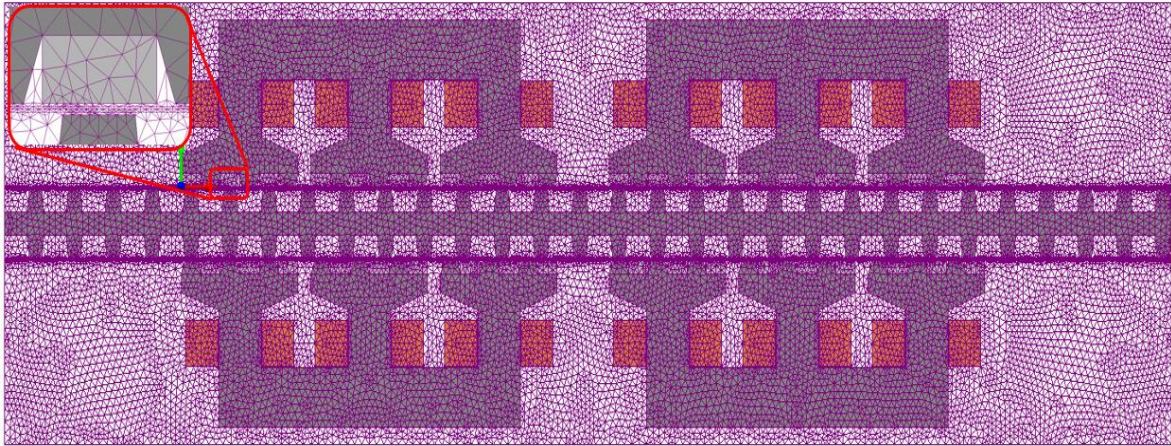


Figure 3. 4: Generated mesh for the proposed IMCP machine

3.6 Investigation of the C-core IMCP Machine

In this section, the C-core IMCP machine is investigated for improving its electromagnetic performance.

3.6.1 PM thickness

PM thickness which is a key parameter was optimised for the optimal thrust force. Figure 3.5 shows the variation of the thrust force with respect to the PM thickness. It can be observed that as the PM thickness increases the thrust force increases rapidly and then slowly until 6mm, after that the thrust force gradually drops due to the effect of magnetic saturation within the ferromagnetic poles. Therefore, the PM thickness was selected to be 6mm.

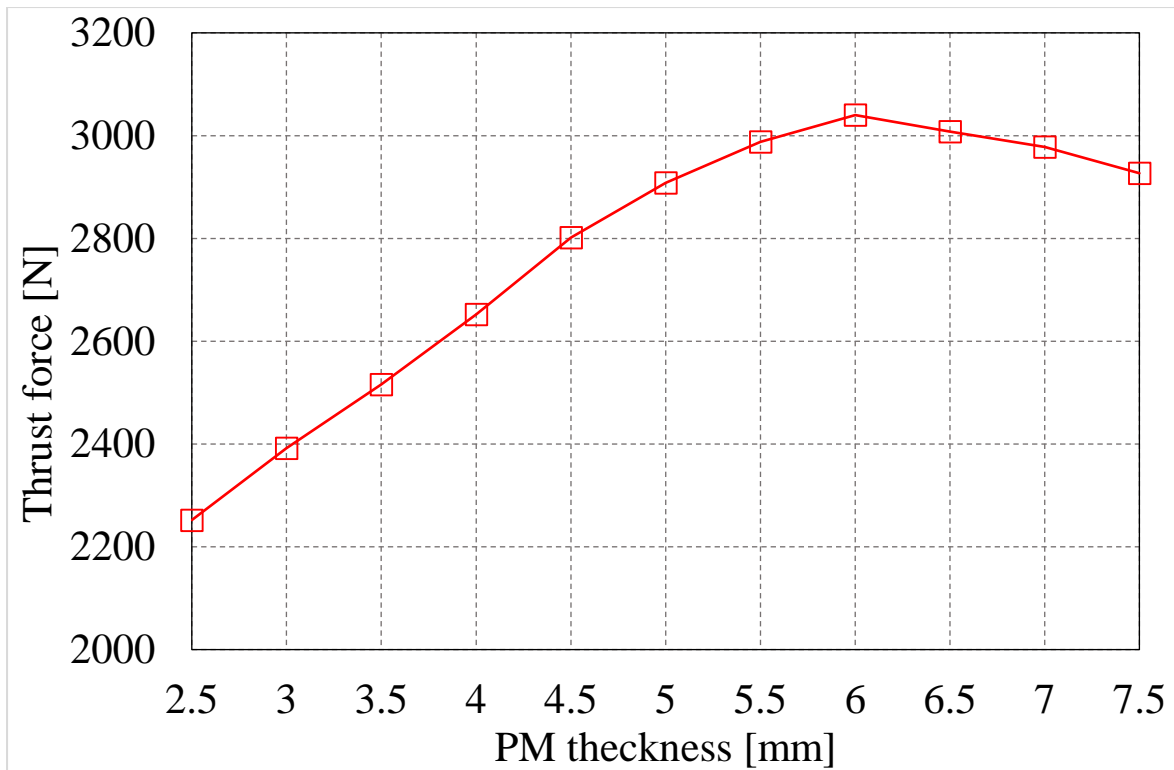


Figure 3. 5: The effect of PM thickness on the thrust force

3.6.2 Translator Tooth Tip

The machine characteristics of the C-core IMCP machine can be influenced by the parameters of the translator tooth such as C_{tip} and C_{root} , which are defined as ratios of the width of the translator tooth tip W_{tip} and the width of the translator tooth root W_{root} to the translator tooth pitch as demonstrated in Figure 3.6. Tapering the translator teeth has been adopted in several studies [97], showing that this technique can improve the airgap flux density as well as reducing the translator mass. The response of the thrust force with respect to the C_{tip} is illustrated in Figure 3.7, while the impact of C_{root} is negligible as validated in the equivalent study [97]. It can be seen that the thrust force gradually increases and then decreases as the C_{tip} decreases. The reason for the drop is that the tooth tip gets smaller and the flux is compressed as the area of the flux path is constrained to the tooth tip when the flux travels towards the stator, and the iron saturates. The maximum thrust force occurs when the C_{tip} is 0.33, so this value was selected.

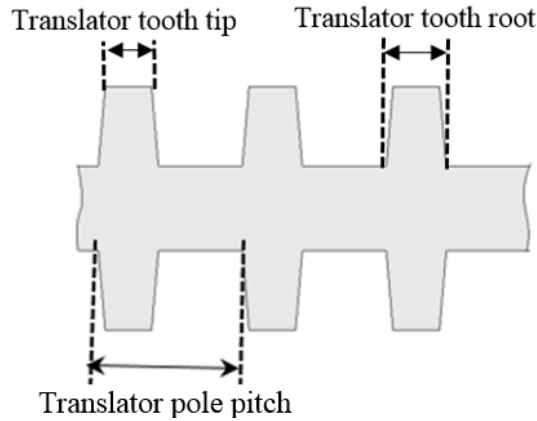
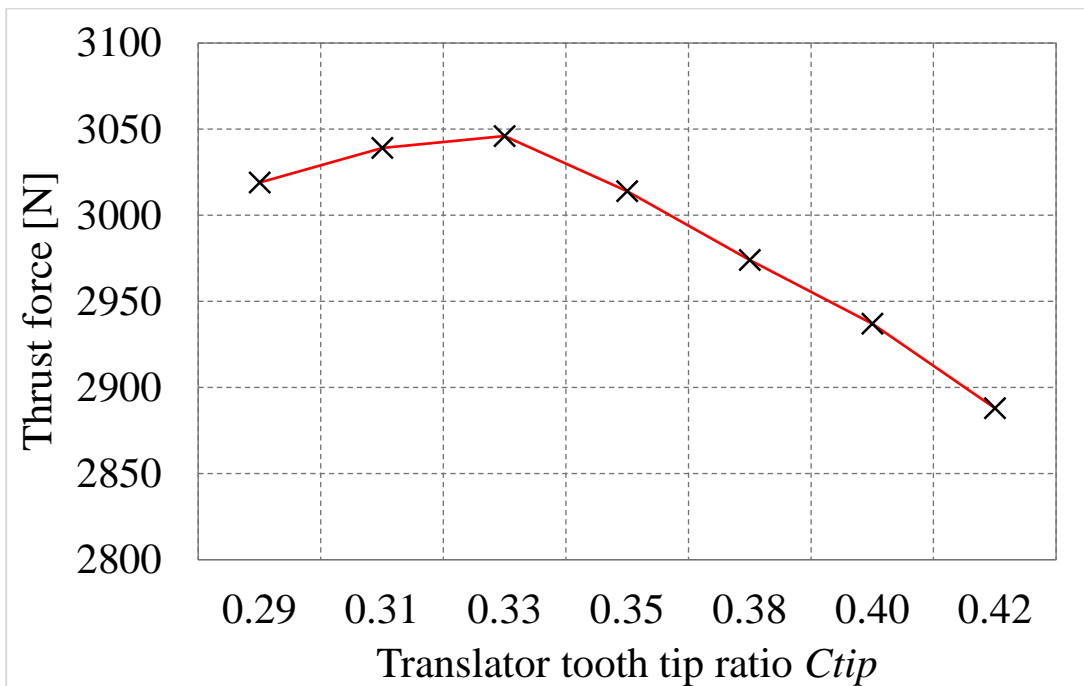


Figure 3. 6: Module of translator

Figure 3. 7: The effect of C_{tip} ratio on the thrust force

3.6.3 Ferromagnetic Pole Ratio

Originally reported in [98], a thorough design study has been carried out. For example, Figure 3.8 shows a tapered and straight version of the soft magnetic poles in a stator with fixed pole pitch. The ferromagnetic pole ratio F_{pr} , is defined as the ratio of the width of the ferromagnetic pole tip to the translator tooth pitch. Figure 3.9 shows the effect of varying ferromagnetic pole ratio on the thrust and cogging forces [51]. It can be seen that the highest thrust force can be achieved when F_{pr} is 0.33, while the minimum cogging force occurs when F_{pr} is 0.39. However, 0.33 was selected as the best trade-off, being a balance between the

reduction in leakage due to the introduction of tapering, and the tooth-tips starting to saturate at low F_{pr} .

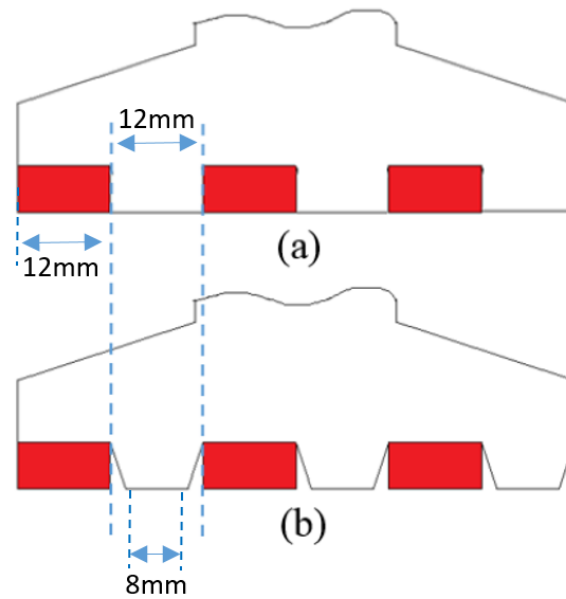


Figure 3. 8: Module of stator tooth (a) straight teeth (b) tapered teeth

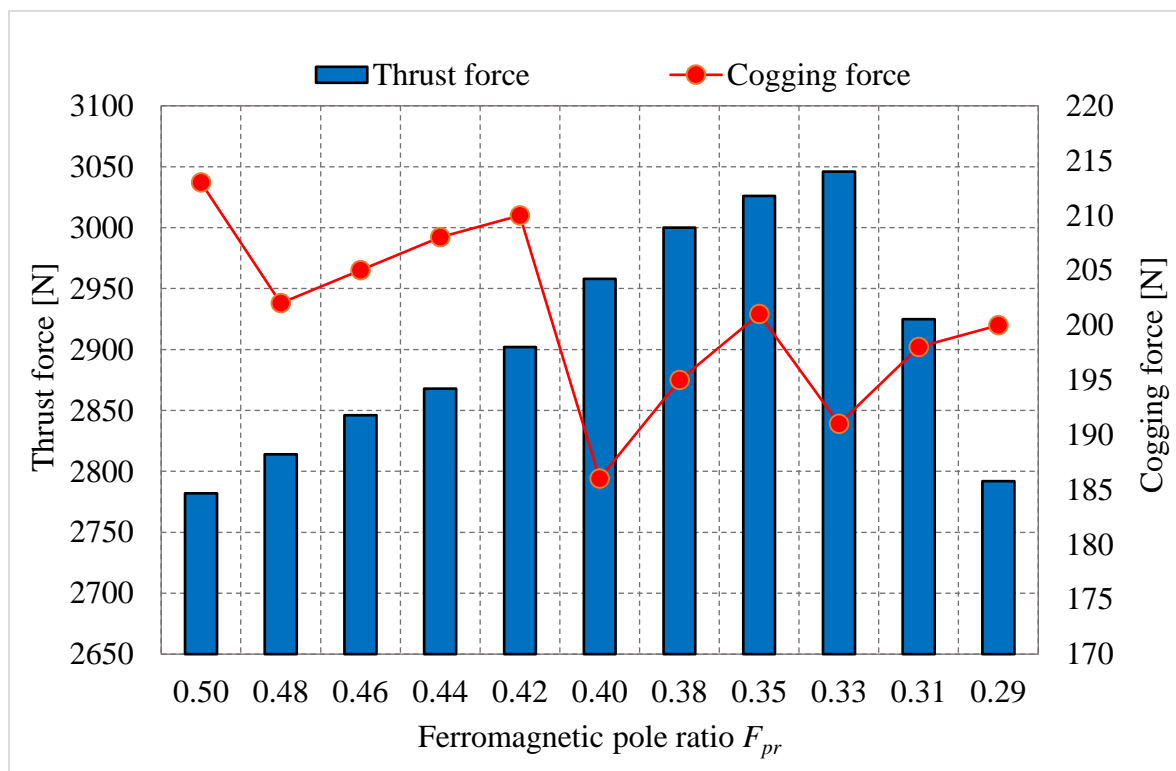


Figure 3. 9: Variation of the thrust and cogging forces with respect to F_{pr}

3.6.4 Thickness of the Translator Coreback

In this C-core IMCP machine configuration, the majority of the useful flux travels straight through the translator teeth allowing the translator coreback to be designed at the minimum possible thickness. The translator coreback was optimised for optimal thrust force and minimum cogging force. The thickness of the translator coreback was varied from 50mm to 10mm, while the translator tooth height was kept constant, 10mm. Figure 3.10 shows the variation of the cogging and thrust forces with respect to the thickness of the translator coreback. It can be seen that at 10mm the effect on the cogging force is negligible, while the thrust force was increased by 9% compared to 50mm. This gives an indication of the possibility of reducing the weight of the translator without sacrificing the machine performance. Therefore, 10mm was selected which is also corresponding to the translator tooth width.

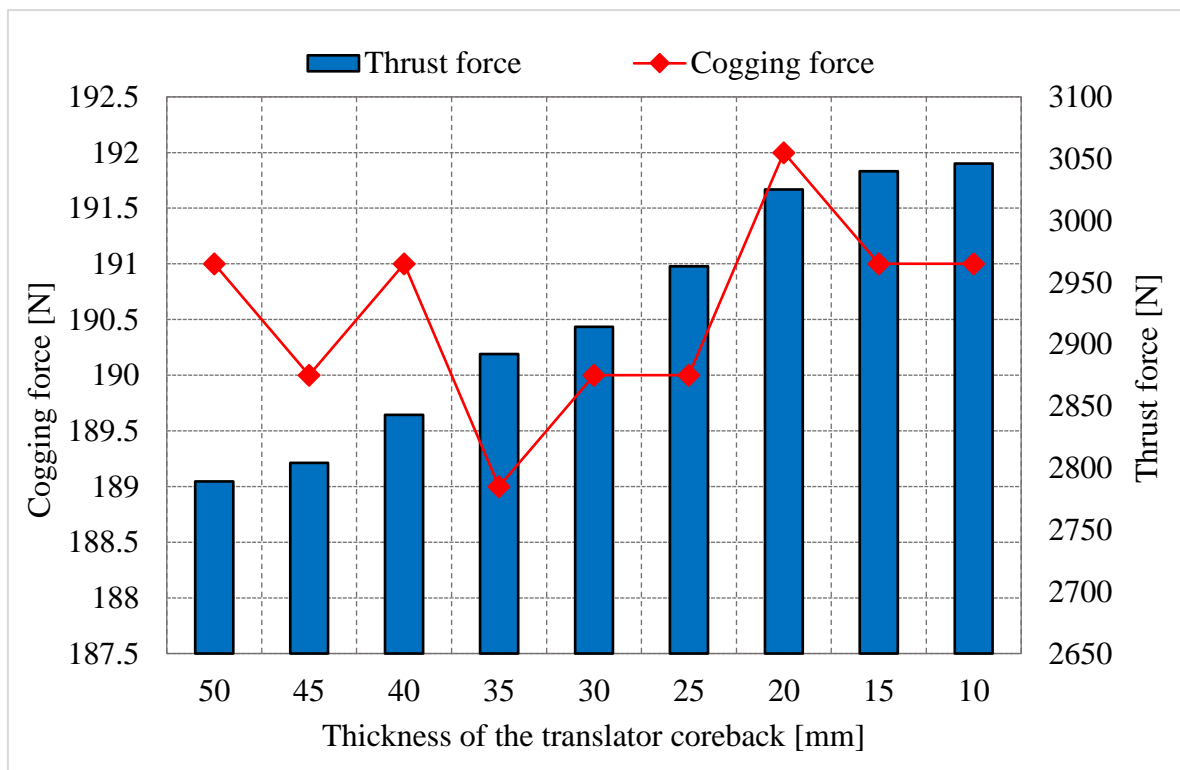


Figure 3. 10: Variation of the thrust and cogging forces with respect to the translator coreback

3.7 Performance Comparison between the C-core Baseline LVHM and the C-core IMCP Machine

To investigate the characteristics of the C-core IMCP machine, the baseline LVHPM machine is also analysed and compared with the former one based on FEA.

3.7.1 Flux Linkage and Back EMF

Figure 3.11 compares the no-load flux linkage waveforms for the C-core IMCP machine and the baseline LVHM. It can be seen that the C-core IMCP machine offers 50% higher flux linkage than that of the baseline LVHM. This is attributable to the reduction in the leakage flux due to the use of the tapered ferromagnetic poles. In addition, the induced no-load back EMF is also greater under the same number of turns of the armature winding and speed condition as shown in Figure 3.12. The generated open-circuit back EMF at rated speed is 138V and 241V for the baseline LVHM and C-core IMCP machine respectively. Hence, a 75% higher no-load back EMF is produced by the C-core IMCP using only 50% of the PM material. As can be seen in Figure 3.11 the flux linkage waveforms for the C-core IMCP machine are symmetrical, balanced and sinusoidal resulting in sinusoidal no-load back EMF which would improve the converter performance and hence the system efficiency. The induced back EMF can be defined as:

$$EMF = \frac{d\Psi_m}{dt} = \frac{d\Psi_m}{dx} \cdot \frac{dx}{dt} = \frac{d\Psi_m}{dx} \cdot v \quad (3.5)$$

Where x is the translator displacement, v is the mechanical speed, Ψ_m is the flux linkage produced by the PMs only.

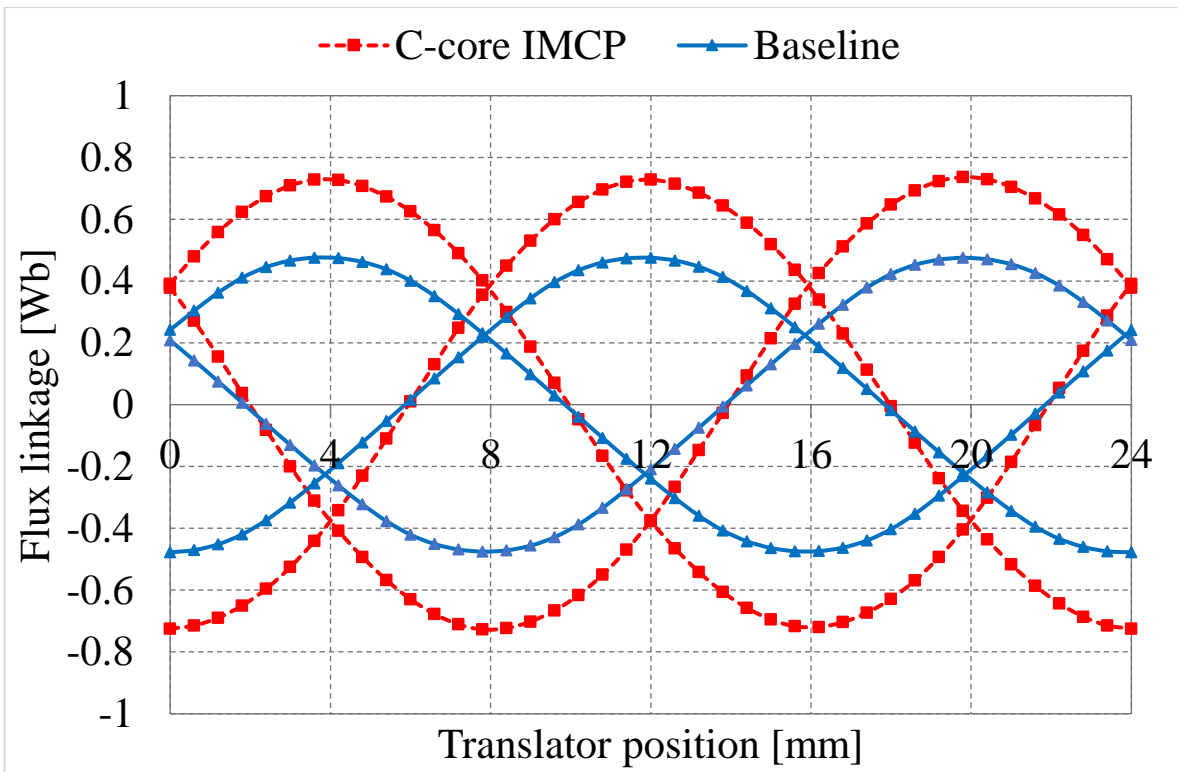


Figure 3.11: Comparison of no-load flux linkage (a) baseline LVHM, (b) C-core IMCP machine

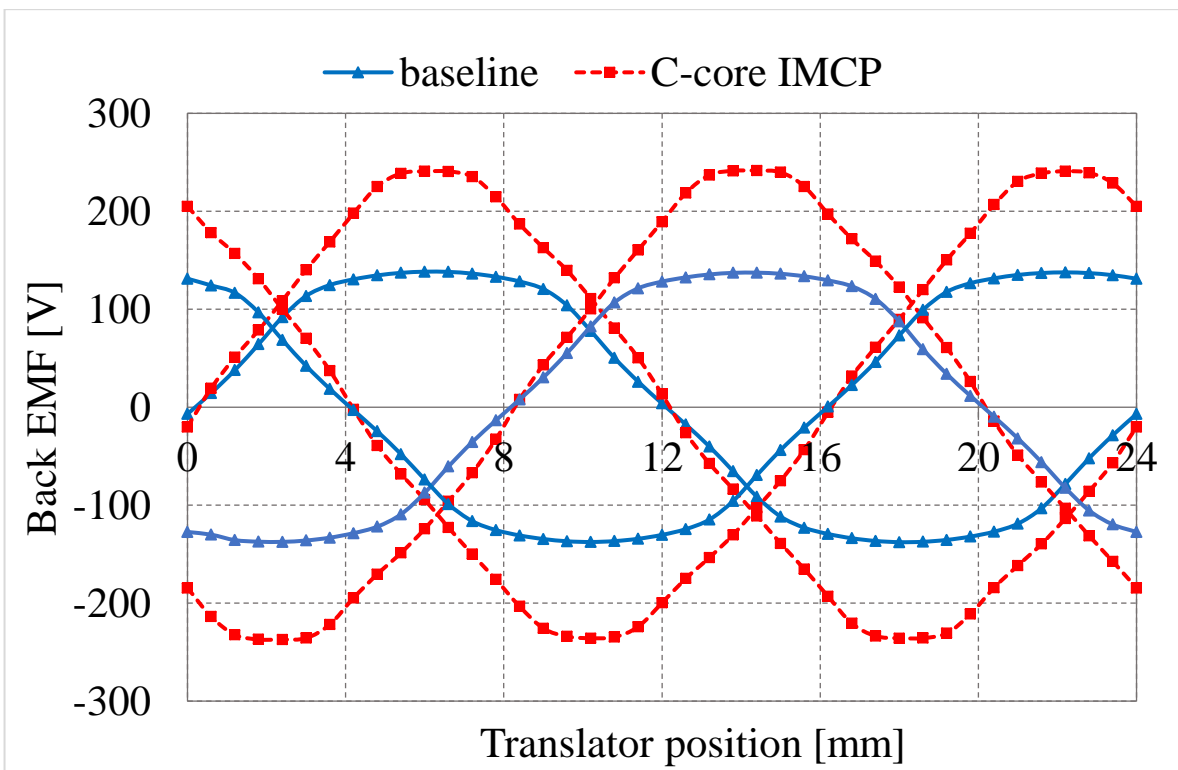


Figure 3.12: Comparison of no-load back EMF (a) baseline LVHM, (b) C-core IMCP machine

3.7.2 Force Capability

Figure 3.13 compares the thrust force performance for both C-core IMCP machine and baseline LVHM under the same armature current. The applied current is assumed to be sinusoidal which smooths the obtained thrust force waveforms. When both machines operate at the same speed and electrical loading, the C-core IMCP machine offers 50% extra thrust force. It can be also observed that the proposed C-core IMCP exhibits only 4% force ripple with respect to the average thrust, while 38% force ripple is shown in the baseline LVHM. In this research, the ratio of the peak to peak force to the average force is defined as force ripple which can be expressed as:

$$F_{ripple} = \frac{F_{max} - F_{min}}{F_{avg}} \times 100\% \quad (3.6)$$

where F_{max} , F_{min} and F_{avg} are the maximum value, minimum value and average value of the thrust force, respectively.

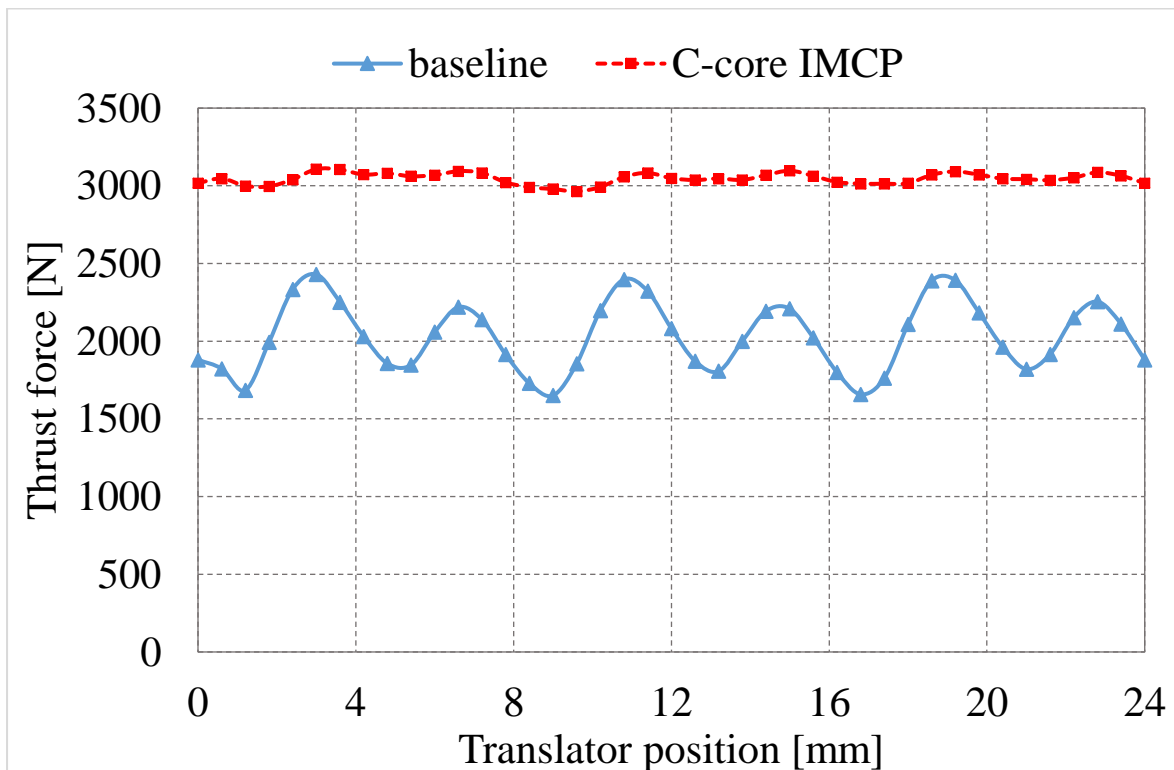


Figure 3.13: Comparison of thrust force (a) baseline LVHM, (b) C-core IMCP machine

Figure 3.14 illustrates the average thrust force characteristics of the baseline LVHM and C-core IMCP machine with respect to the applied current. The armature current is assumed to be sinusoidal and applied in phase with the no-load back EMF. It can be seen that in the baseline LVHM machine as current increases, the average thrust force increases almost linearly. However, in the C-core IMCP machine saturation can be seen to start when the applied current exceeds the rated value, as the consequent pole structure gives a reduced magnetic airgap to the coil driven flux. It should be indicated that the baseline LVHM has better overloading capability.

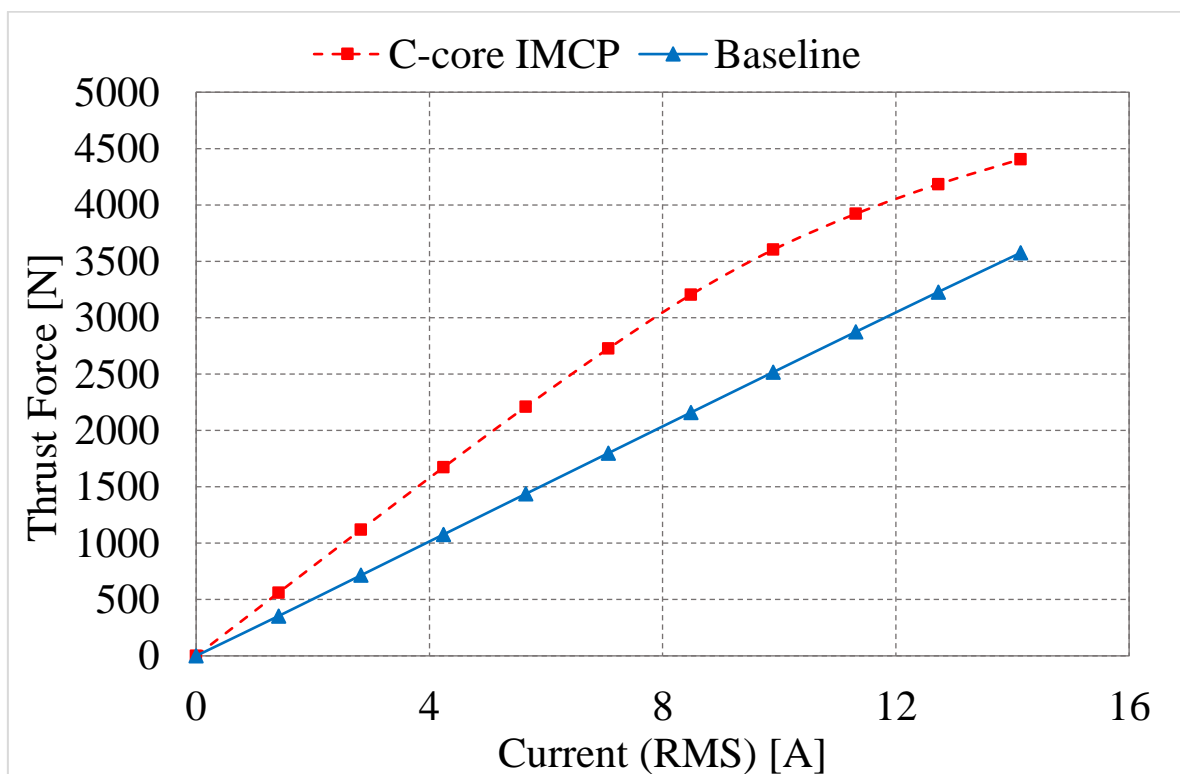


Figure 3. 14: Comparison of thrust force capability (a) baseline LVHM, (b) C-core IMCP machine

In order to assess the cost effectiveness of the force generation of the C-core IMCP machine, the average thrust force per magnet mass for both designs was calculated. It confirms that the C-core IMCP machine is capable of force density of 1.59kN/kg compared to 0.53kN/kg achieved by the baseline one, i.e. a 200% higher force density as calculated using (4.7). In fact the implementation of the tapered ferromagnetic poles in the C-core IMCP machine reduces the effective airgap, and hence the equivalent magnetic reluctance is much less than that of the baseline LVHM machine. Consequently, the power density can be

significantly improved by the C-core IMCP machine as validated in an equivalent study in [97]. The thrust force density has been also calculated based on the following expression:

$$Fd = \frac{F_{avg}}{V} \quad (3.7)$$

3.7.3 Cogging Force

In literature [97, 99, 100, 105, 106], it has been proven that using a consequent pole structure can significantly reduce the undesirable cogging force. Minimizing cogging force is a beneficial requirement for PM machine design for DD-WECs. Figure 3.15 depicts the cogging force waveforms for both the baseline LVHM and C-core IMCP machine. It can be seen that the peak to peak cogging force of the C-core IMCP machine is 191N which represents only 6.2% of the rated thrust force, while the peak to peak cogging force of the baseline LVHM is 782.6N. Which means, the C-core IMCP machine exhibits 75.6% much smaller cogging force than that of the baseline LVHM, hence smoother thrust force is offered by the former machine, particularly at low speed operations.

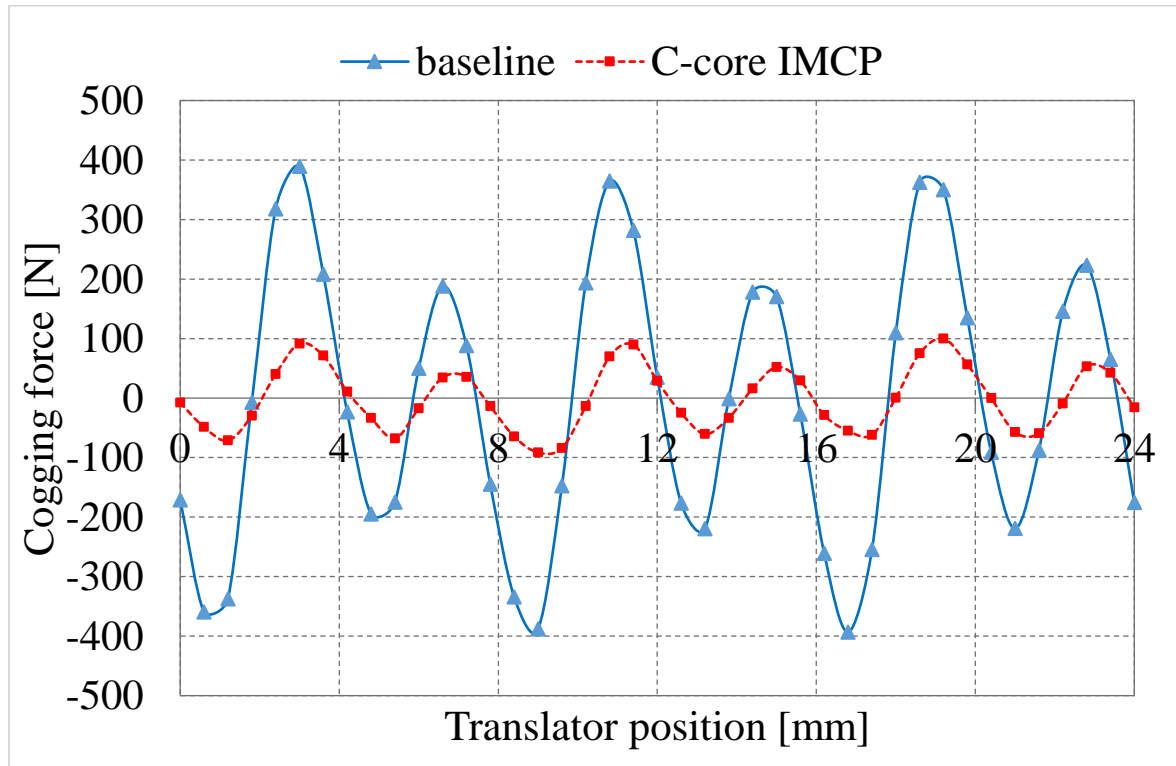


Figure 3. 15: Comparison of cogging force (a) baseline LVHM, (b) C-core IMCP machine

3.7.4 Power Factor

LVHM machines are similar to other variable reluctance machines where the poor power factor is considered as a critical problem [61]. Although a double amount of PM material was utilized in the baseline LVHM compared with C-core IMCP machine, its operating power factor is relatively low, ~ 0.35 . This is mainly caused by the excessive leakage between the adjacent magnets. In the C-core IMCP machine the consequent poles are employed which also affect the PF by reducing the leakage flux. In addition, using trapezoidal translator teeth would vary the field distribution very slightly in the airgap but would allow much flux to be directed to the airgap before saturation happens leading to an increase in the airgap flux density. The adoption of the tapered ferromagnetic poles in the C-core IMCP machine would contribute to further reduction in the fringing flux. Hence, the power factor of the C-core IMCP machine can achieve 0.48, which is 37% higher than that of the baseline.

3.8 Machine Layout Development

The C-core IMCP with modular stator structure discussed above has been proposed for low speed high thrust force applications in [2, 96] and analysed in [95]. However, this type of machine requires a set of individual units to form a three phase machine, e.g. three units with different number of components are required for a single-sided machine [96] or double-sided machine [98].

In this research, it will be shown how the decoupled C-core topology can be modified to form a new version of LVHM that will be known as an E-core topology [107]. As presented by the author in [107], the E-core topology can achieve higher no-load back EMF compared to the C-core machine, whilst reducing the number of parts used in the construction of the machine.

Figure 3.16 shows the C-core IMCP machine initially proposed by the author in [2] and developed in [98, 108, 109]. Three separate C-core units of the IMCP machine have been integrated together to make a three phase integrated machine that reduces the active volume, whilst increasing the robustness and mechanical stability—Figure 3.17(a). After FEA simulation, magnetic flux distribution shows that the integrated C-core design act as two separate E-cores as verified in Figure 3.17(b). So the integrated C-core design is initially converted into two isolated sets of E-core models —Figure 3.18 (a). Another advantage of isolating two E-cores is a reduction in stator volume by eliminating the interconnection iron, which does not provide a useful flux path as verified in Figure 3.18(b). The neighbouring E-

cores are mechanically shifted by 180 electrical degrees and the combined cogging forces of two adjacent sets of E-cores is much less than each of them individually [107]. The resultant lower cogging and force ripple would therefore improve the performance of the machine.

From the aforementioned analysis it can be concluded that the 6 toothed machine behaves as two 3 toothed E-core machines. This gives an indication of the possibility of simplifying the construction by reducing the machine active parts, e.g. number of stator components. Which means, one individual unit of the E-core structure can be used in the final design, in which two identical E-cores facing each other as shown later in Figure 3.20. In addition, the total machine active mass can be reduced by 7% due to the elimination of the laminated iron bridge linking the two adjacent E-cores and the reduction in the machine active length.

3.9 Comparison between C-core and E-core IMCP Machines

This section aims to make a performance comparison between the C-core and the E-core IMCP machines. Table 3.3 compares and summarises the two machines in terms of performance. It can be concluded that the E-core IMCP machine offers higher no-load flux linkage, back EMF, force and force per machine mass owing to the reduction in the active materials. Although the E-core IMCP machine exhibits 3.6% higher cogging force, this disadvantage being offset by a 4% improvement in the power factor, 18.5% reduction in the overall mass and 12.3% reduction in the active length of the E-core IMCP machine. Further to this, the structure of this machine would significantly contribute to facilitating the manufacturing and assembly processes. Therefore, the E-core IMCP machine is the most promising design for further development.

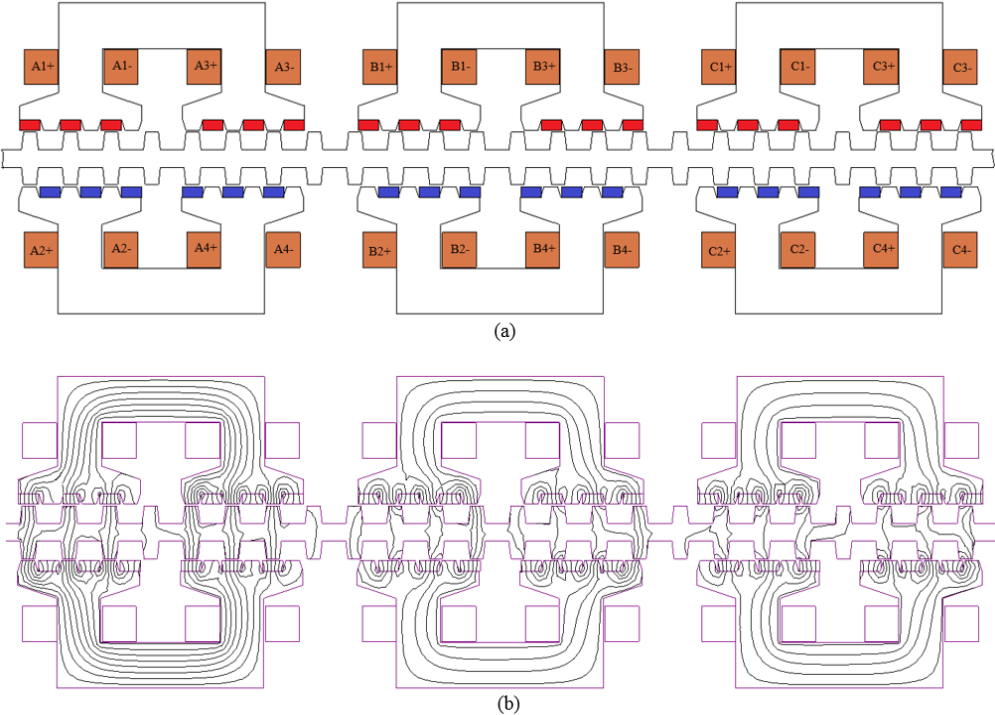


Figure 3.16: C-core IMCP (a) configuration (b) flux distribution

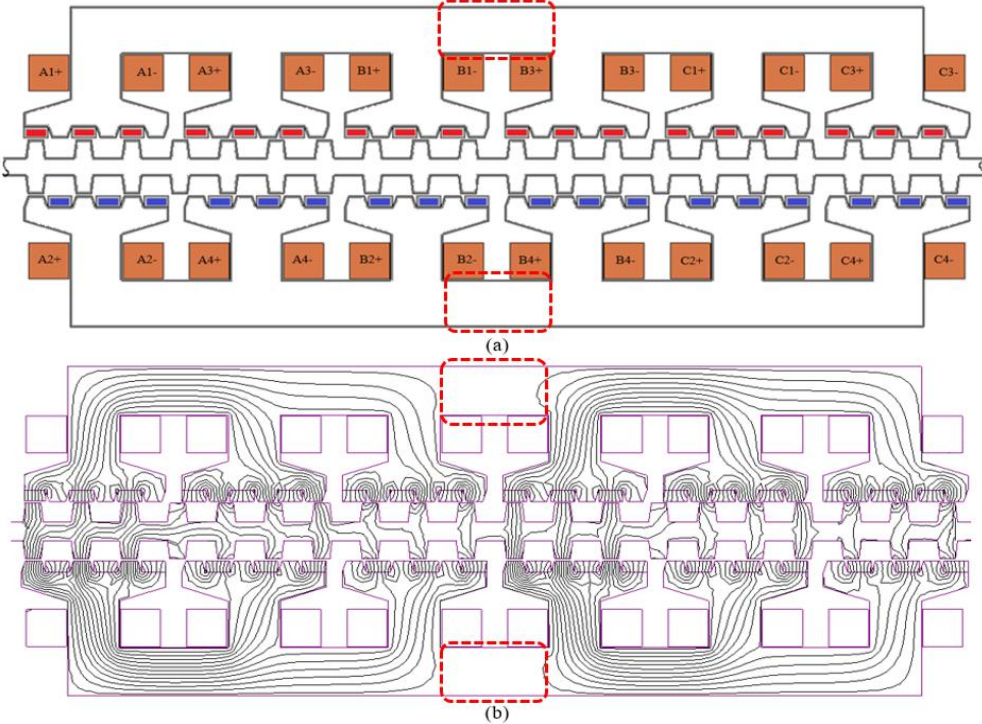


Figure 3.17: Integrated 3-phase E-core IMCP (a) configuration (b) flux distribution

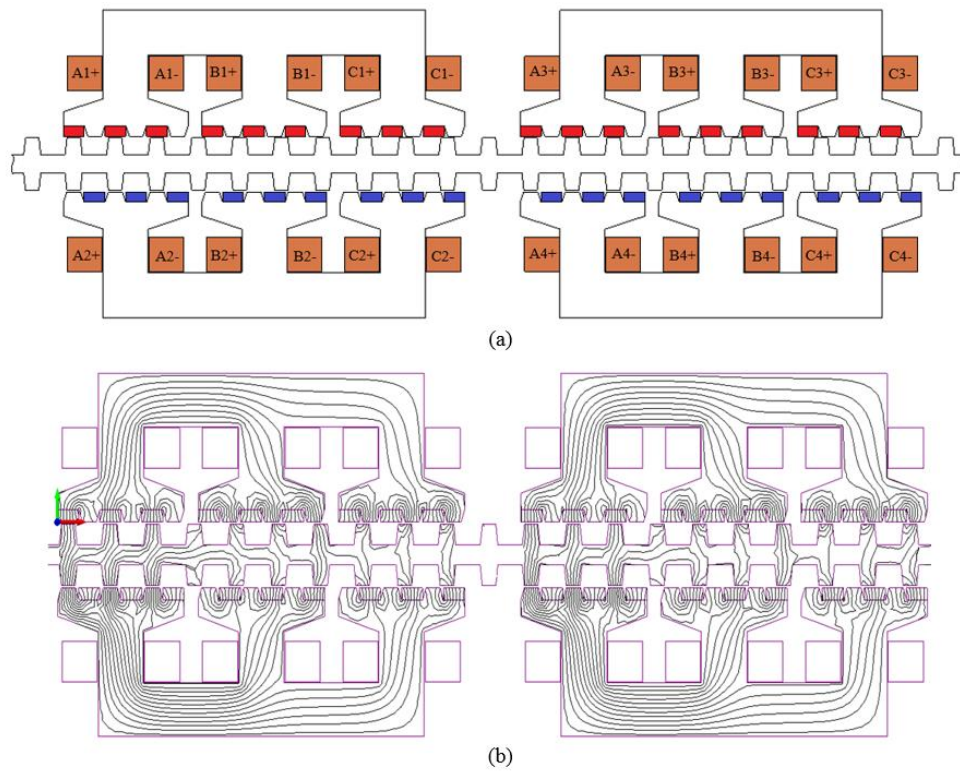


Figure 3.18: E-core IMCP (a) configuration (b) flux distribution

Table 3.3: Performance comparison of baseline LVHM and C-core IMCP machine

Item	C-core	E-core	Difference %
No-load flux linkage [Wb]	0.72	0.76	5.5
No-load back EMF [V]	241	250	3.7
Cogging force [N]	191	198	3.6
Thrust force [N]	3046	3087	1.3
Force/ PM mass [kN/kg]	1.59	1.61	1.3
Force/ active machine mass [kN/kg]	0.6	0.74	23
PF	0.48	0.5	4

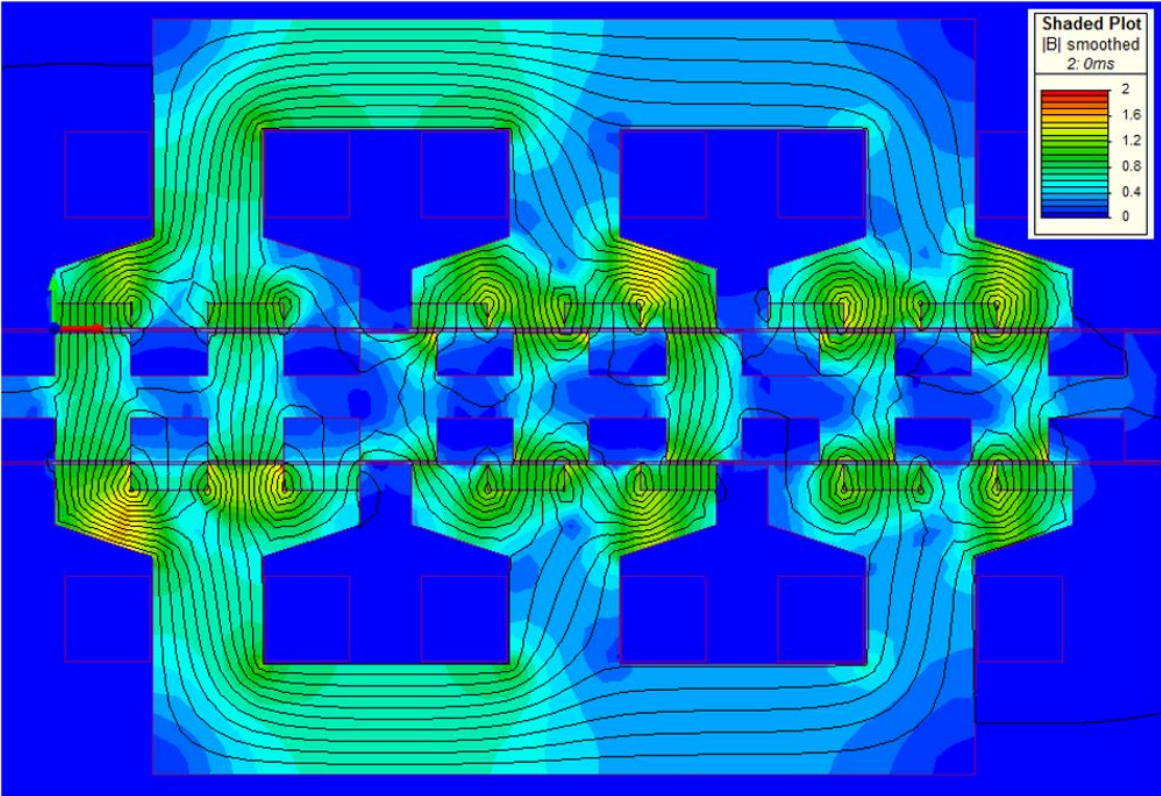
3.10 Final IMCP Machine

In this section, the E-core IMCP machine described above was further investigated for the purpose of facilitating the manufacturing and assembly process.

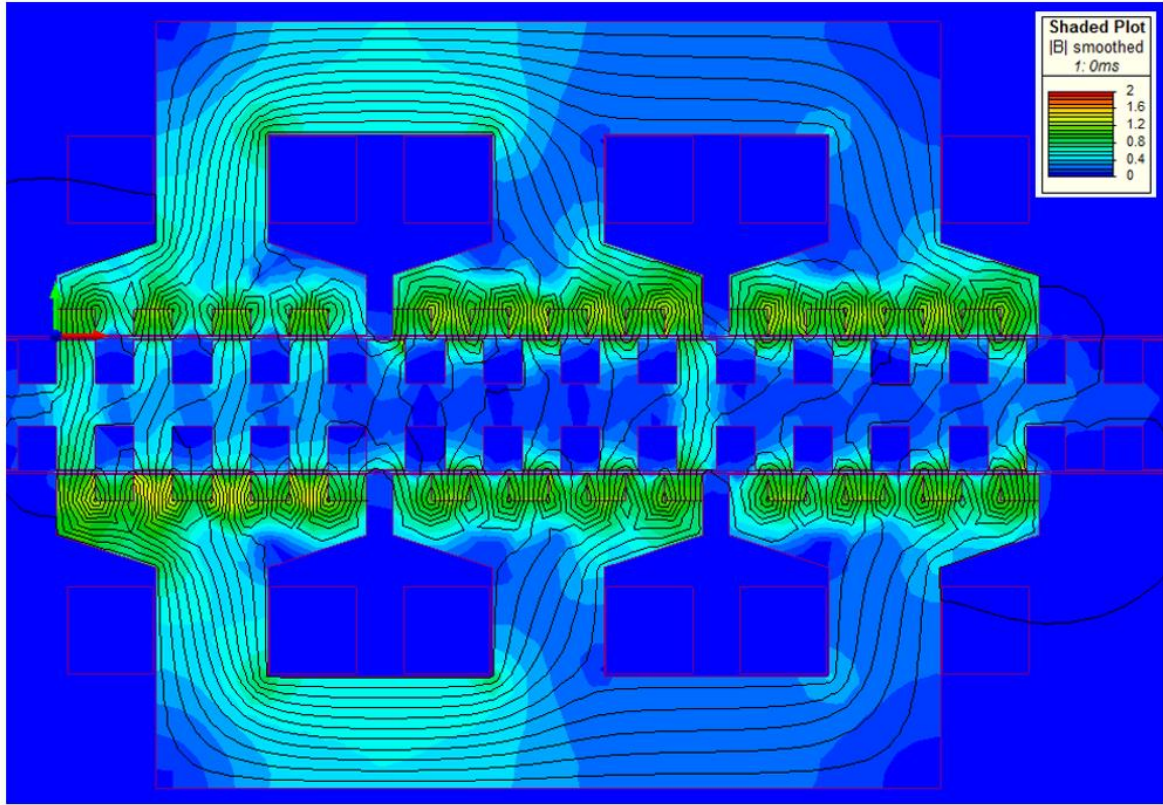
3.10.1 Impact of Number of PM Pole Pairs

In PM machines, to obtain a low speed operation, a suitable number of PM pole pairs is favourable to produce a voltage with an appropriate magnitude and frequency. When the velocity and active length are held constant, a larger number of pole pairs can lead to an increased rate of change of flux linkage, and thus a higher induced back EMF. However, as the number of pole pairs is increased, pole size decreases and the resultant leakage and fringing flux may influence the energy density [110]. When the primary length is given, a higher number of pole pairs requires a small pole pitch resulting in a significant pole-to-pole leakage flux.

The flux distribution under different number of pole pairs is shown in Figure 3.19. It can be seen that when the number of pole pairs is high, a rapid rate of change of the flux linkage can be achieved, thus providing magnetic gearing effect. However, a small amount of the effective flux links the coil and more pole-to-pole leakage flux occurs. On contrary, when the number of pole pairs is small, a large amount of flux links the phase winding. However, this negatively affects the feature of the magnetic gearing as $\frac{d\psi}{dt}$ is reduced. After FEA investigation of the proposed IMCP machine, the convenient number of pole pairs per tooth is 3, which agreed with the similar investigation conducted in [110].



(a)



(b)

Figure 3. 19: The effect of varying the number of PM pole pairs on the flux distribution (a) 2 PM pole pairs (b) 4 PM pole pairs

3.10.2 Description of the Proposed Final IMCP Machine

Figure 3.20 shows the structure of the proposed Final IMCP machine in which the stator is formed of double-sided E-shaped laminated iron cores with a coil wrapped around each stator tooth. Each stator tooth is provided with three ferromagnetic poles and has three PMs mounted on its surface. Tapered ferromagnetic poles [51, 111] are adopted in the proposed design where one polarity of PM is replaced with a piece of iron – the *consequent pole*. Which means, this configuration has one polarity of PM in each stator side (either north or south), while the tapered ferromagnetic poles act as the missing polarities. The tapered ferromagnetic poles are the most distinctive feature of the present machine, which will be discussed in more details in section 3.10.4.2. Moreover, in order to obtain the three phase machine, the mechanical displacement D_{st} between adjacent stator teeth should satisfy

$$D_{st} = (n \pm 1/3)\tau_t \quad (3.8)$$

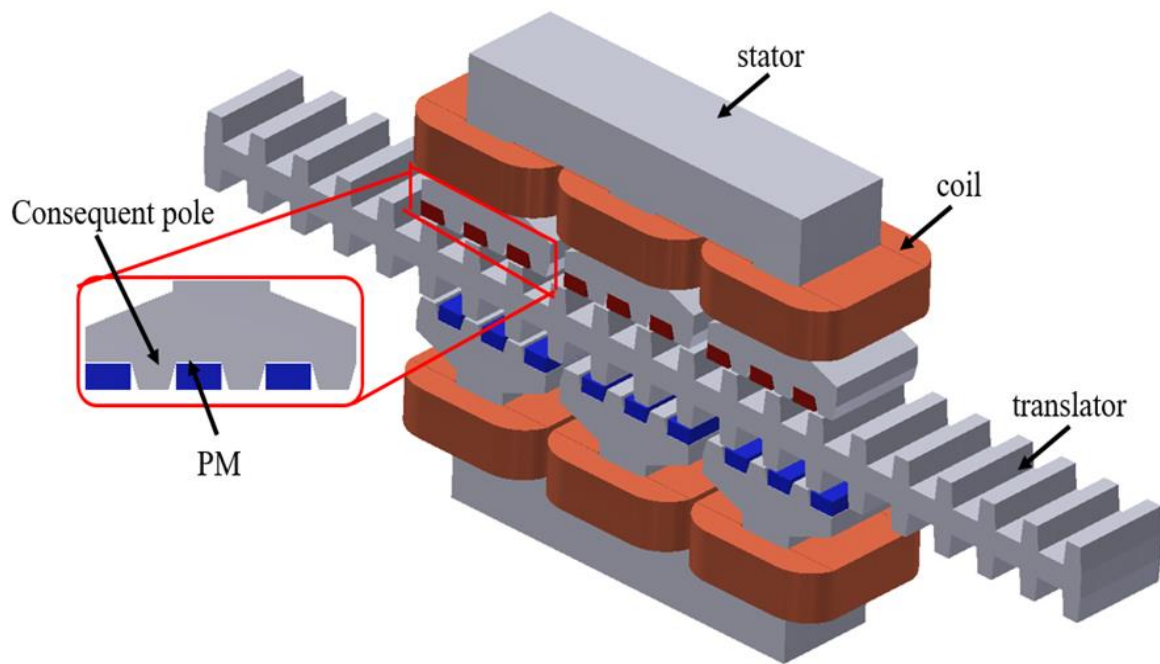


Figure 3. 20: Configuration of the proposed IMCP machine

The specifications of the proposed IMCP machines are listed in Table 3.4.

Table 3. 4: Specifications of the proposed IMCP machine

Item	Unit	Value
Rated speed	m/s	1.2
Number of PMs	mm	18
Airgap length	mm	1
PM width	mm	12
PM thickness	mm	6
Ferromagnetic pole width	mm	12
width of Ferromagnetic pole tip	mm	8
Stack length	mm	50
Mover tooth height	mm	10
PM volume	cm ³	64.8
Number of turns/coil	turn	112
Force	kN	0.77
Power	kW	0.924
Current density (RMS)	A/mm ²	3.5

3.10.3 Operation Principle

The proposed IMCP operates upon the same operation principle of the flux reversal PM machine [96]. Taking phase B as an example, when the translator teeth are aligned with PMs of the middle top stator tooth as shown in Figure 3.21(a), the flux linkage produced by phase B winding reaches its maximum negative value, while the phase back EMF is zero. However, as the translator moves a quarter of its tooth pitch, corresponding to 6mm, the flux linkage becomes zero as illustrated in Figure 3.21(b), while the phase back EMF is positive maximum. Again, when the translator moves half of its tooth pitch, the flux is reversed and reaches the maximum positive value as shown in Figure 3.21(c), while the phase back EMF drops to zero. As the translator moves three quarters of its tooth pitch, the flux linkage is zero as shown in Figure 3.21(d), while the back EMF reaches its maximum negative. Further displacement of one quarter of the translator tooth pitch will allow both the flux linkage and back EMF to complete their full electrical cycles. Consequently, the flux linkage can be rapidly changed over a small translator displacement leading to a significant increase in the thrust force density, hence achieving the magnetic gearing effect [96].

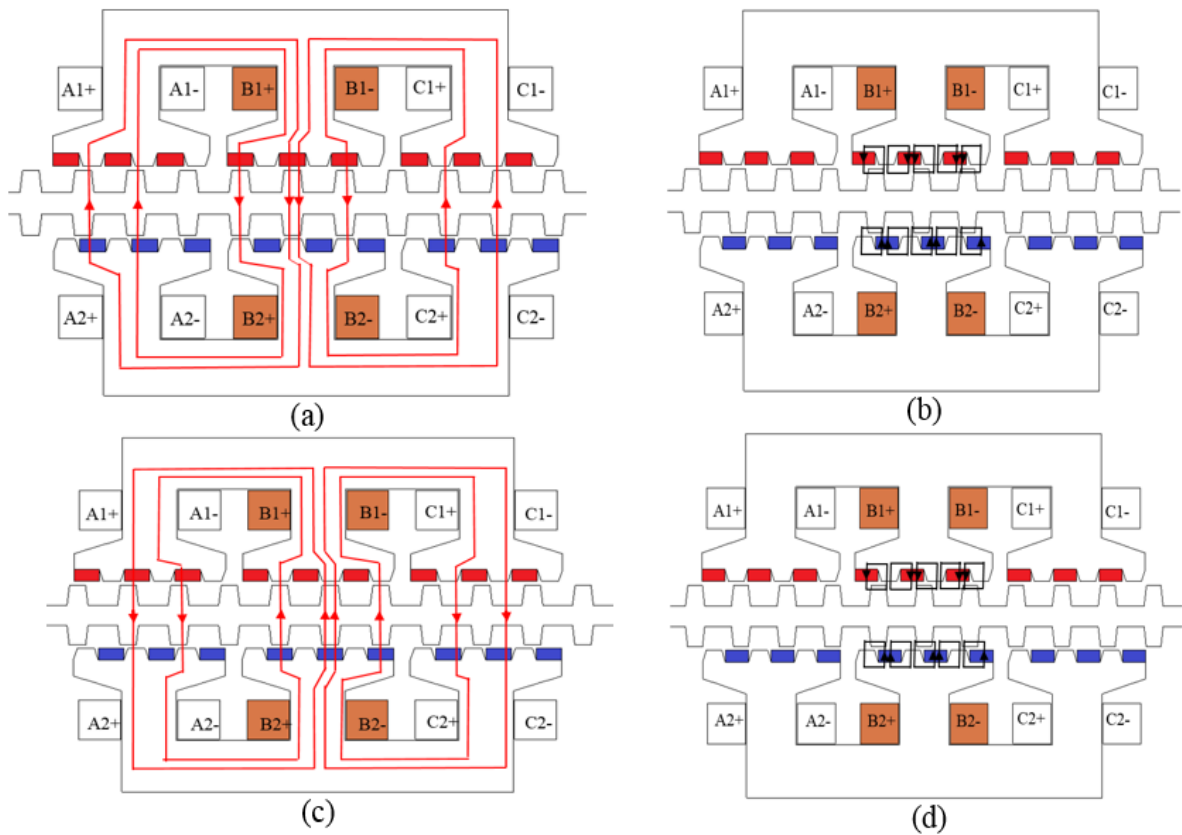


Figure 3. 21: Operation principle at different translator positions. (a) Position a. (b) Position b. (c) Position c. (d) Position d.

Figure 3.22 demonstrates the magnetic gearing effect in the proposed IMCP machine. It can be observed that the flux distribution changes 120 electrical degrees, while the translator moves only 8mm, corresponding to one third of the translator tooth pitch.

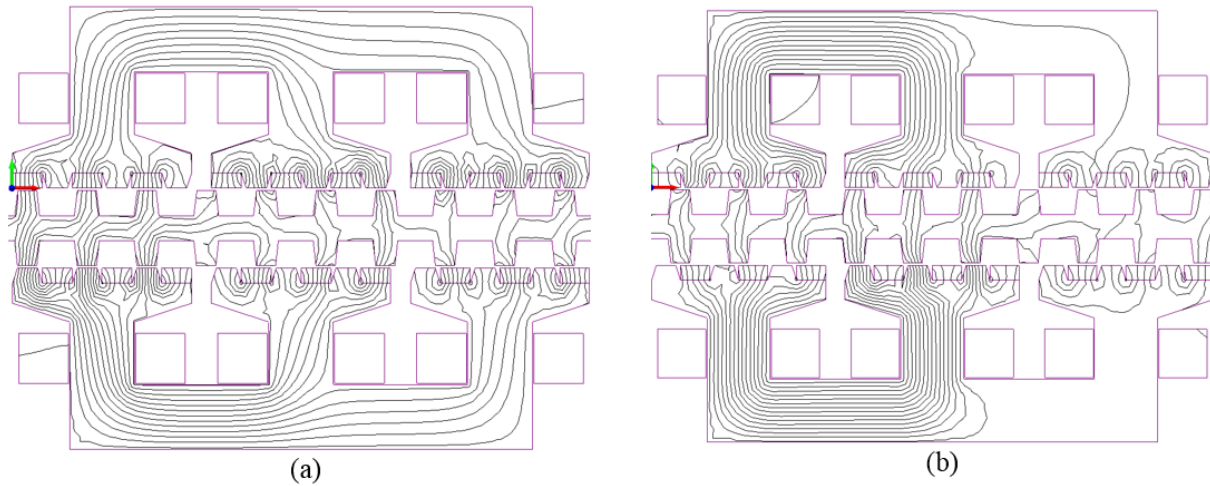


Figure 3. 22: No-load field distribution (a) $x= 0$, (b) $x= 8\text{mm}$

3.10.4 Investigation of the Final IMCP Machine

The influence of different parameters on the machine performance is studied in this section. To begin with, the stator geometry is kept constant while the magnet thicknesses is varied. This parameter is then kept constant, while the influence of some key geometry parameters such as PM width, ferromagnetic pole ratio, translator tooth width, translator tooth tip ratio, airgap length, are also optimized in this research.

3.10.4.1 PM thickness

In literature [97, 99], it has been reported that the PM thickness can significantly influence the machine performance. The variation of the thrust force versus PM thickness is plotted in Figure 3.23. Two key factors were considered during this investigation; e.g. the accidental irreversible demagnetization, which requires the PMs to be thick enough, and the saturation effect, which may occur within the ferromagnetic poles as a result of thicker PM. In this research, the PM thickness was varied from 2.5mm to 7mm. It can be seen from the above-mentioned Figure that thrust force increases with magnet thickness and then appears to reduce above 6mm. This feature is quite different from that of conventional PM machines due to the fact that the greater the PM thickness is, the higher the PM flux density is.

However, the flux modulation effect of the translator teeth on the airgap flux density distribution would be negatively influenced [99]. In addition, the presence of the magnetic saturation within the ferromagnetic poles can affect the thrust force. The average thrust force is maximum when the PM thickness is 6mm. Therefore, the PM width 6mm was selected.

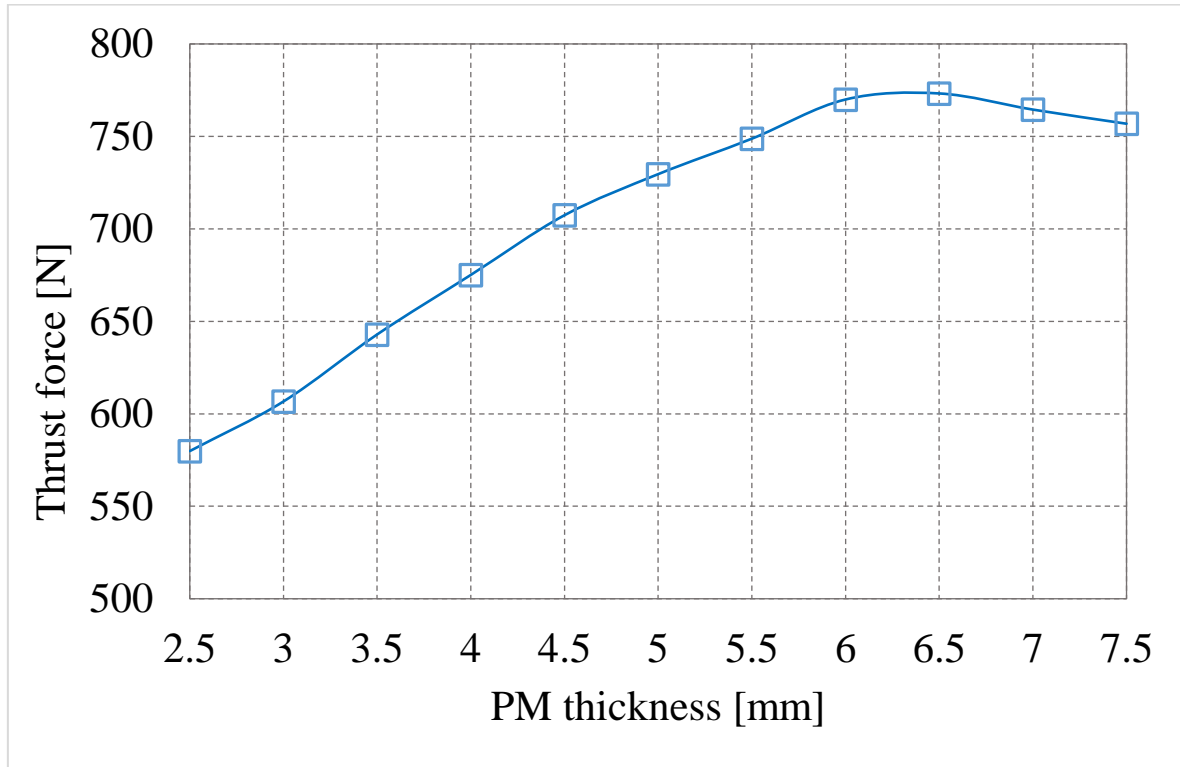


Figure 3. 23: Variation of thrust force with respect to the magnet thickness

3.10.4.2 Ferromagnetic Pole Ratio

Tapered ferromagnetic poles are adopted in the proposed IMCP machine, which act as the missing polarity. Therefore, it is worth to optimise the ferromagnetic pole ratio F_{pr} , which is defined as the ratio of the ferromagnetic pole tip to the translator tooth pitch, identified in Figure 3.24. A proper selection of this ratio would contribute to a noticeable reduction of the undesirable harmonics such as 5th harmonic resulting in approximately sinusoidal no-load back EMF waveforms. In addition, since the no-load back EMF waveforms are close to sinusoidal, the peak to peak amplitude of cogging force is reduced.

Figure 3.25 shows the effect of varying ferromagnetic pole ratio on the thrust force and cogging force. It can be seen that the highest thrust force can be achieved when F_{pr} is 0.33,

while the minimum cogging force occurs when F_{pr} is 0.29. However, the F_{pr} of 0.33 was selected as the ferromagnetic poles starts to saturate when F_{pr} is 0.29, which negatively influenced the thrust force.

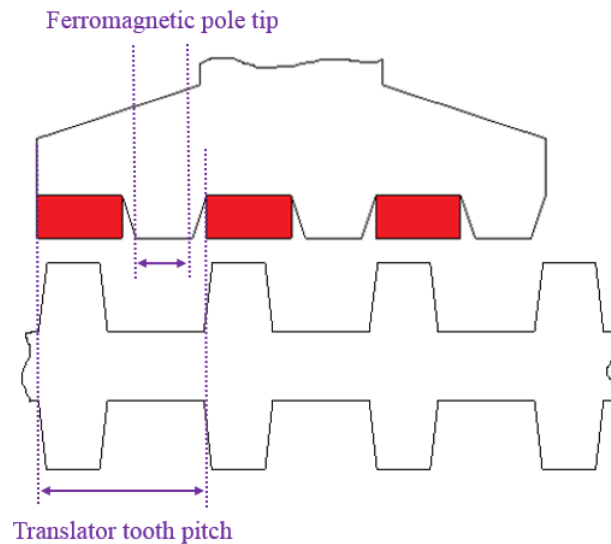


Figure 3. 24: Module of stator and translator

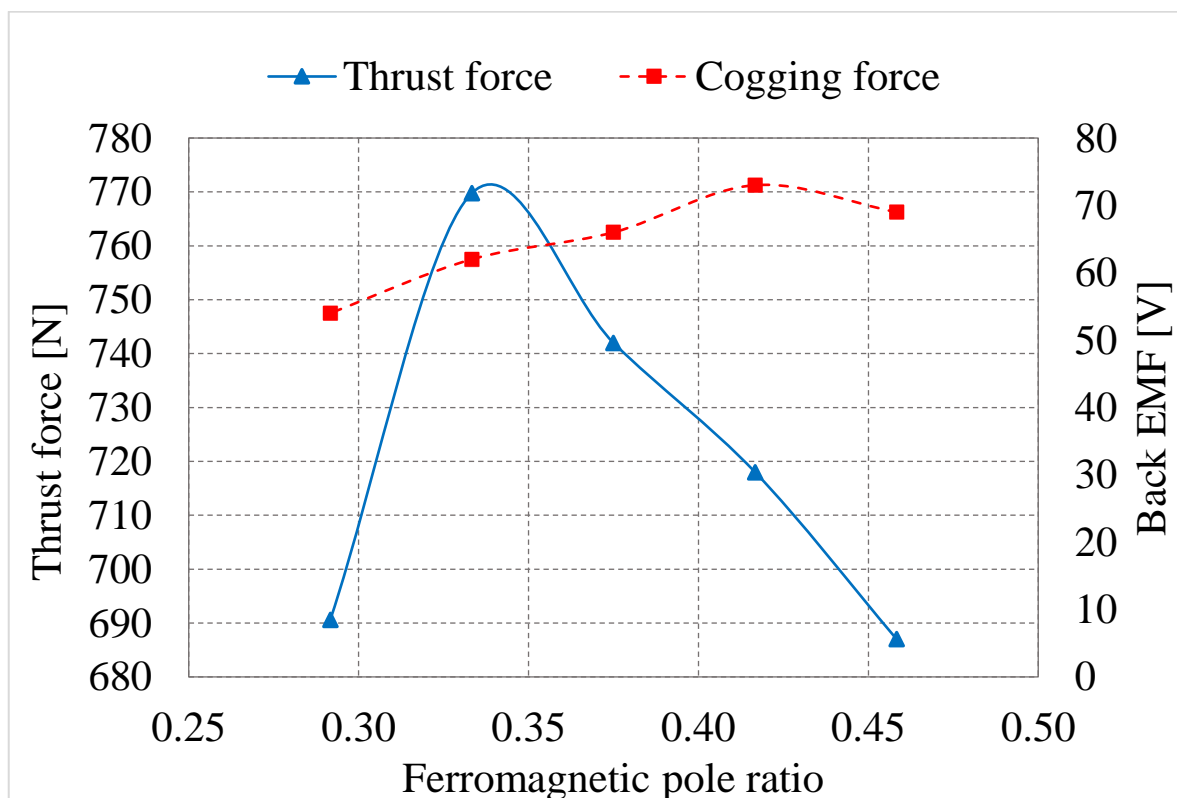


Figure 3. 25: The effect of ferromagnetic pole ratio on the thrust force and cogging force

3.10.4.3 PM Width

Authors [97, 99, 112] have proposed consequent pole Vernier machines with unequal width of PMs and consequent poles for the purpose of improving the magnetic loading. This means that the PM width is bigger than pole pitch. The larger the PM width is, the greater MMF will be produced [97]. However, the tapered ferromagnetic poles are easily saturated, which can significantly influence the magnitude of the thrust force [99]. Furthermore, as the tapered ferromagnetic poles [51, 98] are adopted in the proposed design, the PM width is kept as the same width of the pole pitch, 12mm. The tapered ferromagnetic poles described in the previous section and analysed in [51, 98] have the feature of reducing the fringing flux, allowing the main flux to be increased. This indicates that there is no need to increase the PM width as magnetic loading can be improved by employing the tapered ferromagnetic poles. Figure 3.26 shows the effect of the PM width on the cogging and thrust forces when the conventional rectangular consequent poles shown in Figure 3.27(a) are employed. It can be seen that as the magnet width increases the no-load back EMF and thrust force increase and then decrease, in which their maximum values occur when PM width is 14mm. By looking at the magnitude of the no-load back EMF obtained when the PM width is 14mm, (2mm greater than pole pitch) as shown in Figure 3.27(a) it can be observed that it is very similar to the magnitude of the back EMF obtained when the tapered ferromagnetic poles were employed using the initial PM width, 12mm as verified in Figure 3.28. In other words, tapering the consequent poles is equivalent to increasing the magnet mass by 10.5%. Furthermore, a trapezoidal waveform of the no-load back EMF obtained when the PM width is 14mm as verified if Figure 3.28.

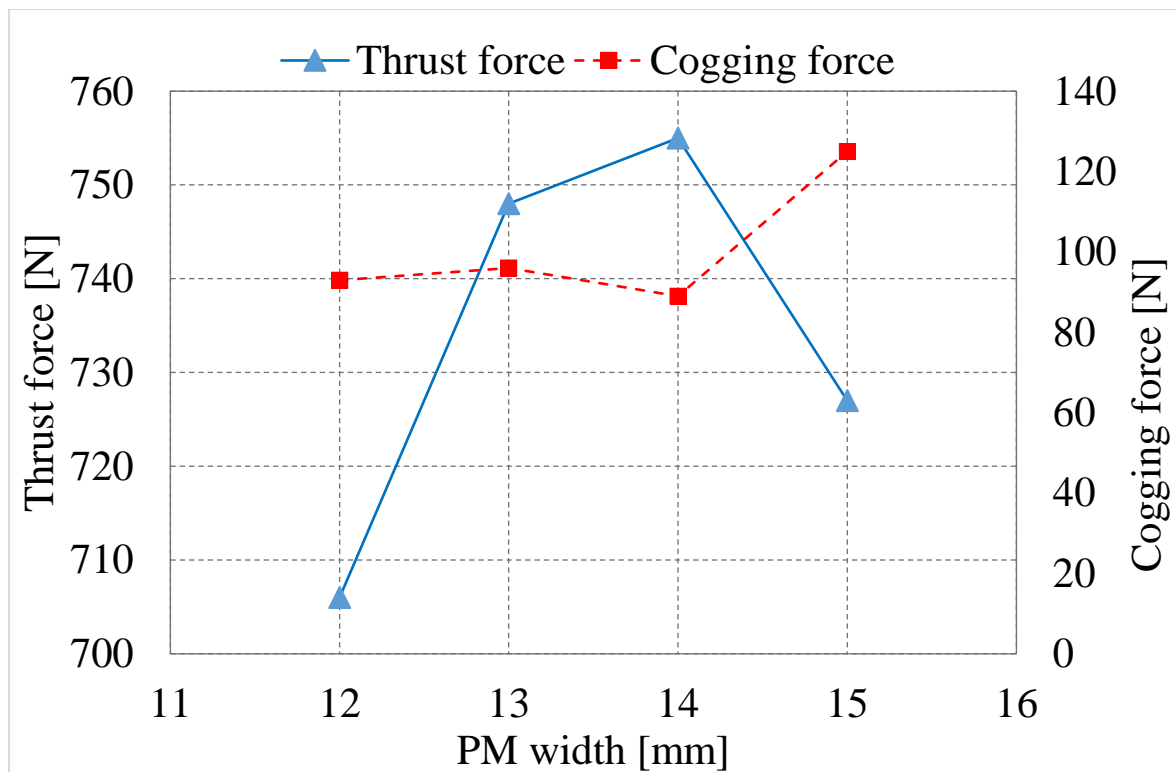


Figure 3. 26: Effect of PM width on the thrust force and cogging force

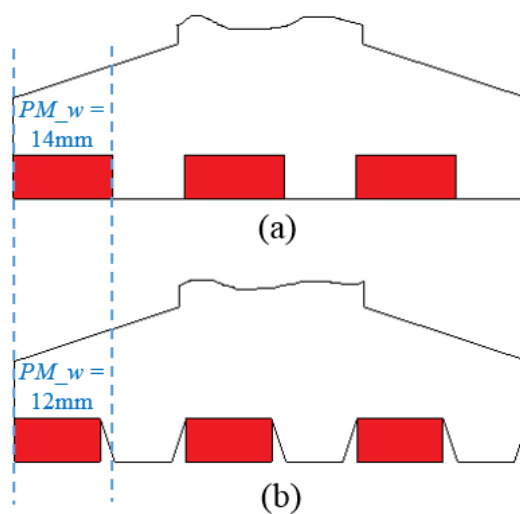


Figure 3. 27: Consequent pole (a) rectangular (b) tapered

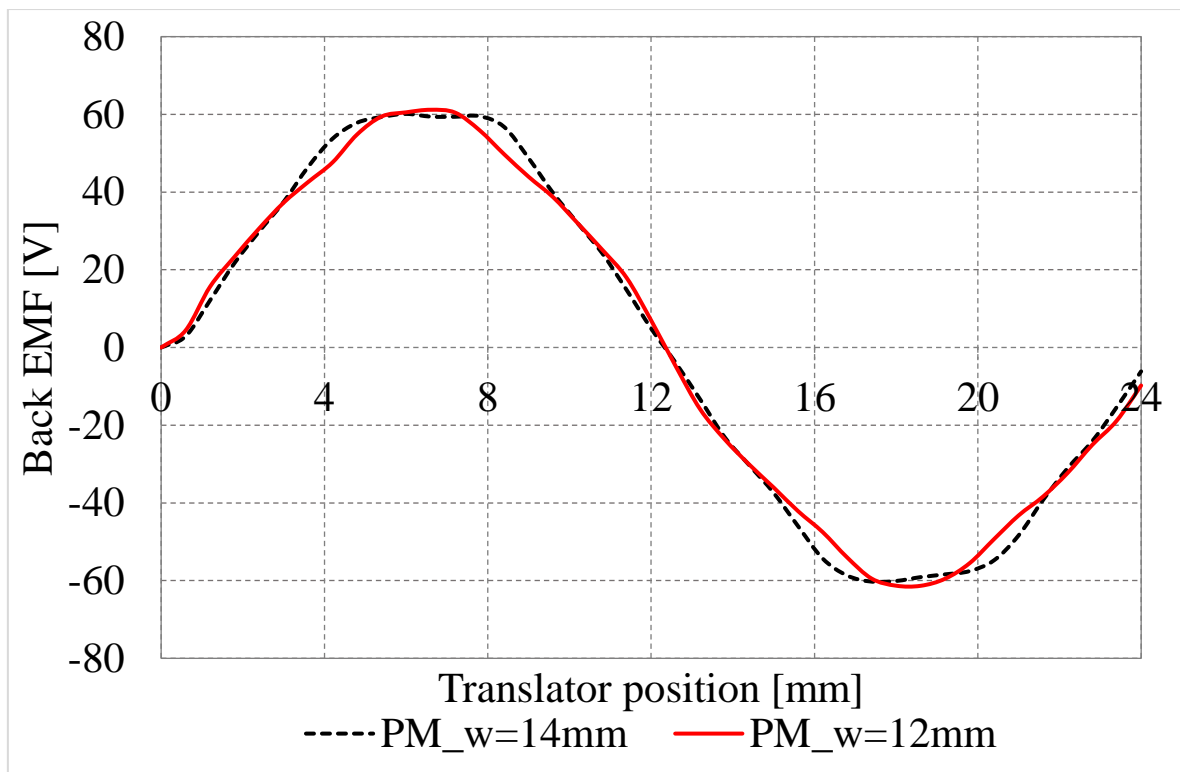


Figure 3. 28: No-load back EMF waveform under different PM width

3.10.4.4 Translator Tooth Width

In the VHM proposed in [2] the translator tooth width was designed to be equal to the pole pitch, 12mm. In this research, the effect of varying the translator tooth width on the machine performance has been investigated. This may improve the machine performance and reduce the translator mass. The translator tooth width was varied from 12mm (the initial width) to 8mm with an interval of 0.5mm. Figure 3.29 shows the variation of the peak no-load back EMF and cogging force with different translator tooth width. It can be seen that the thrust force increases gradually as the tooth width getting smaller. However, the cogging force is minimum when the tooth width is 10mm. Moreover, a negligible increase of the thrust force is seen when the translator tooth width is smaller than 10mm. Therefore, the tooth width of 10mm was selected, which would also result in an 8.3% reduction in the translator mass compared to the initial translator tooth width.

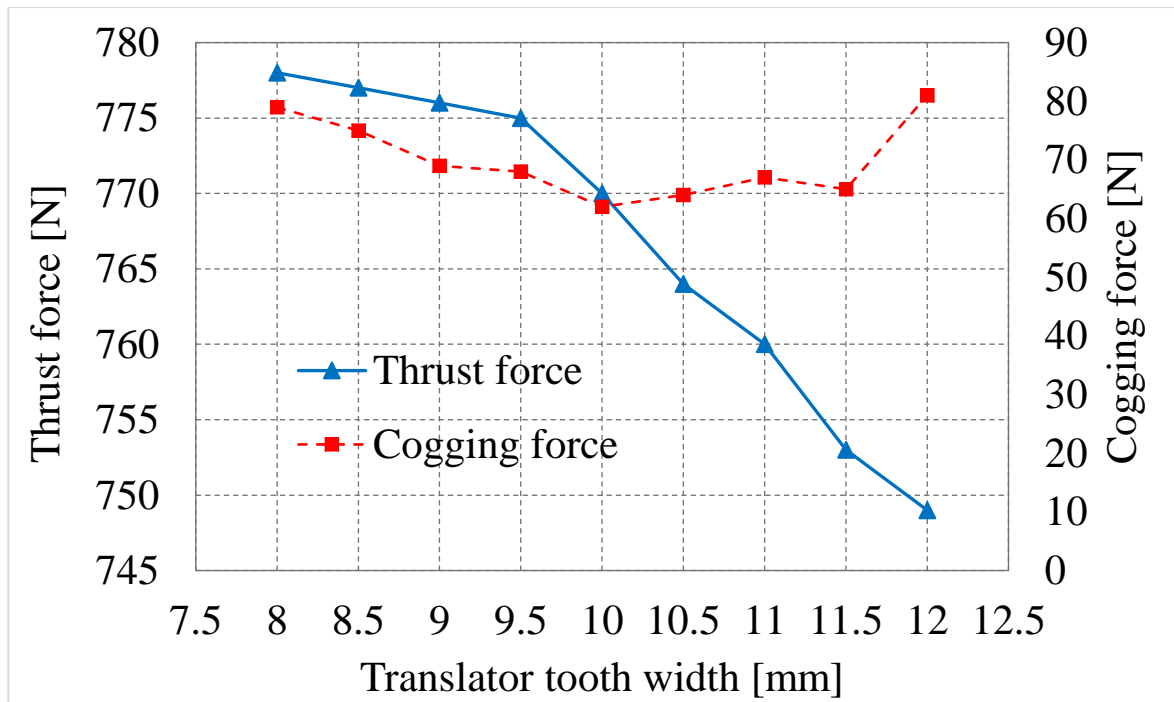


Figure 3. 29: Effect of translator tooth width on the thrust force and cogging force

3.10.4.5 Translator Tooth Tip

Using trapezoidal translator teeth would vary the field distribution very slightly in the airgap but would allow much flux to be directed to the airgap before saturation happens leading to an increase in the airgap flux density [44, 97]. Figure 3.30 shows the effect of varying C_{tip} ratio which is identified in section 3.6.2 on the thrust and cogging forces. It can be seen that the thrust force is maximum when C_{tip} equals 0.33, (the minimum possible width of the tooth tip before the saturation starts). On the other hand, while the minimum cogging occurs when C_{tip} equals 0.34. However, 0.33 shows the best compromise and hence was selected.

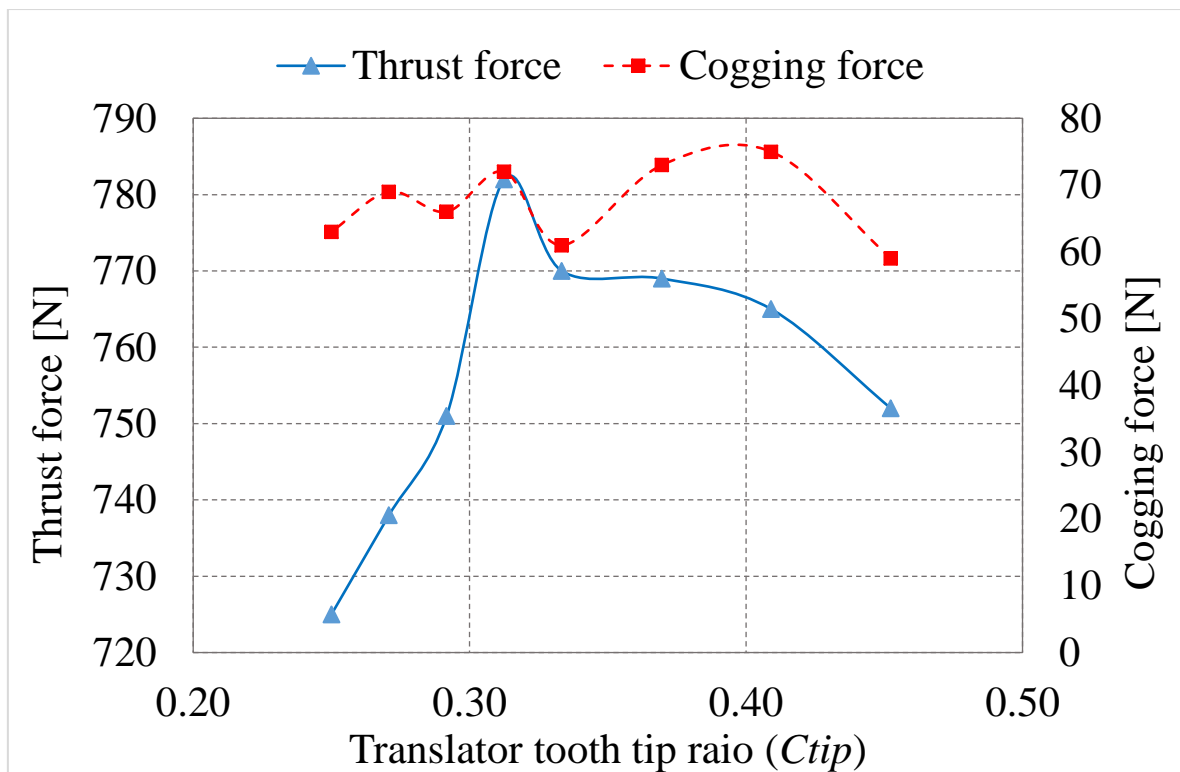


Figure 3. 30: Variation of the thrust force and cogging force with respect to the C_{tip} ratio

3.10.4.6 Airgap Length

Airgap is one of the main concerns of electrical machines to realize electromechanical energy conversion [97]. Hence, airgap length is an essential design parameter for the proposed IMCP machines. Generally speaking, as the airgap length reduced, the machine electromagnetic performance improves. However, a small the airgap length may result in complexity of manufacturing and assembling accuracy.

The airgap size of the proposed IMCP machine has a significant influence on the flux modulation effect of airgap structures apart from the airgap flux density amplitude. Therefore, the performances, such as force capability of the proposed IMCP machine are more sensitive to the airgap length [99]. Figure 3.31 shows the variation of thrust force with airgap length. It can be seen that the thrust force decreases linearly due to a linear increase in the airgap reluctance with the airgap length. However, the airgap is selected to be 1mm to avoid mechanical issues.

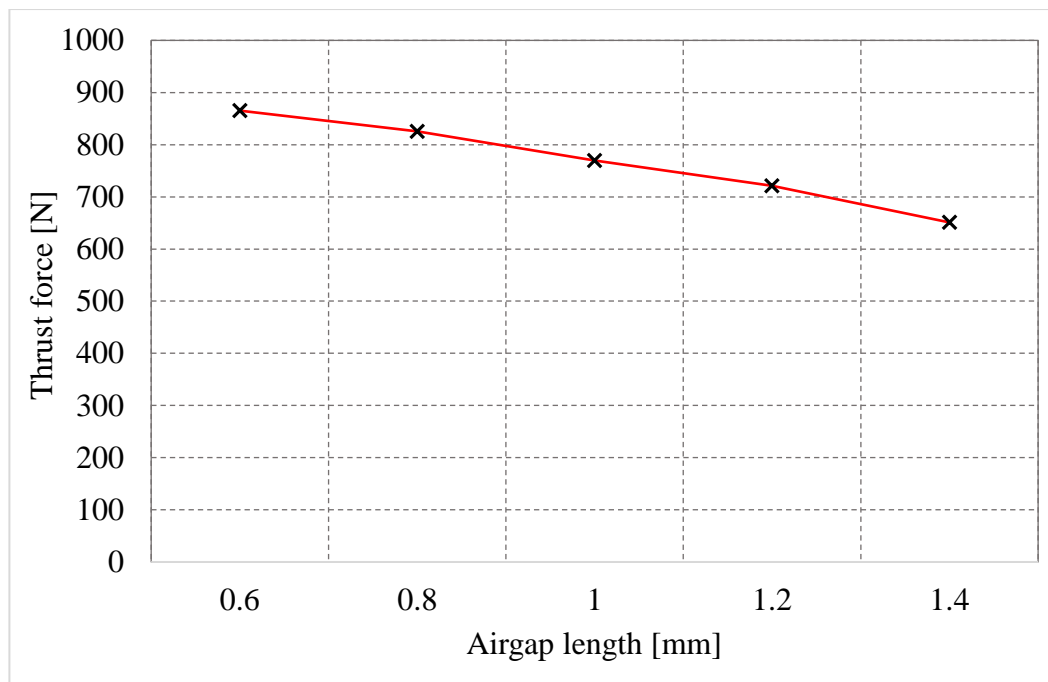


Figure 3. 31: The effect of the airgap length on the thrust force

3.10.5 Armature Winding

The machine has a total of six coils, two per phase. Phases consist of an upper and lower stator coil connected in series, namely Coil A₁, and A₂ belong to phase A, Coil B₁ and B₂ for phase B, and coil C₁ and C₂ for phase C. Figure 3.32 shows the winding arrangement for both top and bottom stators. The coil parameters are summarized in Table 3.5.

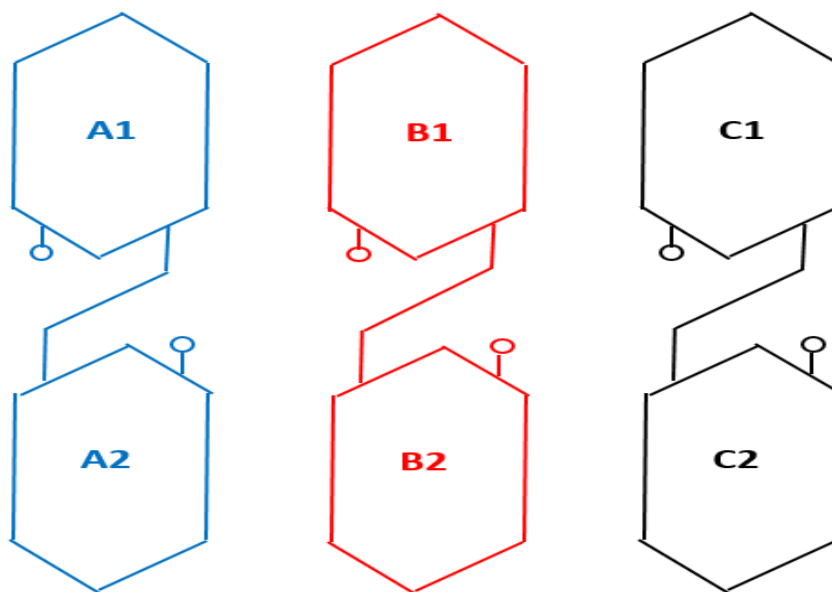


Figure 3. 32: Schematic of armature winding for the upper stator

Table 3. 5: Slot and coil parameters

Slot area	1000 mm ²
Fill factor	35%
Coil cross sectional area	350 mm ²
Conductor cross sectional area	1.55 mm ²
Conductor diameter	1.4 mm
Number of turns/ coil	224 turns

3.10.6 Initial Performance Analysis

3.10.6.1 No-load Flux Linkage

In order to check the balance of the flux linkages a no-load simulation was carried out. Figure 3.33 shows the no-load flux linkage waveforms over a full electrical cycle with no current applied to the coil. It can be seen that the three flux linkage waveforms are very sinusoidal and are electrically shifted by 120°. This confirms that the displacements between the stator teeth have given the proper shift between phases

Table 3.6 gives the peak positive and negative values along with the resultant peak to peak amplitude of the flux linkage for the three phases of the IMCP machine. The peak to peak amplitude of the middle phase can be seen to be 0.5% higher than that of the other phases, indicating that the end effect is apparent in the outer two phases.

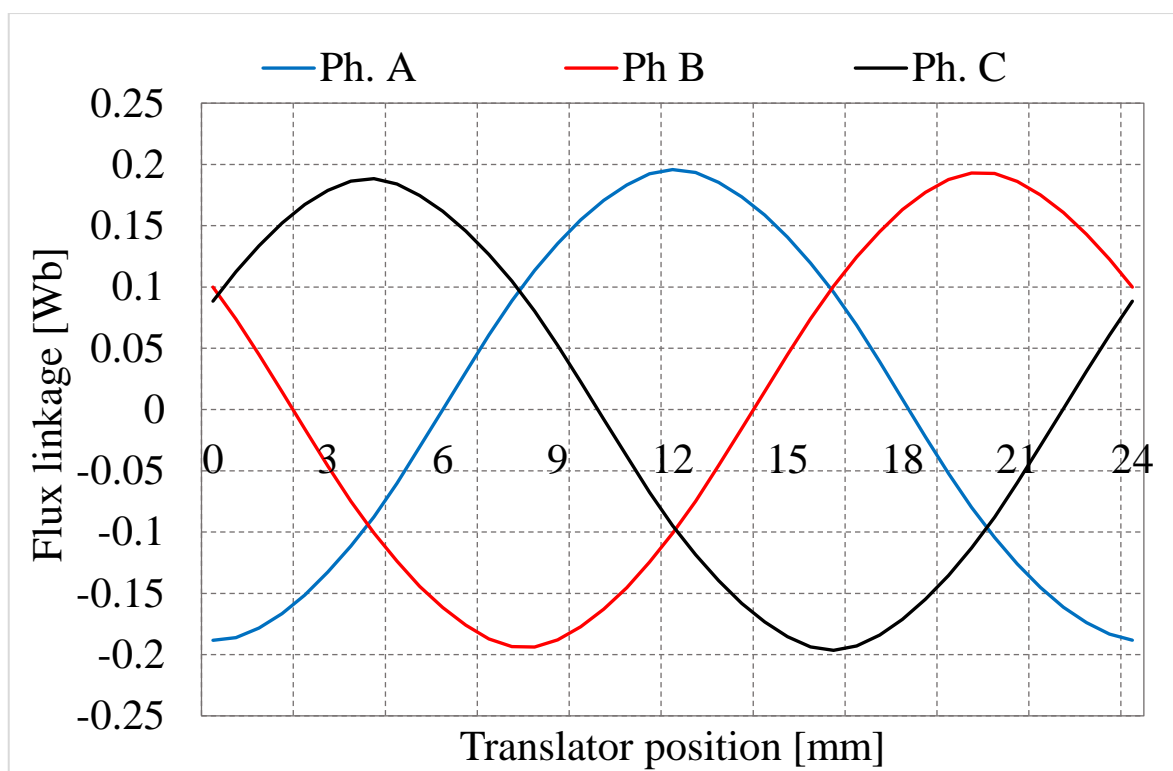


Figure 3.33: Flux linkage waveforms

Table 3.6: No-load flux linkage

Phase	Peak positive [mWb]	Peak negative [mWb]	Peak to peak amplitude [mWb]
A	196	-188	384
B	193	-193	386
C	188	-196	384

3.10.6.2 Force Capability

The variation of the static DC force over a range of excitation currents is plotted in Figure 3.34. They are all periodic over the 24mm translator tooth pitch. Currents of the same value but with reverse orientation would result in curves which are mirrored about the x axis, or shifted by 180° . Cogging force waveform is seen when the injected current is zero. This unwanted force is caused by the natural tendency of the translator teeth to align themselves with the PMs: the position of smallest

reluctance. It can be seen that the electromagnetic force increases gradually as the injected DC current increases and the armature flux begins to dominate. More importantly, the cogging force is more noticeable at lower value of the electromagnetic force and the armature current. Further investigation on the thrust force and its ripple will be presented in the proceeding Chapter.

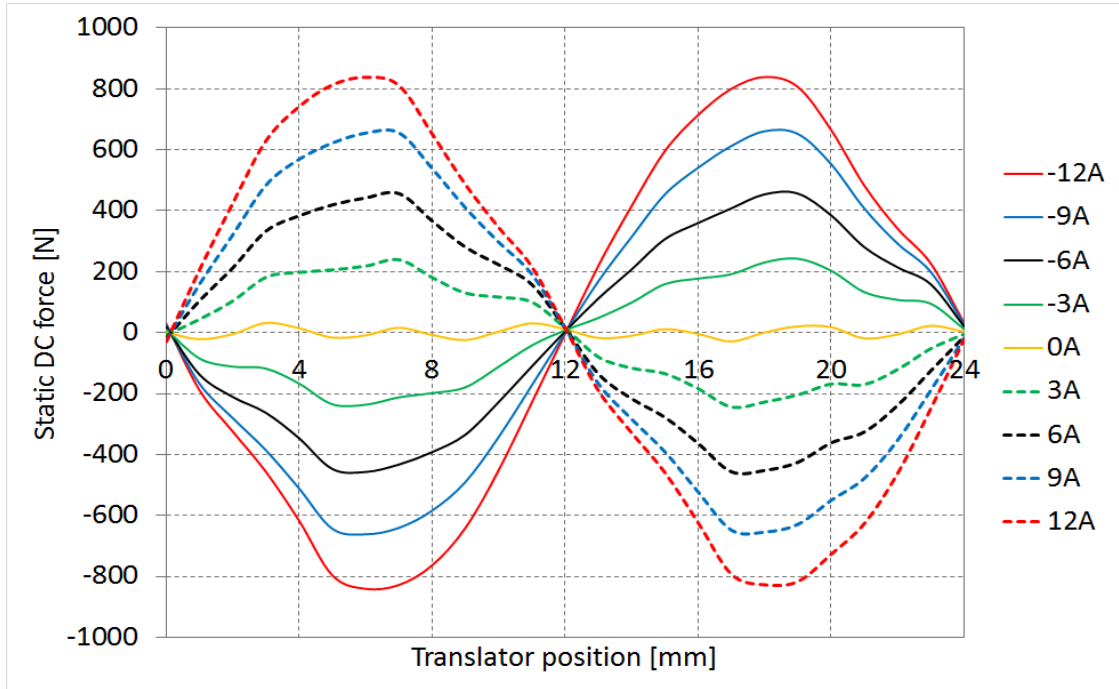


Figure 3. 34: Variation of the static force with applied DC current

3.10.6.3 Cogging Force

Interaction between the translator teeth and stator PMs would lead to an increase of an undesirable force component for the machine operation known as cogging force. This force may contribute to mechanical vibrations that can damage the translator teeth or stator PMs [113], as well as negatively affect the airgap [114]. In addition, output power variations can be produced by the cogging because of the resultant variation in velocity of a wave energy device.

As this IMCP machine is used in a low speed application, it is therefore desirable to reduce the magnitude of the cogging force with respect to the average force. Minimising the cogging force would result in a reduction of the mechanical vibration and acoustic noise. It

was shown in [97-100] that by employing the consequent poles, the cogging torque/ force can be significantly reduced.

Figure 3.35 shows the cogging force waveform as a function of the translator position. It can be seen that the peak to peak cogging force is 62N, which represents only 8% of its average force. This indicates that the IMCP machine is capable of exhibiting lower cogging force than the baseline design, where PMs are existing in both polarities offering a double number of low reluctance positions where the translator teeth tend to align.

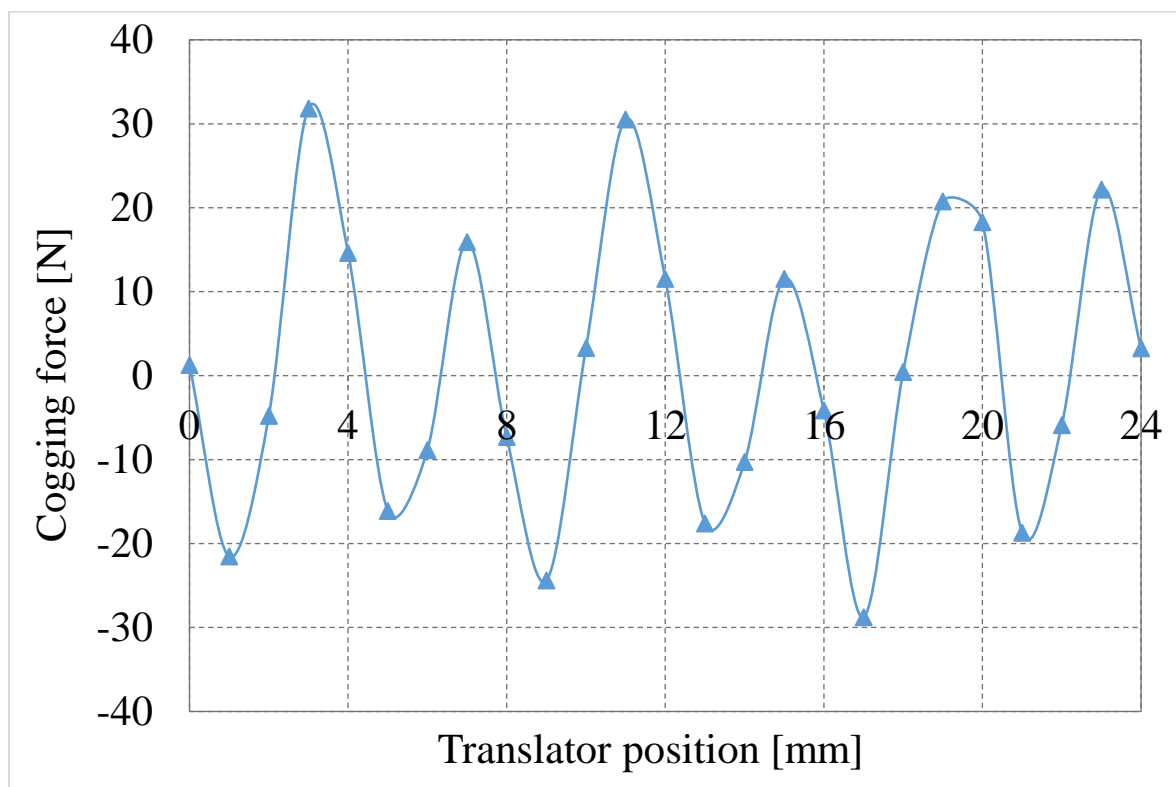


Figure 3. 35: Cogging force waveform

3.11 Conclusion

In this Chapter the C-core IMCP machine has been introduced as a developed version of the baseline LVHM with lower magnet mass. The implementation of the tapered ferromagnetic poles has been investigated and it has been shown that this technique is capable of reducing the pole-to-pole leakage flux and enhancing the main flux. Based on FEA the C-core IMCP machine has been optimised and analysed with the aim of improving the machine electromagnetic performance. It seems from the FEA simulations that the C-

core IMCP machine can offer 50% higher thrust force, 37% higher power factor and exhibit 75.6% lower cogging force compared to the baseline LVHM.

The C-core IMCP machine has been further developed and converted to another version known hence as an E-core IMCP machine to facilitate the mechanical integrity by reducing the number of active parts, i.e. stator cores and shortening the active length. The results of the analysis show that the latter machine is capable of delivering 23% higher force per machine mass owing to an 18.5% saving in the overall mass, indicating that this machine is the most promising design.

The final IMCP design which has fewer components has been optimised and analysed for the purpose of further facilitating the manufacturing processes. The FEA simulations imply that the proposed IMCP machine can offer a simple structure showing that this machine is suitable for low speed high force applications. This work therefore provides a foundation for the investigation of modifications to the design and of new machines, which is the aim of the proceeding Chapter. The following Chapter will also introduce a further investigation on the IMCP machine including the force density, shear stress, attraction force and electrical efficiency. To facilitate ease of manufacturing and testing, a small prototype has been designed and built to validate the predicted results. A deeper discussion of the machine manufacturing and assembly processes as well as the experimental tests will be presented in Chapters 5 and 6.

Chapter 4. New Configurations of Linear Vernier Hybrid Machine with V-shape Magnets

4.1 Introduction

In this Chapter two novel versions of the LVHM with different magnet configurations are proposed with the aim of improving the power factor without increasing the magnet volume, while keeping the cogging force as minimal as possible. The first proposed machine is an alternative design for the IMCP machine discussed in the previous Chapter incorporating consequent poles with V-shape PM arrays to provide a flux concentration effect. The second proposed machine also adopts V-shape PM arrays but is not based on the consequent pole concept and so includes both polarities of PMs. The concept of using the V-shape in both machines is to achieve a higher flux density and hence further improving the power factor. Both proposed machines have been investigated and analysed using the 2D-FEA. Furthermore, a comparison between the initial IMCP design discussed in Chapter 3 and the two modified designs has been made in terms of the electromagnetic performance and electrical power factor. Considering the complexity of manufacturing and the associated costs, one of the two proposed machines has been selected later to be constructed in the laboratory.

4.2 Power Factor Improvement in the VHMs

One method of improving power factor is to increase magnetic loading, and reduce electric loading. Magnetic loading can be increased by exploiting flux concentration effect [48], for example, by splitting pole magnets into a V – shape. The use of conventional V-shape PM arrays in rotary VHM has been proposed in [115, 116], and for the linear version with magnets mounted in the stator [117]. However, the use of the V-shape PM arrays without iron ribs discussed in section 4.3.2 has not been reported elsewhere in either rotary or linear machines.

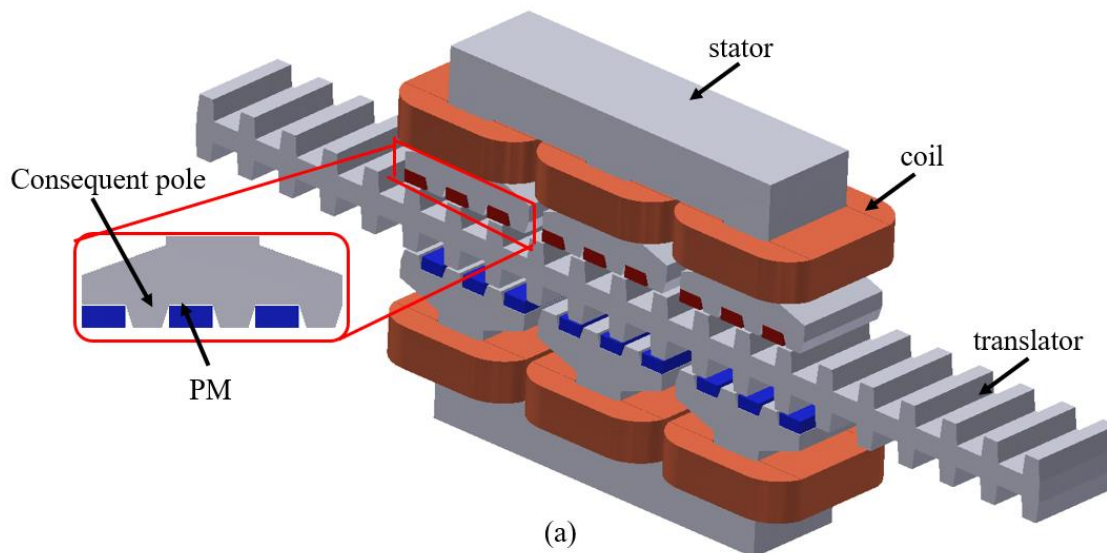
As the V-shaped magnet arrays are adopted in both proposed LVHMs, which will be described in depth in sections 4.3 and 4.4. The flux can be concentrated in the triangular spacers between each pair of magnets offering higher flux densities than is possible in the IMCP machine discussed in Chapter 3, which in turn contributes to the power factor improvement [48, 118].

Authors [48, 118, 119] have shown that the power factor of the VHM can be improved by either reducing the inductance or by increasing the PM flux linkage.

4.3 V-shape Consequent Pole (VCP) Topology

4.3.1 Machine Configuration

The proposed VCP machine has the same structure of the IMCP machine shown in Figure 4.1(a), with different magnet arrangement. The individual magnet segments adopted in the IMCP machine are split into a V-shape configuration as shown in Figure 4.1 (b). Magnet flux is channelled by a triangular pole piece, which is glued in place without the need for iron ribs, as has been proposed in rotary machines [120]. As for previous machine, the translator which is inserted between both stator sides is constructed as a simple laminated iron core with salient teeth offering a rigid structure to deliver high thrust force.



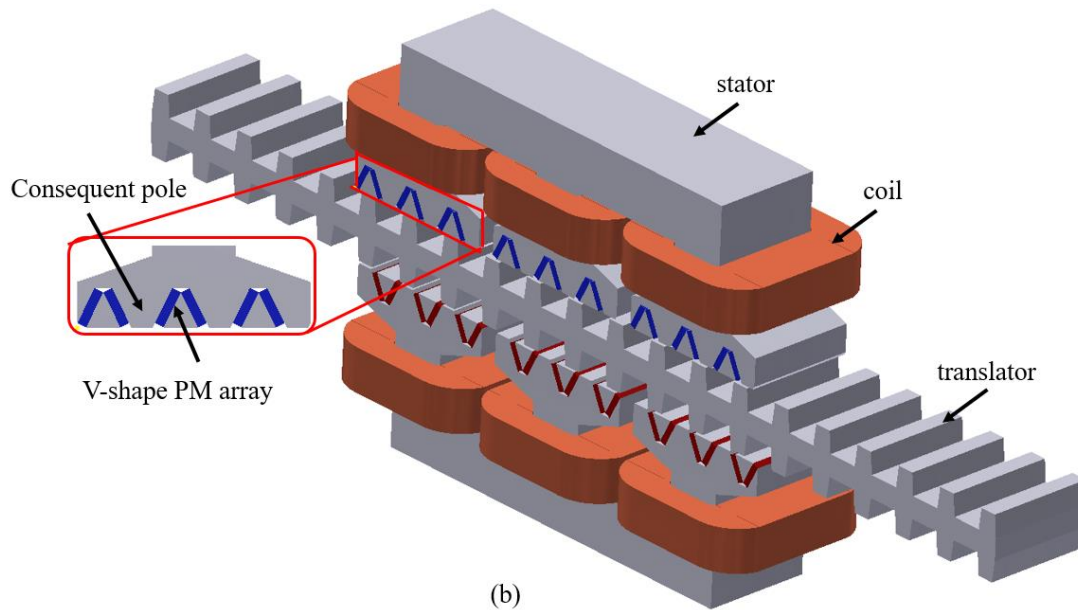


Figure 4. 1: Machine configuration (a) IMCP machine (b) VCP machine

4.3.2 Modified V-shape PM Arrays

The conventional V-shape structure normally has small iron ribs (which is also known as iron bridges) to hold the triangular-shaped spacers located between each pair of magnets as shown in Figure 4.2 (a). These small pieces are to provide the required mechanical stiffness against any force applied to the stator [120]. However, the conventional V-shape PM array has four flux leakage paths per pole, which allow the flux to be circulated around the magnets' edge as highlighted in Figure 4.2 (a). Furthermore, in the same Figure a very high level of magnetic saturation is seen within the iron ribs, which may contribute to a reduction in the thrust force and worsening the force ripple. This undesirable phenomenon also occurs in the existing linear Vernier machine, as that proposed in [117] and verified in Figure 4.3.

In this research, these iron ribs were removed and the triangular-shaped spacers were glued to the magnets. The result is the absence of the four leakage paths as shown in Figure 4.2 (b), leading to an increase in the thrust force by 17%. It should be indicated that this structure has been used in both proposed V-shape topologies covered in this Chapter.

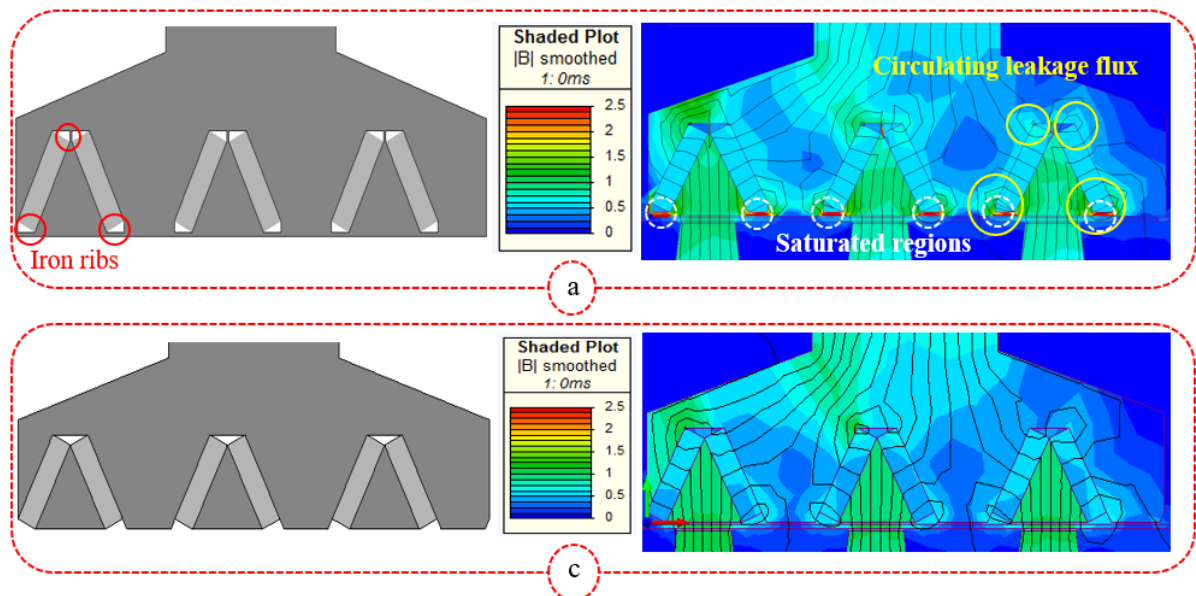


Figure 4. 2: V-shape PM array structure (a) with ribs (b) without ribs

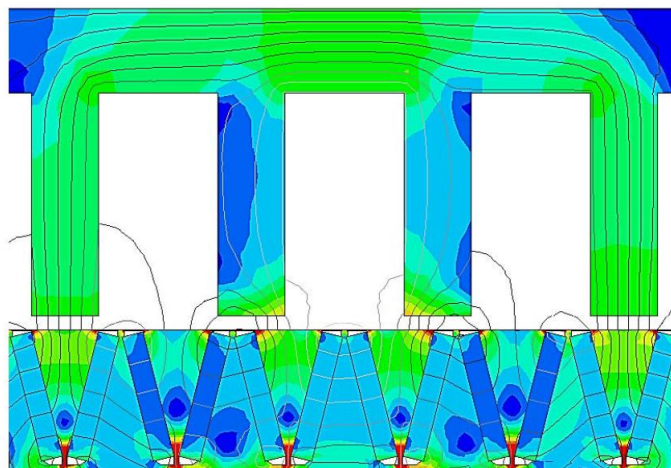


Figure 4. 3: The effect of iron ribs in the linear Vernier machine proposed in [117]

4.3.3 Design Investigation

This section provides an overall description of the design procedures used to achieve the optimum thrust force in the proposed VCP machine. Authors [99] and [97] reported that in consequent pole machines the magnet pitch can be larger than the pole pitch, leading to an increase in magnetic loading. In this study, in order to allow more room for assembling the V-shape PM arrays, the magnet pole span was designed to be bigger than pole pitch as illustrated in Figure 4.4. To determine the optimal magnet span, the magnet span ratio (m_{sr}), which is defined as the ratio of magnet span (m_s) to the width of the stator tooth shoe (W_{sts})

was investigated in terms of the maximum thrust force. The optimal magnets position that can provide the flux concentration effect is shown in Figure 4.5, in which the maximum achievable thrust force occurs. In Figure 4.6 (a), it can be seen when the $m_{sr} = 0.18$ the triangle iron spacers became smaller and get saturated as a result. On the other hand, when the $m_{sr} = 0.24$ the magnetic saturation was seen within consequent poles as shown in Figure 4.6. (b). It is worth mentioning that maximizing magnet span ratio m_{sr} gives larger iron triangular spacers between each pair of magnets, which the author believe has advantages in the machine assembly. However, due to the saturation limitations in either the triangular piece or the consequent pole, the ratio of 0.22 was found as the most suitable option.

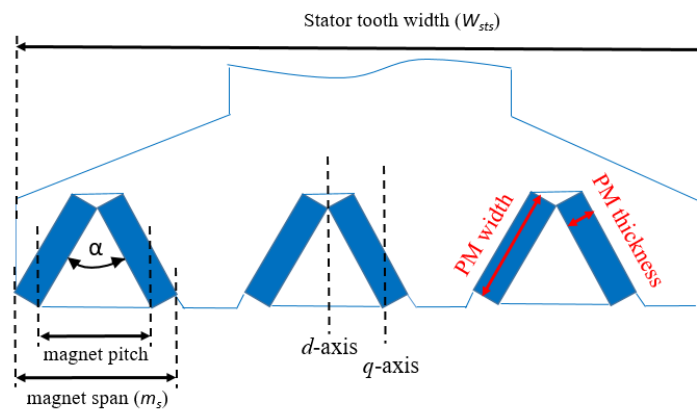


Figure 4. 4: Geometrical parameters for VCP machine

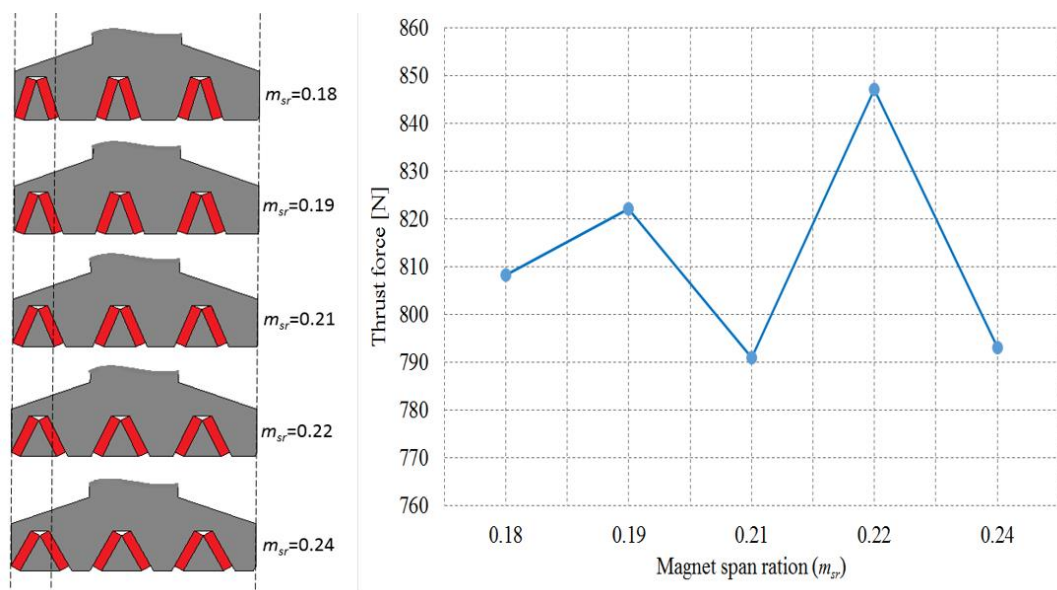


Figure 4. 5: The effect of the magnet span ratio on the thrust force

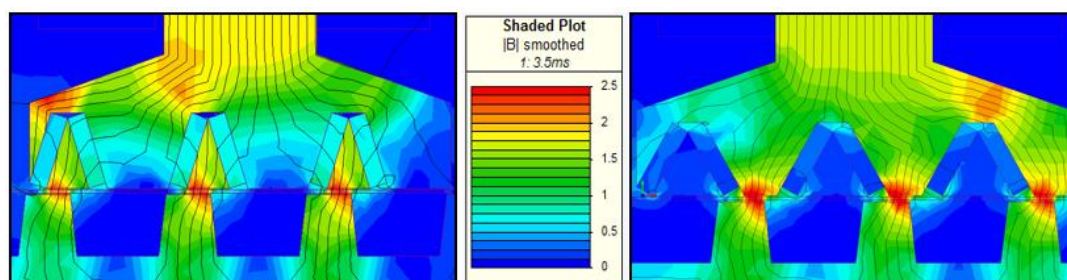


Figure 4. 6: Saturation effect (a) $M_{sr} = 0.18$ and (b) $M_{sr} = 0.24$

The design study was conducted using 2D-FEA with the main parameters fixed as discussed in Table 4.1. Current density was assumed to be 3.5 A/mm^2 RMS, and magnet mass was held constant.

Other key geometry parameters identified in Figure 4.4 were investigated including the angle between the two segments of PMs (the V-angle (α)), the PM width and the PM thickness. In total, six variants of the PM dimensions, all with a fixed volume, are shown in Figure 4.7 and described in Table 4.1. They were analysed in terms of the optimal average thrust force and minimum peak to peak cogging force. Figure 4.8 compares the performance of all six designs. It can be deduced that design A can offer the highest average thrust force, while it exhibits the minimum cogging force. Due to the fixed magnet mass, the V-angle is forced to reduce in designs B-E which, which in turn can lead to more saturated circuit in laminated triangles. In other words, as the laminated triangles get smaller, more magnetic saturation can occur resulting in a reduced thrust force. Therefore, design A was taken forward and compared to the IMCP topology.

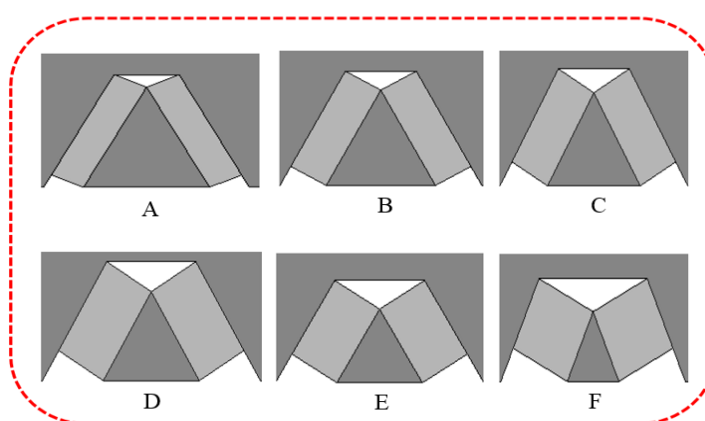
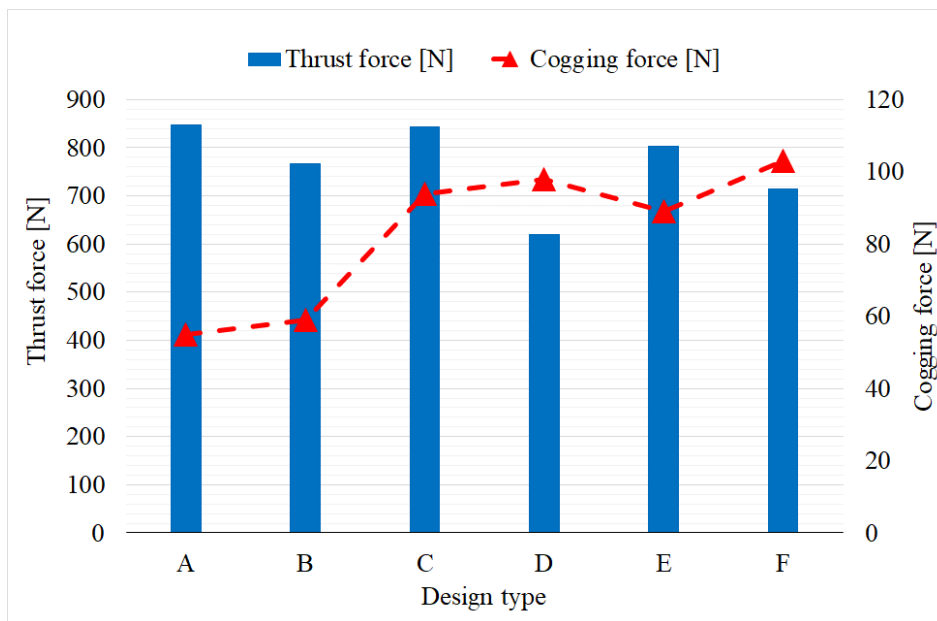


Figure 4. 7: Different designs with different PM dimensions and fixed PM volume for VCP machine

Table 4. 1: PM dimensions and V-angle for the six designs

Design type	A	B	C	D	E	F
PM width [mm]	12	10	9	8	7.5	6
PM thickness [mm]	3	3.6	4	4.5	4.8	6
PM volume [cm ³]	64.8	64.8	64.8	64.8	64.8	64.8
V-angle [degree]	52.5	58.1	59.6	61.8	62.8	50.8

**Figure 4. 8: Variation of the thrust force and cogging force with respect to the design type**

4.3.4 Validation of the VCP Machine

In this section, the balance of the no-load flux linkages is checked with no current applied to the coils. The no-load flux linkage characteristics were predicted by a transient FEA simulation for one translator pitch. Figure 4.9 shows the variation of the flux linking the three phase coils over a full electrical cycle, where the waveforms of the three phases are shifted by 120°. It can be also seen that the waveforms are sinusoidal, which is attributable to the near absence of the 5th and 7th harmonics as verified in Figure 4.10.

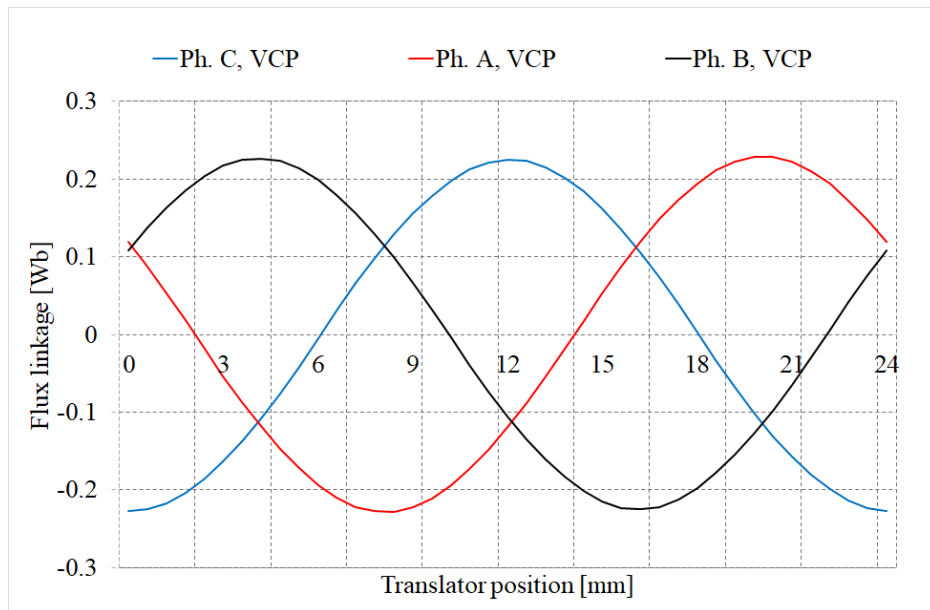


Figure 4. 9: No-load flux linkage waveforms over an electrical cycle

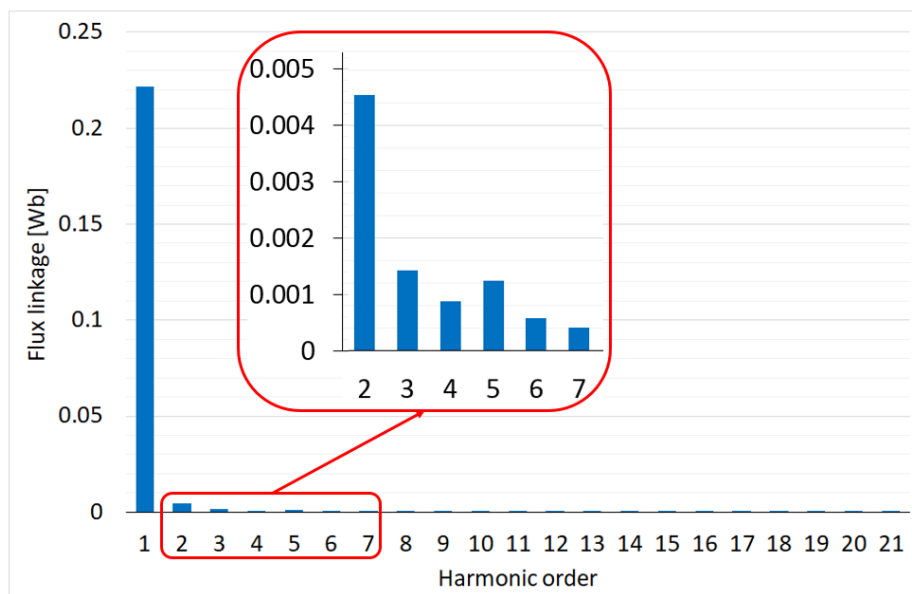


Figure 4. 10: No-load flux linkage harmonic spectrum

Table 4.2 gives the peak positive and negative values along with the resultant peak to peak amplitude of the flux linkage for the three phases of the proposed VCP machine. The peak to peak amplitude of the middle phase can be seen to be 0.9% higher than that of the other phases, as the end effect reduces the flux in the outer two phases.

Table 4. 2: Flux linkage for the VCP machine

Phase	Peak positive [mWb]	Peak negative [mWb]	Peak to peak amplitude [mWb]
A	225	-227	452
B	229	-228	456
C	226	-225	452

4.4 V-shape Topology

In this section, the V-shape topology is further investigated in terms of the power factor improvement. The developed version of the V-shape machine copies the same specifications of the two machines discussed earlier except the magnet arrangement, in which the V-shape PM arrays are employed in both polarities, north and south. A comparison between both V-shape topologies and the IMCP machine will be carried out later in this Chapter.

4.4.1 Machine Configuration

In the baseline LVHM discussed in Chapter 3, the use of alternating polarity highly contributes to the leakage flux, which influences the machine electromagnetic performance and its electrical power factor. Although the consequent pole topologies were proposed to reduce the leakage flux and improve the magnet utilisation, these topologies still suffer from some leakage flux [103]. However, in the proposed V-shape machine shown in Figure 4.11, the V-shape PM arrays are employed in both polarities allowing the flux to be concentrated in the triangular-shaped iron spacers located between each pair of magnets, which in turn improves the airgap flux density.

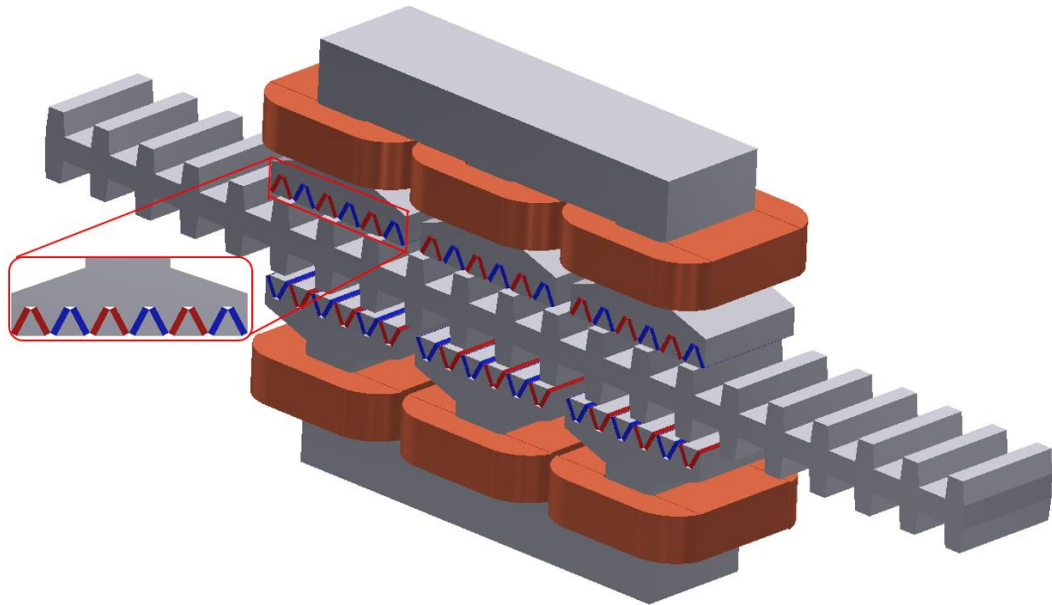


Figure 4. 11: V-shape machine configuration

The difference between this topology and the VCP machine described early in section 4.3 is the substitution of the consequent poles with V-shape magnet arrays. Which means, both polarities provides the flux concentration effect offering a significant improvement of the airgap flux density, and hence the power factor. However, as the magnet mass was held constant, the number of magnets is doubled.

4.4.2 Machine Investigation

In order to obtain a fair comparison between the three machines, the key parameters are kept the same in all the three machines. These include the machine volume, rated speed and current density. The pole pitch and magnet volume are also fixed in the V-shape machine as the magnet V-angle (α) and magnet dimensions were optimised based on these constraints. The optimization of the magnet thickness, magnet width and V-angle (identified in Figure 4.12) is conducted in this section to achieve the optimum thrust force and minimum cogging force. Four designs shown in Figure 4.13, with different PM dimensions as illustrated in Table 4.3 were analysed and the thrust force was calculated as summarised in Figure 4.14. From the obtained results it can be seen that the highest thrust force can be achieved by design B, followed by design A, with a 2.5% lower thrust force. However, the design B produces a 125% higher cogging force compared to that of the design A. Therefore, the design A was selected instead.

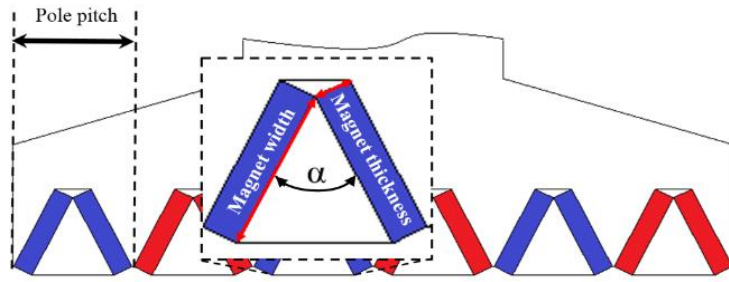


Figure 4.12: Geometrical parameters for V-shape machine

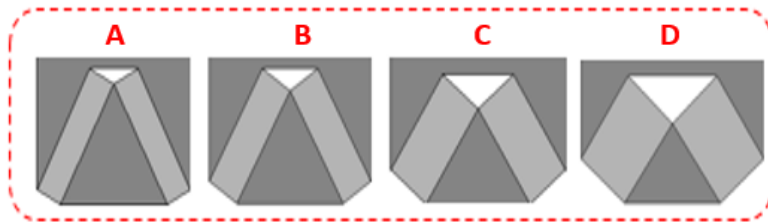


Figure 4.13: Different designs with different PM dimensions and fixed PM volume for V-shape machine

Table 4.3: PM dimensions and V-angle for the four designs

Design type	A	B	C	D
PM width [mm]	9	7.5	6	5
PM thickness [mm]	2	2.4	3	3.6
α [degree]	55.4	63.2	70.2	77.4
PM mass [kg]	0.48	0.48	0.48	0.48

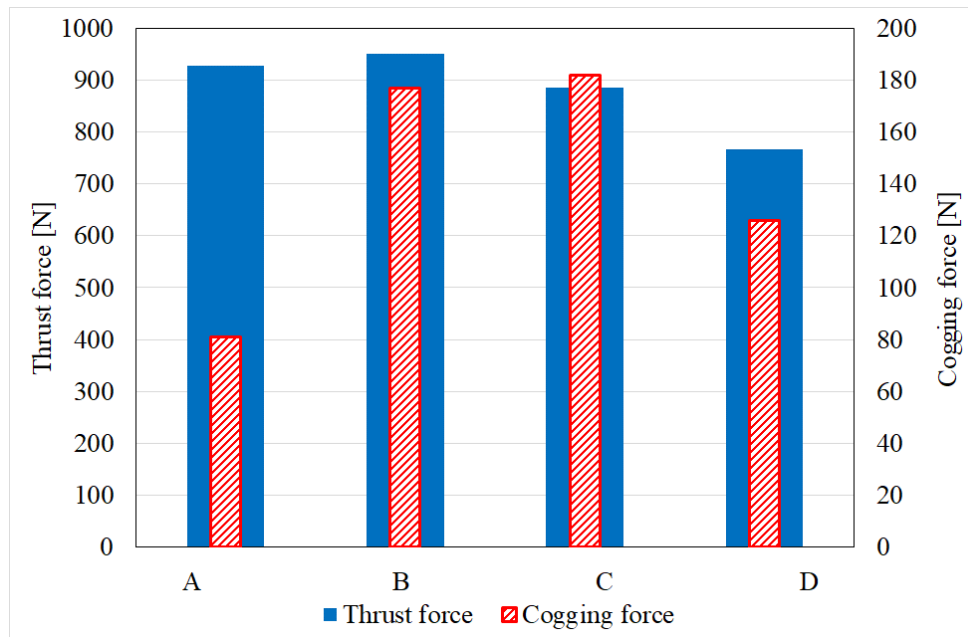


Figure 4. 14: Variation of the thrust and cogging forces with respect to the design type

4.5 Performance Comparison

In this section, a comparison between the three developed machines discussed in Chapters 3 and 4 is made. These machines are the IMCP, VCP and V-shape machines. The comparison is carried out based on the 2D-FEA to evaluate the electromagnetic performance and the operating power factor. The comparison considers the following aspects:

1. No-load airgap flux density
2. No-load flux linkage
3. No-load back EMF and harmonics
4. Force and force ripple
5. Force capability
6. Cogging force
7. Inductance
8. Losses and efficiency
9. Mass
10. Attraction force
11. Power factor

4.5.1 Airgap Flux Density and Flux Density Distribution

The no-load airgap flux density is calculated based on the 2D-FEA in order to verify performances of the three proposed machines. Figure 4.15 illustrates the radial component of the airgap flux density distributions within the upper airgap under a single stator tooth for PM excitation only. As can be seen in this Figure, the highest airgap flux density can be achieved by the V-shape machine with the peak value of 1.22T, followed by 1.1T achieved by the VCP machine, while the IMCP machines has the lowest airgap flux density of 0.85T. These results indicate that the flux concentration effect significantly contributed to an improvement of 43.5% and 29.4% of the no-load airgap flux density in the proposed V-shape and VCP machines, respectively, in comparison with the IMCP machine. It should be noted that more flux concentration effect was provided by the V-shape machine compared to the VCP machine, which can be attributed to the adoption of the V-shaped PM arrays in both polarities.

Magnetic flux plots of the three investigated machines (IMCP, VCP and V-shape) are shown in Figure 4.16 (a), (b) and (c), respectively, where it is noticed that the highest flux density distribution is exhibited by the V-shape machine followed by the VCP machine, while the lowest flux density distribution is seen in the IMCP machine, which confirms the effective magnet utilisation in the two former machines. From the Figure it can be also seen the effect of flux concentration within the triangle iron spacers in both the V-shape and VCP machines.

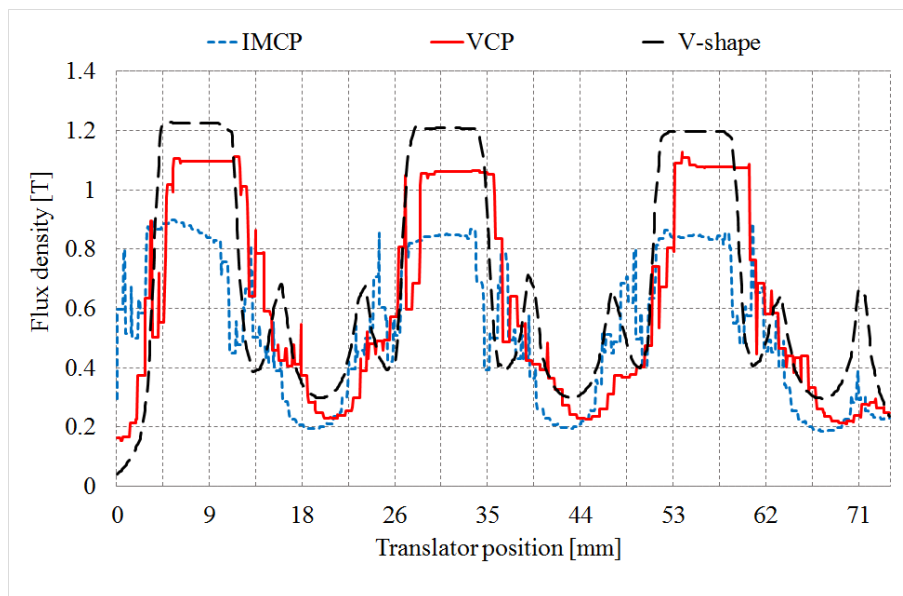
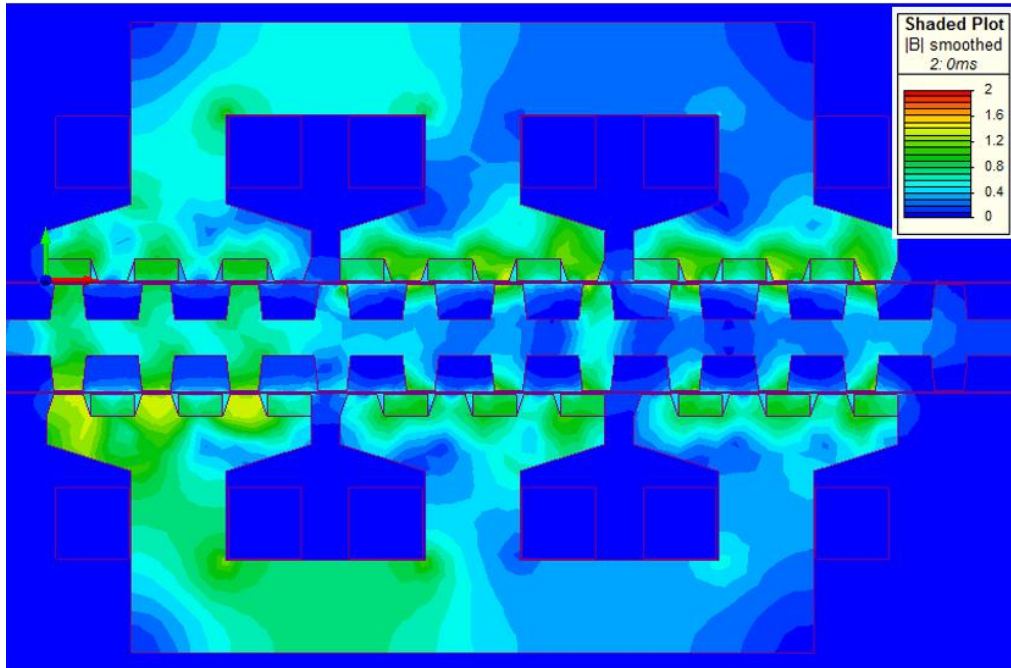
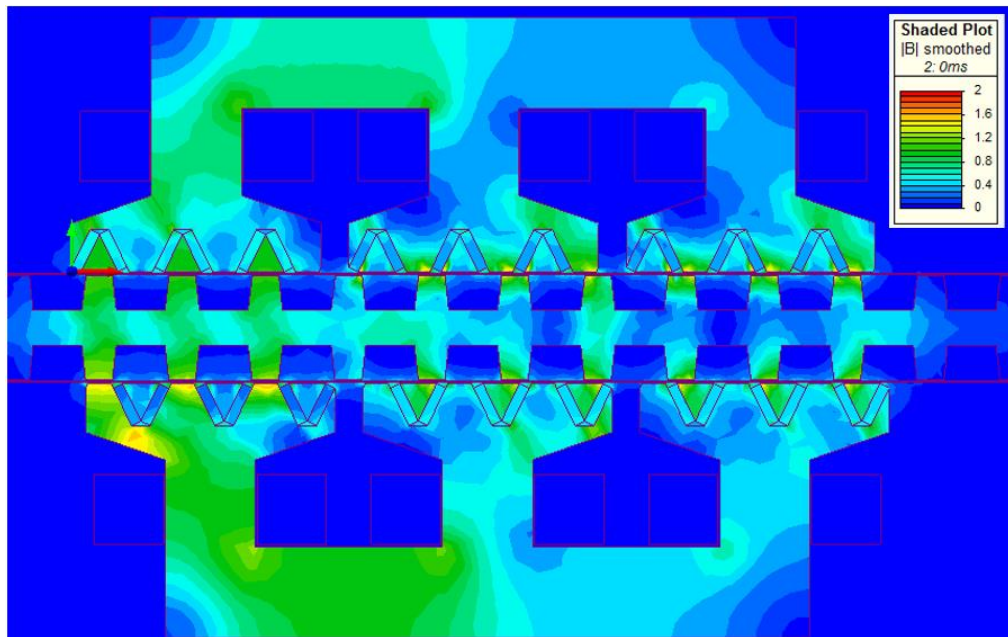


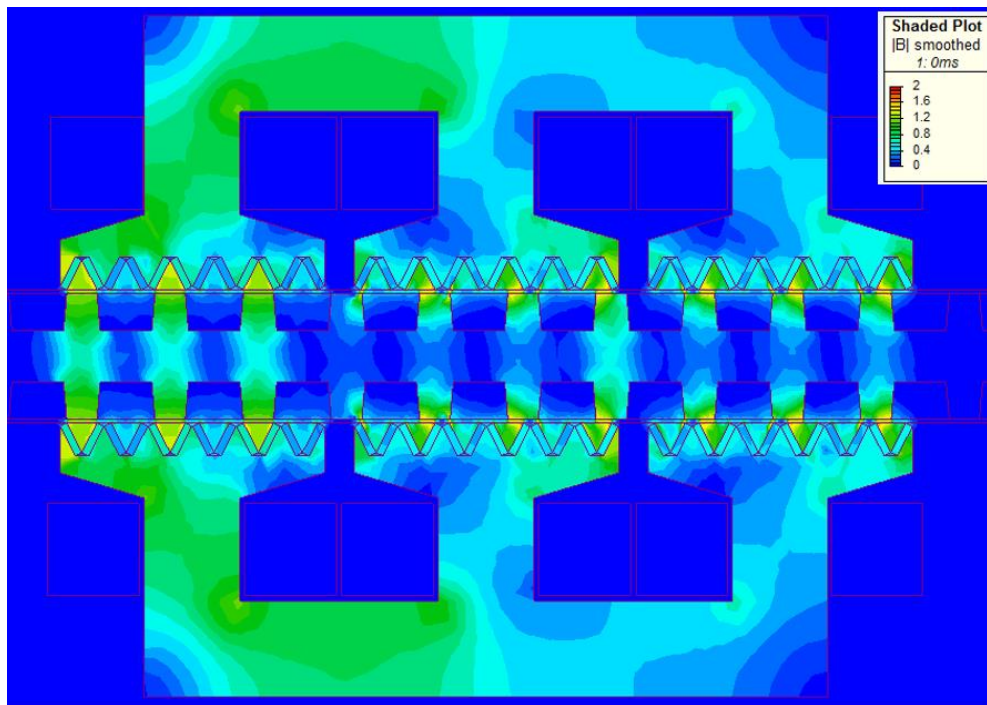
Figure 4. 15: No-load airgap flux density under one stator tooth for the three machines



(a)



(b)



(c)

Figure 4. 16: No-load flux density plot (a) IMCP (b) VCP and (c) V-shape machines

4.5.2 No-load Flux Linkage

Authors [51, 98, 99] verified that by employing consequent poles, the undesirable leakage flux can be greatly reduced. Although the tapered ferromagnetic poles described earlier in Chapter 3 were employed in the IMCP machine, there is still leakage flux travelling between the PMs and tapered ferromagnetic poles rather than linking the coil. This leakage can be further reduced in the V-shape and VCP machines, where the natural structure of the V-shape PM arrays can influence the leakage flux, which in turn enhances the main flux.

The field distribution predicted by the 2D-FEA for the three machines studied here is plotted in Figure 4.17. From the Figure it is obvious that both V-shape proposed machines have lower leakage flux than that of the IMCP machine, with a superiority to the V-shape machine. In addition, the flux concentration in the V-shape machine results in a higher main flux – thus further reducing the flux leakage as a proportion.

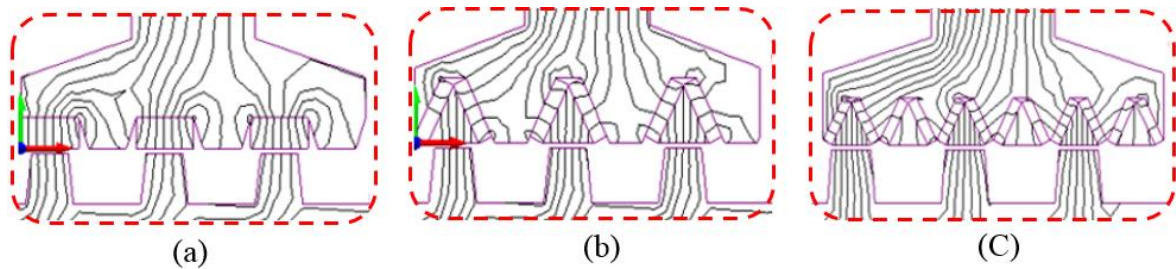


Figure 4.17: Effect of machine configuration on the leakage flux and flux linkage (a) IMCP (b) VCP and (c) V-shape machine

Assuming the same rated speed, number of turns per phase, magnet mass and translator pitch, Figure 4.18 compares the open-circuit flux linkage waveforms for the three machines. As expected from the above analysis, the V-shape machine has higher no-load flux linkage compared to the other machines, while the IMCP machine exhibits the lowest value.

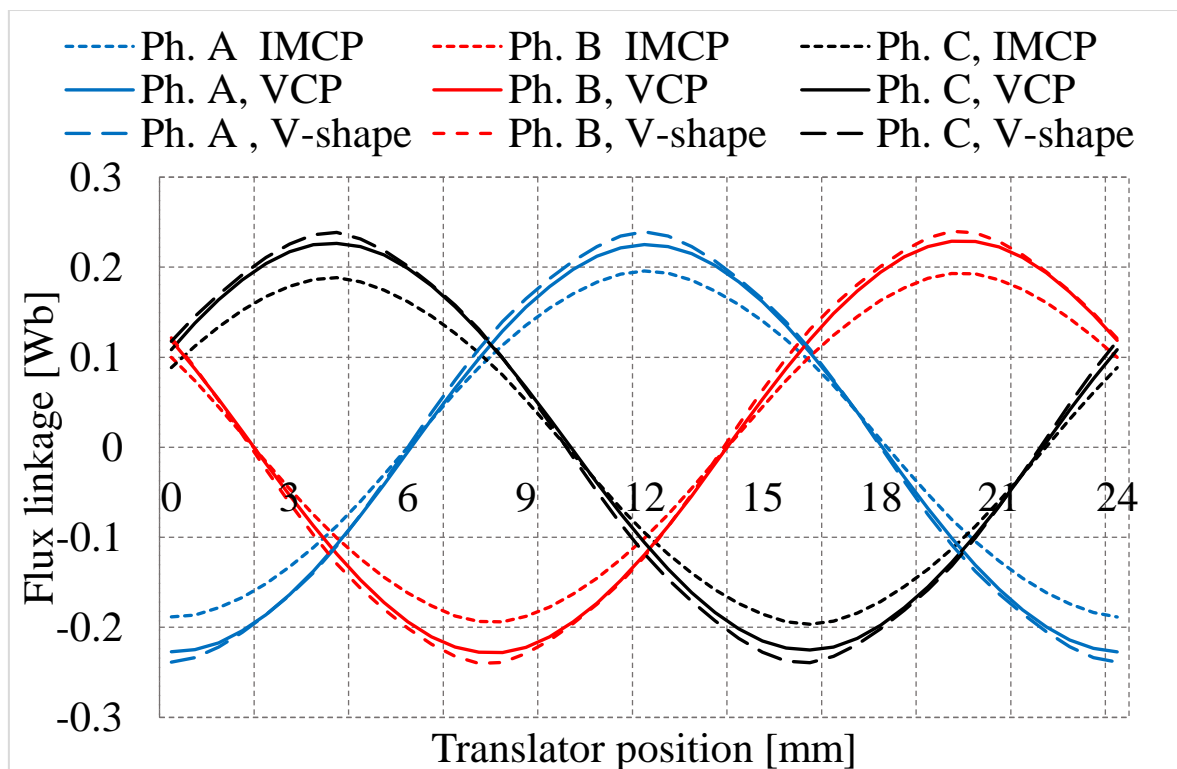


Figure 4.18: No-load flux linkage waveforms for the three machines

4.5.3 No-load Back EMF

The induced no-load back EMF for the three machines are analysed and compared as shown in Figure 4.19 and summarised in Table 4.4. It can be seen that the V-shape machine produces a higher no-load back EMF for a given speed. In comparison with the IMCP

machine described in the previous Chapter, this is a 26% and 18% higher back EMF achieved by the two proposed machines, which adopted the V-shape PM arrays, i.e. the V-shape and VCP machines, respectively. More importantly, the no-load back EMF waveforms of the VCP machine are more sinusoidal than that of the other two machines. In terms of frequency components, this is seen as a reduction in the 5th harmonic in Figure 4.20. It should be indicated that the distortion appeared in the waveforms of the no-load back EMF for the V-shape is mainly caused by the increase in the 2nd, 5th and 7th harmonics.

Table 4. 4: Comparison of Peak and RMS values of the back EMF

	V-shape	VCP	IMCP
Average peak EMF [V]	78	72	61
Average RMS [V]	52.4	50.3	42.4
Average fundamental EMF [V]	74.3	70.8	59.7

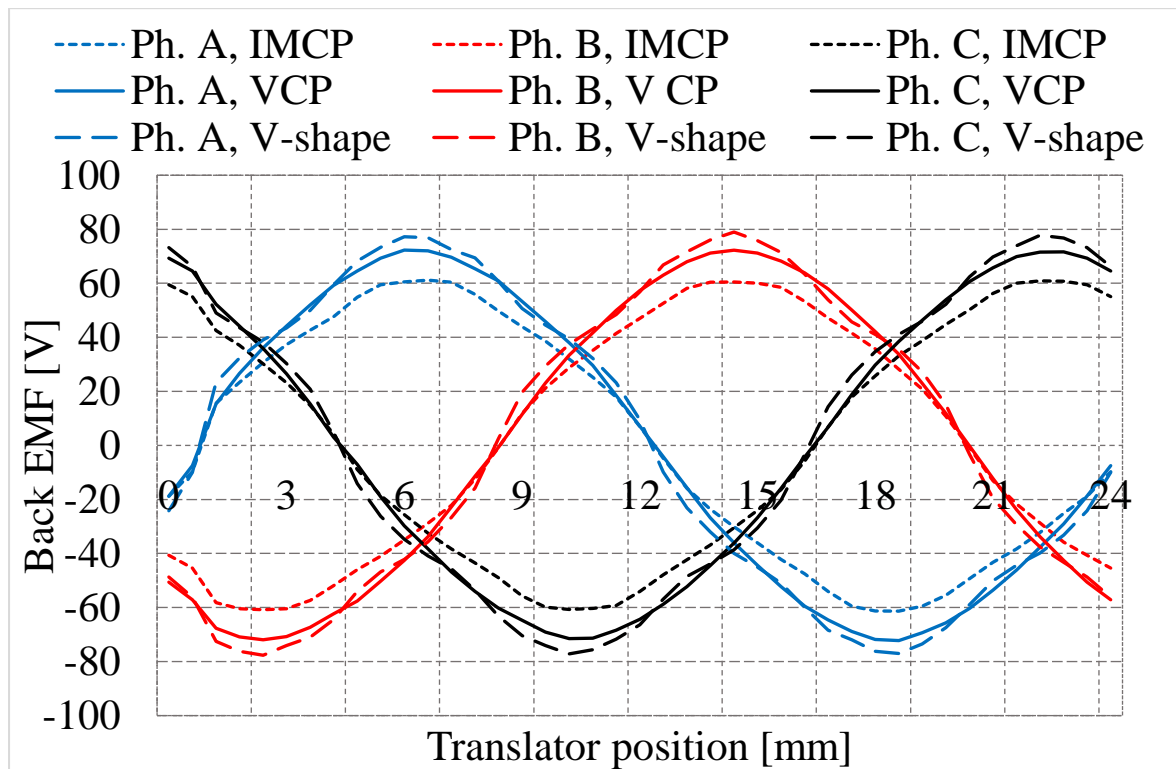


Figure 4. 19: No-load back EMF waveforms for the three machines

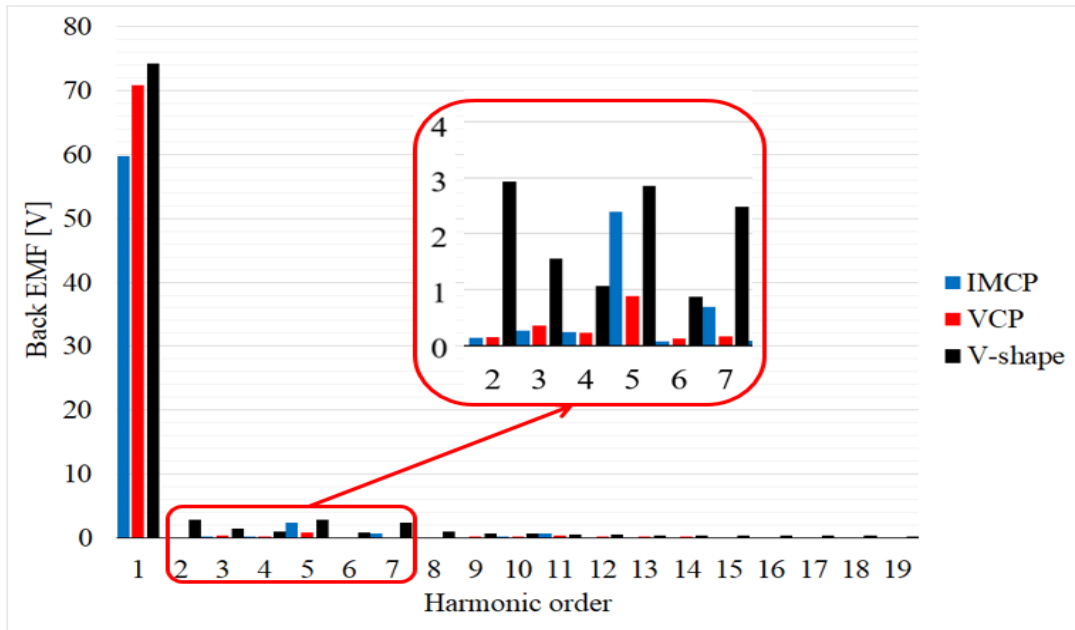


Figure 4. 20: No-load back EMF harmonic spectrum

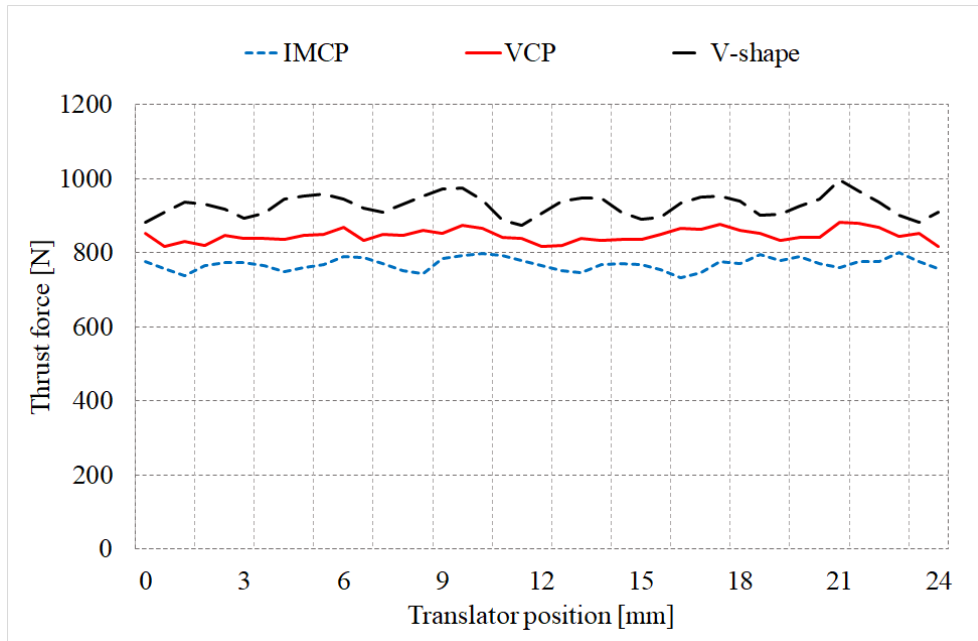
4.5.4 Force Production

A comparison of the thrust force characteristics for the three machines is shown in Figure 4.21 for a $3.5\text{A}/\text{mm}^2$ (RMS) current density. As expected, the V-shape machine produces a 20.5% and 10.5% higher average thrust force compared to that of the VCP and the IMCP machines, respectively. Hence, the V-shape machine has the highest force density for the same machine volume. The reason of this improvement in the thrust force generated by the V-shape machine is the contribution of the significant increase in the magnitude of the fundamental of the back EMF.

Force ripple was also analysed and compared based on the Equation (5.1). Table 4.5 lists the thrust forces and the associated force ripple for the three machines. From the Table it can be observed that the V-shape machine suffers from greater force ripple, in which the distorted no-load back EMF waveforms considered as the main contributor to this undesirable pulsation. The minimum force ripple was obtained by the VCP machine, which reflects the effect of the sinusoidal back EMF resulted from the near absence of the 7th harmonic and the significant reduction in 5th harmonic as verified in Figure 4.20.

Table 4. 5: Comparison of the average thrust force and force ripple

	V-shape	VCP	IMCP
Average thrust force [N]	928	847	770
Force ripple [%]	8.4	7.4	7.8

**Figure 4. 21: Thrust force waveforms for the three machines**

4.5.5 Force Capability

By using zero d -axis control, the characteristics of the thrust force with respect to the applied current for the three designs are compared in Figure 4.22. It can be seen that in all machines as the armature current increases the thrust force increases linearly until the applied current reaches its rated value of 11A, after which there is a significant deviation from linearity at higher currents because of the effect of the magnetic saturation in the iron core. The results show that the highest force capability can be achieved by the V-shape machine, while the IMCP machines shows the lowest force capability. The current-force curve of the VCP machine shows a lower increase in thrust force at high currents due to the magnetic saturation in the consequent poles. This proves that the V-shape machine has better overloading capability than that of the VCP machine.

In order to assess the cost effectiveness in terms of the thrust force production of the three machines per unit of material, force density of the machines was calculated. From the

results it can be seen that the V-shape machine is superior to the other machines in terms of the force density when all machines consume the same amount of the magnet material. This is a 9.5% and 20.6% higher force density was obtained by V-shape machine compared to the VCP and IMCP machines, respectively.

The force per magnet volume was also calculated, again the V-shape machine offers the highest force per magnet volume, while the IMCP machine has the lowest value, which is lower than that of the former machine by 31.2%. This high force density of both proposed machines is attributed to following reasons:

- 1) The magnet utilisation is significantly improved and the magnet flux leakage is reduced due to the special structure of the V-shape PM arrays.
- 2) The improvement of the airgap flux density gained from the V-shape PM arrays structure.

The thrust force per active airgap area, or shear stress for the three machines can be found using (5.2). The shear stresses for the V-shape, VCP and IMCP machines are 86kN/m², 76.6kN/m² and 71.2kN/m², respectively. Which confirmed the improvement in both proposed designs which adopted the flux concentration effect (the V-shape and VCP topologies). Table 4.6 summarises the force production for all three machines.

$$\sigma = \frac{F}{A_{Ag}} \quad (4.1)$$

Where A_{ag} is the airgap active area.

Table 4. 6: Comparison of force density and shear stress

	V-shape	VCP	IMCP
Force/PM mass [kN/kg]	1.93	1.76	1.6
Force/PM volume [kN/m]	1.73	1.31	1.19
Force/ active machine volume [kN/m ³]	454.9	405.4	337.5
Shear stress [kN/m ²]	86	76.6	71.2
Force ratio to IMCP machine	1.21	1.1	1

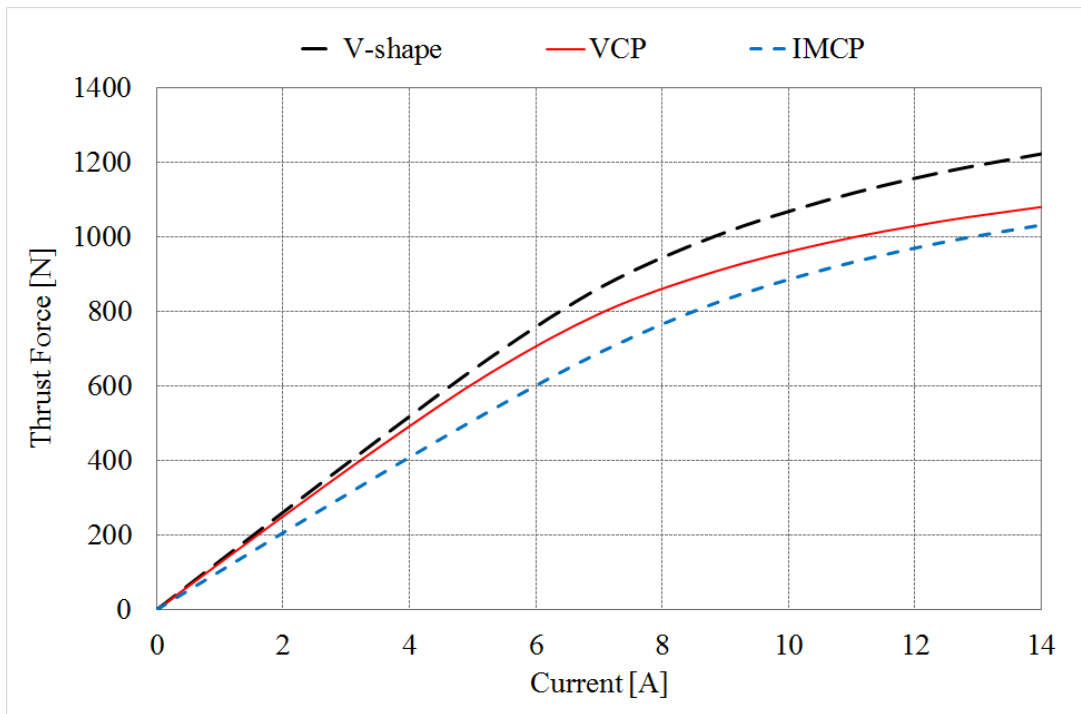


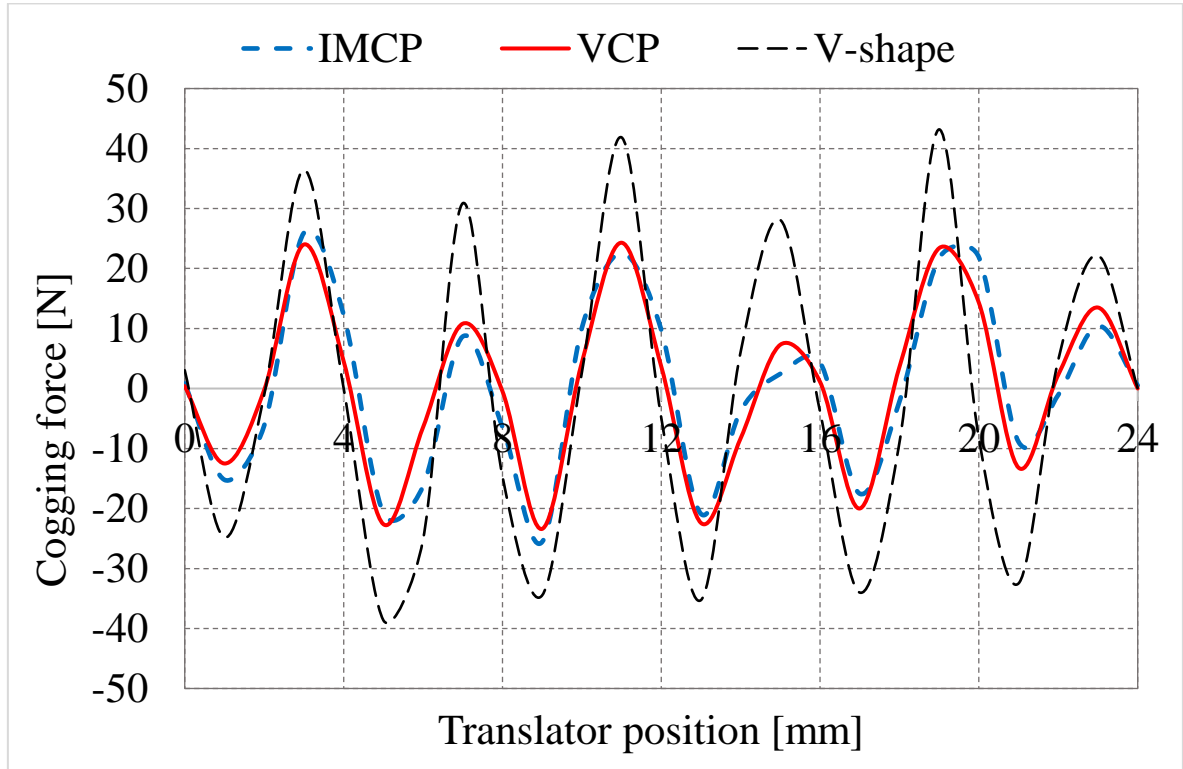
Figure 4. 22: Force capability for the three machines

4.5.6 Cogging Force

In PM machines, undesirable multiple effects can be produced by cogging force, such as fluctuations in the output power, velocity and mechanical vibrations, which in turn could lead to bearing failure. This common phenomenon is caused by the interaction between the stator PMs and translator teeth. In linear PM machines both slot effect and longitudinal end effect contribute to cogging force, producing larger cogging force compared to their rotary counterparts [121]. The cogging force waveforms for the three machines are depicted and compared in Figure 4.23. It can be seen that the peak to peak magnitude of the cogging force of the V-shape machine is 47.3% higher than that produced by the VCP machine, and 30.6% higher than the cogging force value produced by the IMCP machine. The peak to peak values of the cogging force for the three analysed machines are tabulated in Table 4.7. It can be seen that the VCP machine produces an 11.3% lower peak to peak cogging force compared to the IMCP machine. Moreover, the VCP machines has the lowest ratio of the cogging force to the average force. Once more, this is due to the improved distribution of flux in the airgap in the VCP machine giving a THD of only 2%.

Table 4. 7: Comparison of cogging force and cogging force/ thrust force ration

	V-shape	VCP	IMCP
Peak to Peak cogging force [N]	81	55	62
pk-pk cogging/ average force [%]	8.7	7.8	8

**Figure 4. 23: Cogging force waveforms for the three machines**

4.5.7 Inductance

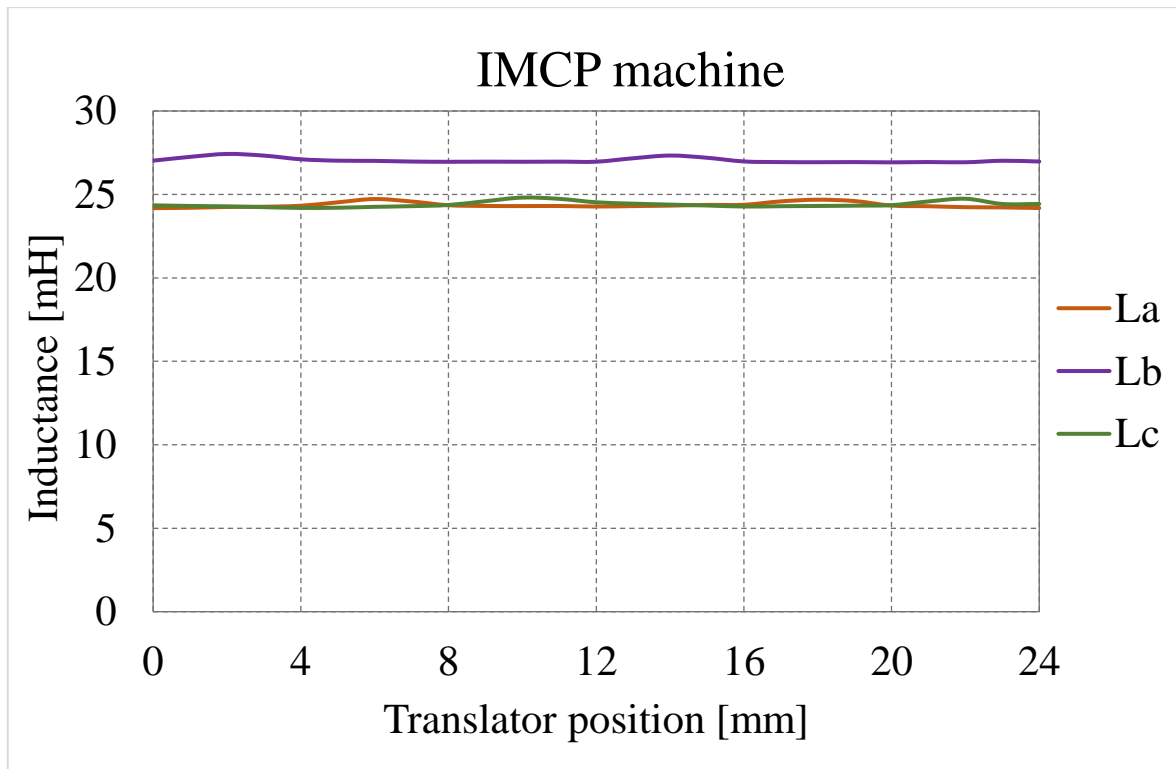
The winding inductance profile plays an important role in the performance of the LVHMs. Thus, determination of this parameter with a good precision is very important. The winding inductance can be calculated from the flux linkage (Ψ_{dc}) according to the following equation:

$$L = \frac{\Psi_{dc}}{I_{dc}} \quad (4.2)$$

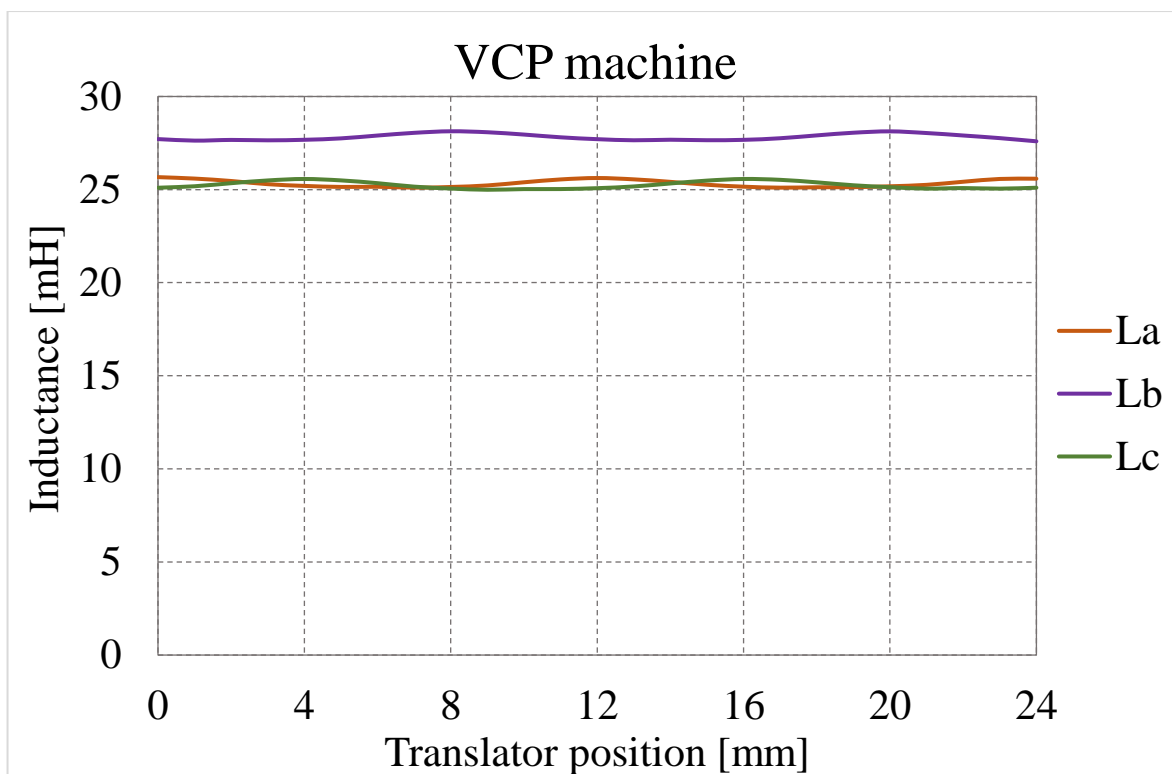
The self-inductances were calculated based on the flux linkage predicted by the FEA. First, the PMs were replaced with air. Then, taking phase A for example, a DC current with a value of 11A was applied to phase A, while no current was applied to the other two phases,

e.g. $I_a=I$, $I_b=I_c=0$. The variation of the flux linkage with respect to the translator position for the three machines was found. After that, Equation (5.3) was used to calculate the self-inductance for the three machines.

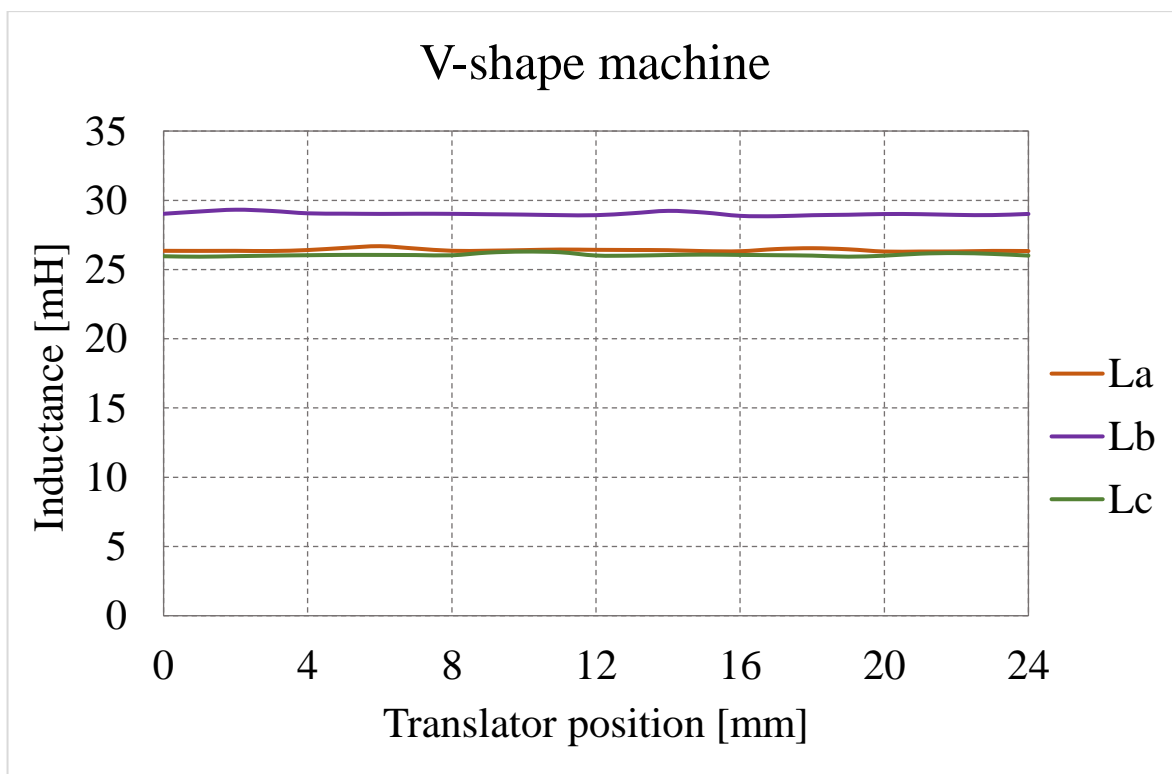
The self-inductance waveforms for the three machines are shown in Figure 4.24 (a), (b) and (c). It can be observed that in all the three machines the inductance of the middle phase (phase B) is higher than that of phases A and C, which reflect the effect of their high leakage flux. Table 4.8 shows the values of the self-inductances L_a, L_b and L_c , which include the average values of the self-inductance L_{avg} and the peak to peak values of the self-inductance L_{pk-pk} . From the results it can be seen that the variation of the self-inductance of the V-shape machines is smaller than that of the other consequent pole machines. However, the ripple of all inductances for the three machines with respect to the translator position is small enough to be ignored.



(a)



(b)



(c)

Figure 4. 24: Self inductances (a) IMCP (b) VCP and (c) V-shape machine

Table 4. 8: Comparison of self and mutual inductances

	V-shape		VCP		IMCP	
	L_{avg} [mH]	L_{pk-pk} [mH]	L_{avg} [mH]	L_{pk-pk} [mH]	L_{avg} [mH]	L_{pk-pk} [mH]
L_a	26.4	0.39	25.3	0.56	24.3	0.54
L_b	29	0.47	27.8	0.53	27.4	0.5
L_c	26.1	0.37	25.2	0.58	24.4	0.62

4.5.8 Losses and Efficiency

The losses and efficiency for the three machines calculated by the FEA are given in this section. In general, electrical machines losses consist of mechanical losses which require measurement setup to be determined, copper losses, core losses including translator and stator losses, and eddy current losses within the PMs. In this research, only the electromagnetic losses for all designs were investigated.

The losses for all machines at rated load operation and constant speed, i.e. 1.2m/s were calculated and compared as shown in Figure 4.25. The copper losses are dominant and as all machines operate with a fixed current density and coil area, it is equal in all three machines.

Iron losses in electrical machines primarily consist of:

- Eddy currents which rise with frequency; they are directly proportional to the frequency squared.
- Hysteresis losses which are directly proportional to the frequency.

The prediction of the iron losses was conducted through the MagNet™ software, which uses Steinmetz equation.

$$P_{iron} = K_h f B^2 + K_e (f B)^2 \quad (4.3)$$

Where K_h is hysteresis and K_e is eddy current coefficient, f and β represent the frequency and flux density, respectively. The iron losses for all machines are calculated and compared as shown in Figure 4.25. It can be seen that the V-shape machine exhibits higher iron losses of 1% and 17% compared to that of the VCP and IMCP machines, respectively. This is attributed to the improvement of the airgap flux density.

Since the PMs see a large change in flux, eddy current are induced with them and they hence suffer from eddy current losses. Eddy currents in the magnets directly lead to a temperature rise, which in turn can change the operating point of the magnet. Losses in the magnets are also included in Figure 4.25. It can be observed that the V-shape and VCP machines have almost the same PM eddy losses with a percentage of 11% compared to the IMCP machines. This is attributable to the increase in the flux density which again is a result of the flux concentration effect.

The three machines have different force capability at rated current and hence for a fixed velocity input have a different output power. Even though the V-shape machine has slightly higher losses it can still achieve the efficiency of 90.7% compared to 90% and 89.4% were achieved by the VCP and the IMCP machines, respectively, as illustrated in Figure 4.26. In fact this is due the increase in the mechanical power in both V-shape and VCP machines. The electrical efficiency is calculated by:

$$\eta_{predicted} = \frac{P_{out}}{P_{out} + P_{cu} + P_{iron} + P_{eddy}} \% \quad (4.4)$$

where P_{iron} and P_{eddy} are the iron losses and the PM eddy current losses respectively.

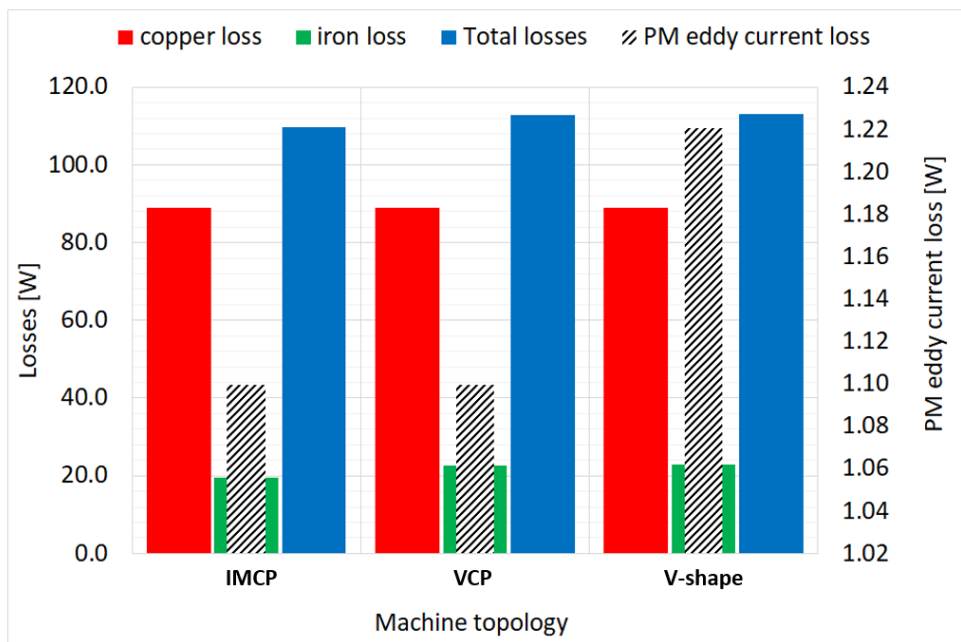


Figure 4. 25: Losses in the three machines

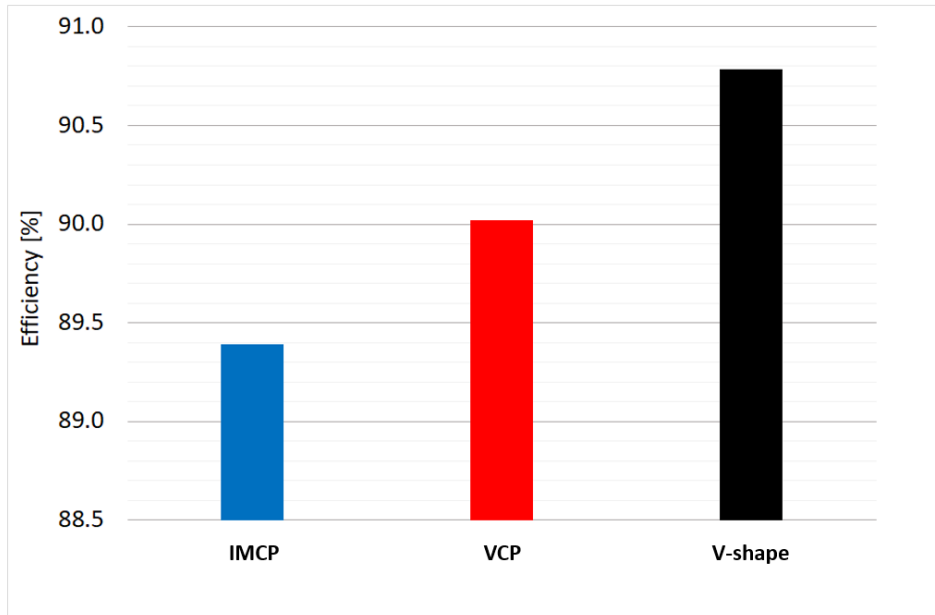


Figure 4. 26: Efficiency for the three machines

4.5.9 Mass

According to the thrust force analysis conducted in section 4.5.4, it can be concluded that both proposed V-shape and VCP machines are capable of generating the same force achieved by the IMCP machine with a shorter axial length, or alternatively for the same overall volume both the V-shape and VCP machines can produce higher force of 20.5% and 10%, respectively.

To facilitate the manufacturing and assembly processes, a common axial length is preferred and the latter of these two options was adopted. This contributes to the cost reduction of the prototypes, in which the most promising machines can share the same translator. In addition, a fair comparison can be obtained since all machines have the same dimensions, current density and copper losses.

The mass of active parts for the three machines are compared and presented in Table 4.9. As the same translator is used in all designs the laminations mass of the translator is constant, as are the magnet and copper masses. A negligible difference is shown between the three machines in terms of the stator mass, which is resulted from the difference between the required spaces for the PMs arrangements for each topology.

Table 4. 9: Mass comparison

Part	V-shape	VCP	IMCP
Laminated stator mass [kg]	7.82	7.77	7.81
Laminated translator mass [kg]	3	3	3
Copper mass [kg]	3.35	3.35	3.35
PM mass [kg]	0.48	0.48	0.48
Total mass [kg]	14.65	14.6	14.64

4.5.10 Attraction Force

The magnetic force with respect to the unit area between the stator and translator can be expressed by (5.8),

It is also known as the attraction force or closing airgap force. The manufacturing and assembling tolerances can lead to a non-uniform airgap, which in turn produces the attraction force. The resultant force can be 5-10 times the tangential shear stress [73]. The absence of the iron core in either the stator or translator (usually the part that is stationary) can tackle this problem as proposed in [95]. However, a significant reduction in the shear stress would occur as a result.

In order to assess the effect of the attraction force on the three machines, a series of simulations were conducted. The desired airgap length in both sides of the machine is identical and equal to 1mm. In this study, the airgap length was varied from 0.1mm to 0.9mm with a step of 0.1mm to achieve non-uniformity within the two airgaps. It should be noted that the displacement in one side will result in an equivalent displacement in the other side, for example, the displacement of 0.1mm means that the airgap length is 0.9mm in one side, while the airgap length in the other side would be 1.1mm as demonstrated in Figure 4.27. The three machines were investigated using the same technique. The attraction force was calculated under a DC current range from -11A to 11A, with an interval of 2.75A. The resultant attraction forces for the three machine (V-shape, VCP and IMCP machines) are shown in Figure 4.28 -4.30, respectively. From the graphs it can be seen that for all the three machines as the airgap displacement increases the attraction force is increased consequently. It should be indicated that among all these machine the highest values of the attraction force is felt by the translator of the V-shape machine when the airgap displacement is 0.9mm, with the peak value of 4.1kN, while the worst scenario for the same airgap displacement are

3.92kN and 2.49kN for the VCP and IMCP machines, respectively. This is attributable to the increase in airgap flux density of the V-shape and VCP machines. This analysis would give an indication for selecting the suitable bearings and supportive structure, which are capable of reacting against these potential forces.

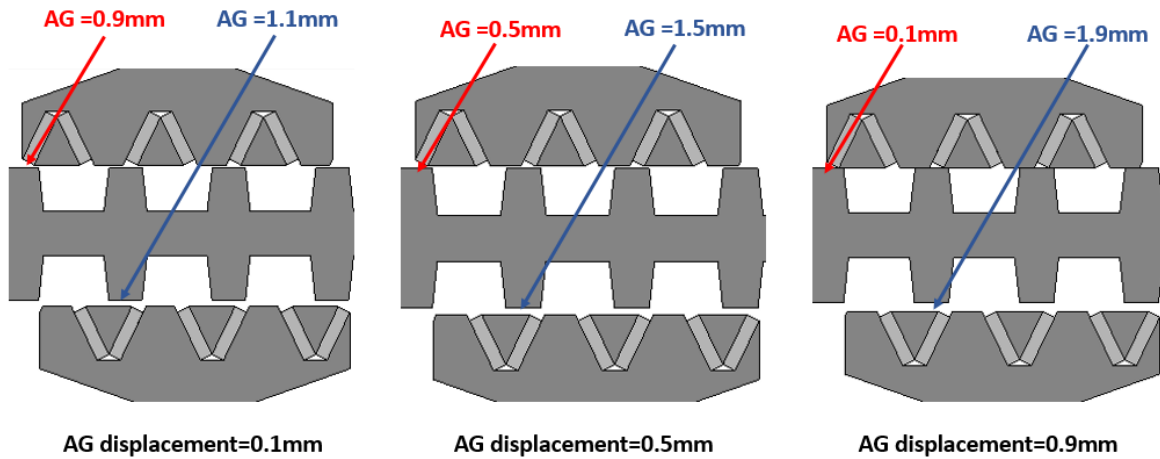
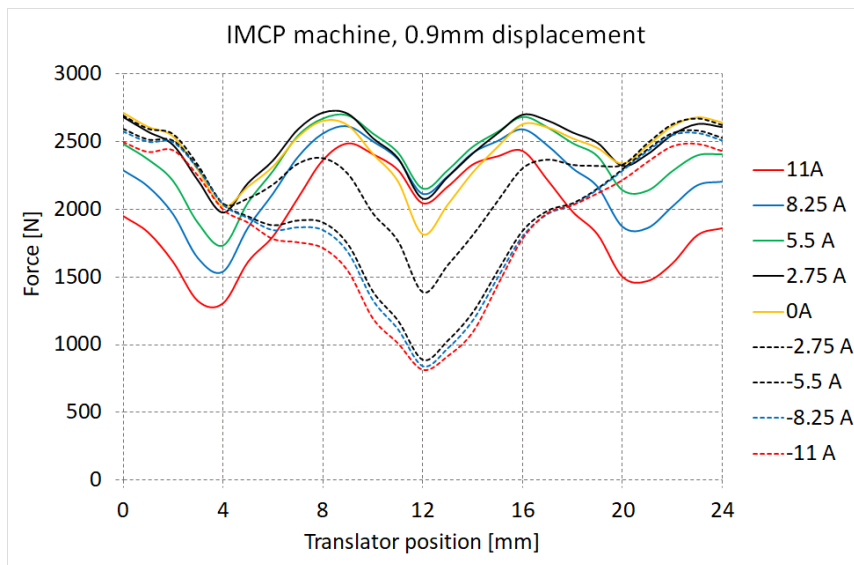
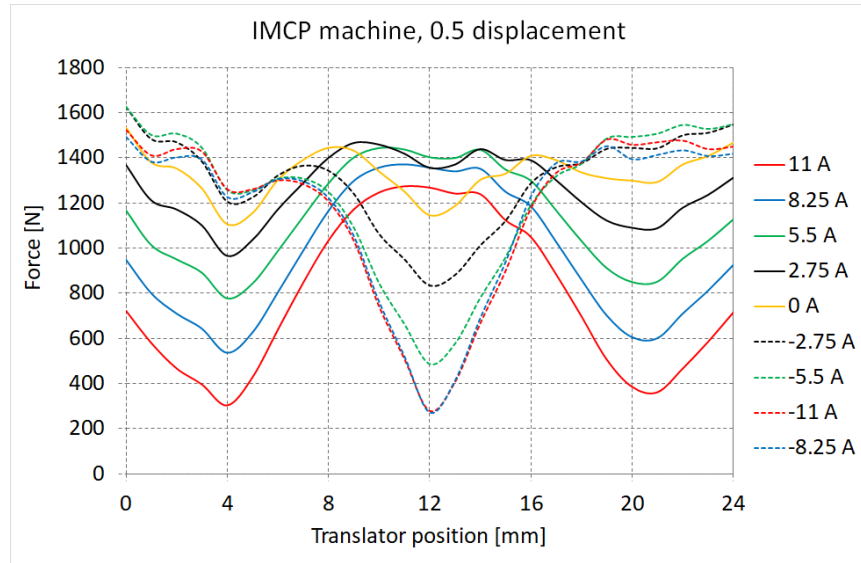


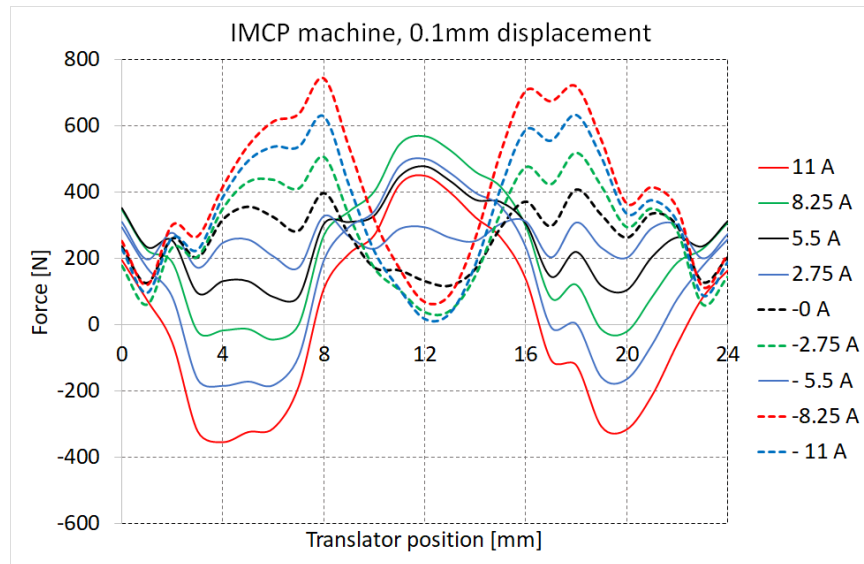
Figure 4. 27: VCP with different airgap displacements



(a)

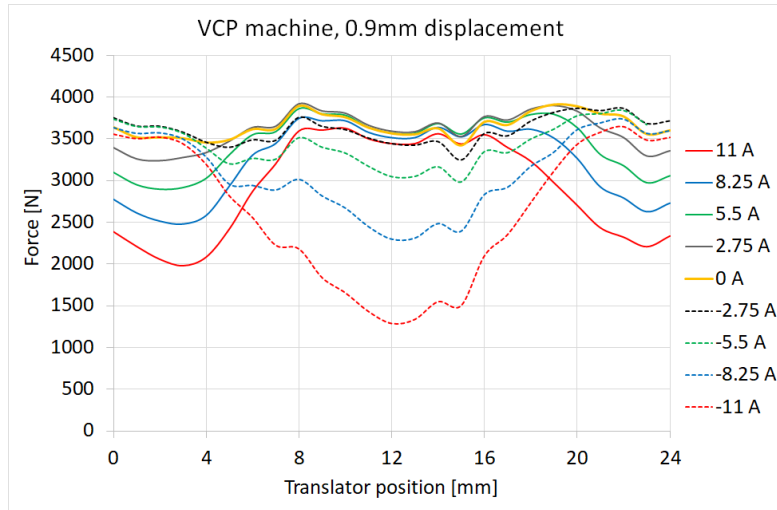


(b)

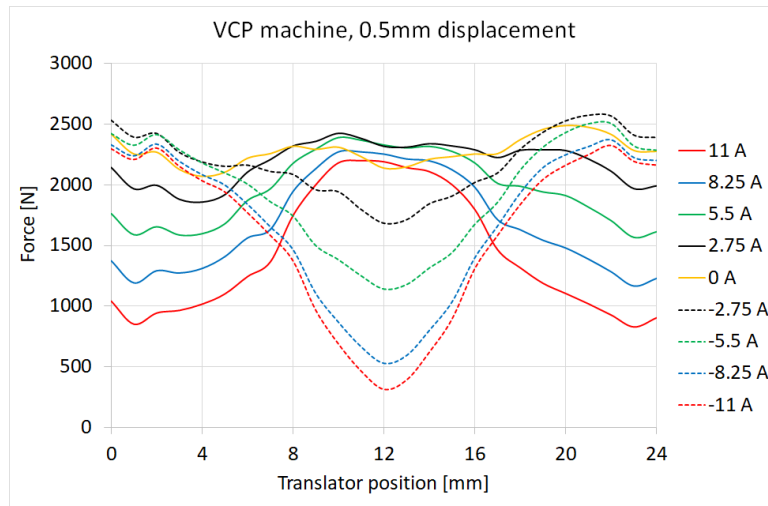


(c)

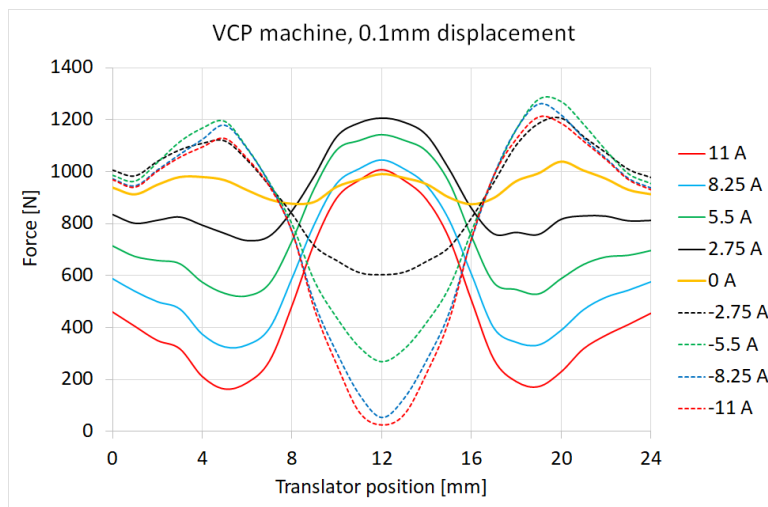
Figure 4. 28: Attraction force between stator and translator for the IMCP machine (a) 0.1 mm displacement, (b) 0.5 mm displacement and (c) 0.9 displacement



(a)

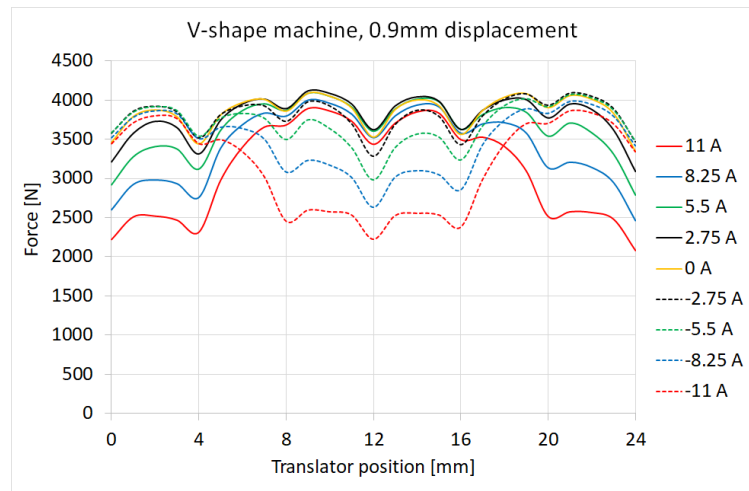


(b)

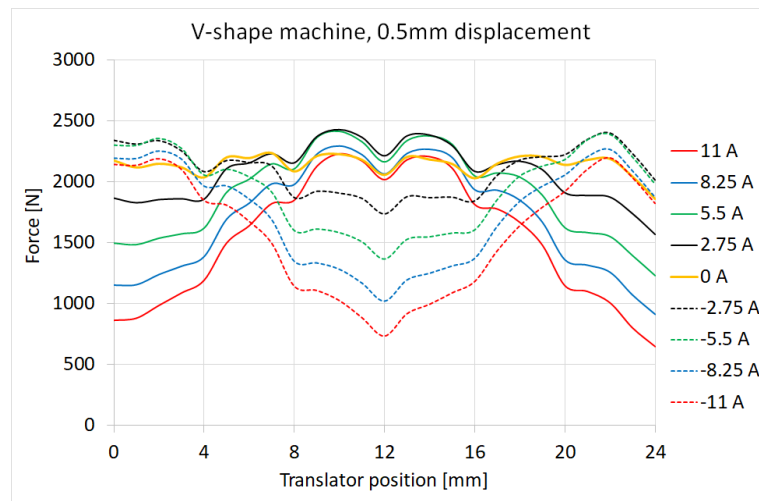


(c)

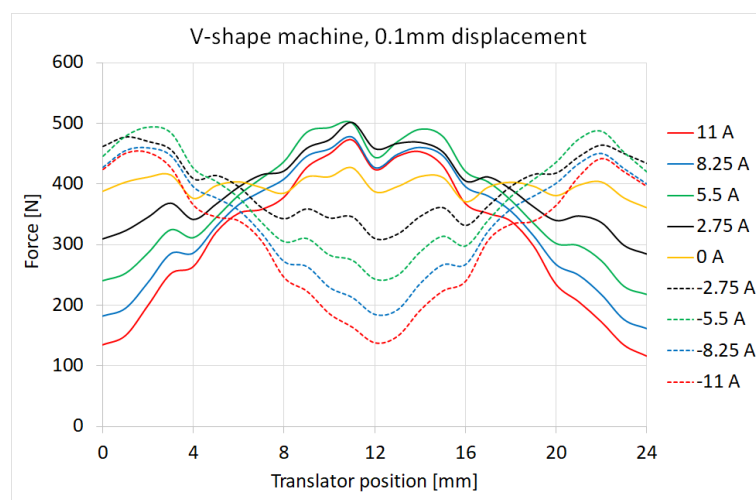
Figure 4. 29: Attraction force between stator and translator for the VCP machine (a) 0.1 mm displacement, (b) 0.5 mm displacement and (c) 0.9 displacement



(a)



(b)



(c)

Figure 4. 30: Attraction force between stator and translator for the V-shape machine (a) 0.1 mm displacement, (b) 0.5 mm displacement and (c) 0.9 displacement

4.5.11 Power Factor

The power factor for the three machines was calculated and compared using transient FEA simulation. The power factor was estimated based on the amplitudes of the values of the terminal voltage drop and the phase current. For this class of machine, high inductance is always a factor, and they can only run when connected to a fully rated converter. Assuming the converter controls the current to be sinusoidal and in phase with the back EMF, and further assuming the resultant terminal voltage is sinusoidal, the power factor is obtained by the cosine of the phase angles between them. It was found that the phase angles between phase current and terminal voltage are 46° , 50° and 60° for the V-shape, VCP and IMCP machines, respectively, meaning that the former machine can achieve a power factor of 0.7 compared with only 0.65 and 0.5 achieved by that of the latter ones, respectively. Thus, it can be concluded that the flux concentration design not only improves PM utilization but can also be operated at a higher power factor.

4.6 Selection of Prototype Machines

Based on the aforementioned analysis, the V-shape topology has been shown to offer the highest shear stress, no-load back EMF, force density, efficiency and power factor. Which means, a smaller machine would be required to react a given force. However, these advantages must be offset against the complex structure, high cogging force and force ripple. In addition, this topology requires double components of that used in the VCP machine, i.e. double number of PMs and triangle iron spacers, which may affect the construction cost. A trade off therefore must be made between performance and construction, where the VCP was selected instead. For comparative purposes the IMCP machine was also selected to be built.

The two candidates represent extremes in terms of magnet consumption and translator structure, where both machines need only 0.48kg of Nd-Fe-B, yet has a non-uniform cross-sectional area in the direction of motion. The relative merits of these factors provide the designer with an interesting choice when selecting a machine topology for wave energy applications [95]. The manufacturing and assembly process for the two options will be outlined in detail in the proceeding Chapter.

4.7 Conclusion

In this Chapter, two versions of the LVHM with V-shape PM arrays have been developed, analysed and investigated in terms of the power factor improvement. A more in depth comparison between these machines and the IMCP machine covered in Chapter 3 has been made based on the electromagnetic and electrical performances. The obtained results indicated that the V-shape topology is superior to the other machines, in which a higher no-load back EMF, force density, efficiency and power factor can be achieved by the V-shape topology. However, this machine was shown to exhibit higher cogging force and require a double number of PMs and triangular iron spacers than that of the VCP machine, making the V-shape machine more complex in terms of manufacturing. This is due to the removal of the iron ribs which influences the triangular iron spacers to be constructed and assembled as individual parts.

Due to time limitations, it has been decided that the VCP will be built along with the IMCP for comparative purposes. Even though the V-shape machine has the superiority to the other machines, consideration has been given to the VCP machine for the following reasons:

- The VCP has an advantage of a reduced number of components when building the prototype, i.e. a 50% less number of PMs and triangle iron spacers are required in the selected topology compared to its V-shape counterpart, which would therefore facilitate the complex manufacturing processes.
- The cogging force produced by the VCP machines is 32% lower than that of the V-shape machine.
- The closing airgap force felt by the translator of the VCP machine is 4.4% lower than that of the V-shape machine.
- The power factor achieved by this machine represents 93% of that obtained by the V-shape machine.
- The force density is only 8.8% lower than that of the V-shape machine.

However, the work presented here on V-shape machine is in the early stages of development and it would be interesting to verify these results through experiment. Therefore, strong recommendations and a more formed plan are given of further V-shape research for the next PhD student.

Chapter 5. Prototype Manufacturing and Assembly

5.1 Introduction

This Chapter will describe all the manufacturing and assembling processes for the prototype machines that have been built to validate the simulation results for both machines analysed and presented in the previous two Chapters. As such it will introduce a new flexible structure, which allows the mechanical airgap to be adjusted. This structure has two adjustable aluminium caps, which are used as stator support. Thus, both machines can share the same stationary aluminium housing frame. Finally, the integration of the test rig and test machines will also be described later in this Chapter.

5.2 Parameters of Prototypes

The key parameters for both laboratory prototypes are listed in Table 5.1. As described in Chapters 3 and 4, both machines have the same parameters except the magnet configurations, while their mass is kept constant.

Table 5. 1: Key parameters for both prototypes

Parameter, unit	Topology	
	IMCP	VCP
Stator width [mm]	232	232
Stator tooth width [mm]	72	72
Stator height [mm]	73	73
Slot width [mm]	54	54
Machine axial length [mm]	50	50
Translator length [mm]	490	490
Translator height [mm]	30	30
Translator tooth height [mm]	10	10
Width of translator tooth root [mm]	10	10
Width of Translator tooth tip [mm]	8	8
Number of turns/ coil [turn]	112	112
Airgap length [mm]	1	1

5.3 Stator Construction

In order to reduce the iron loss of the machine, the stator is made of laminated electrical steel sheets to break up the eddy currents paths. Hence, the magnetic field would be allowed to pass through the material at a non-negligible frequency. Steel sheets with a thickness of 0.35mm were used; made of silicon and bounded by specialist epoxy resin to obtain the required stack thickness, 50mm. The stacked sheets were exposed to a heat of 160C° for three hours to cure the epoxy. To achieve high tolerance, the laminations were cut by wire erosion. It is a very precise method, where less burrs and localised pressure point can be achieved compared to laser cutting. The DXF format of the CAD drawings shown in Appendix A were used in the cutting machine to automatically produce the required components. Figure 5.1 shows the laminated stator cores for both machines, inset CP and VCP machines.

For the VCP prototype, the stator structure has the same dimensions of the IMCP machine. The key difference between the two stators is the magnet arrangement, which requires 18 small triangular-shaped pieces (iron spacers); made of the same electrical sheets to obtain the proposed V-shape PM structure. These pieces were attached between each pair of magnets and glued using an advanced materials epoxy resins & hardeners (ARADUR 5052CH & ARADLDITE LY5052), as described in the specifications of this product in Appendix B to avoid the failure happed in [122], for example.



Figure 5. 1: Laminated stators (a) IMCP (b) VCP

5.4 Stator Aluminum Support

Each prototype machine requires two aluminium caps, either the IMCP machine or the VCP machine as shown in Figure 5.2. These parts are made of aluminium 6082 to accommodate the stator laminations, PMs and windings in both sides of the machine. Using

these aluminum caps can provide more flexibility in controlling the airgap length with the aid of adjustable screws shown later in Figure 5.17. The whole stator core-back was fully buried into the stator aluminium support as shown in Figure 5.2. Six holes were drilled into each aluminium cap and fitted by banana plug socket female connectors to provide a path for the coil terminals.



Figure 5. 2: Stator Aluminium Support

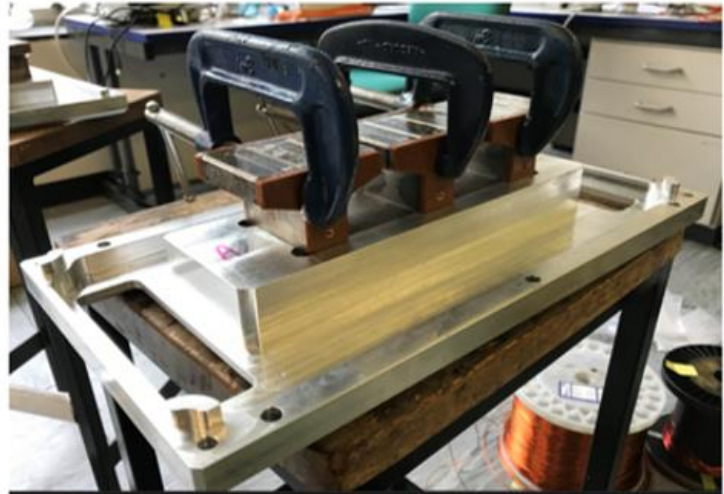
5.5 Winding

Since the tooth shoe is adopted in the stator design for the purpose of reducing the consumption of the steel material and the machine active length, pre-manufactured bobbin windings cannot be used in either prototype. Therefore, the coils were manually tightly wound in layers through the slot opening leading to short end windings. Prior to this step, the slots were lined with Nomex thermal insulating sheets with a thickness of 0.13mm and maximum temperature resistance of 205 °C. The edges around the slot opening were covered with a plastic tape to protect the insulation of the conductor from damage during the coil winding process. Tufnol sheets with a thickness of 5mm shown in Figure 5.3 (a) and (b), described in the previous section, were used here to facilitate curving the end-winding and to protect the conductor from being damaged due to the sharp edges surrounding the stator tooth. A single strand copper wire illustrated in Figure 5.3 (c) was used, which has a diameter of 1.4mm according to the calculation made in section 3.10.5. Each coil has 112 turns with a thermocouple connected to the middle phases in both sides as shown in Figure 5.3 (d) to monitor the temperature. The coils were treated with varnish to improve their resistance to humidity; and to bond turns together and to the stator tooth.

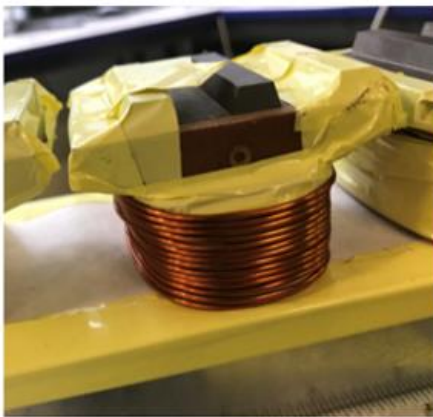
After finishing winding the coils, the insulation tests around the conductors were performed using a small portable instrument - as Megger shown in Figure 5.4. All tests have shown high resistance values of approximately $2.92 \text{ G}\Omega$, which confirm the validity of the insulation. Finally, all coils' terminals were connected and soldered to banana plug socket female connectors shown in Figure 5.3 (d) to provide a path for the coil terminals.



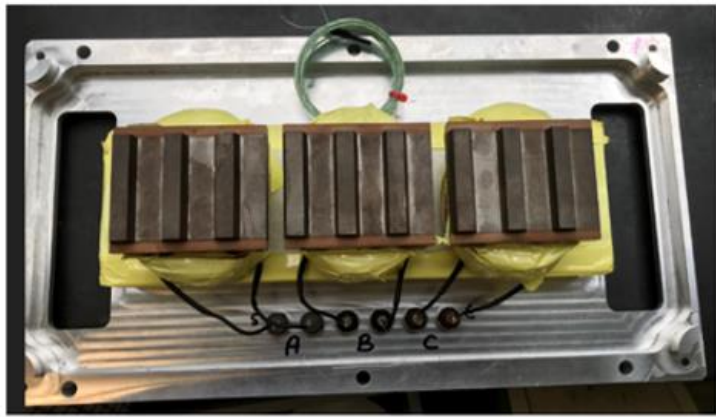
(a)



(b)



(c)



(d)

Figure 5. 3: Winding process(a) Tufnol sheet (b) Tufnol sheet assembly (c) coil (d) final winding connection (banana plugs)

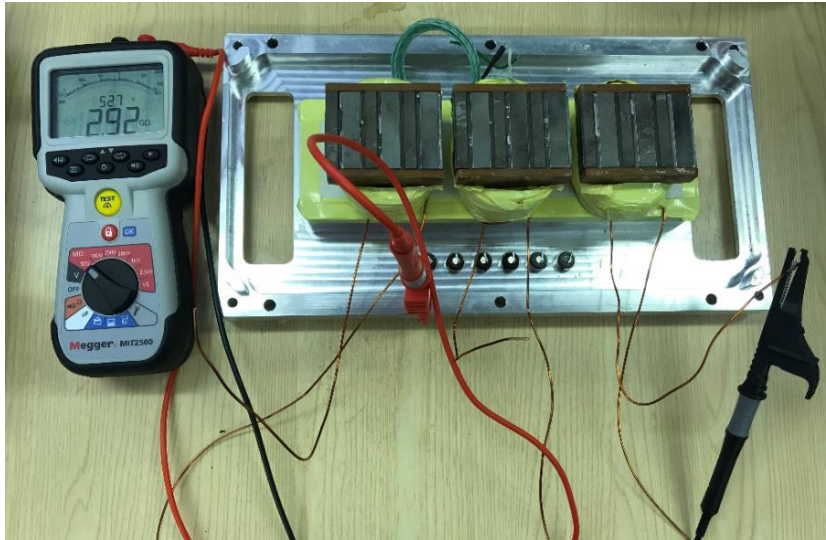


Figure 5. 4: Insulation test using Megger

5.6 The Permanent Magnets

The magnets used in both prototypes shown in Figure 5.5 have the same specifications. They are constructed from N42H grade Neodymium Boron magnets capable of operating in temperatures up to 120°C. The magnets were manufactured and assembled by Bunting Magnetics Europe Limited and have a specified remanence of 1.24T. They possess high coercive forces, high energy product and high performance to cost ratio. The dimensions of magnets used in both topologies are illustrated in Table 5.2. A dimensional tolerance of +/- 0.1mm was advised by Bunting Magnetics Europe Limited.

Table 5. 2: Magnet dimensions

Machine topology	Topology		
	Width	length	length
IMCP	12	50	6
VCP	12	50	3

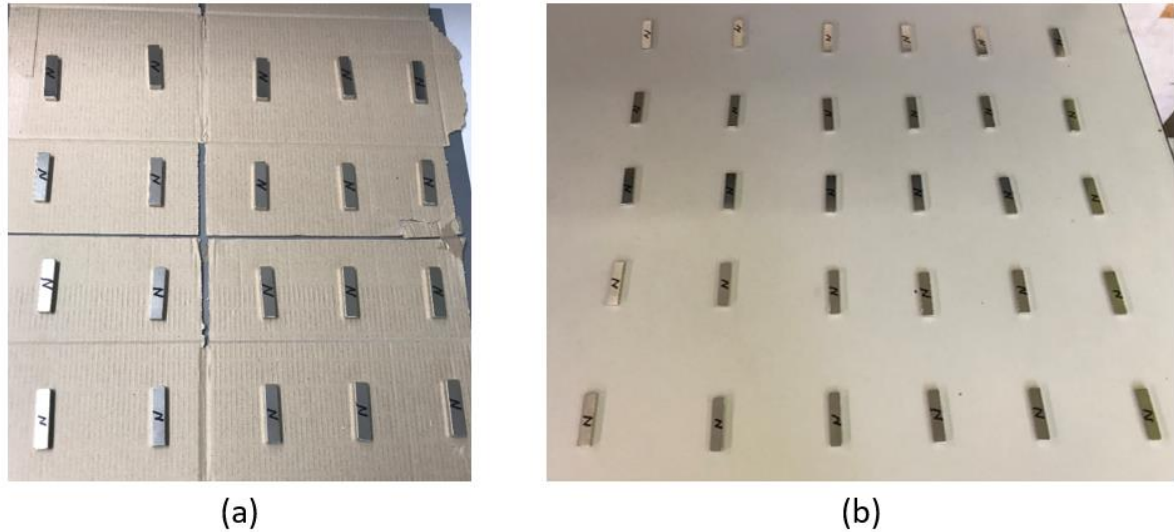


Figure 5. 5: Un-assembled magnets after checking and marking their polarities (a) IMCP magnets (b) VCP magnets

In the inset CP prototype machine with tapered ferromagnetic poles, the magnets were glued and placed in their allocated position beside the tapered ferromagnetic poles as shown in Figure 5.6 (a). The glue was selected with the help of well experienced technicians in the mechanical workshop at Newcastle University. The glue showed sufficient tensile strength to support the magnets in withstanding against magnetic pull force. After mounting and gluing the magnets, a special mixture of epoxy was applied to the top of magnets, which also completely filled the gaps between the magnets and tapered ferromagnetic poles.

In the VCP machine, the magnet segments were first glued and placed on the pre-cut V-shaped slots, which are available on each stator tooth. Then, the small triangular iron spacers were fitted into the gaps between each pair of magnets and glued to form the V-shape structure discussed earlier in Chapter 4. Next, the special mixture of epoxy was applied to the surface of the completed constructed stator tooth. After that, two G-clamp were used to hold both the magnets and iron spacers until the glue gets dried as illustrated in Figure 5.6 (b). Finally, plastic Tufnol sheets with a thickness of 5mm were machined to match the shape of the stator tooth. One of the goals of using this material is to support and hold the magnets with the aid of glue as illustrated in Figure 5.6 (c).

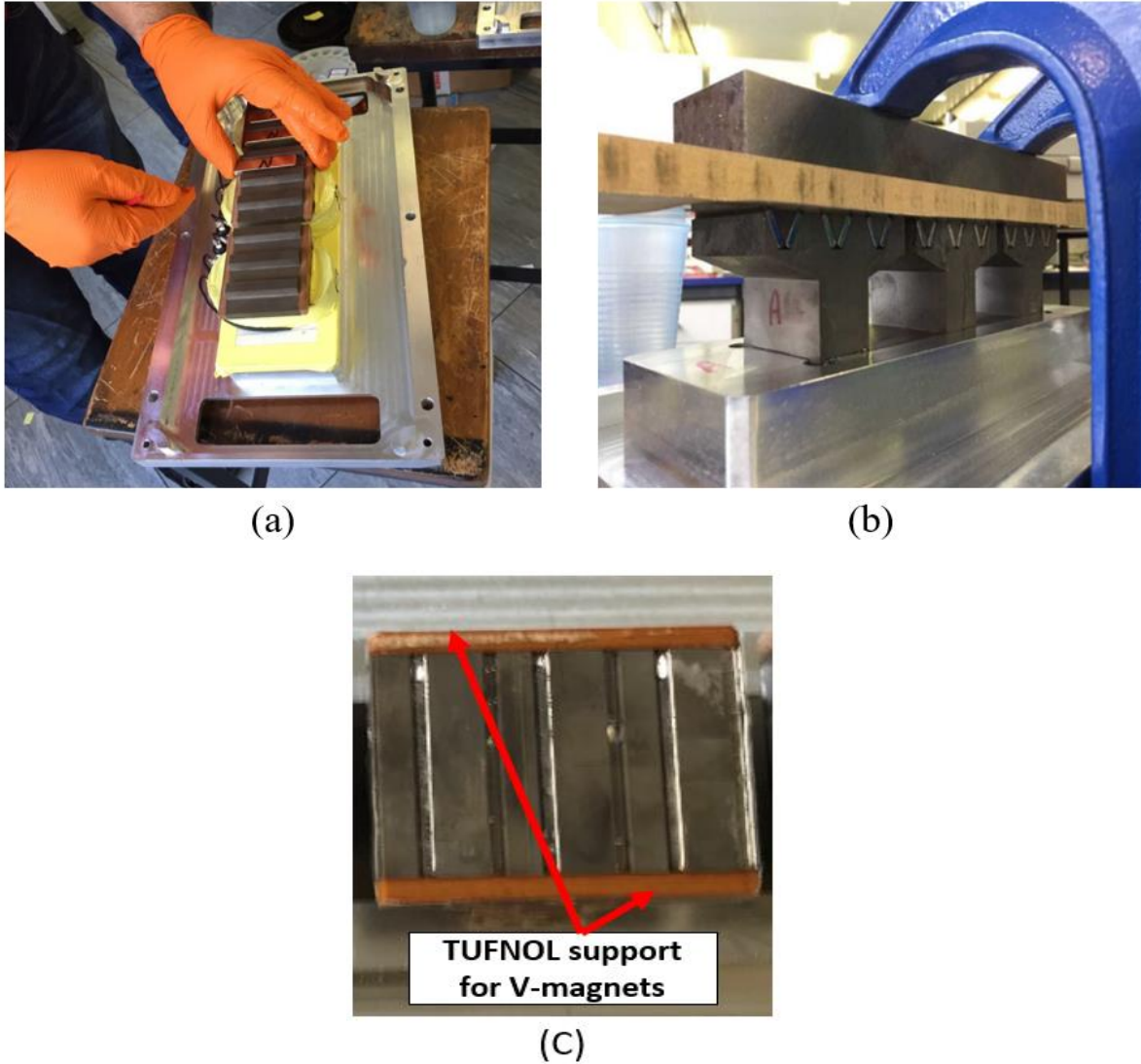


Figure 5. 6: Magnet assembly (a) IMCP (b) VCP (c) Tufnol support for V-shape magnets

5.7 Translator Construction

As the translator mass reduction is one of the specific objectives of this research, the translator core-back was designed for a minimum possible thickness. The construction processes and materials are the same as that used in the stator. To increase the rigidity of the translator, ten holes with a diameter of 4mm were made by the same wire-cut machine, allowing carbon fibre rods to pass through them in the transverse direction, while the ends of these components were attached to the Tufnol support in both sides of the translator. Figure 5.7 shows the physical translator with the pre-drilled holes along its core-back.



Figure 5. 7: Laminated translator

5.8 Translator Support

In order to assemble the translator three different types of material were used as described below:

5.8.1 Translator Aluminium Support

Two aluminium I-beams were employed in the stator assembly, in which one side of the I-beam is attached to the T-shaped Tufnol bar, which will be described in the next section. While another side of the I-beam is designed to house the carriages as illustrated in Figures 5.8 and 5.9. The reason of choosing aluminium material is to reduce the mass.

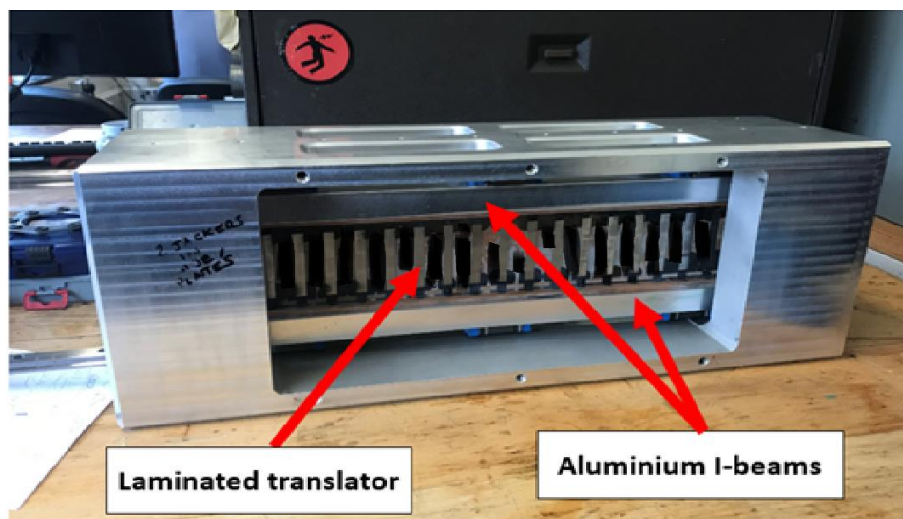


Figure 5. 8: Assembled aluminium I-beam

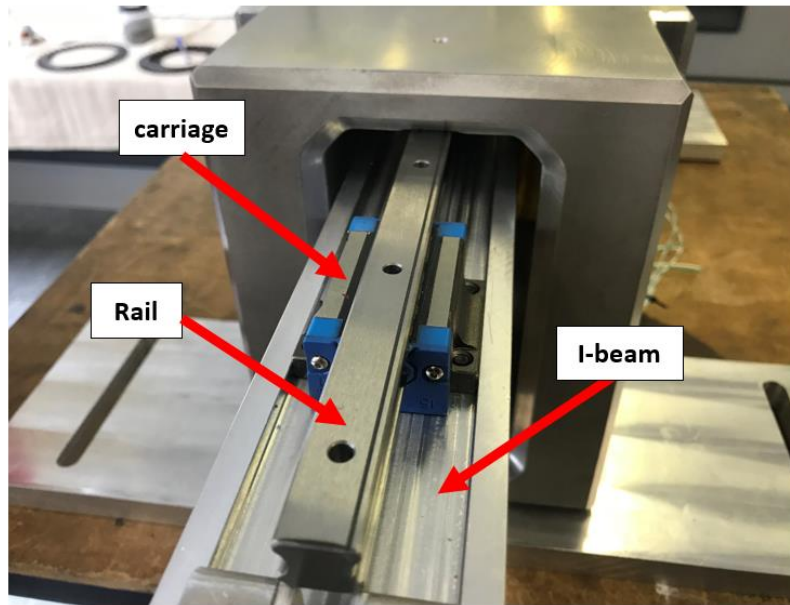


Figure 5. 9: Assembled I-beam and carriage

5.8.2 Translator Tufnol Support

Tufnol is a plastic material designed for applications requiring mechanical strength, low thermal conductivity and electrical insulation at elevated temperatures. This material has great features of high strength and rigidity, with good dimensional stability and moisture resistance and strong electrical properties. According to the aforementioned advantages, two T-shaped Tufnol bars were machined and used in the translator assembly, as shown in Figure 5.11 and 5.12 respectively. The reasons of choosing T-shaped Tufnol rather than rectangular-shaped Tufnol bars can be summarised as follows:

- By using rectangular-shaped Tufnol bars, the laminated stators and the Tufnol bars might come in contact during the translator movement as illustrated in Figure 5.10 (a), which may lead to mechanical issues. To stop that from happening, the T-shaped Tufnol bars was employed to maintain a fixed distance between them as shown in Figure 5.10 (b).
- By using the T-shaped Tufnol bars, the total translator mass can be saved as a result of removing the four areas marked in Figure 5.10 (a).

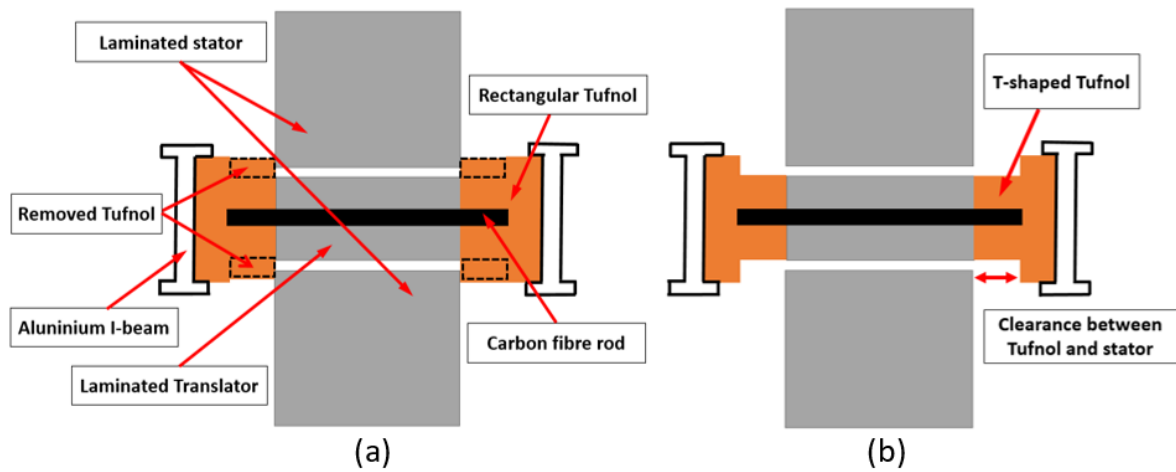


Figure 5.10: Tufnol shape effect (a) rectangular-shaped Tufnol (b) T-shaped Tufnol

Each piece of Tufnol bar was sandwiched between the aluminium I-beam and the laminated translator. The Tufnol bars are non-conductive material which can prevent the eddy currents from passing through the aluminium I-beams, which may degrade the machine performance.

Ten holes with a diameter of 4mm were drilled along the centre of each Tufnol bar to provide an access for the carbon fibre rods described in the proceeding section and shown in Figure 5.11 to pass through. There are also twelve holes with a diameter of 5mm drilled into the top and bottom sides of each Tufnol bar to align with the pre-manufactured holes provided in the carriages. Thus, screws and nuts were used to fix the aluminium I-beam, Tufnol bars and carriages together. A strong glue was also used to strengthen the attachment of the translator laminations, Tufnol bars and aluminium I-beams. Finally, the translator slots were filled with epoxy as shown in Figure 5.12, to improve rigidity. The datasheet for the Tufnol used in both prototypes can be found in Appendix C.

5.8.3 Carbon Fibre Rods

Ten solid non-magnetic carbon fibre rods with a diameter of 4mm have been used in the translator assembly as shown in Figures 5.11 and 5.12. They are manufactured for maximum rigidity with minimum mass which can lead to great structural reinforcements, while minimizing the weight. These were inserted into the allocated holes in both translator laminations and Tufnol bars. The product data sheet is shown in Appendix D.

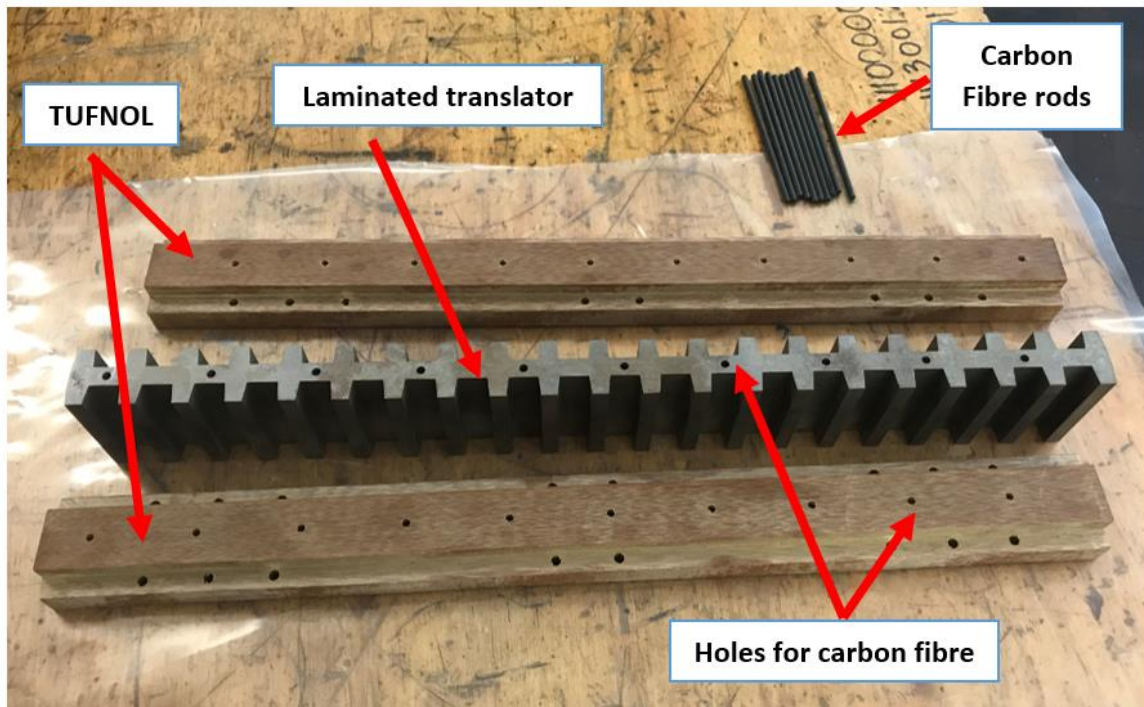


Figure 5. 11: Laminated translator and Tufnol bars before the assembly

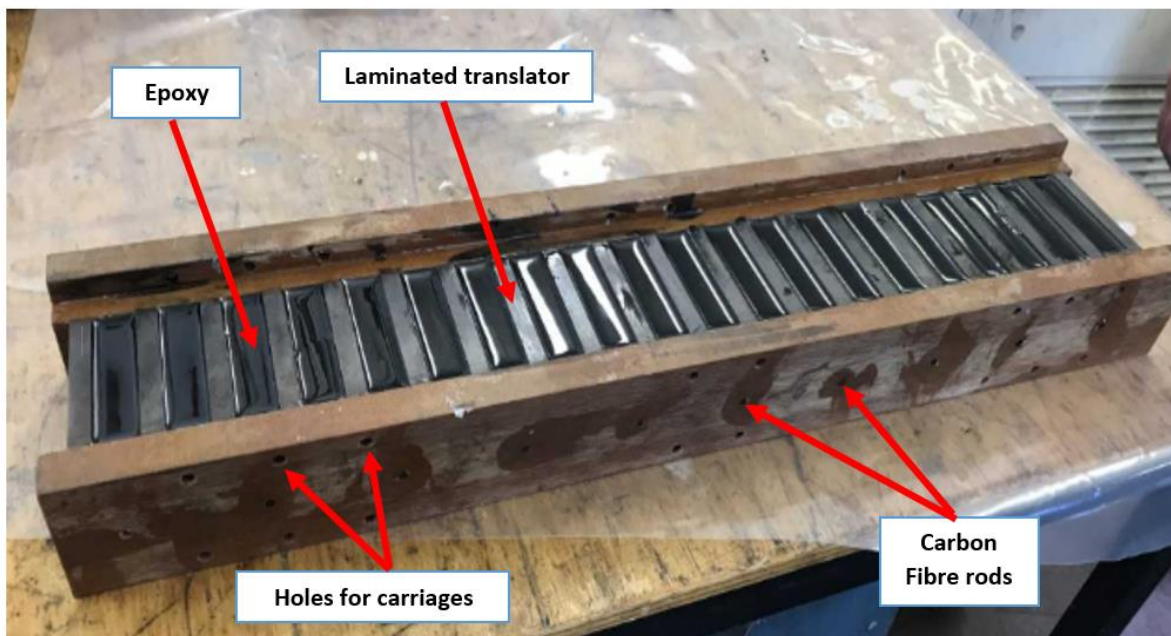


Figure 5. 12: Laminated translator and Tufnol bars after the assembly

The flux linkage contour is plotted in Figure 5.13 for the purpose of comparing the translator laminations with and without the carbon fibre rods. From the Figure it can be observed that using the carbon fibre rods has no effect on the flux passing through the translator. This is due to the fact that this type of material is non-magnetic.

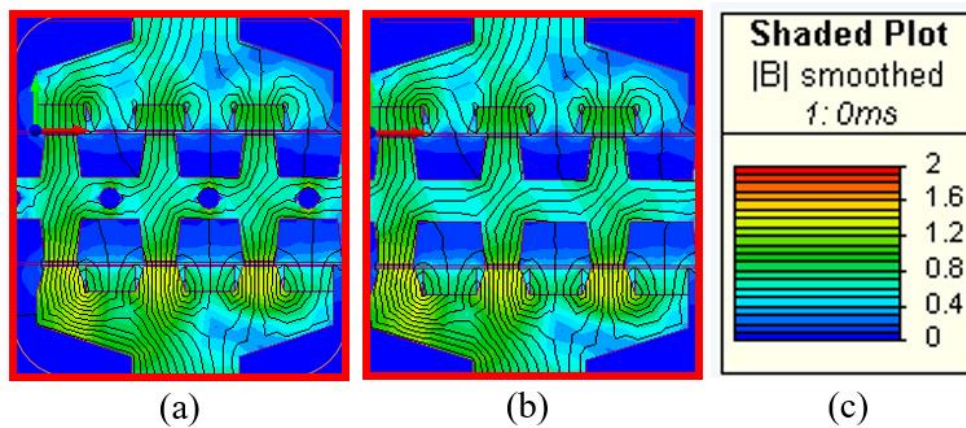


Figure 5. 13: Flux linkage contour plot (a) with carbon fibre rods (b) without carbon fibre rods

5.9 Machine Aluminum Housing

This part of the machine was the most time consuming in terms of the manufacturing process. It represents the main aluminium body of the machine, which contains the stator and translator. It is mainly designed to house the linear guide rails that attached to the upper and bottom sides of the aluminium frame as shown in Figure 5.14. The structure of the aluminium housing allows the mechanical airgap to be adjusted at any length up to 7mm by setting the aluminium stator support (aluminium caps), which will be described in the next section. Another advantage of using this structure is that the stator can be easily swapped with the VCP machine, which requires less material and hence reduce the total construction cost. In order to achieve these advantages effectively, the translator must be mounted perpendicular to a ground plane as adopted in this study. Aluminium 6082 was used in the construction of the machine housing, which leads to significant overall mass savings of the prototypes.

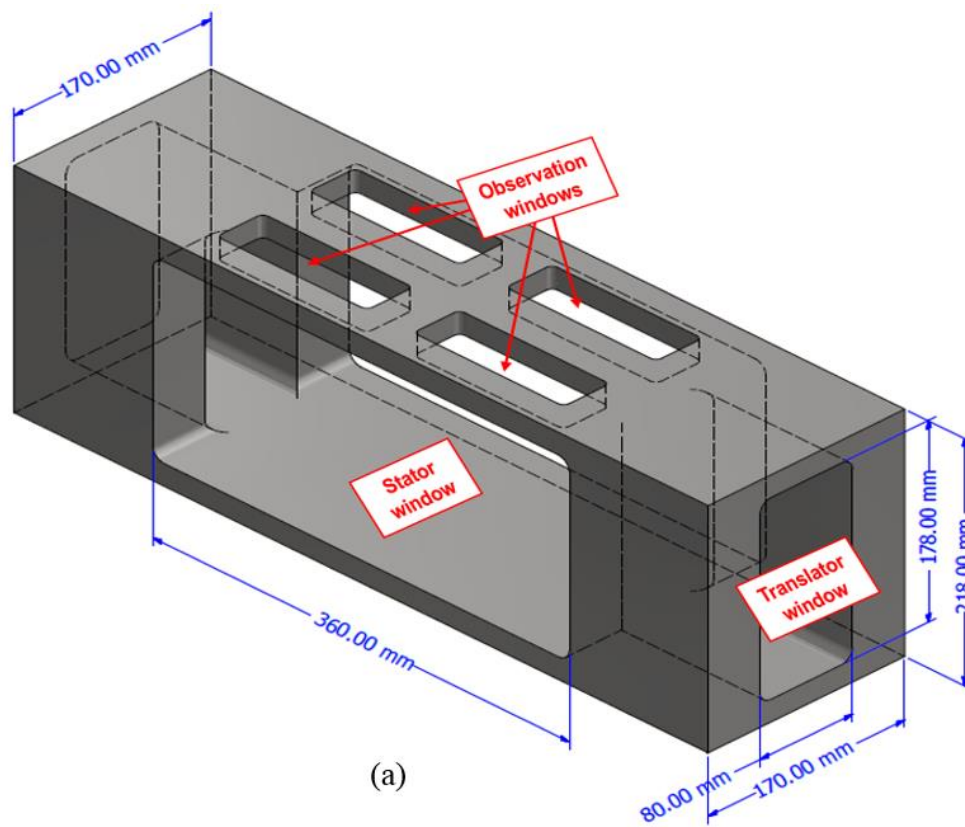


Figure 5. 14: Stationary aluminium housing with mounted linear guides (a) CAD drawing (b) photo

5.10 Attaching Linear Guide (Rail) to the Machine Aluminium Housing

There are a wide variety of types of linear bearings that can be used in the prototype. Some of them offer high rigidity but require a large space due to their bulky sizes, which cannot be fitted in the machine housing such as that shown in Appendix E. However, considering the required spaces and the stiffness of the bearings set, the linear guide and carriages were chosen as the most suitable option in terms of stiffness, reliability, size and cost. In addition, since the bearings can be overloaded because of the attraction force between the stator and translator caused by the difference between the two airgaps length, the worst case of the unbalanced airgaps that discussed in section 4.5.10 was taken in to account. This bearing set can withstand attraction magnetic force up to 9.8kN, thus allowing the translator to be assembled without any overloading issues on the bearings. The linear guides have pre-drilled holes distributed along their length to accommodate screws that attached to the stationary aluminium housing. Figure 5.14 shows the linear guides after attaching them to the inner surface of the stationary aluminium housing.

5.11 Attaching Carriages to the Translator Support

It was decided that six carriages would be used in the translator assembly, in which each side of the translator support accommodates three carriages distributed on the aluminium I-beam as shown in Figure 5.15 (a) and attached to the aluminum I-beam using four screws. One side of the aluminium I-beam was machined to match the carriage height as shown in Figure 5.15 (b). This gives the carriages support from the flanges available in both sides, which ease maintaining the alignment of all carriages. The two middle carriages in both sides give an extra support to prevent the translator from being bend as a result of the attraction magnetic force.

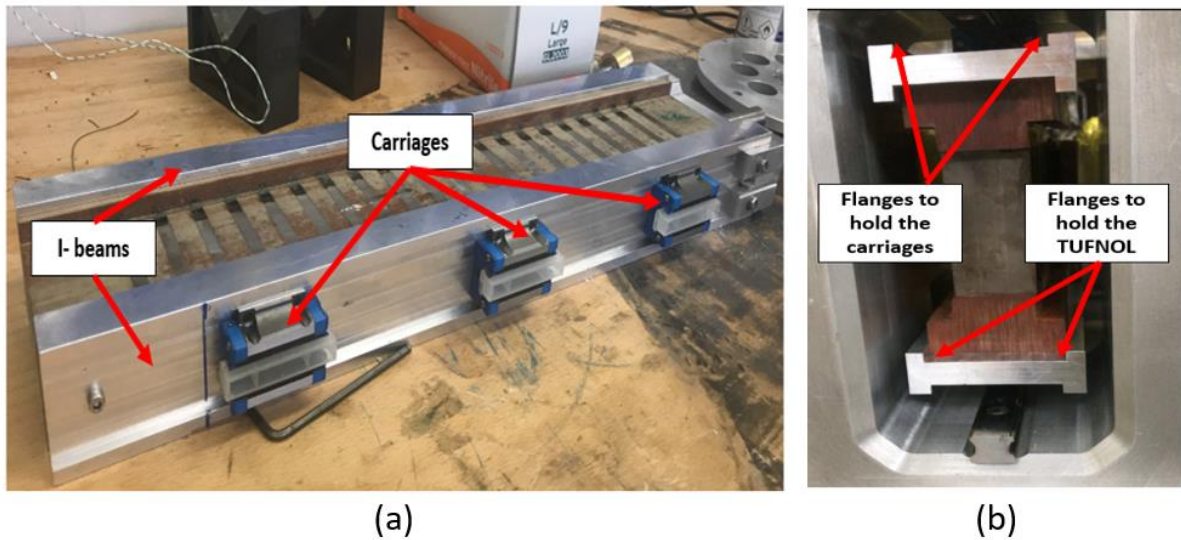


Figure 5.15: Attachment of the carriages

5.12 The Shaft

The shaft shown in Figure 5.16 was constructed from non-magnetic stainless steel as an intermediate between the translator structure and the actuator shaft. A U-shaped piece of aluminium, shown in Figure 5.16, was designed for three purposes: to provide a base for the shaft; to hold the two aluminium I-beams; and finally to limit the stroke of translator's in both directions.

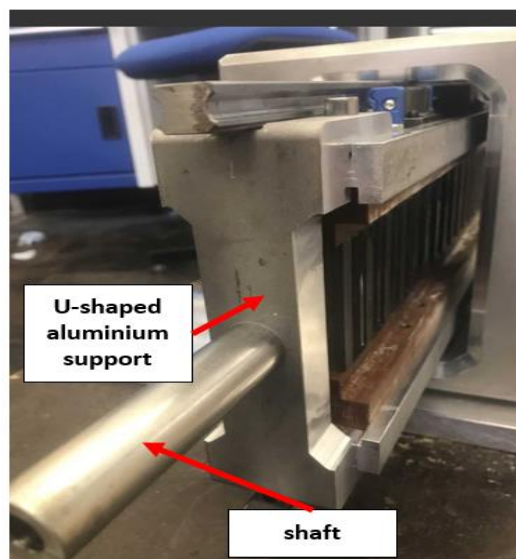


Figure 5.16: U-shaped aluminium support

5.13 General Assembly and the Test-rig

Figures 5.17 and 5.18 illustrates the complete assembled machine and test rig where the above-mentioned casing components can be seen. Both completed prototype machine and ball screw (actuator) are mounted on the test rig, in which the translator shaft was directly coupled to the actuator shaft. The force transducer was connected to the translator shaft for the purpose of measuring linear static DC force. Appendix F shows the IMCP machine integrated with a full test rig which was tested in wave tank at Edinburgh University.

The Actuator Control Solutions Integrated (ACSI) is all-in-one servo motor/drive/controller for cost-effective servo control mount to Tolomatic for a complete motion system. It can be controlled simple digital I/O, analog input or robust industrial Ethernet. The ACSI has an input supply of 10VDC to 60VDC, while the I/O controller is powered with 24VDC. The ACSI is capable of peak force loads up to 17.8kN with a maximum stroke of 200mm at a maximum linear velocity of 316mm/s.

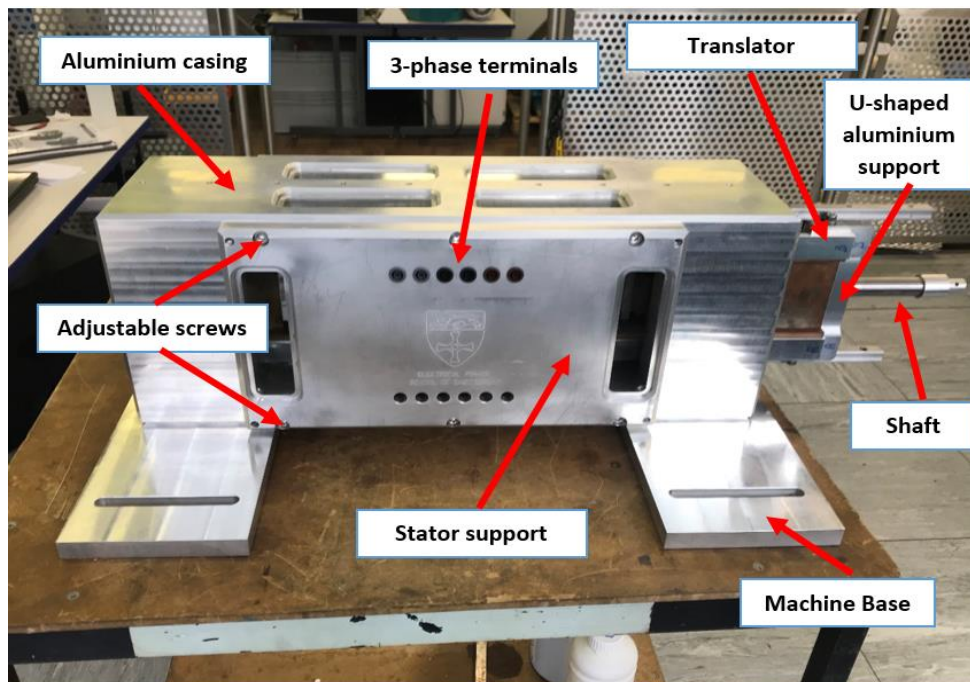


Figure 5. 17: A complete assembled linear machine

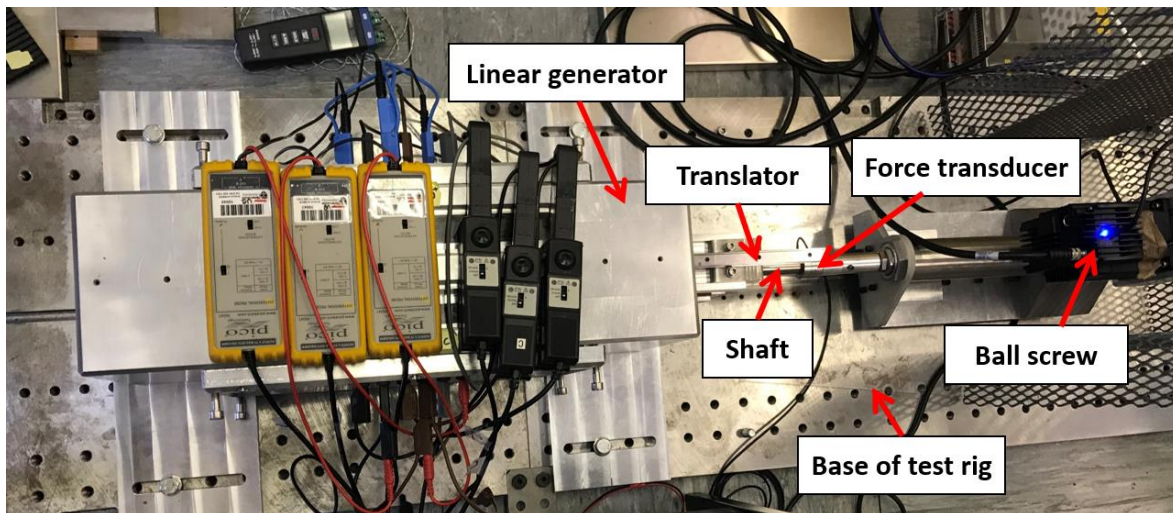


Figure 5. 18: A complete assembled test rig

5.14 Conclusion

The prototype machine with two different stators' structure has been successfully designed, constructed and integrated into a complete test rig. A flexible aluminium housing has been introduced, allowing the mechanical airgap to be adjusted. In addition, using the stator aluminium caps contributed to a reduction of manufacturing lead time and the material used in the prototype machines, where both machines discussed in Chapter 3 and 4 shared the same aluminium housing. The concepts and processes of the translator assembly presented in this Chapter led to a noticeable saving of the overall translator mass and required a minimum space for linear bearings. With the aid of Tufnol sheets and bars, the translator laminations were properly insulated from the any conductive material. Furthermore, a method for winding all stators' coils around each individual stator tooth was also described in detail. Finally, the complete test rig has been designed and constructed for testing purposes.

Chapter 6. Experimental Results and Evaluation

6.1 Introduction

This Chapter presents and discusses the experimental results obtained from a number of tests that were conducted on the two prototype machines, namely the IMCP machine and the VCP machine. For fair evaluation, the measured results have been compared to the simulated results obtained from the FEA models reported in Chapters 4 and 5. Afterwards, the key measured results for both prototypes have been compared and discussed. The errors in the attained results have been elucidated and some conclusions have been drawn.

The following experimental tests will be analysed and covered for both machines in this Chapter:

- Resistance and inductance measurement
- No-load back EMF
- Cogging force
- Force production
- Force variation with current
- Resistive load tests
- Thermal performance

6.2 Phase Resistance and Inductance Measurements

6.2.1 Phase Resistance Measurement

The resistance tests are conducted to test the integrity of the coils after they have been wound to detect any short circuit or open circuit in the coil or phase connection, or any error in turn number.

The DC winding resistance is an important measurement in electrical machines' tests. The phase resistance can be measured straightforward by connecting a DC current source to the stator winding as shown in Figure 6.1(a). This process would result in an induced voltage across the stator winding. Thus, the resistance can be calculated by dividing the obtained voltage by the applied current. The resistances for all phases were measured and the final value is the average value of these. It should be indicated that the measurements were carried out at ambient temperature of ($\approx 20\text{C}^\circ$), since the resistance mainly depends on the temperature.

A digital multimeter shown in Figure 6.1(b) was also used as an alternative method to measure the winding resistance.

6.2.1.1 IMCP machine

The attained values from these experimental tests were compared to the predicted values as shown in Table 6.1.

The phase resistance was also calculated according to (6.1), giving a 0.52Ω , in which a close agreement is observed between the measured and calculated values.

$$R = \frac{N_{coil} \cdot l \cdot \rho}{A} \quad (6.1)$$

Where N_{coil} is the number of coils connected in series per phase, l is the length of the conductor, ρ is the electrical resistivity of the copper and A is the cross-sectional area of the conductor.

From Table 6.1 it can be seen that both methods show a good agreement between the measured and predicted resistances with an average error of 4.3% and 6.2% between the predicted and the measured values obtained from the first and second method, respectively, and an average error of 1.9% between these two methods. Furthermore, the negligible errors between the resistance values of the three phase imply that the three phase windings have the same number of turns.

It should be mentioned that the coils per phase were connected externally using a conductor with different diameter, which may influence the accuracy of these measurements.

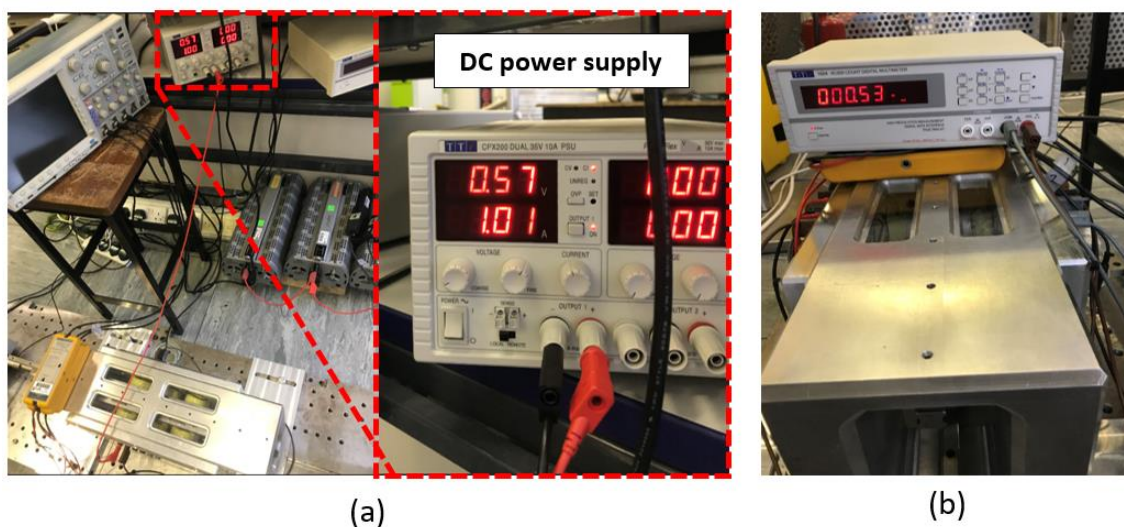


Figure 6. 1: Resistance measurement setup (a) method 1 and (b) method 2

Table 6. 1: Comparison of predicted and measured resistance values of the IMCP machine

Phase #	Resistance value [Ω]				
	FEA	measured method 1	error [%]	measured method 2	error [%]
Phase A	0.53	0.553	4.3%	0.563	6.2%
Phase B	0.53	0.552	4.2%	0.562	6%
Phase C	0.53	0.554	4.5%	0.564	6.4%

6.2.1.2 VCP Machine

To detect any short circuit or open circuit in the coils or phase connection, the resistance measurement was initially performed. As this machine has the same number of turns and conductor diameter as that of the IMCP machine, the measured resistances are expected to be close to that measured early in the previous section. Table 6.2 shows the measured and predicted values of the phases' resistances using the same methods adopted above. From the Table it can be observed that an average error of 4.3% and 6.1% between the predicted and the measured values obtained from the first and second method, respectively, and an average error of 1.8% between the two methods used in this test. However, a good agreement is shown between the predicted and measured values.

Table 6. 2: Comparison of predicted and measured resistance values of the VCP machine

Phase #	Resistance value [Ω]				
	FEA	measured method 1	error [%]	measured method 2	error [%]
Phase A	0.53	0.553	4.3%	0.563	6.2%
Phase B	0.53	0.552	4.2%	0.562	6%
Phase C	0.53	0.554	4.5%	0.563	6.2%

6.2.2 Phase Inductance

6.2.2.1 IMCP Machine

This test was carried out using two methods. In the first method, a variable AC power supply with a frequency of 50Hz was connected across the terminals of a single-phase as shown in Figures 6.2 and 6.3. By measuring the current flowing through the circuit, it is possible to calculate the phase impedance. Using the measured value of the phase resistance for that phase, the inductance was then calculated according to (6.2) and compared to the FEA results. Table 6.3 shows the simulated and measured values of the three phases' inductances.

$$L = \frac{\sqrt{\left(\frac{V}{I}\right)^2 - R^2}}{\omega} \quad (6.2)$$

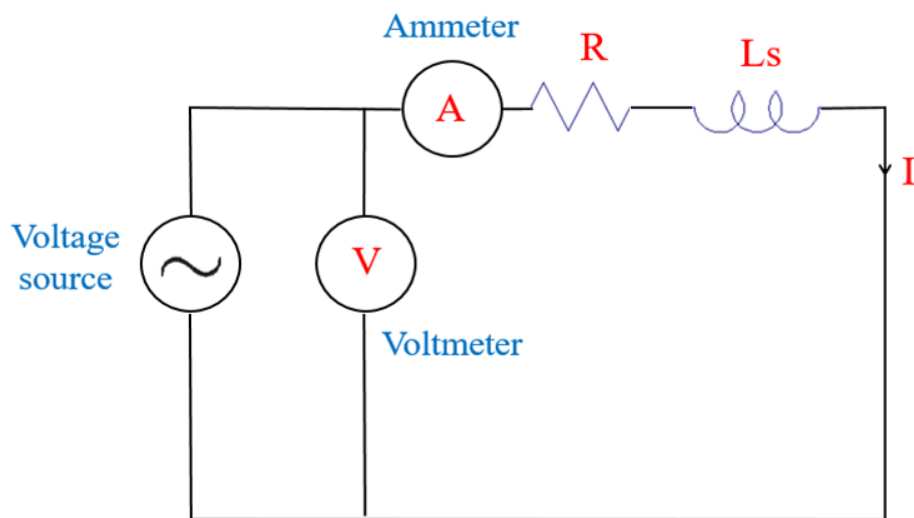


Figure 6. 2: Inductance measurement scheme

In the second method, the phase self-inductances were also measured straightforward using an inductance- capacitance- resistance (LCR meter) shown in Figure 6.4, the measured values are listed in the same Table. It can be seen that there are average error of 4.5% and 5.1% between the predicted and the measured values obtained from the first and second method respectively, with an average error of 0.5% between the two methods. In addition, the measured values for the three phases' inductances are higher than that obtained by the FEA. These differences are attributable to the end effect which is not considered in the 2D-

FEA. These differences are also likely to be due to a combination of the non-uniform nature of hand wound coils and a degree of uncertainty with the prototype airgap.

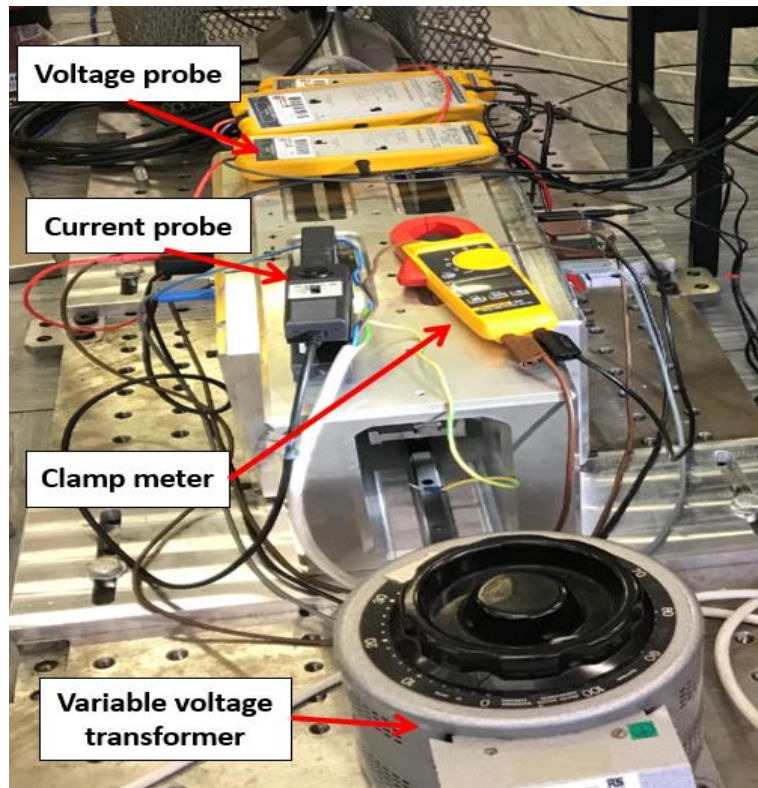


Figure 6. 3: Inductance measurement setup (method 1)

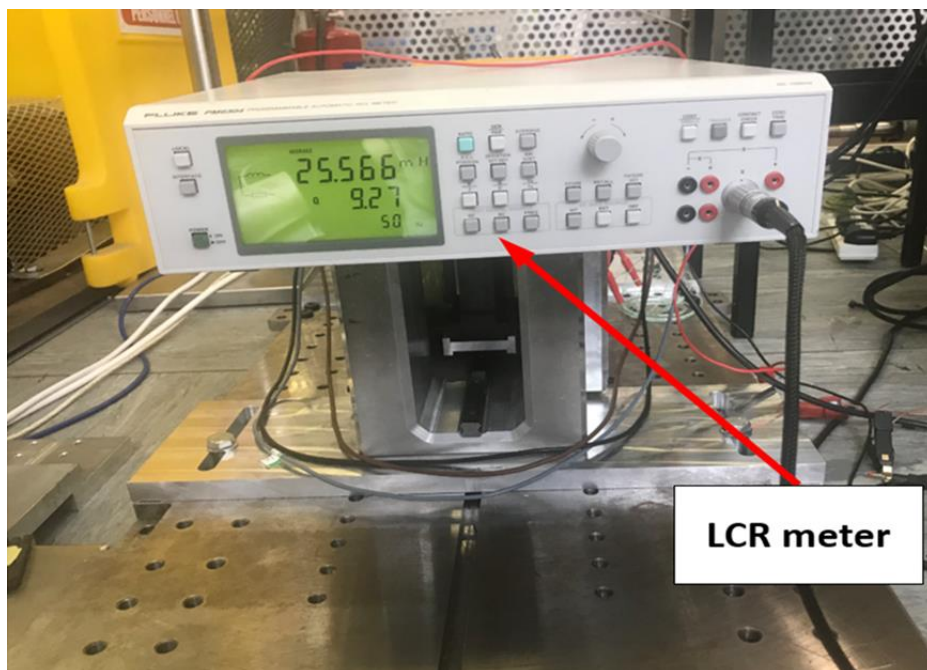


Figure 6. 4: Inductance measurement setup (method 2)

Table 6. 3: Comparison of predicted and measured inductance values of the IMCP machine

Phase #	Inductance [mH]				
	FEA	measured	error [%]	measured [RLC]	error [%]
Phase A	24.3	25.4	4.5	25.7	4.7
Phase B	27.4	28.5	4	28.8	5
Phase C	24.4	25.6	4.9	25.8	5.7

6.2.2.2 VCP Machine

After testing the first prototype (IMCP machine), the stators were replaced with that of the VCP machine. The previous series of tests were repeated and results compared to the simulation data as shown in Table 6.4. Again, the experimental data shows higher inductance values for the three phases compared to the FEA data. The absence of the end effect due to the use of 2D-FEA may contribute to this disagreement.

Table 6. 4: Comparison of predicted and measured inductance values of the VCP machine

Phase #	Inductance [mH]				
	FEA	Measured	error [%]	Measured [RLC]	error [%]
Phase A	24.7	25.5	3.2	25.8	4.4
Phase B	27.8	28.5	2.5	28.7	3.2
Phase C	24.6	25.4	3.3	25.8	4.9

6.3 No-load back EMF

This test was performed to fulfil the following purposes:

- To find the open-circuit induced voltage in the coils at a given velocity.
- To determine the balance between the no-load back EMF of each phase of the machine – this confirms the prototype machines were configured properly.
- To check the variation of the no-load back EMF with respect to the airgap length.

In this test, the prototype was directly driven by a programmable ball screw (actuator) with a maximum velocity of 0.3m/s.

6.3.1 *IMCP Machine*

The variation of the induced no-load back EMF with respect to the translator position is shown in Figure 6.5. These waveforms show very little harmonic distortion but their shapes match well the simulated ones. For a better comparison, the no-load back EMF waveforms obtained from simulation and experimental results for all three phases are plotted on the same graph mentioned above. It can be seen that the peak value of the measured no-load back EMF is 14.2V, 7% lower than that value obtained from the transient FEA. This may be due to a number of reasons:

- The characteristics of the material used in the FEA model may not match the characteristics of the real material used in the prototype.
- The design tolerance in the manufacturing process also plays a significant role, which may result in inaccurate dimensions.

Figure 6.6 compares harmonic spectra for the simulated and measured no-load back EMF. There is some differences between these results; this differences are owing to the variance in the resolution of the data range between the simulated and measured waveforms. In the calculation process of the harmonic spectra, about 1983 data points were used in the measurement, compared to only 253 data points used in simulation for one electrical cycle. A Total Harmonic Distortion (THD) of 3.3% was produced in the measured data, whereas a 4.6% of THD was present in the simulation results for the phase back EMF.

In Figure 6.7 the three-phase waveforms of the no-load back EMF at a constant speed of 0.3m/s are plotted. The three-phase waveforms were captured by an oscilloscope for a stroke of 120mm, which corresponds to five electrical cycles. From the Figure it can be seen that the displacements between all waveforms are identical (120 electrical degrees), which confirm the accuracy of the stator teeth offset. Figure 6.8 shows the similar waveforms at a variable speed with peak value of 0.3/m. It can be seen from the Figure that as the speed increases the effect of the harmonic distortion within the waveforms decreases, hence more sinusoidal waveforms were obtained.

The variation of the no-load back EMF with respect to the speed of the machine will vary linearly with speed due to Faraday's law, as confirmed in Figure 6.9. However, a drop of 7% is seen at the maximum achievable speed by the actuator, compared to the FEA. This difference between the simulated and measured values can be justified as follows:

- The no-load losses produced in the machine increase proportionally as speed rises. They are expected to be more in the experimental results than the predicted ones,

because of the negligible end effect. These losses can lead to an increase in the magnet temperature, which in turn reduces the effective flux, and hence the no-load back EMF.

- The errors in the measuring instruments.

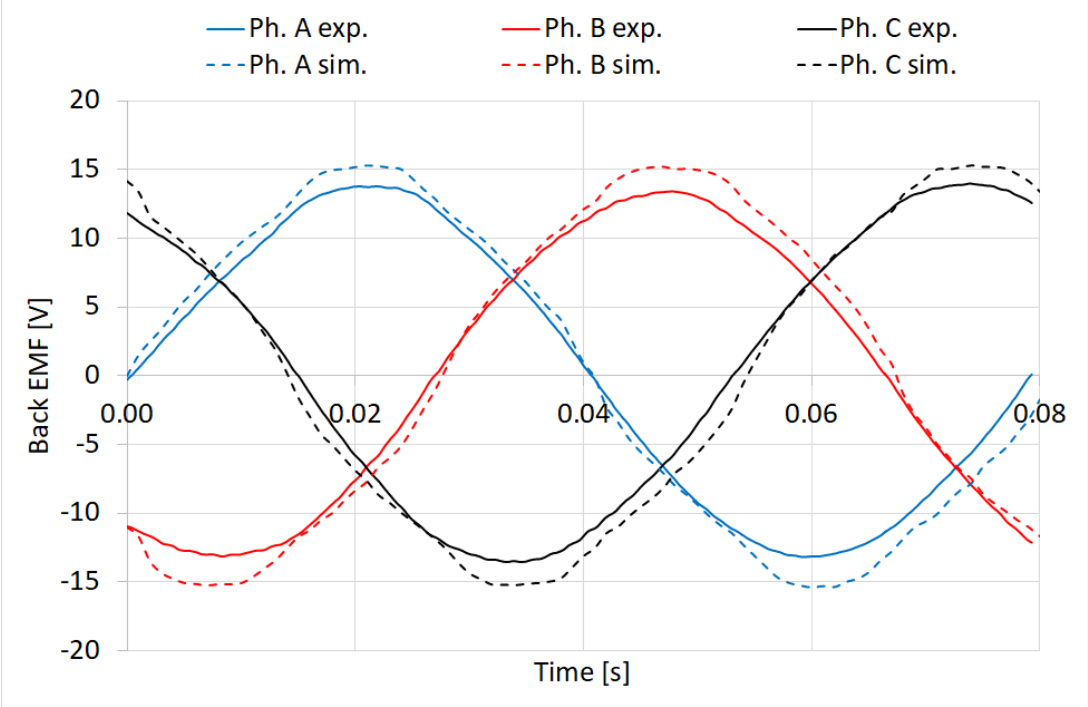


Figure 6. 5: Comparison of predicted and measured no-load back EMF of the IMCP machine at 0.3m/s

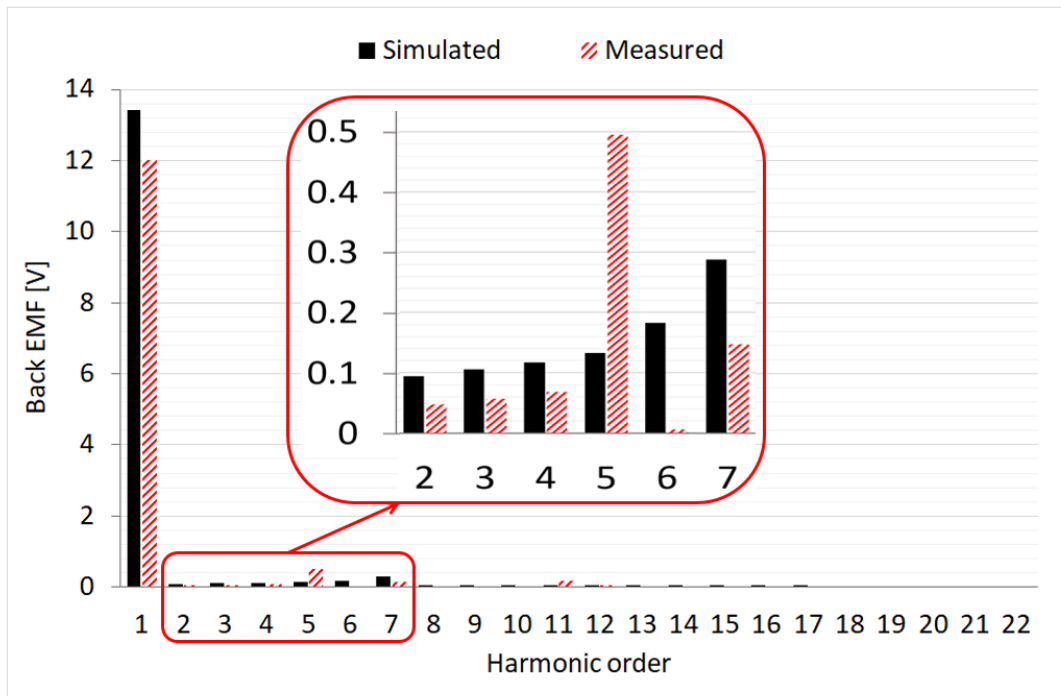


Figure 6. 6: Comparison of predicted and measured harmonic spectra for the IMCP machine

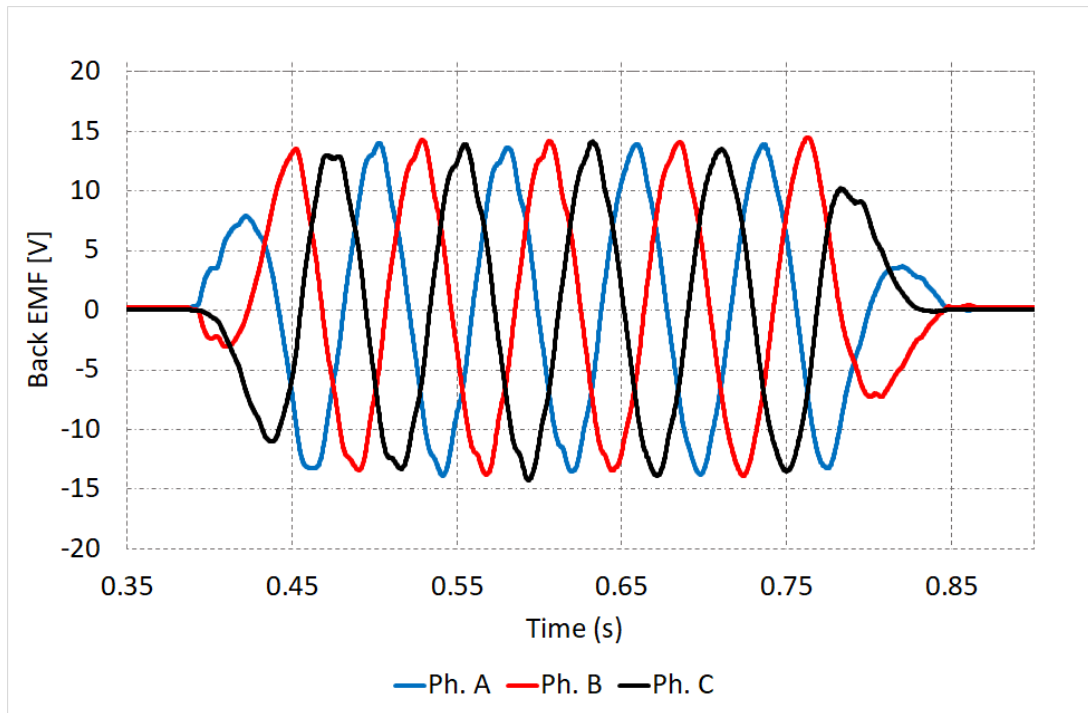


Figure 6. 7: Measured no-load back EMF of the IMCP machine at constant speed of 0.3m/s for one stroke, 120mm

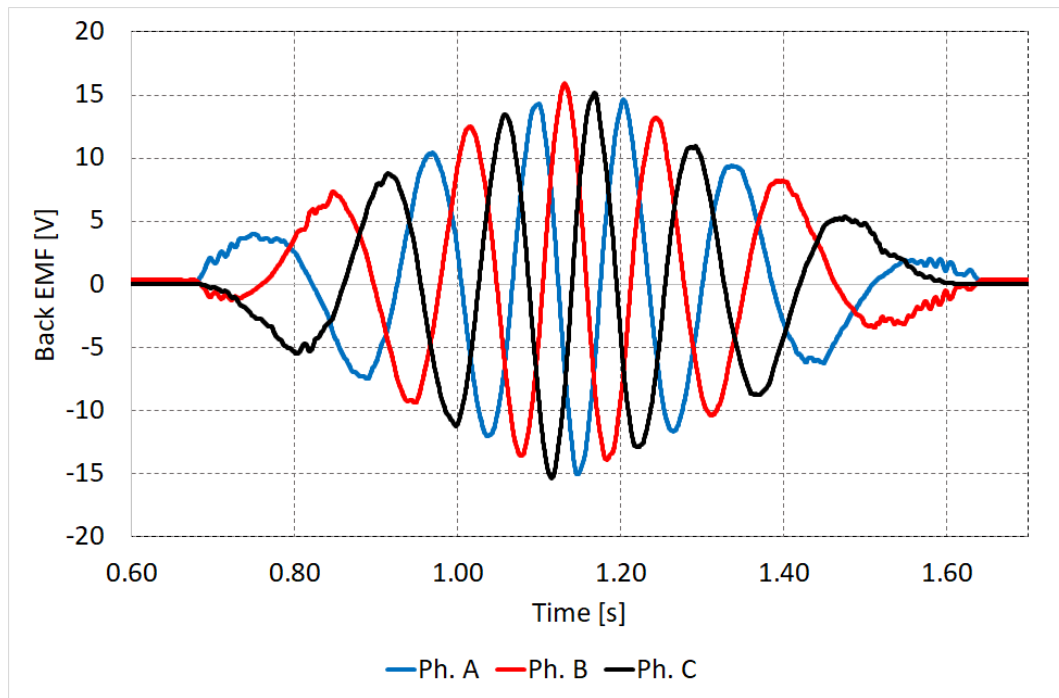


Figure 6. 8: Measured no-load back EMF of the IMCP machine under variable speed for one stroke, 120mm

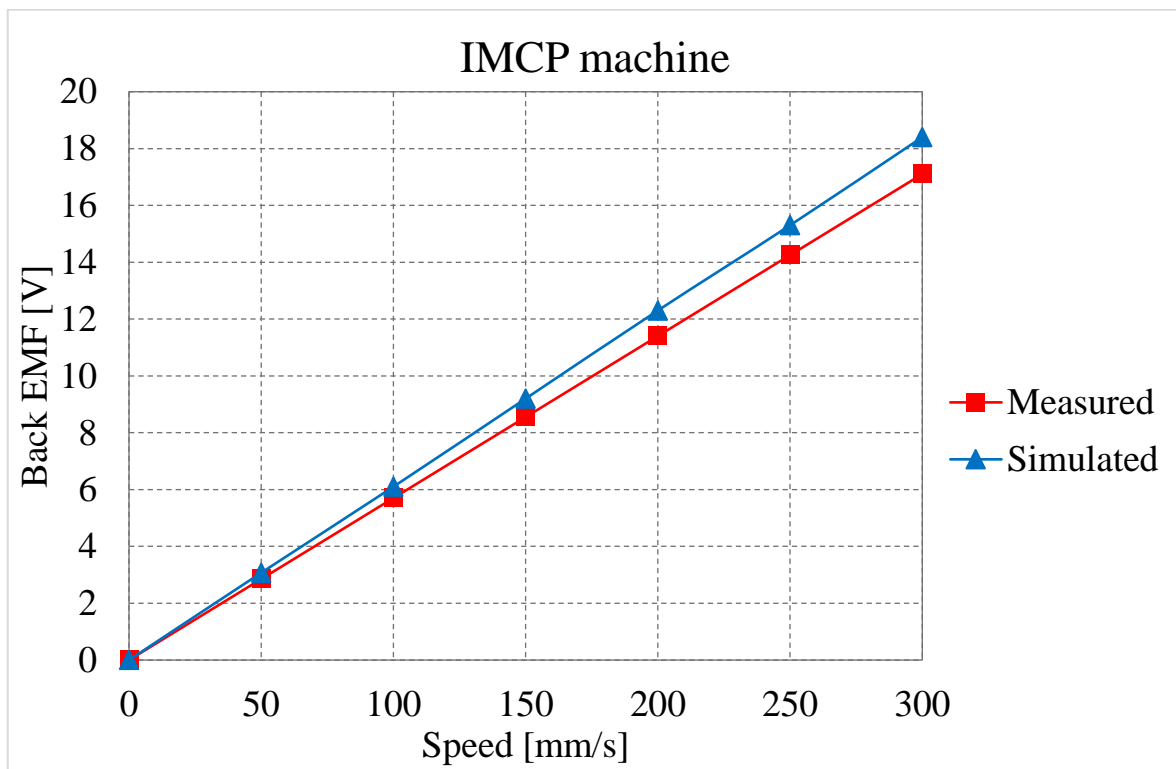


Figure 6. 9: Voltage-speed characteristics at open circuit for the IMCP machine

Since the prototype possesses the feature of adjusting the airgap length, the effect of varying the airgap length on the induced back EMF was investigated and the results are summarised in Table 6.5. As expected from theory, with a small airgap the fringing and leakage fluxes are reduced leading to an increase in the main flux that links the stator winding. Hence, as the airgap length decreases the induced back EMF is increased as a consequence. It can be seen in the Table that at a 3mm airgap the error between the simulated and experimentally measured values for RMS no-load back EMF is about 15.8%. However, as the airgap length gets smaller, the error gradually decreases, where only 9.4% error is shown at 1mm airgap.

Table 6. 5: Variation of the no-load back EMF with different airgap length for IMCP machine

Airgap length [mm]	Back EMF RMS[V]		Error [%]
	2D-FEA	measured	
1	10.6	9.6	9.4
2	6	5.4	10
3	3.8	3.2	15.8

6.3.2 VCP Machine

Figure 6.10 shows the no-load back EMF waveforms for the VCP topology obtained from simulation and experimental data at 0.3m/s according to the capability of the actuator. It can be seen that these waveforms are symmetrical and have identical oscillation, and are of a similar shape to those obtained from the transient FEA. The tendency to symmetry and sinusoidal shape resulted from the near absence of the 5th harmonic in the harmonic spectra analyses. In the measured results of the phase back EMF, the 7th harmonic is the predominant harmonic after the fundamental, which represents about 1% of the fundamental as shown in Figure 6.11. As in the IMCP topology, when the line back EMF is considered, the triplen harmonics are eliminated. A THD of 2.3% was presented in the simulated results compared to only 1.6 % in the measured results. An error of 6.6% is shown between the simulated and measured results, in which the simulated is higher than the measured value.

This is a 120° phase shift between the three phases; this means that 0°, 120°, 240°, corresponding to 8mm mechanical displacements between the stator teeth resulted in a set of balanced voltages with the right phase shift.

The three-phase no-load back EMF waveforms measured across three adjacent coils at variable speed were also captured using a Techtronix oscilloscope as shown in Figure 6.12. It can be seen that as the speed increases, the phase back EMFs are approaching sinusoidal waveforms.

Table 6.6 shows the effect of varying the airgap length on the induced no-load voltages. It can be seen that the discrepancy between the simulated and measured results increases as the airgap length increases.

In order to obtain the open circuit characteristics, the phase no-load back EMF was measured with the two coils of each phase connected in series. This was conducted over a range of speeds resulting in characteristics shown in Figure 6.13. As expected, the simulated and measured induced no-load back EMFs are increased proportionally with speed. However, the error between the simulated and measured results increases with speed, which is attributable to the no-load losses.

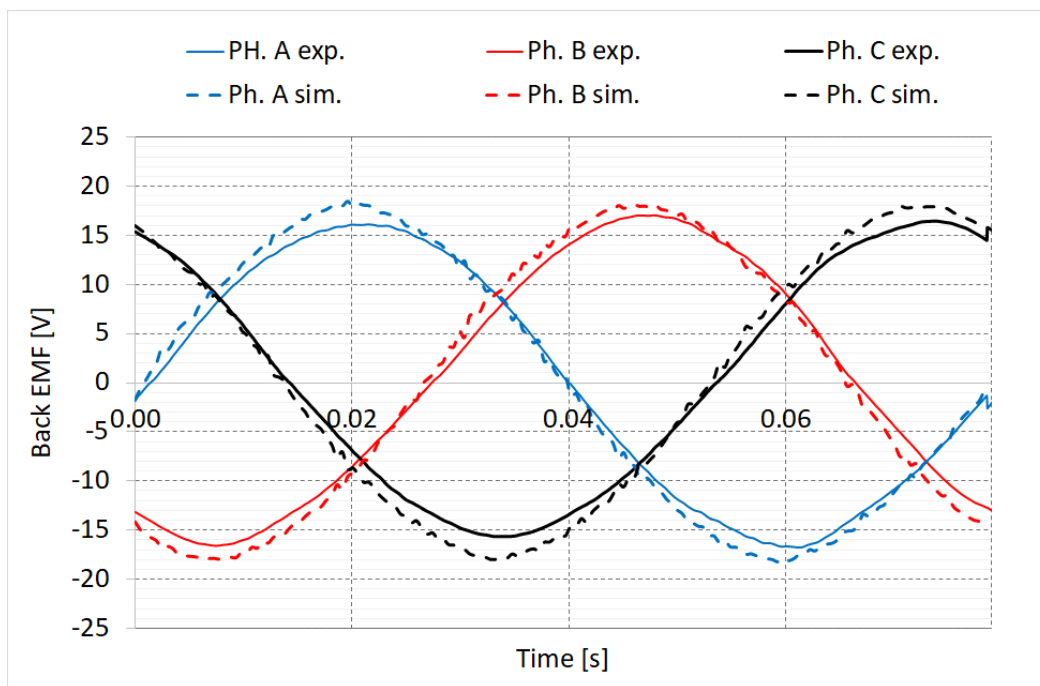


Figure 6. 10: Comparison of predicted and measured no-load back EMF of the VCP machine at 0.3m/s

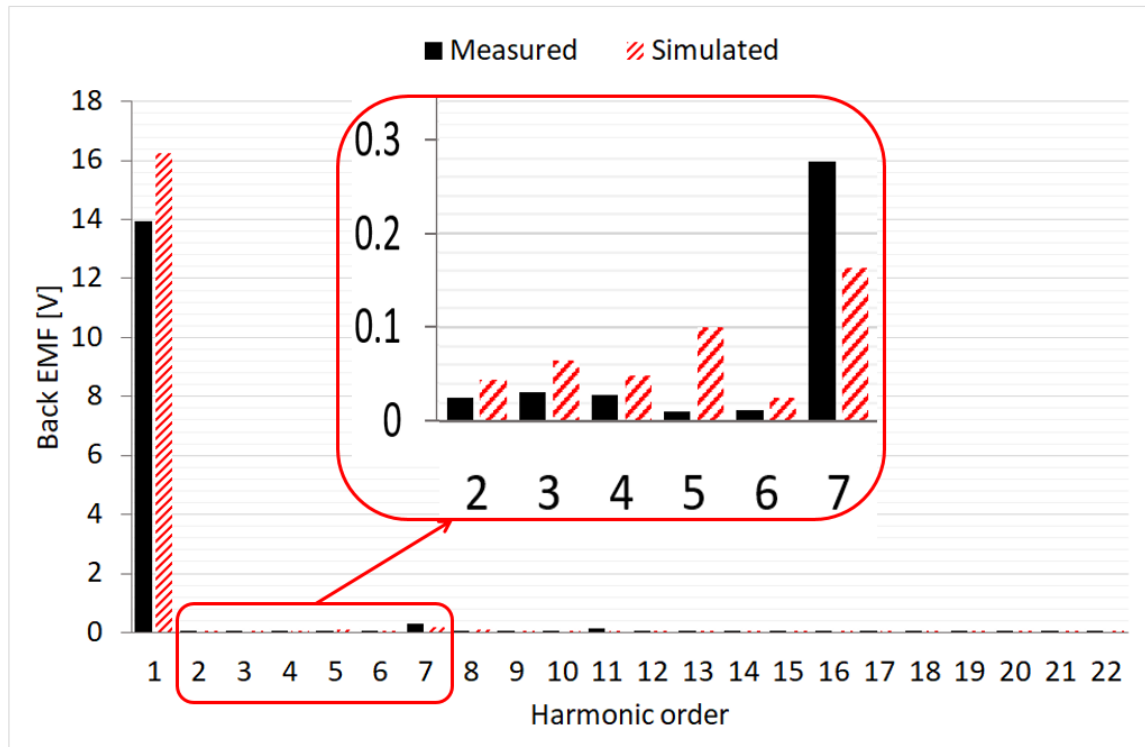


Figure 6. 11: Comparison of predicted and measured harmonic spectra for the VCP machine

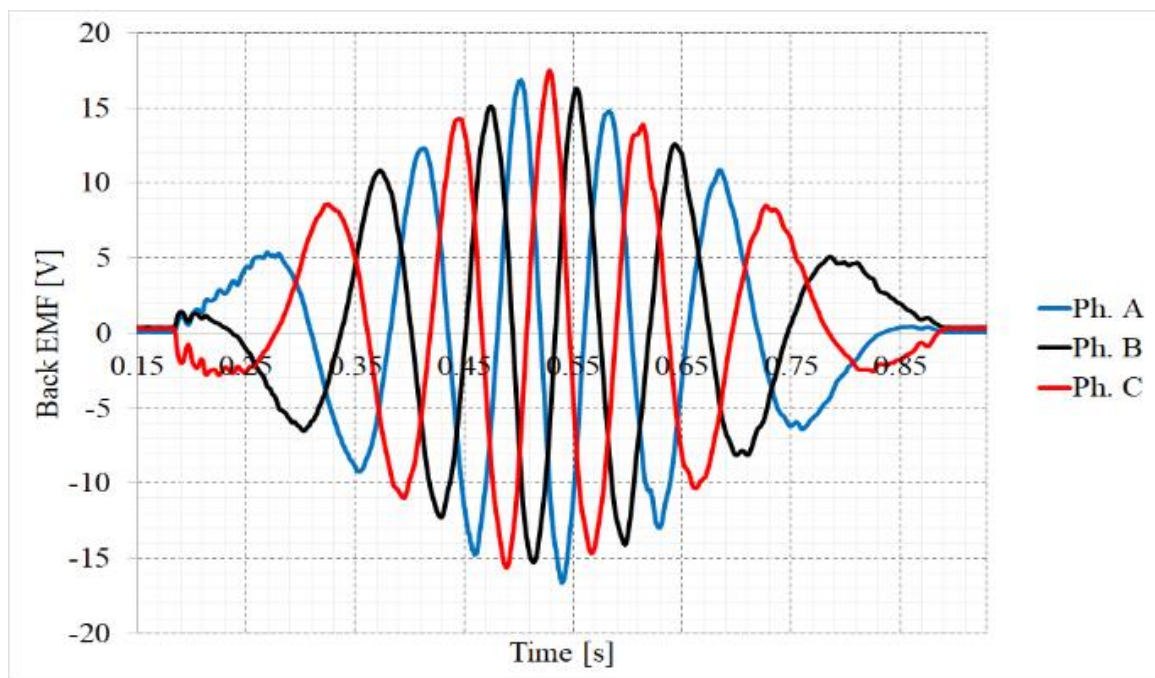
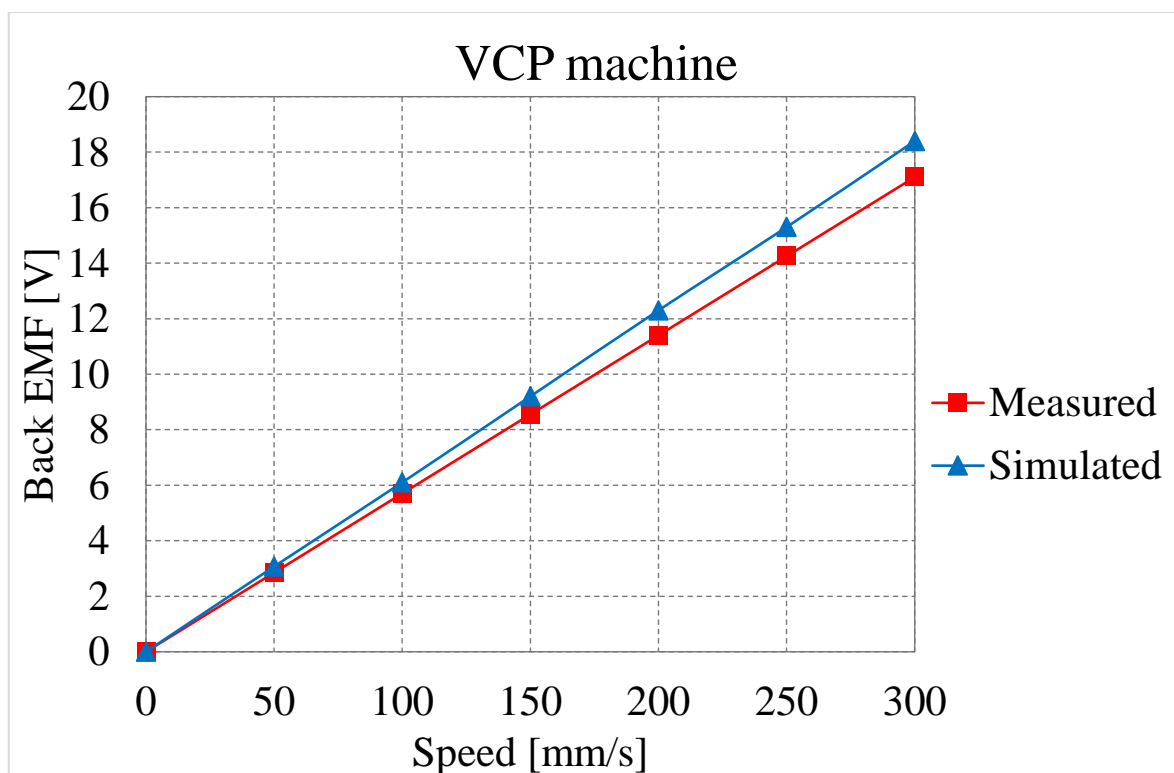


Figure 6. 12: Measured no-load back EMF of the VCP machine under variable speed for one stroke, 120mm

Table 6. 6: Variation of the no-load back EMF with different airgap length for VCP machine

Airgap length [mm]	Back EMF RMS[V]		Error [%]
	FEA	measured	
1	12.5	11.6	7.2
2	6.3	5.6	11
3	3.7	3.1	16.2

**Figure 6. 13: Voltage-speed characteristics at open circuit for the VCP machine**

6.4 Cogging Force

The cogging force characteristics for both prototypes were taken over one translator tooth pitch (360 electrical degrees, corresponding to 24mm). The complete test rig is shown in Figure 6.14; the generator was coupled through the in-line force transducer to a ball screw actuator, which locks the translator in position and allows for fine small movements of the translator, i.e.1mm.

The force transducer output is a voltage which is proportional to the measured force. The measured voltage values were multiplied by the ratio of (2000/1.983), as recommended by the manufacturer of the force transducer, allowing the force to be calculated.

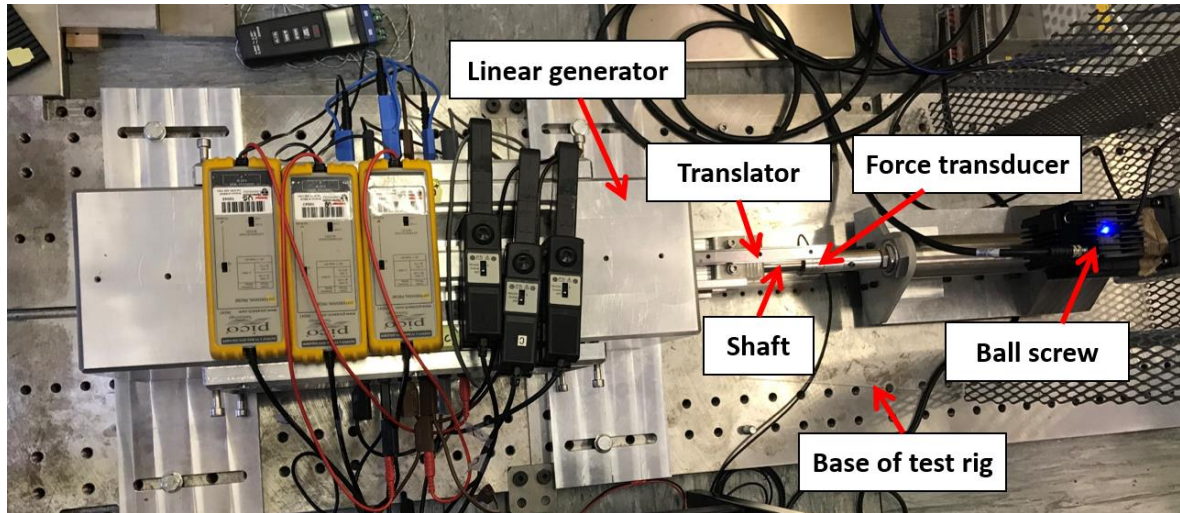


Figure 6. 14: Complete test rig

6.4.1 IMCP Machine

In this test, the variation of the cogging force with respect to the translator position is investigated as shown in Figure 6.15. The measurement of the cogging force was performed without injecting current to the stator winding. The translator was directly driven by the programmable actuator with an interval of 1mm. With the aid of the force transducer connected to the shaft, the measurement was recorded at each position over one electrical cycle, corresponding to a displacement of 24mm. The output of the force transducer is a voltage proportional to the measured force. As can be seen in Figure 6.15 only a positive net force was obtained from the experimental results. However, by removing the offset from the measured values, the agreement between the simulated and measured results is very good as verified in Figure 6.16. The offset occurred in the experimental data can be resulted from the friction losses. However, no further investigation on this was made.

Moreover, the amplitude of the measured results is slightly lower than that obtained from the FEA. The difference between both results can be justified as follows:

- The force transducer and its cable are very sensitive to any slight touch or movement, which in turn may negatively affect the measured values.
- An inaccuracy of the translator position, as the translator was moved by an interval of 1mm for each step, the interaction between the magnets and translator teeth can influence

its desired position, for example, when the actuator was programmed to move the translator by 5mm, the actual displacement appeared on the Tolomatic software was 5.1mm, indicating that the translator position was affected by the magnetic force.

- The errors in the measuring instruments.

The effect of varying the airgap length on the cogging force is also investigated in this study. Using the adjustable screws distributed around the aluminium stator support, the airgap length was varied from 1mm to 3mm, with a step of 1mm. The obtained results are listed in Table 6.7. From the Table it can be observed that as the airgap length increases, the peak to peak values of the cogging force are reduced.

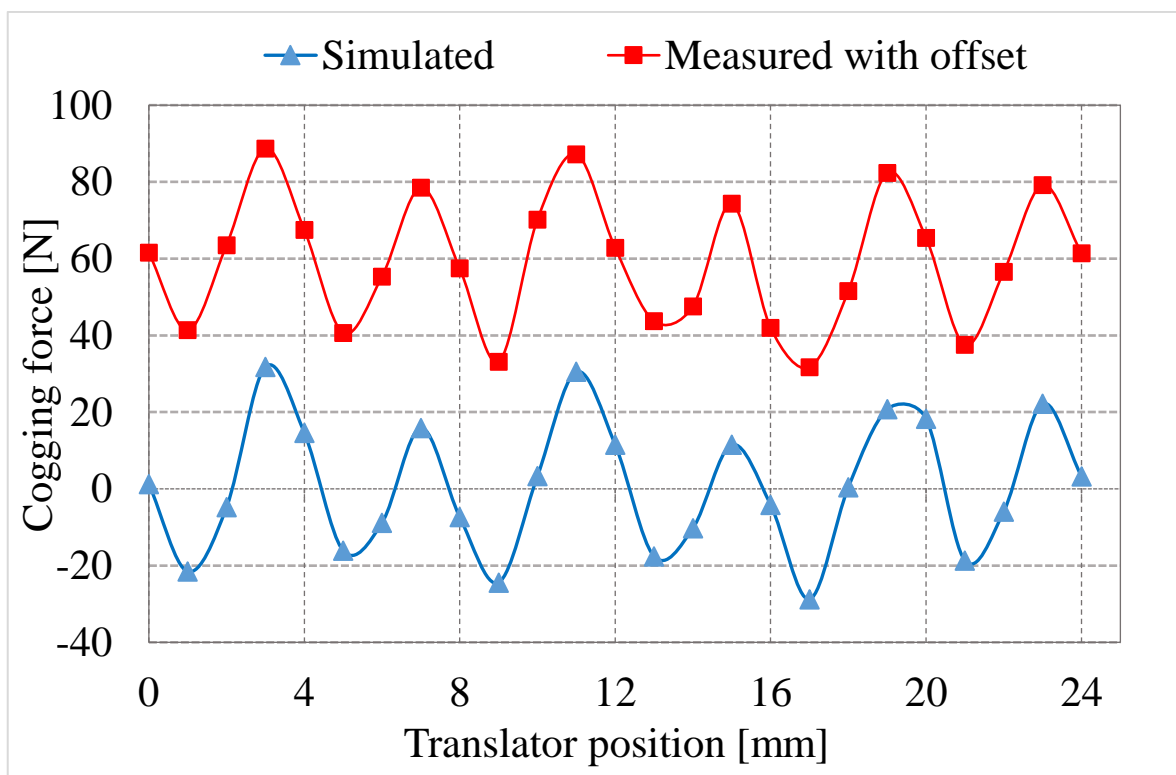


Figure 6. 15: Variation of the measured cogging force of the IMCP machine with translator displacement over two pole pitches with offset

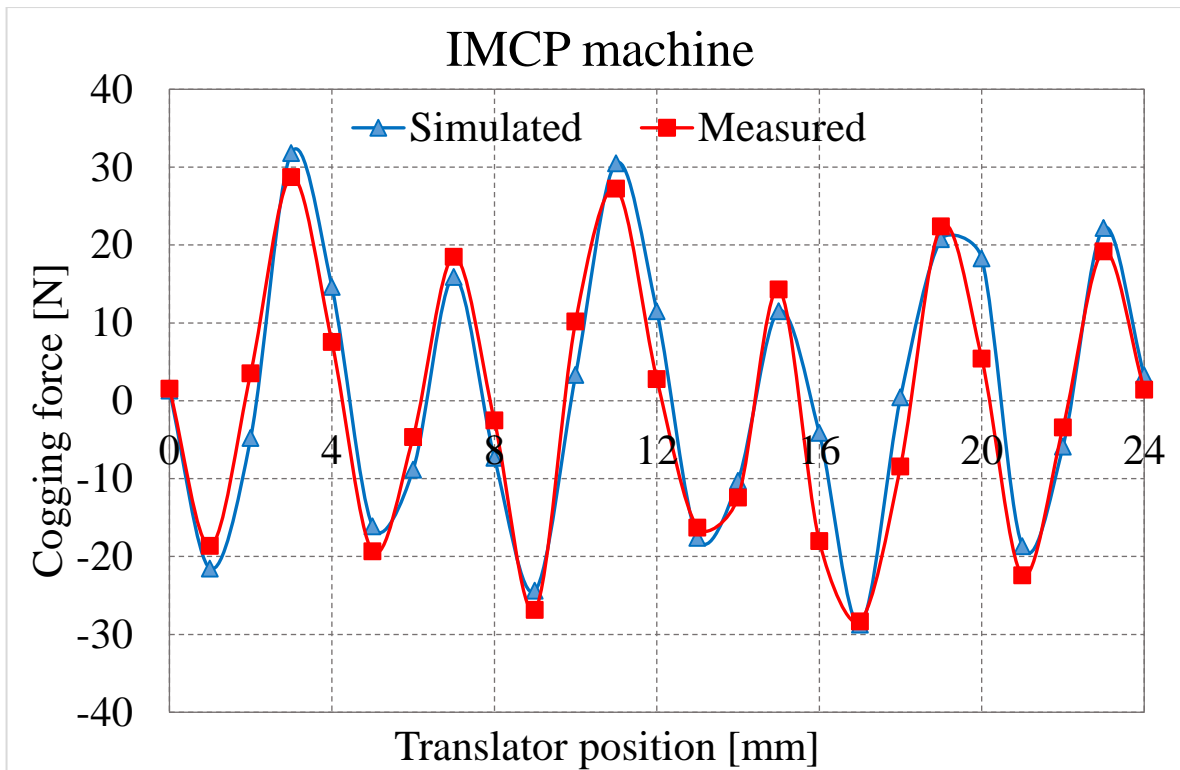


Figure 6. 16: Comparison of predicted and measured cogging force of the IMCP machine after removing the offset

Table 6. 7: Variation of the cogging force with different airgap length for IMCP machine

Airgap length [mm]	Peak-Peak cogging force[N]		
	FEA	measured	Error [%]
1	62	57	8
2	29	26	10.3
3	16	12	15

6.4.2 VCP Machine

The measured cogging force waveform for the VCP machine is shown in Figure 6.17 and compared to that obtained from static simulation results. As can be seen in the Figure both results show a good correlation, where variations of both waveforms with respect to the translator position are very similar, with an error of 5.9% between the peak to peak values of both results, in which the measured magnitude being slightly lower than that of the simulated one. This difference is believed to be due the same reasons stated for the IMCP topology discussed earlier in the previous section.

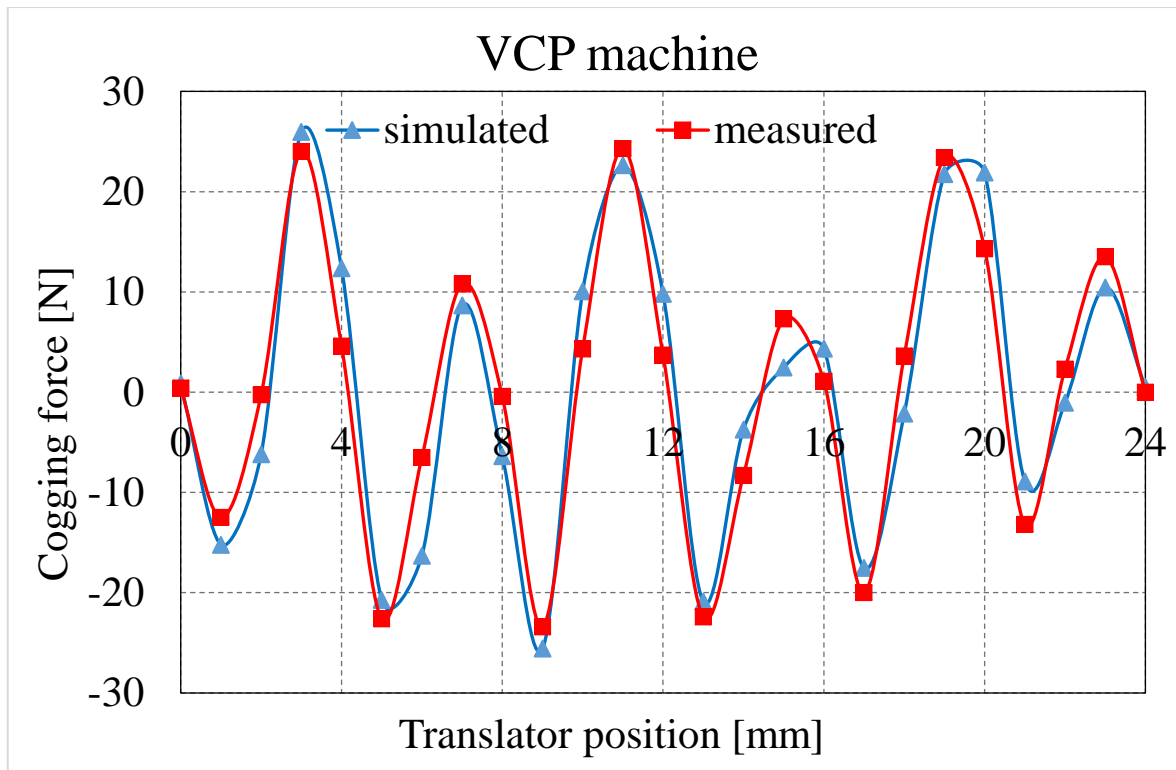


Figure 6. 17: Comparison of predicted and measured cogging force of the VCP machine after removing the offset

Table 6.8 demonstrates the simulated and measured peak to peak values of the cogging force under different airgap length. It can be seen that as the airgap length increases the magnitude of cogging force decreases.

Table 6. 8: Variation of the cogging force with different airgap length for VCP machine

Airgap length [mm]	Peak-Peak cogging force[N]		
	FEA	measured	Error [%]
1	51	48	5.9
2	27	24	11
3	14	12	14.3

6.5 Force Production

The static force characteristics for both prototypes were taken over one translator tooth pitch (360 electrical degrees, corresponding to 24mm). The DC force setup shown in Figure 6.18 was used to perform this test. The stator windings were connected as per the diagram shown in Figure 6.19. As it can be seen from the Figure the end terminals for all phases are short circuited and the start terminal of phase-A winding is connected to the positive terminal of the DC supply, while phases B and C are connected in parallel in which their common start terminals are connected to the negative terminal of the DC supply. This connection allows a 11A to flow through phase A, while half of this value flows through phases B and C in a negative direction. This current distribution represents an instance of a sinusoidal current injected to the stator windings. After that, the translator was driven slowly with a step of 1mm and the static force was measured by the force transducer at each step over a full translator tooth pitch.

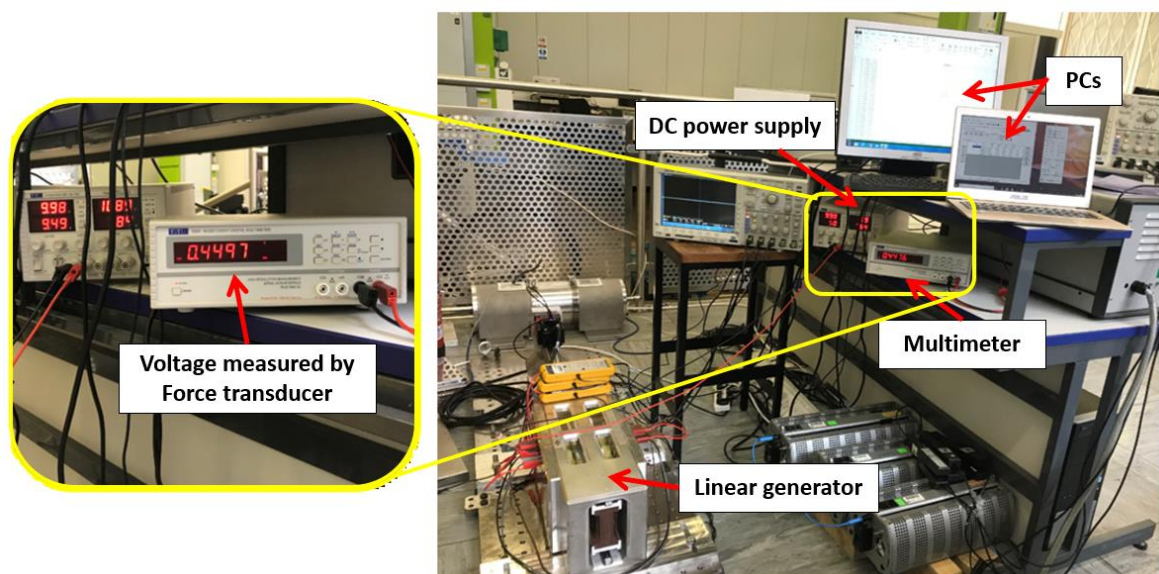


Figure 6. 18: Static DC force measurement setup

6.5.1 IMCP Machine

Figure 6.20 compares between the obtained experimental and the predicted results. As can be seen from the Figure, the experimental results agree well with the simulated results with an error of 6.8%. This is potentially due to the drop in the open-circuit voltage that has been justified in section 6.3.1.

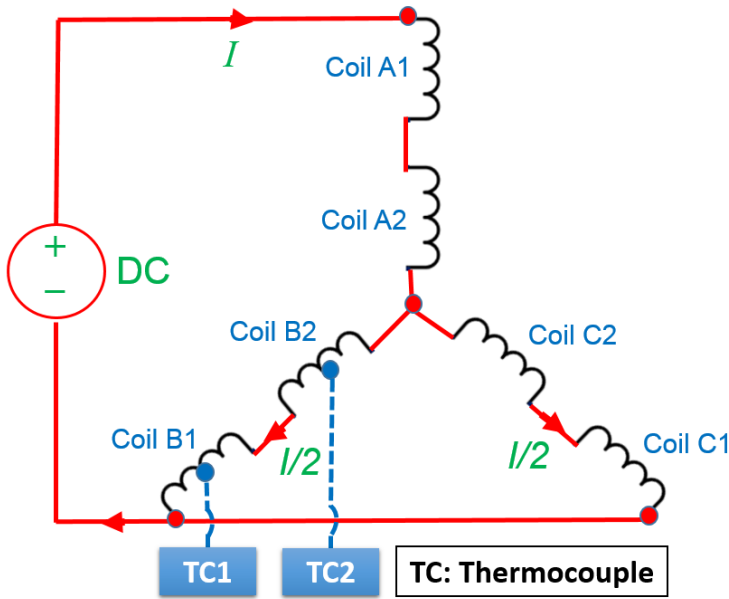


Figure 6. 19: Winding connection diagram used for static DC force measurement

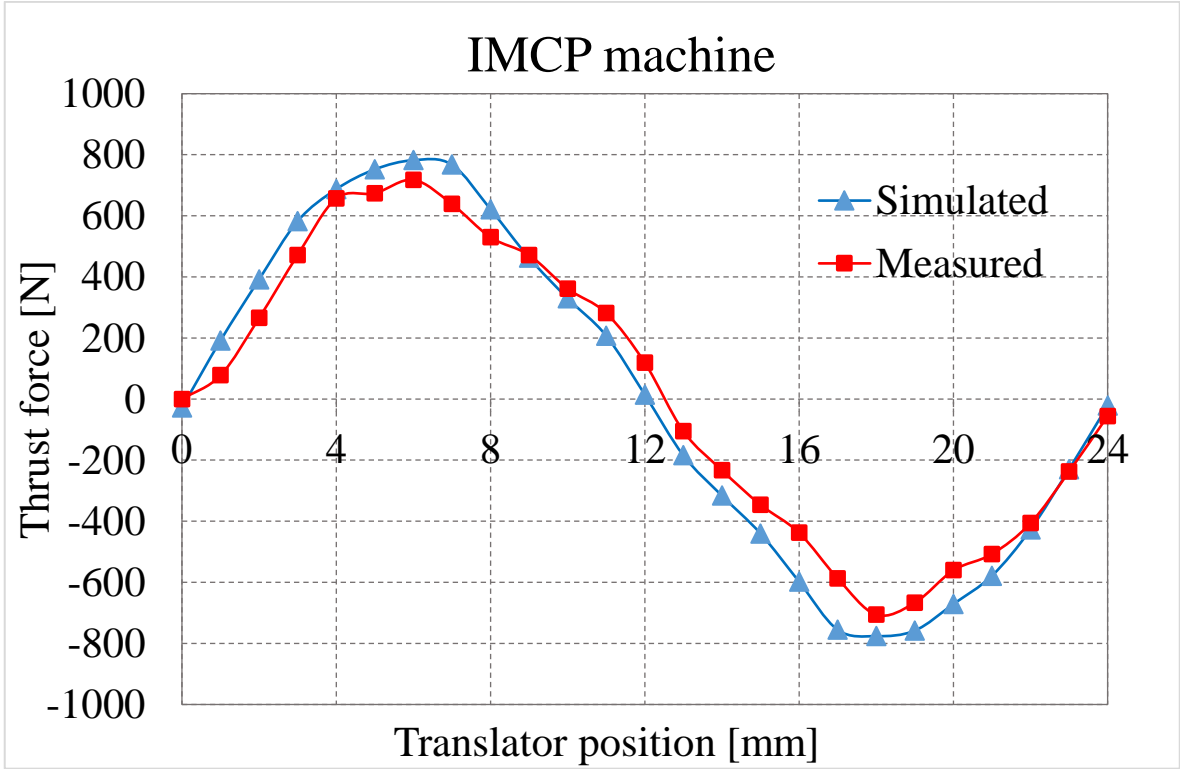


Figure 6. 20: Comparison of predicted and measured static DC force of the IMCP machine

6.5.2 VCP Machine

This test was performed in the exact same manner adopted earlier in the previous section. Figure 6.21 shows a comparison of the experimentally measured values for static DC force to that predicted by the FEA simulation. Overall, the measured values closely match the simulated values, the peak values in particular, with an error of 4.6 % under the armature current of 10A, in which the highest values were seen in simulation results.

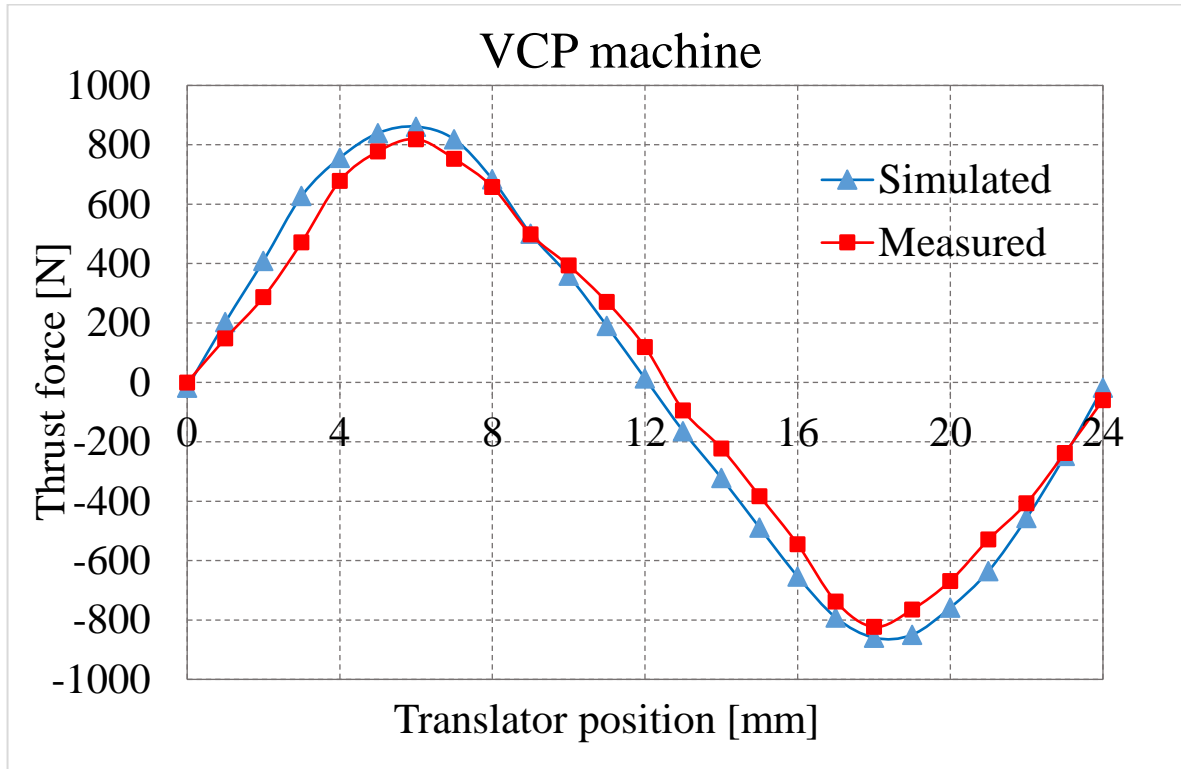


Figure 6. 21: Comparison of predicted and measured static DC force of the VCP machine

6.6 Force Variation with Current

Force capability of the machine is one of the key points of interest of the experimental tests. In order to perform the force capability measurements, the previous test was repeated here over a range of DC excitation currents using a variable DC power supply. The applied DC current was varied from 0 to 20A with a step of 2.5A. The force transducer was used to measure the linear force produced by both machines.

6.6.1 IMCP Machine

Figure 6.22 illustrates the current-force curve for both simulated and experimental results. The Figure shows the variation of the static DC force with respect to the applied DC current (up to 20A), where the force varied linearly against the applied currents until the current reaches its rated value. As the machine overloaded further, non-linearity is shown in

this relationship as a result of the magnetic saturation. It can be also observed that there is a very good agreement between the predicted and measured results, which validates the result obtained from the FEA model. Any remaining prediction errors can be attributed to inaccuracies in measurement due to the transducer tolerance, human error and manufacturing tolerances.

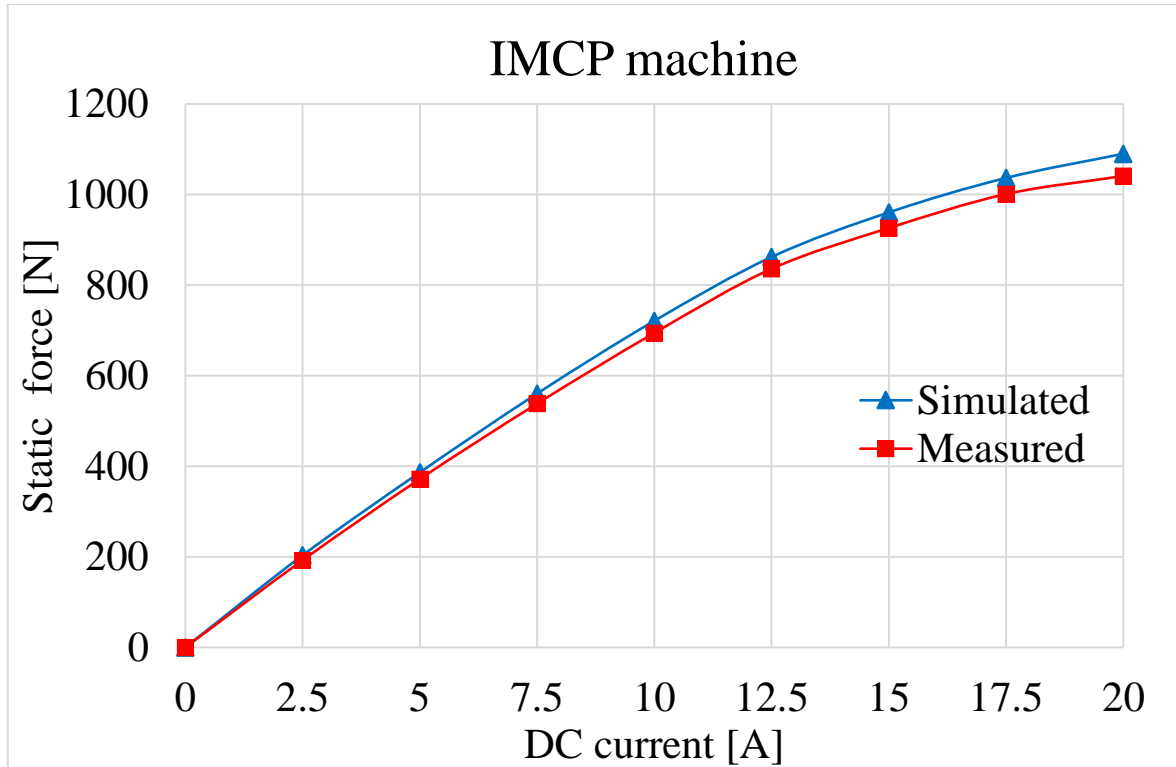


Figure 6. 22: Comparison of predicted and measured static DC force of the IMCP machine under different excitation currents

6.6.2 VCP Machine

In this test, the processes implemented in the previous section were repeated again. It can be seen that the force measured throughout the experiment increases linearly with the applied DC current. The rise in the force is expected to continue at the same rate up to 11A before the consequent poles start to saturate. After which, due to the saturation effect the force variation becomes non-linear when the applied current exceeds its rated value. A comparison between the simulated and measured results is plotted in Figure 6.23. From the Figure it can be observed that the prototype achieved reasonable force values against the applied current in comparison with the simulated ones, with a maximum error of 2.4%.

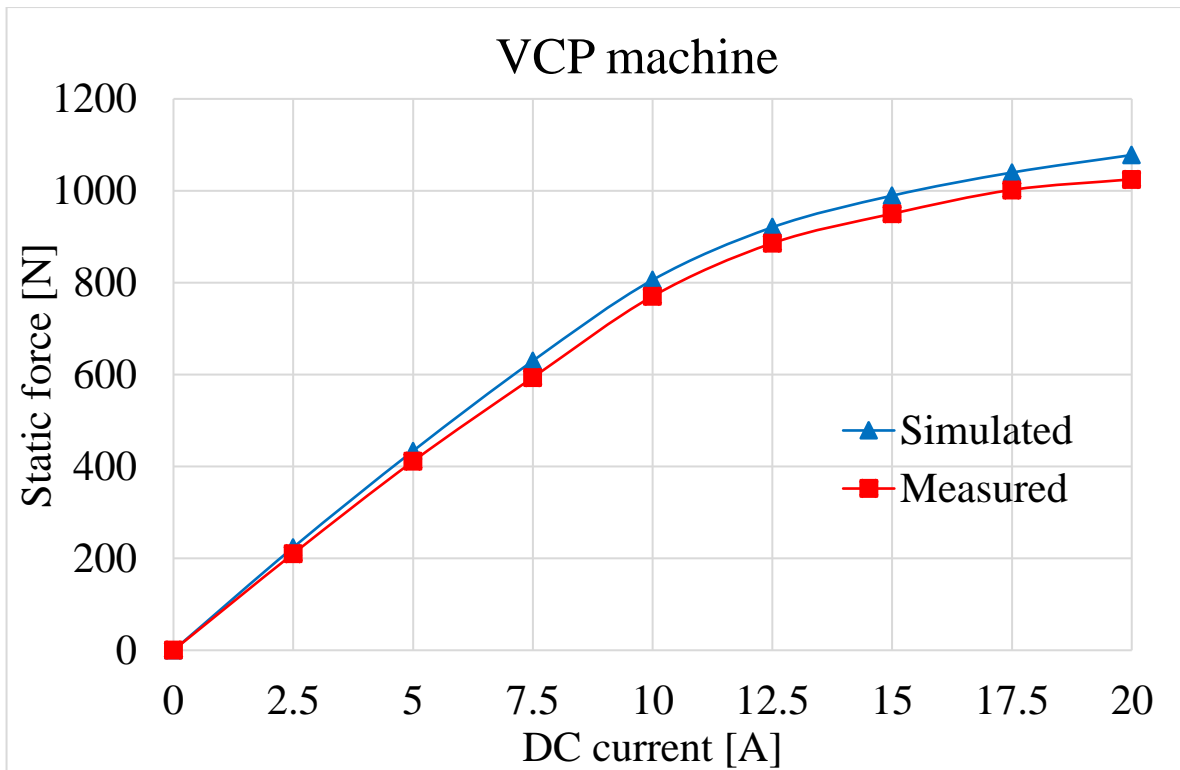


Figure 6. 23: Comparison of predicted and measured static DC force of the IMCP machine under different excitation currents

6.7 Resistive Load Tests

In these tests, the IMCP and VCP prototypes were connected to a star-connected three-phase resistive load as shown in Figures 6.24 and 6.25. According to theory the maximum power transfer occurs when the load impedance equals to the machine internal impedance. In order to find the maximum output power of the IMCP and VCP machines, the machines should be tested under the rated speed operation, 1.2m/s. However, due to the speed limitations of the actuator, the machine was tested at maximum achievable velocity of 0.3m/s. The resistive load R_L was varied within the range of 0 to 8Ω and the maximum power was measured at a steady state. The obtained findings will be discussed in the next two subsections

6.7.1 IMCP Machine

Figure 6.26 shows the variation of the machine output power as a function of the applied load. It can be seen from the Figure that the maximum output power that can be achieved is 65W when the machine was loaded with a resistive load of $R=3\Omega$. At a resistive load, power is inversely proportional to the value of the load resistance (i.e. $P=V^2/R$). Thus, the output power decreases and then stabilizes with a gradually increasing load.

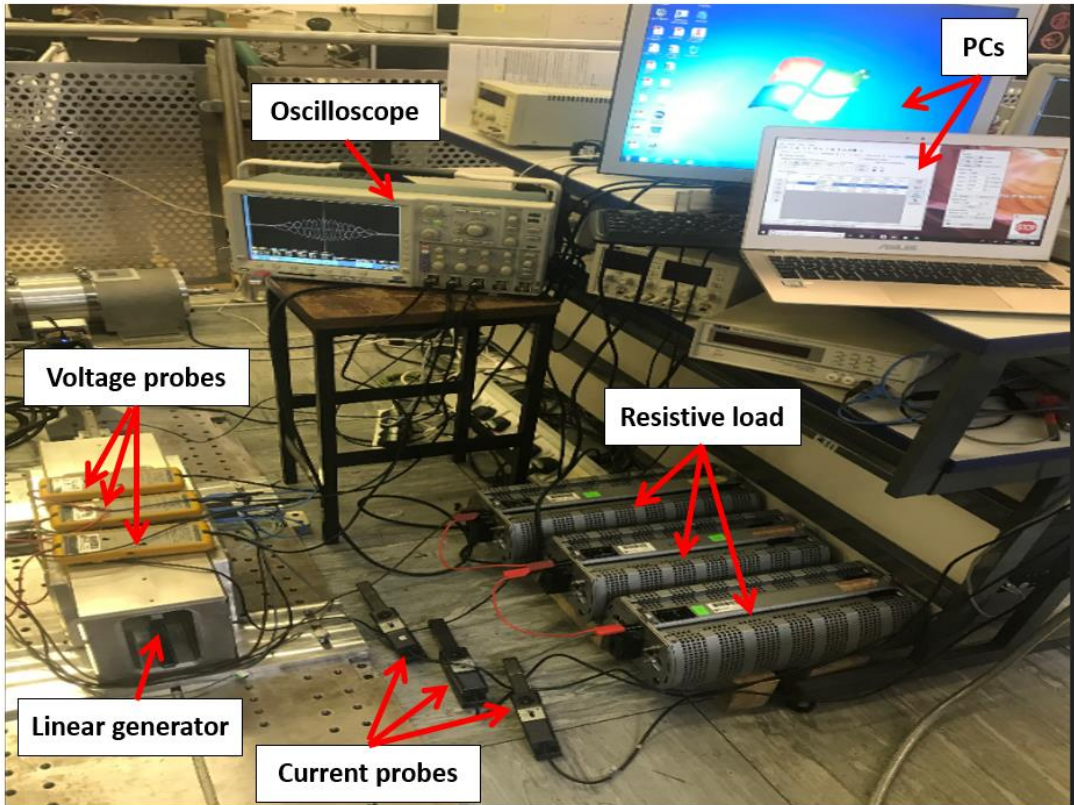


Figure 6. 24: Resistive load tests measurement setup

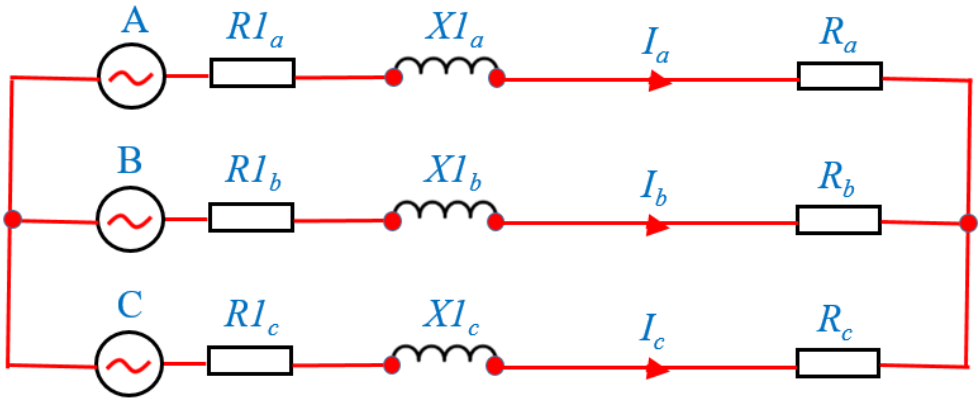


Figure 6. 25: Generator equivalent circuit connected to a 3-phase resistive load

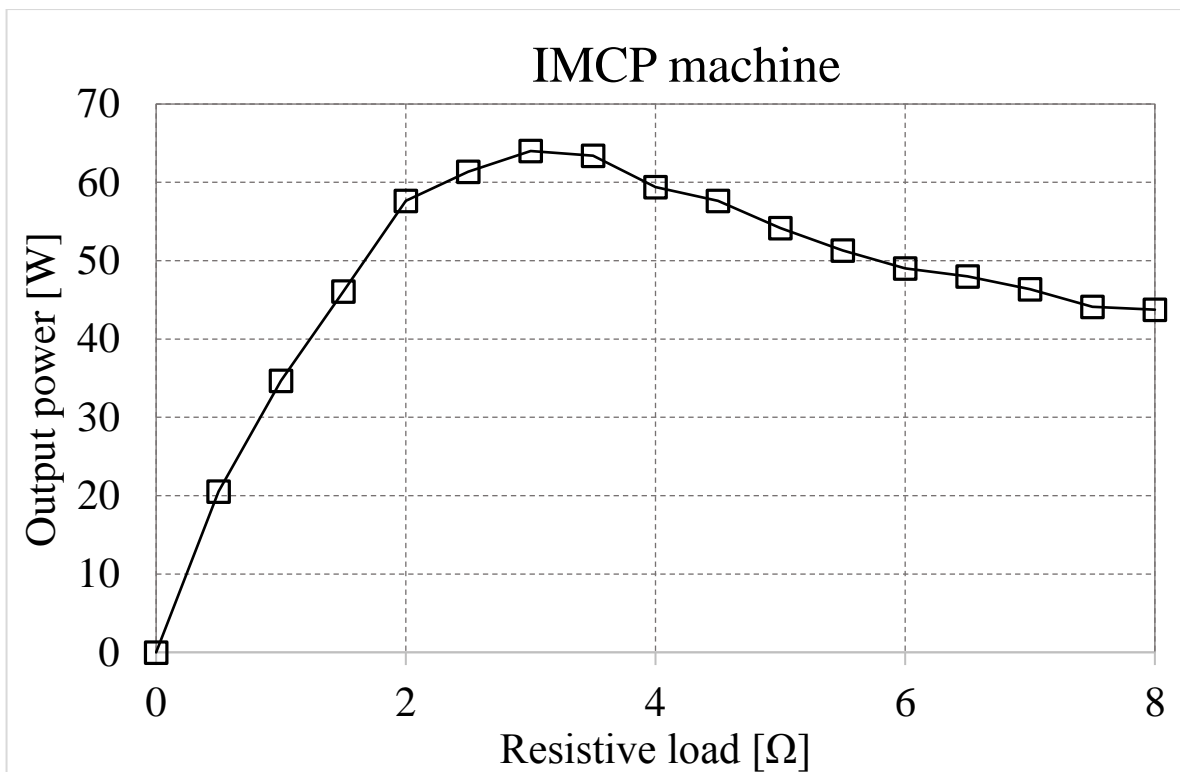


Figure 6. 26: Variation of the output power of the IMCP machine under different resistive loads

6.7.2 VCP Machine

The VCP machine was tested following the same procedures described in the previous section. The load was varied from 0 to 8Ω, with an interval of 0.5Ω. Figure 6.27 shows the variation of the output power as a function of load. It can be seen that the maximum power occurs when the load is $R= 3\Omega$, with the value of 73W. This gives an indication of the improvement in the output power compared to the IMCP machine. This is attributed to the increase in the open-circuit voltage.

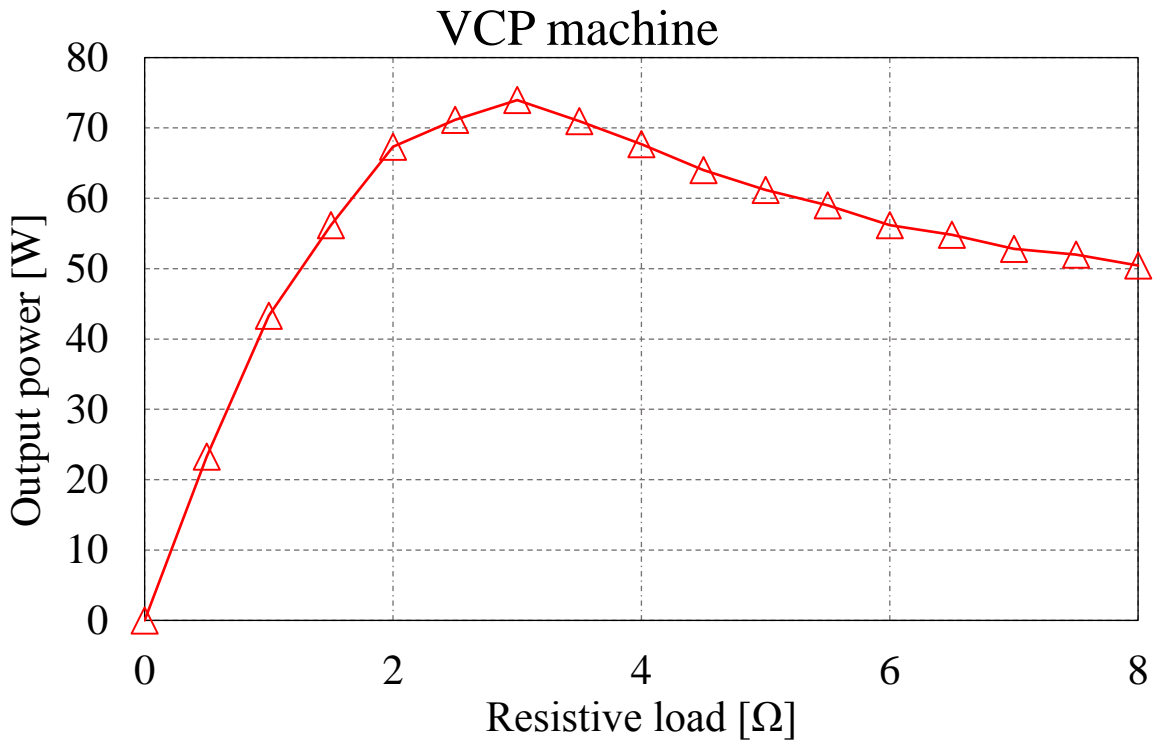


Figure 6. 27: Variation of the output power of the VCP machine under different resistive loads

6.8 Thermal Performance

In order to be able to observe and record the coils operating temperature point, the IMCP and VCP prototypes were fitted with three thermocouples as shown in Figure 6.28. One thermocouple is attached to the conductor of the middle coil, allowing the temperature measurements to be performed at the hottest point of the coil. The other two are attached to the magnet surface/ the surface of the stator tooth and the aluminium case of the machine. The hot-spot temperature of phase-A under a DC current of 7.8A, for a period of four hours was investigated, in which the test was carried out at the room temperature ($\approx 20\text{ }^{\circ}\text{C}$).

6.8.1 IMCP machine

Figure 6.29 shows the phase temperature obtained from the experimental test stabilised to a temperature of almost $77\text{ }^{\circ}\text{C}$, while the temperature of the magnet surface and the aluminium case stabilised to a temperature of almost $54\text{ }^{\circ}\text{C}$ and $50\text{ }^{\circ}\text{C}$, respectively. Taking into consideration the temperature rating of $220\text{ }^{\circ}\text{C}$ for both the insulation class of the copper used in the prototype, and the thermal paste used for potting, which indicates that this temperature can be considered as safe.

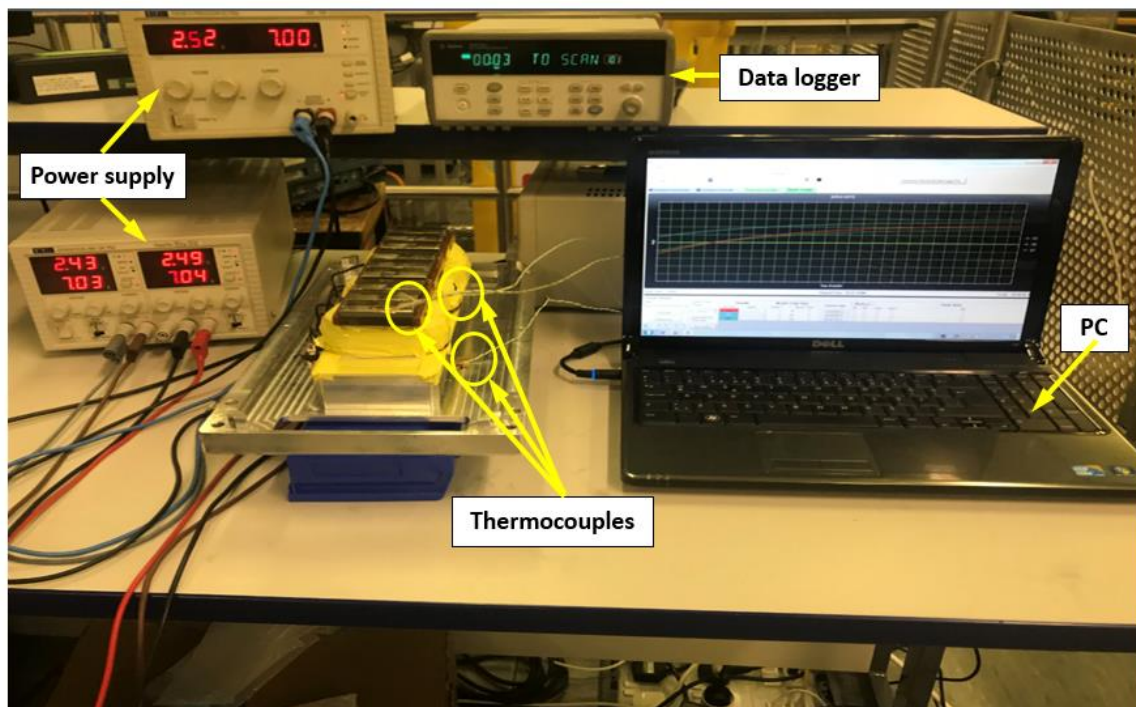


Figure 6.28: Thermal test measurement setup

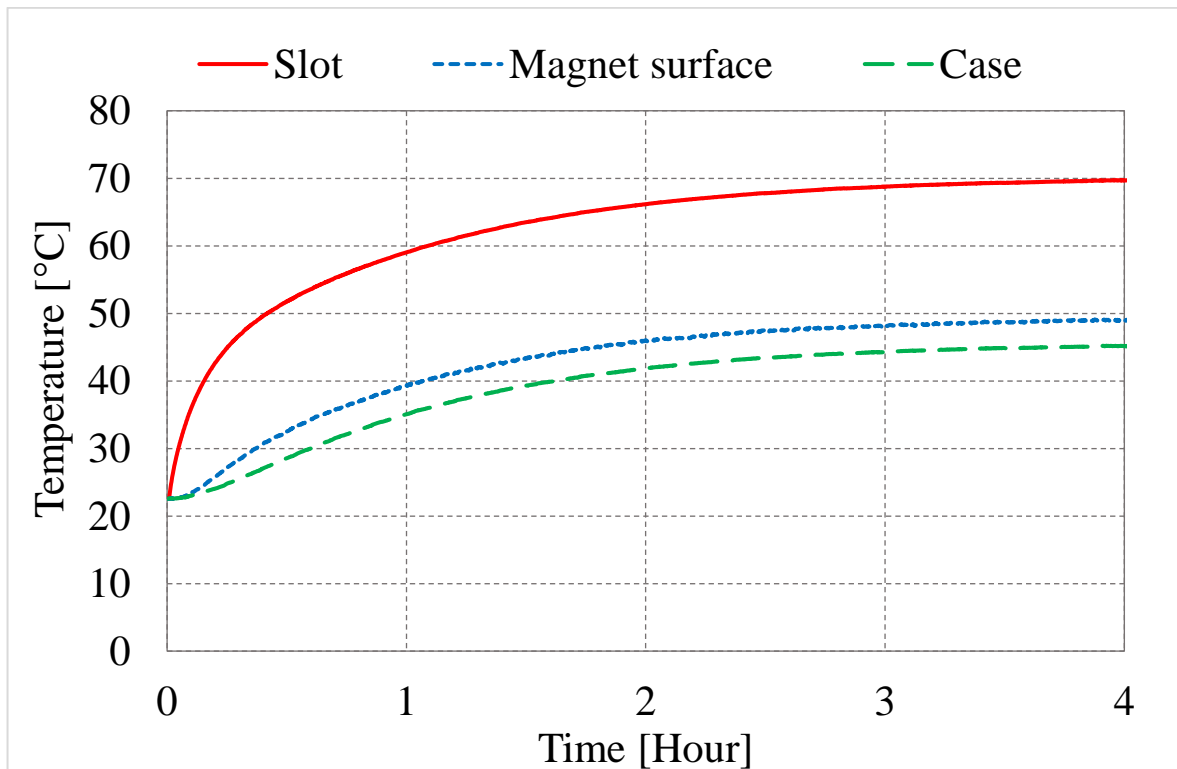


Figure 6.29: Thermal behaviour of the IMCP machine

6.8.2 VCP Machine

Figure 6.30 shows the temperature rise during a period of four hours when 7.8A DC current was injected to the coil. It can be seen that the temperature obtained from the experimental test stabilised to a temperature of almost 78 °C, while the temperature of the magnet surface and the aluminium case stabilised to a temperature of almost 53 °C and 50°C, respectively. Taking into consideration the temperature rating of 220 C° for both the insulation class of the copper used in the prototype, and the thermal paste used for potting, which indicates that this temperature can be considered as safe. Furthermore, the back EMF was measured after this test and compared to that obtained in section 6.3.2 –Figure 6.10. It was found that the back EMF remains the same after this test which confirms that the PMs was not demagnetised under this condition.

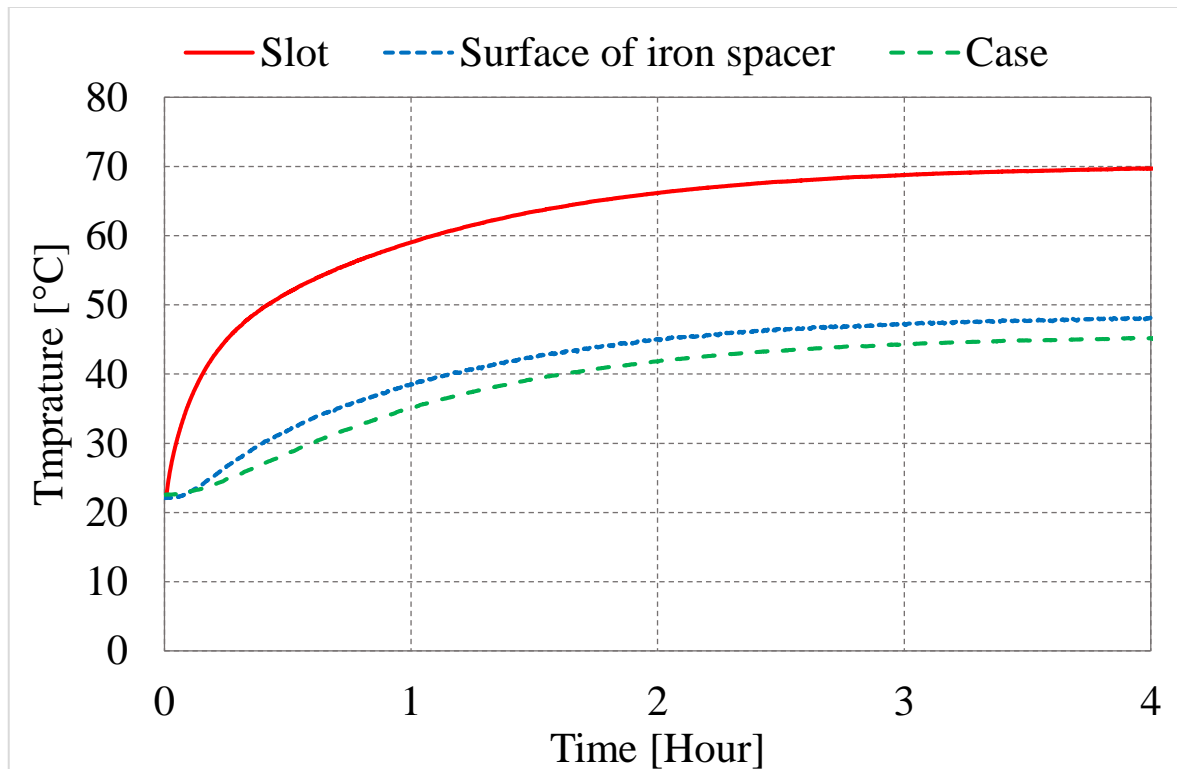


Figure 6. 30: Thermal behaviour of the VCP machine

6.9 Comparison of the IMCP and VCP Prototype Machines

The experimental results from the constructed prototype of the IMCP and VCP machines are shown to be close to the FEA results. As the performances of these two machines have been evaluated and compared in Chapter 4, it is therefore worth making a comparison between the two prototype machines based on the measured results. The purpose of this

comparison is to show that the VCP machine can produce higher no-load back EMF, force production and output power, while exhibiting lower cogging force compared to its IMCP counterpart,

6.9.1 No-load Back EMF

Figure 6.31 shows a comparison of the IMCP and VCP prototype machines in terms of the no-load phase back EMF. The VCP machine generates higher no-load back EMF for a given velocity as illustrated in Table 6.9 where an increase of 21% is shown in the RMS values. More importantly, the fundamental of the no-load back EMF of the VCP machine is 17% greater, showing that the harmonic content is reduced in the VCP. It should be indicated that the THD in the measured results of the phase back EMF is about half of that produced by the IMCP topology as previously discussed in section 6.3.

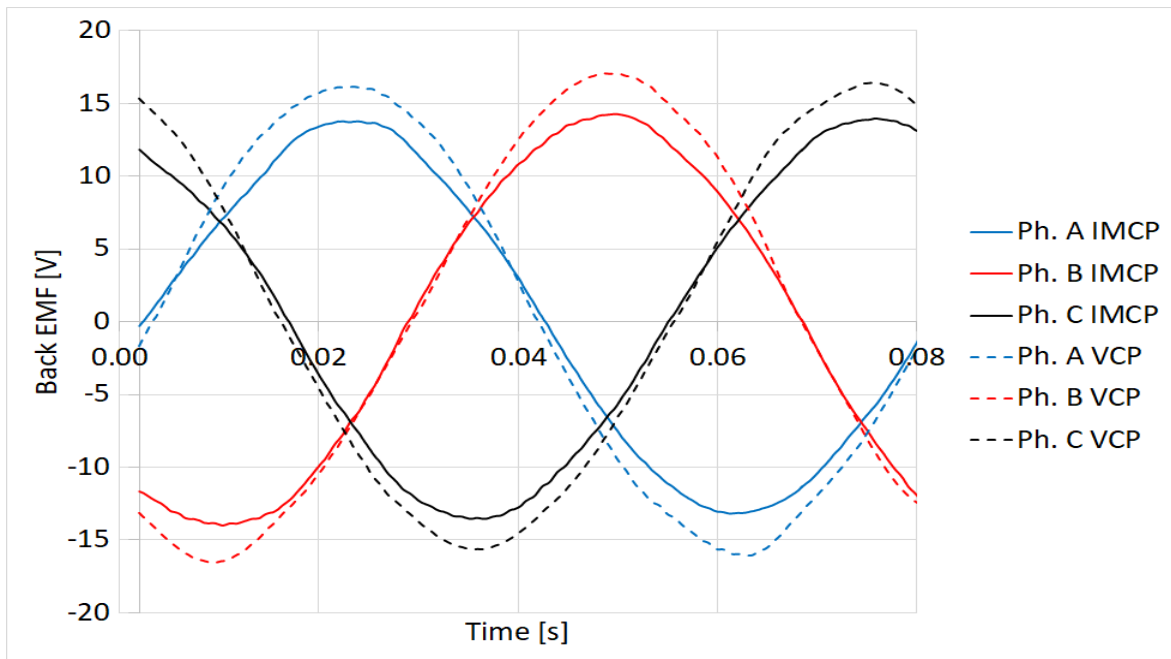


Figure 6. 31: Comparison of the measured no-load back EMF at 0.3m/s for IMCP and VCP machines

Table 6. 9: Comparison of the measured magnitude of the back EMF for IMCP and VCP machines

Across the three phases	IMCP	VCP	difference [%]
Average peak voltage [V]	14.2	17	20%
Average RMS voltage [V]	9.6	11.6	21%
Average fundamental [V]	12	14	17%

6.9.2 Cogging Force

According to the results obtained from the experimental tests, the VCP prototype machine has a peak to peak value of 48N, which is 17.2% lower than that of the IMCP prototype machine as verified in Figure 6.32. This reduction is attributable to the resultant sinusoidal waveforms of the phase back EMF caused by the near absence of the 5th harmonic discussed earlier in section 6.3.2, which in turn influenced the magnitude of the cogging force. It should be highlighted that both machines exhibited a low level of the cogging force owing to the adoption of the consequent pole topology.

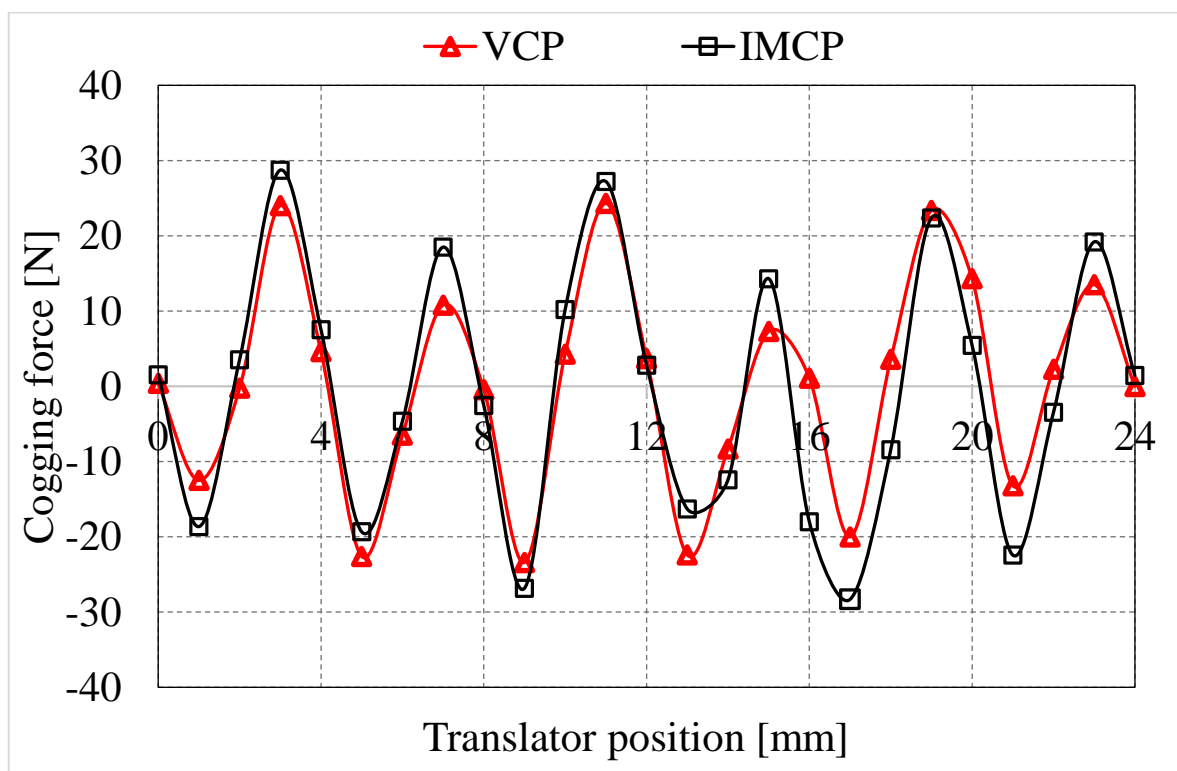


Figure 6. 32: Comparison of the measured cogging force for IMCP and VCP machines

6.9.3 Force Production

Figure 6.33 shows the graphical comparison of the measured static DC force of IMCP and VCP prototype machines under a DC excitation current of 10A, which confirms the superiority of VCP prototype machine.

Table 6.10 gives the peak values of the static DC force with respect to the applied DC current. This shows that the static DC force produced by the VCP machine is between 14% and 16.5% greater than that of the IMCP machine. It should be indicated that for both

prototype machines the applied DC current was limited by the test equipment available and not by the investigated machines.

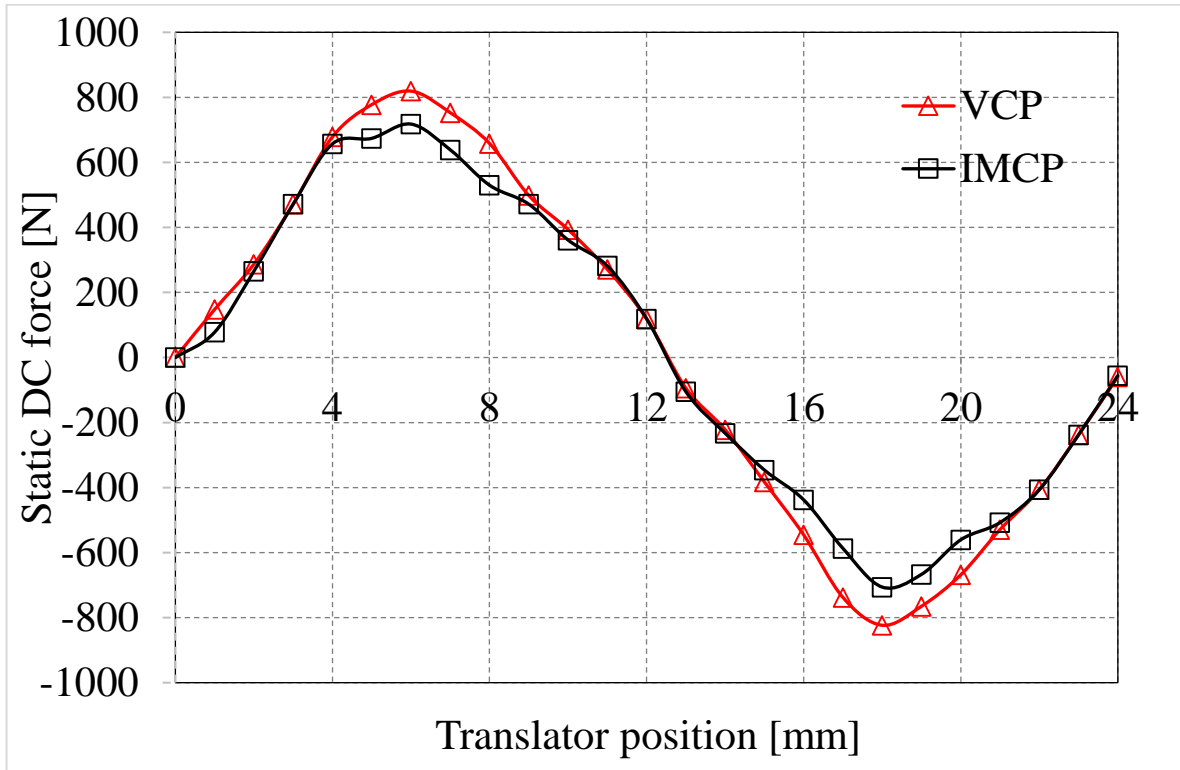


Figure 6. 33: Comparison of the measured static DC force for IMCP and VCP machines

Table 6. 10: Comparison of the measured DC static force for IMCP and VCP machines

Across the three phases	IMCP	VCP	difference [%]
Peak DC force [N] at 11A	718	819	14
Peak DC force [N] at 5.5A	358	417	16.5

6.9.4 Output Power

The output power of the IMCP and VCP prototype machines is compared in this section. Both machines were investigated under variable resistive load as discussed in section 6.7. Figure 6.34 shows the variation of the output power with respect to the applied load. It can be seen that the output power of the VCP machine offers 14% higher output power compared to its counterpart. It should be indicated that the obtained values do not reflect the expected

output power for both investigated machines due to the limitations of the velocity of the actuator.

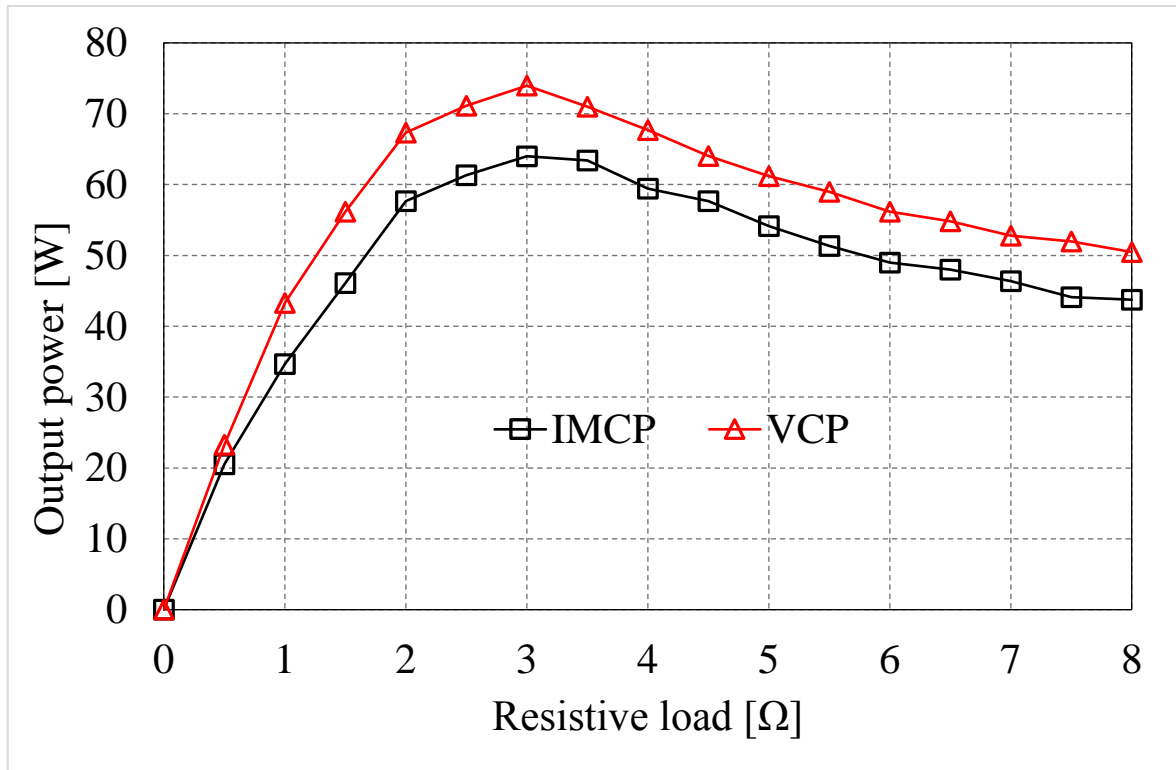


Figure 6. 34: Comparison of the resistive load test for IMCP and VCP machines

6.9.5 Power Factor

Due to the speed limitation of the ball screw actuator, we were not able to directly measure the power factor at the rated speed. However, by looking at the back EMF constant, the back EMF value at the rated speed can be predicted hence calculating the power factor is possible.

The power factor and terminal voltage can be calculated as:

$$\text{Power factor} = \cos\Phi = \frac{E + R_a I_a}{V_a} \quad (6.3)$$

$$V_a = \sqrt{(E + R_a I_a)^2 + (\omega L_a I_a)^2} \quad (6.4)$$

Where V_a is the terminal voltage and I_a is the phase current. The results show that the power factor of the IMCP and VCP machines are 0.63 and 0.5 respectively, which confirms

that the proposed VCP machine has a higher operating power factor compared to its counterpart.

6.10 Conclusion

In this Chapter, the experimental results of testing the IMCP and VCP prototype machines have been presented and compared to the predicted FEA results. The Chapter started with some initial DC and AC measurements performed to find the winding resistances and inductances for both prototype machines. Since both prototype machines have the same winding specifications, the measured phase resistances are expected to be the same. These measured values agreed well with predicted ones, with an average error of 6.2%. The measured phase inductances are slightly higher than that obtained from the FEA results, which is attributable to the negligible end effect.

Both prototypes exhibited a good balance of the induced no-load back EMF between phases along with the expected 120° phase shift. However, the measured no-load back EMF magnitudes of the IMCP and VCP prototype machines are 7 and 6.6%, respectively, lower than the predicted values.

The VCP prototype possesses almost the same thermal behaviour of that of the IMCP prototype owing to the common specifications between them.

The performance of the two prototype machines has been then compared as summarised in Table 6.11. From that Table it can be concluded that a close agreement is observed between the experimental and FEA results. The VCP prototype machine shows a higher no-load back EMF, static DC force, output power and power factor, while it exhibits lower cogging force for the same overall volume, verifying that the VCP prototype machine could actually be smaller than the IMCP machine. More importantly, the captured phase back EMF waveform of the VCP prototype has only a 2.3 THD and is very sinusoidal.

Table 6. 11: Summary of the performance comparison for IMCP and VCP machines

	IMCP			VCP		
	FEA	Exp.	Error[%]	FEA	Exp.	Error[%]
Peak back EMF [V]	15.3	14.2	7	18.2	17	6.6
pk-pk cogging force [N]	62	58	6.4	51	48	5.9
Peak DC force [N] at 10A	721	652	9.5	805	763	5.2
Output power at 0.3m/s	-	64	-	-	73	-
Power factor	0.5	0.5	-	0.65	0.63	3

Chapter 7. Proposed VCP Machine for a 30kW Wave Energy Device

7.1 Introduction

In this Chapter the VCP machine developed in this thesis and described in Chapter 4 is scaled up for use in the 30kW DD-WEC developed by Uppsala University [123]. The study is intended to investigate the effect of using different support structures on the overall machine size and mass. Estimated required quantities of active materials for each design are provided. The dimensions and the main specifications of the Linear Permanent Magnet Generator (LPMG) proposed by Uppsala have been used as the input parameters for a design study of the VCP machine. Five variants have been investigated and their dimensions, mass and cost of compared. Due to the lack of data provided in [123], there are limitations to the electromagnetic performance and PM mass comparison.

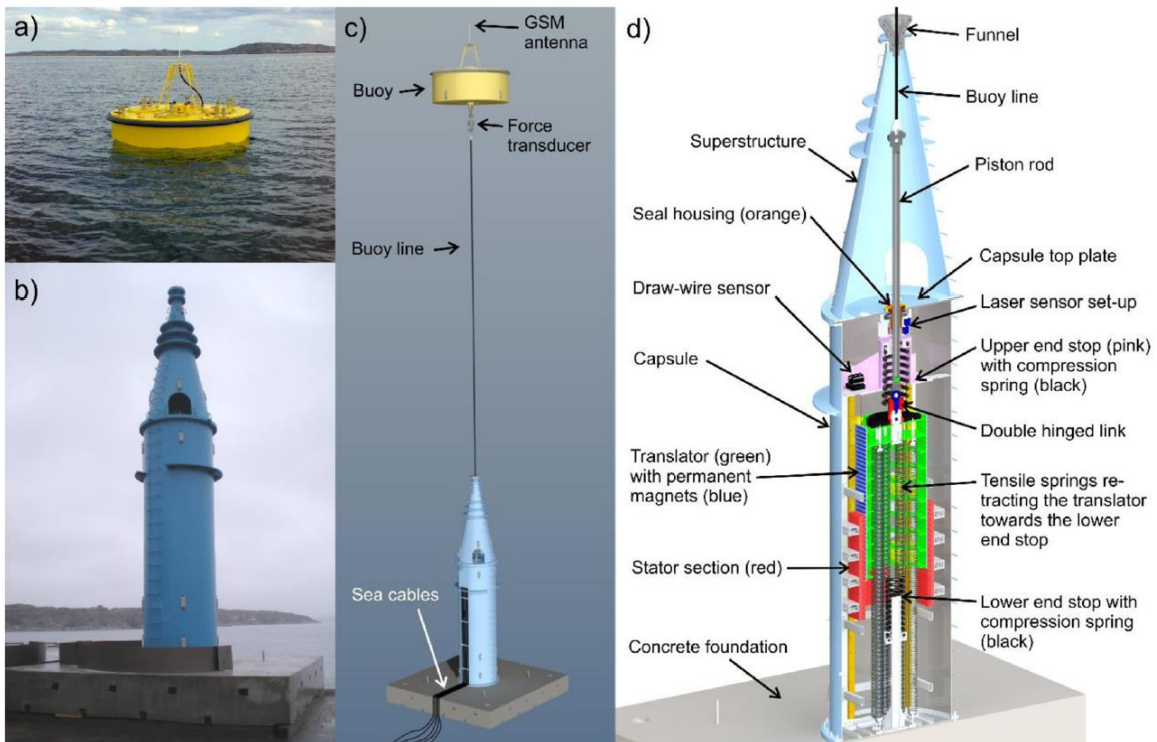
7.2 Description of the Existing LPMG Developed by Uppsala University

Development of the LPMG used in the wave energy device developed by Uppsala has been well reported [123-126]. A company called Seabased AB is currently developing and commercialising this technology further [127]. The UU-LPMG has a multiple-sided configuration with an outer stator and inner translator as shown in Figure 7.1.

It is an iron-cored machine which has a stator with a vertical length of 6m, and stack length of 0.4m. The winding arrangement for the three-phase is shown in Figure 7.1(f), which uses standard PVC insulated cables with stranded conductors. Although this is unusual for machine winding, the insulated, stranded cable is easy to handle, flexible and relatively cheap making it ideal for winding a large machine[126]. Furthermore, in the harsh marine environment, a good insulation can be provided by the PVC. The translator length is 3m in which surface-mounted NdFeB PMs are accommodated with aluminium spacers for accurate positioning of the PMs as shown in Figure 7.1(e). The LPMG-UU has been assembled robotically as detailed in [125, 126]. The key specifications of the LPMG-UU is listed in Table 7.1.

Table 7. 1: Main specifications for the LPMG developed by UU

Item	Value	Unit
Hull height	6000	mm
Hull diameter	1091	mm
Vertical stator length	1967	mm
Vertical translator length	3000	mm
Translator mass	2700	kg
Average power	30	kW





(e)



(f)



(g)

Figure 7. 1: (a) buoy (b) hull (c) UU-WEC (d) system layout (e) Translator with PM mounted on (f) top view of stator (g) laminated single side of the stator [123, 125, 126]

7.3 Multiple-Side Structure

In this thesis, it was decided to choose eight-sided structure as it is close to a tubular machine and possesses lower pronounced undesirable impacts in comparison with a double, four or six-sided linear machine [75].

The aim of using a multiple-sided VCP machine is to minimise the attraction forces acting on the mechanical bearings by balancing the magnetic attraction forces [75].

The windings of the multiple-sided linear PM machines can be assembled in different ways; either a wave winding on each stator individual module as shown in Figure 7.2 (a), which can be connected externally, or a lap winding that encircles all stator modules [35], as shown in Figure 7.2 (b). In the latter technique, the stator modules for all machine sides share the same winding. The result is the absence of the end windings and hence lower copper losses can be obtained. However, sharing the common winding between the stator sides can lead to a potential complexity of the stator disassembly, especially during the routine maintenance. On the other hand, by adopting the design shown in Figure 7.2 (a), the disassembly of the machine would be much easier. However, greater copper losses would occur as a result of the extra conductor length.

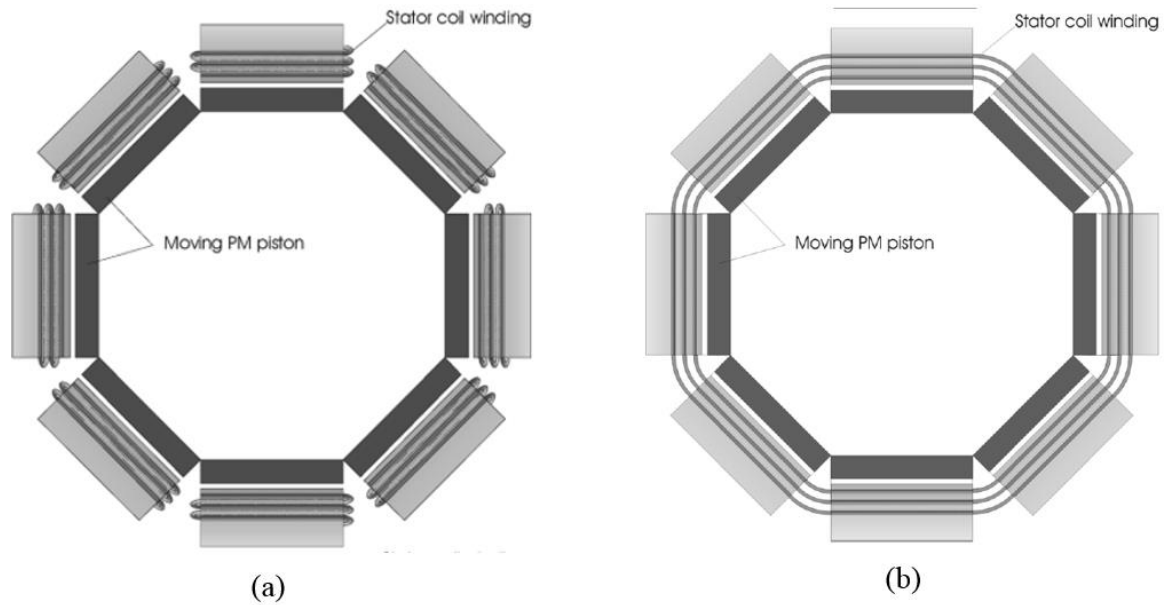


Figure 7. 2: Possible winding configuration for multiple-sided machine [35]

7.4 Potential Advantages of Using the VCP Machine as an Alternative Generator for UU-WEC

- The PMs are mounted in the stator in which the issues of the mechanical integrity and thermal instability can be avoided and the amount of PM can be saved.
- The translator consists of laminated iron core with salient teeth so that it is very robust to transmit high thrust force for direct drive application, with potential of reducing translator cost and maintenance.
- The proposed VCP machine can be designed in a compact size to react the same force of the LPMG-UU, thus reducing the construction cost.
- The proposed VCP machine can offer high force density and shear stress at low operating speeds due to the inherent magnetic gearing effect.
- Concentrated windings are used in the proposed VCP machine offering short end windings, thereby low copper loss can be achieved due to the small winding resistance.

7.5 Description of the Proposed Variants

7.5.1 Design A

In this design, the VCP machine described earlier in Chapter 4 was scaled up using the same method adopted in [2]. Details of the selection and calculation of the machine dimensions are provided in the proceeding paragraphs.

First, the diameter of the hull used for accommodating the LPMG used in UU-WEC [123] and shown in Figure 7.1(b), was assumed to be the maximum space available for this design study. This gives an indication of the maximum axial length can be used for the proposed design, design A. According to the FEA calculation, the VCP machine with a single stator module (double-sided E-core) with an axial length of 50mm is capable of generating 818N at a velocity of 1m/s. Therefore, in order to achieve the equivalent force produced LPMG used in UU-WEC [123], the axial length of the VCP machine was extended to 700mm and five identical stator modules were arranged in the direction of the motion as shown in Figure 7.3. Equation (3.8) was used to obtain the desirable displacement between the stator modules. The mass of all active parts are given in Table 7.2.

To use the hydraulic bearings adopted in [128], the thickness of the translator was designed to be 0.14m (The translator coreback was scaled up in proportion to the axial length).

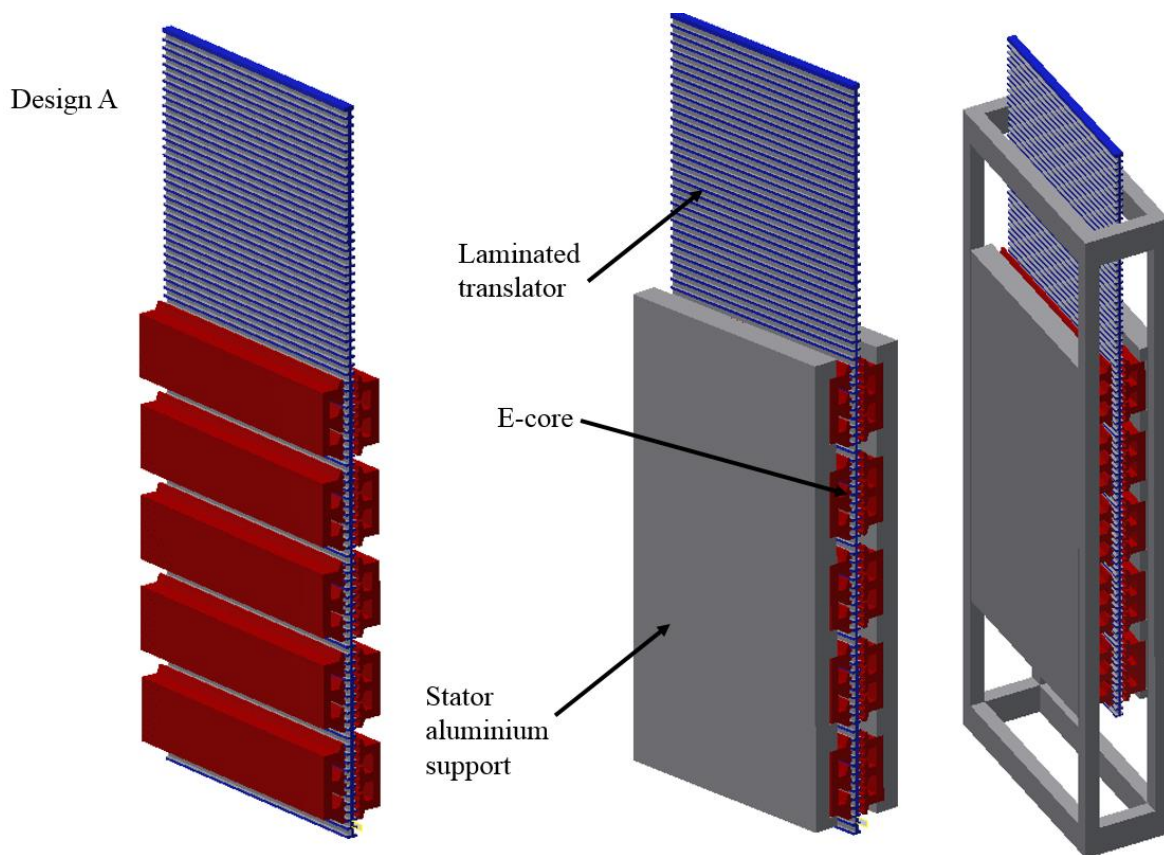
An investigation of scaling up the LVHM by extending the axial length has been carried out in detail in [95, 128]. However, no real large-scale LVHM has been constructed and tested.

Some disadvantages of employing this topology are summarised below:

- Extending the axial length of the double-sided VCP topology would make it difficult to wind the stator windings due to small slot area available within the stator module. Which means, a bigger slot area is required to facilitate the winding assembly leading to an increase in laminated material, vertical stator length and hence the associated mass. In addition, this can result in a very poor fill factor due to the increase in the slot area.
- The attraction force between the stator and translator and cogging force are proportional to the machine axial length. Therefore, more structural support is required to react against the predicted unwanted forces.
- To construct this machine large PM bars are needed, which can be easily damaged due to their small thickness (3mm).

Table 7. 2: Mass of design A

Item	Mass	Unit
Magnets	33.6	kg
Copper	213	kg
Laminated stator	540	kg
Laminated translator	1007	kg

**Figure 7. 3: Design A structure**

7.5.2 Design B

A new design presented in this section was developed from the double-sided topology. A topology with a similar concept of multiple double-sided air-cored LPMGs distributed around a central support was developed by [129, 130] as shown in Figure 7.4. The new design consists of eight double-sided VCP machines in which each machine is perpendicularly attached to each side of an octagon structure, and all being magnetically independent. Each individual machine has five stator modules sharing the same translator; they are adjacent to each other on the same plane and are displaced by a distance satisfying (8.1). The purpose of

this design is to minimise the translator mass and vertical height for a given force. Figure 7.5 shows the structure and the required components for the proposed design. The dimensions of the design and number of active components were identified based on the available space and force required by the initial LPMG-UU [123]. Aluminium structural support is assumed to be used in both translator and stator support. A set of linear guides and carriages employed, which require small space compared to the other type of mechanical bearings. The full structure was designed using Autodesk Inventor software and then each component was extracted by MagNet™ software to predict its mass. The mass of all active parts are presented in Table 7.3. There are three key advantages can be gained from this design which are as follows:

- A compact size can be achieved in comparison to the LPMG-UU.
- The design has an eight double-sided VCP machines sharing the same structure support, meaning that each machine can be assembled and disassembled individually.
- The free spaces surrounding the centre of the design can be used to accommodate the converter elements.

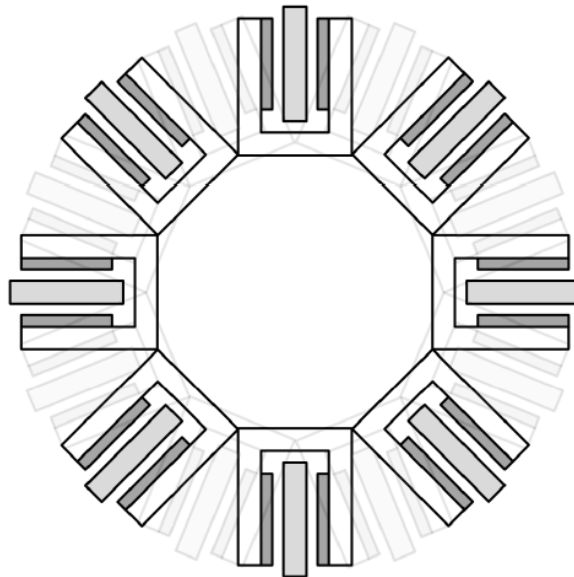


Figure 7. 4: Multiple double-sided structure developed in [130]

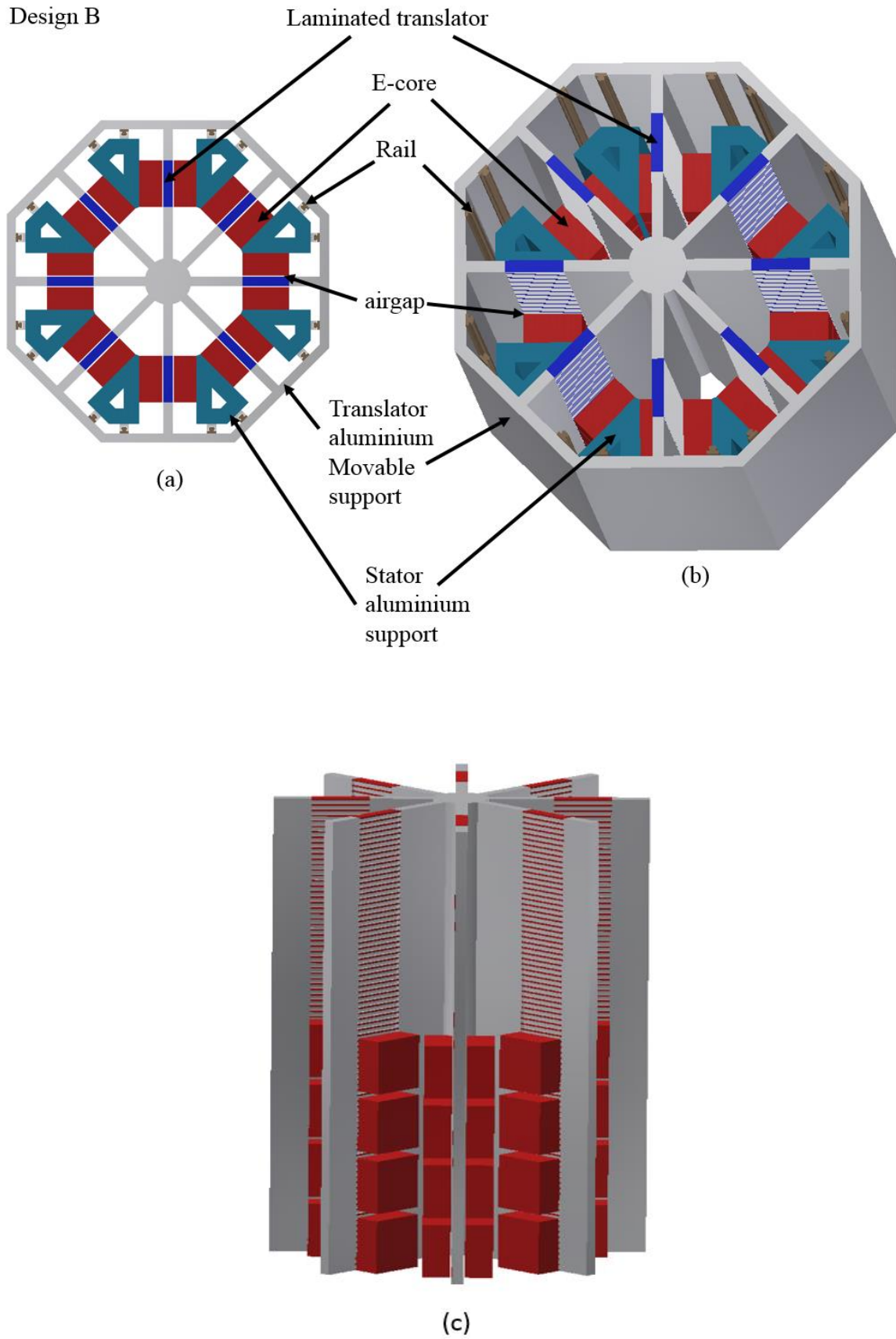


Figure 7. 5: Design B structure (a) top view (b) 3D rendered view and (c) side view

Table 7. 3: Mass of design B

Item	Mass	Unit
Magnets	33.6	kg
Copper	317	kg
Laminated stator	540	kg
Laminated translator	515	kg

7.5.3 Design C

This design copies the main structure of the design B discussed in the previous section. It contains eight double-sided VCP machines in which each machine has five modules sharing the same translator, and are evenly displaced as per (8.1) along the motion direction as shown in Figure 7.6. The key difference between the two designs is that the translator structural support of the present design is split into two parts: namely, the movable aluminium support highlighted in pink in the same Figure and the stationary aluminium support. This structure provides a free space between the movable and stationary aluminium support to accommodate roller bearings. The dimension of the design and number of active components were identified based on the available space and required force of the initial LPMG [123]. Again, the full structure was designed using Autodesk Inventor software and then each component was extracted by MagNet™ software to predict its mass. The mass of all active parts are shown in Table 7.4. There are three key advantages can be gained from this design which are as follows:

- A compact size can be achieved in comparison to the LPMG-UU.
- The design has an eight double-sided VCP machines sharing the same structure support, meaning that each machine can be assembled and disassembled individually.
- As the translator structural support has two main parts, the overall movable translator mass can be reduced.

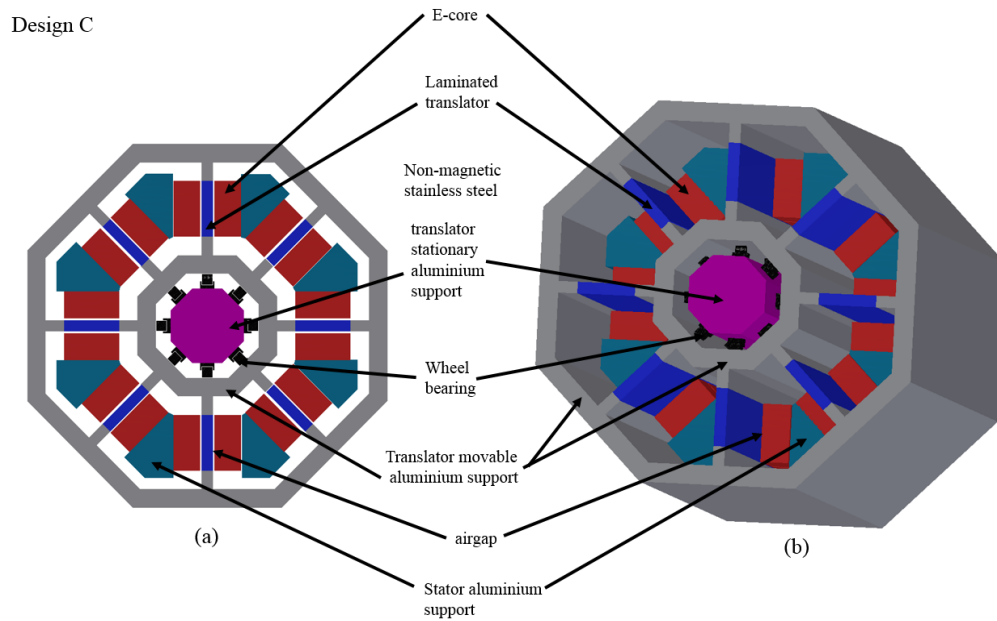


Figure 7. 6: Design C structure (a) top view (b) 3D rendered view

Table 7. 4: Mass of design C

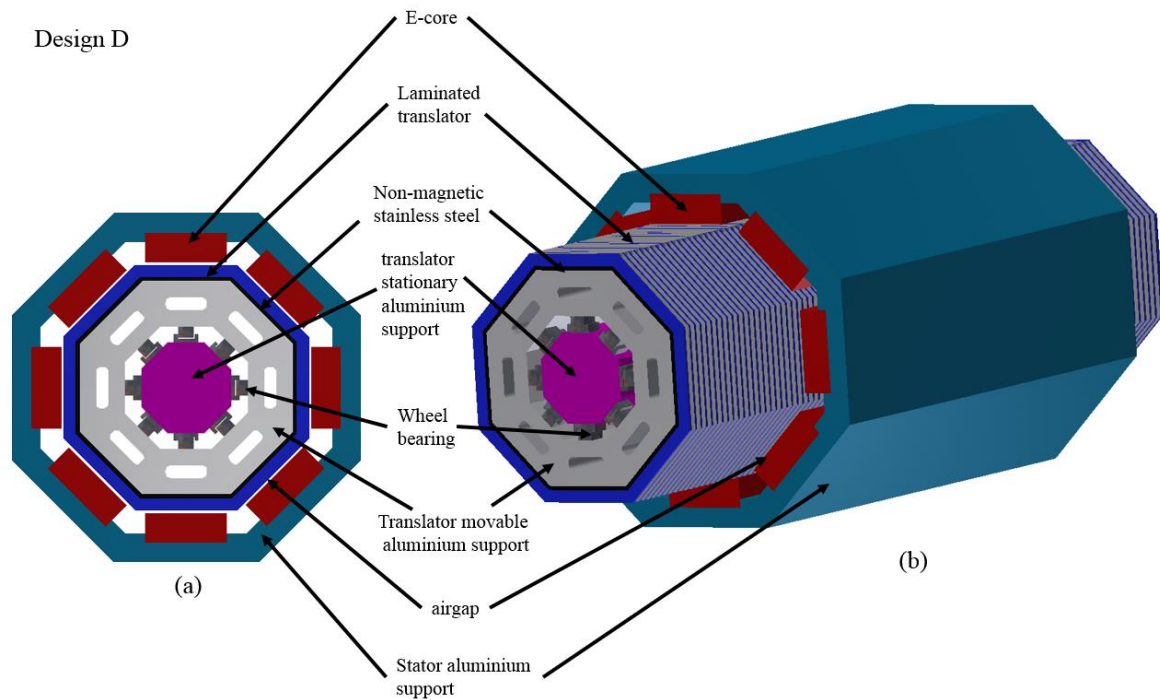
Item	Mass	Unit
Magnets	33.6	kg
Copper	317	kg
Laminated stator	540	kg
Laminated translator	515	kg

7.5.4 Design D

In this design, multiple single-sided machines are placed around a central octagon-shaped structure. Five identical modules which are placed with respect to one another in the direction of motion such that they are displaced as per (8.1) to form a three-phase single-sided machine. Each stator module is capable of reacting 1.5kN, making up a three-phase single sided-machine with a combined average force of 7.5kN, thereby 60kN for all eight sides.

Figure 7.7 shows the proposed configuration; it is similar to that used in UU-WEC in terms of number of sides. The translator structural support comprises mainly of two parts: aluminium stationary part fixed to the seabed, and movable aluminium part to support the laminated translator core. The aluminium translator movable support was designed with eight holes in parallel with the motion direction, and distributed around the centre of the

translator, leading to a further reduction in the structural material used. The stationary aluminium translator support highlighted in pink in Figure 7.7 is designed for the purpose of providing paths for movements of wheel roller bearings, which are sandwiched between the movable and stationary aluminium support. The mass of active parts are listed in Table 7.5.



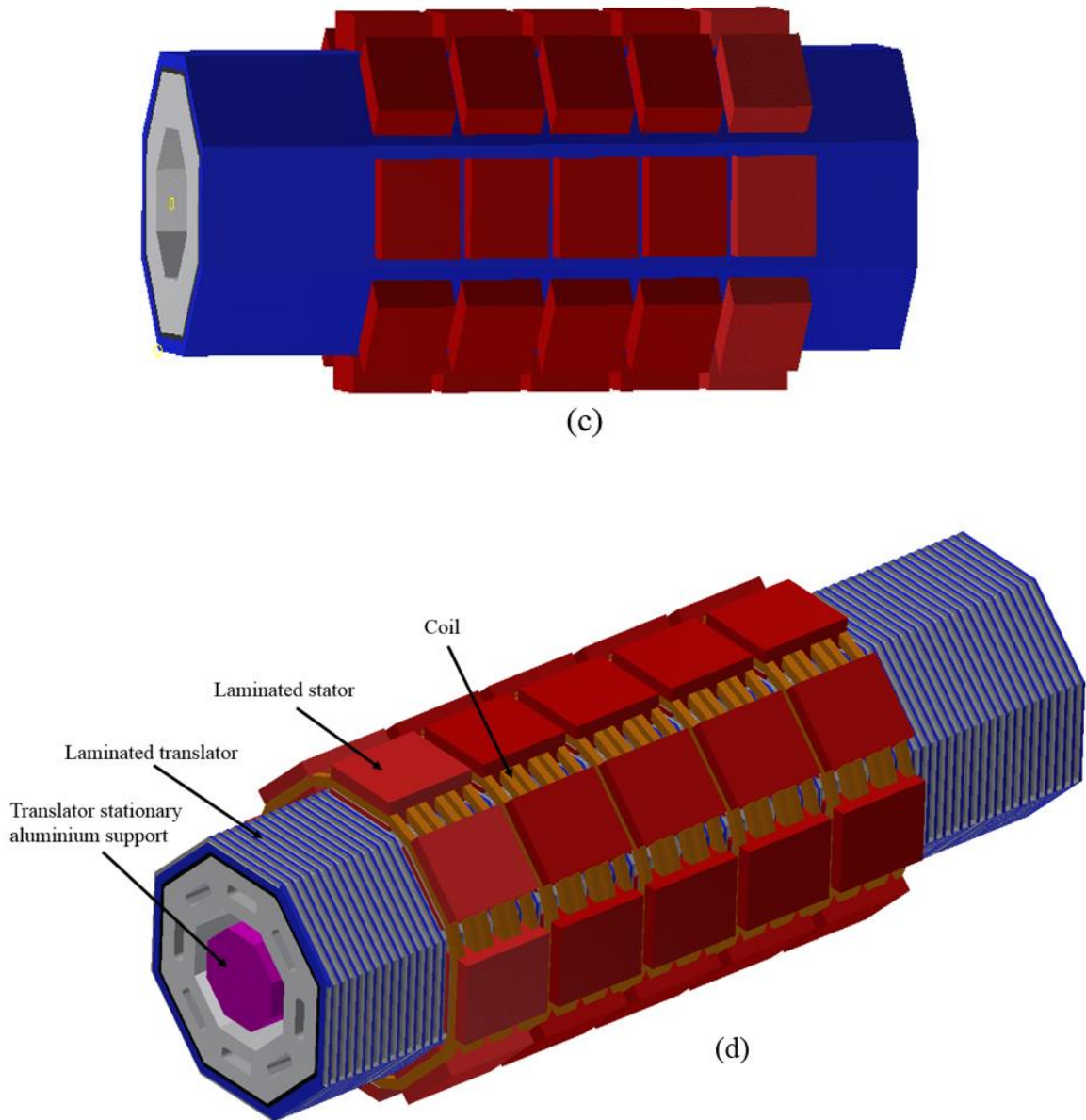


Figure 7. 7: Design D structure (a) top view (b) 3D rendered view (c) side view (d) winding configuration described in section 7.3

Table 7. 5: Mass of design D

Item	Mass	Unit
Magnets	33.6	kg
Copper	276	kg
Laminated stator	540	kg
Laminated translator	465	kg

7.5.5 Design E

This design has a double-sided stature in which an octagon-shaped translator is sandwiched between two octagon-shaped stators as illustrated in Figure 7.8. The width of the octagon-shaped structure was designed based on the available space within the hull occupied by the LPMG-UU [123]. There are four stator modules placed with respect to one another in the direction of motion such that they are displaced by a distance satisfying (8.1). The number of these modules was selected based on the required force. Each side of the octagon represents an individual double-sided VCP machine. The total height of the translator is 2048mm, and the overall translator mass is 438kg. The predicted mass for all active components are listed in Table 7.6. A number of Linear Ball Bushing bearings were integrated into junctions located within each edge of the octagon-shaped structure, which are capable of supporting linear motion over the likely annual distance travelled by WECs. The following advantages are expected to be obtained from this design.

- This design provides a large free space in the centre, which can be exploited to house the converter components.
- The machine can be assembled and disassembled as individual machines, in which each machine represents one side of the overall octagon-shaped structure, which contains an individual double-sided CVP machine.
- This configuration has eight-sided structure hence is anticipated to behave as tubular machine in terms of attraction and cogging forces [75].

Design E

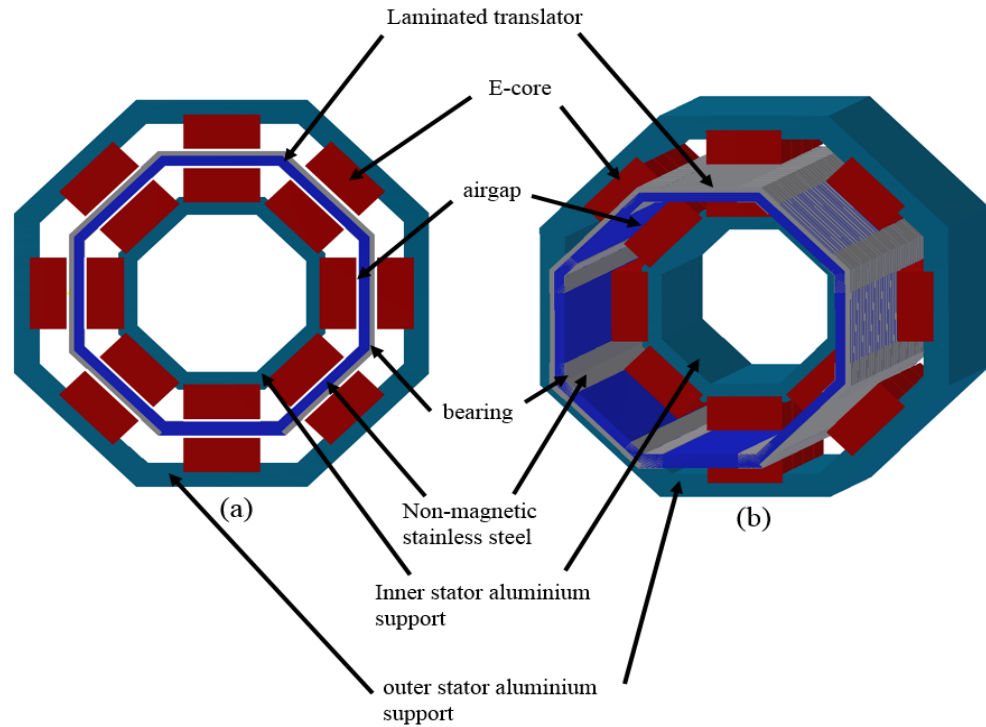


Figure 7. 8: Design E structure (a) top view (b) 3D rendered view

Table 7. 6: Mass of design E

Item	Mass	Unit
Magnets	33.6	kg
Copper	317	kg
Laminated stator	540	kg
Laminated translator	438	kg

7.6 Comparison of Mass and Cost of Active Materials

Table 7.7 gives a summary of the alternative machines and the number of modules which would be required to provide comparable machine for the LPMG-UU. It can be seen that all the five designs require the same amount of PM to react the same force in which the designs B, C and E have the same translator and stator vertical length, while designs A and D have a 25.8% and 13% longer stator and translator vertical length, respectively in comparison with the former designs. Although design A has the lowest number of stator modules and end windings, it needs a large amount of electrical steel sheets compared to the other designs.

Moreover, making the stator windings can be an issue due to the extended axial length and small slot area.

Figure 7.9 allows a direct comparison of the five investigated configurations in terms of mass and approximate active materials' costs, which were estimated based on [131, 132], based on the raw material prices in December 2018 as given in Table 7.8. Comparison of the mass of copper and PM material used in each machines is more reliable. In fact these prices vary depending on the quantity of materials and the date of purchase, but the relative price between the five configurations would likely remain the same. It is shown that design B, C and E have the total active mass, but it is expected that design E will place less demands on the support structure. In addition, the latter configuration acts as tubular machine in which the unwanted forces such as cogging and closing airgap forces can be reduced as verified in [75].

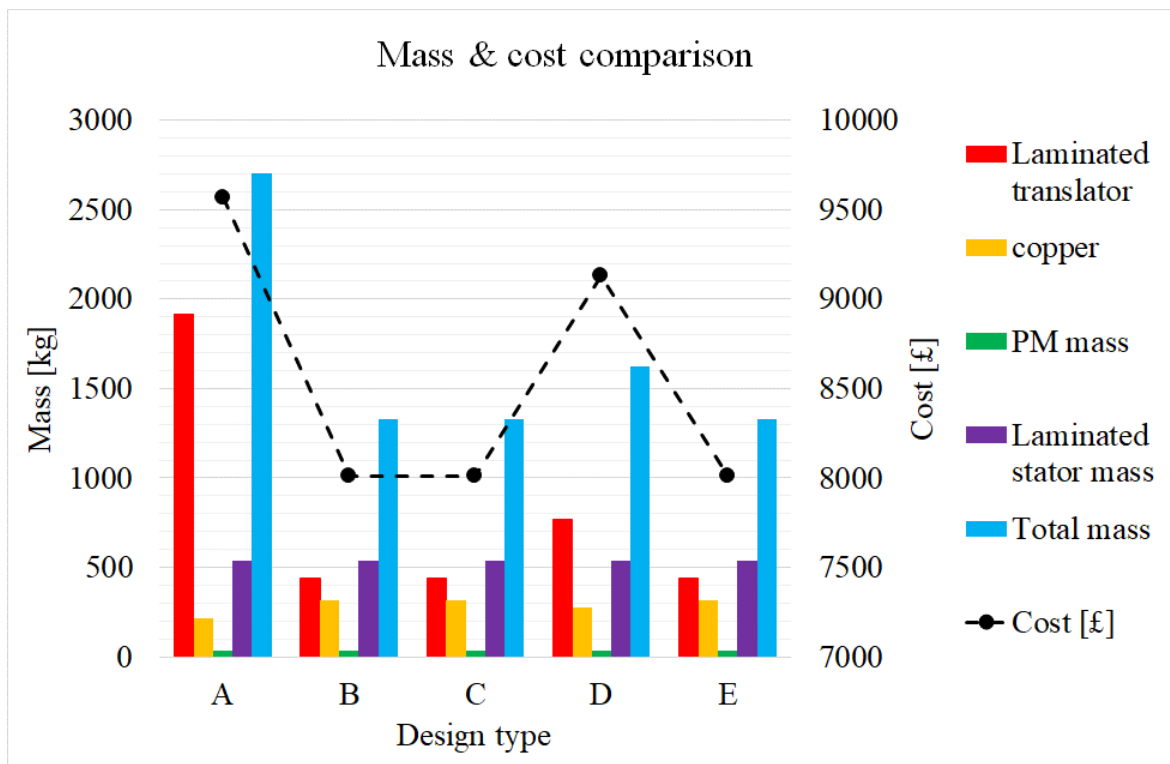
Comparison results imply that the proposed design E with double-sided octagon-shaped structure is more promising for a large-scale UU-WEC in terms of both physical parameters and economics.

Table 7. 7: Comparison between five configurations

Design Type	A	B	C	D	E
Number of modules/ layer	1	8	8	8	8
Number of modules/ side	5	4	4	5	4
Total number of modules	5	32	32	40	32
Stator vertical height [mm]	1288	1024	1024	1288	1024
Translator vertical height [mm]	2312	2048	2048	2312	2048
Mass of the laminated stator [kg]	540	540	540	540	540
Mass of the laminated translator [kg]	1007	438	438	770	438
Copper mass [kg]	213	317	317	276	317
PM mass [kg]	33.6	33.6	33.6	33.6	33.6

Table 7. 8: Material prices used in cost analysis

Design Type	Cost (£)
PM	65.3
Copper	5.55
Electrical steel	4

**Figure 7. 9: Mass and cost comparison**

7.7 Conclusion

Five possible configurations of a large-scale version of the VCP machine have been presented, capable of reacting the maximum force required by the LPMG used in the UU-WEC. These configurations have been compared in terms of size, mass of the active materials and the associated cost. The results reveal that design E is considered as the most promising alternative for the UU-WEC in terms of active mass, cost and the expected required structural support. It is also demonstrated that by employing the nominated configuration for use in the UU-WEC the following advantages can be obtained:

- The translator and stator vertical length can be reduced by 32% and 48%, respectively compared to the LPMG-UU, which in turn may lead to a significant reduction in the machine overall size and cost.
- The translator active mass represents only 16.2% of that used in LPMG-UU.
- The PMs are mounted on the stator hence the issue of mechanical integrity and thermal instability can be avoided.
- The proposed design requires only 33.6kg of PM to react the same force of that of the LPMG-UU.
- Small PM blocks can be used compared to that adopted in the LPMG-UU; they are much easier for manufacturing and handling.

Chapter 8. Conclusion and Future Work

8.1 Introduction

The question posed at the start of this work was whether it is possible to design a Linear Vernier Hybrid Machine in order to maximise its utility/performance for direct drive wave energy applications. Using consequent pole structure has been shown to reduce the pole-to-pole leakage flux resulting in an increased force density of the Linear Vernier Hybrid Machine. This means that by careful design a feasible machine is possible. This has since been constructed and successfully tested.

There has been a particular focus on the power factor improvement without increasing the magnet mass taking into consideration the complexity of manufacturing and cogging force. By examining new configurations of PM arrays this aim was achieved and two machines with high force density and improved efficiency have been designed and analysed. The V-shape Consequent Pole machine has been built and tested in the laboratory due to its simple structure and exhibited cogging force compared to the V-shape machine. However, the work presented in this thesis on V-shape non-consequent pole machine is in the early stages of development and it would be interesting to verify the obtained simulated results through experiment. Therefore, strong recommendations and a more formed plan are given of further V-shape research for the next PhD student.

Further improvements to the V-shape Consequent Pole topology have been explored, which can provide a machine suitable for real world applications.

8.2 Chapter / Results Summary

An introduction to the importance of wave energy exploitation has been presented in Chapter 1. The aim of the research, study objectives and contribution to the knowledge have also been highlighted.

In Chapter 2, the idea, need and history of utilising energy from ocean waves have been introduced. An overview of the most common existing technologies of wave energy converters has been provided, which are driven through mechanical intermediates such as pneumatic or hydraulic systems, or can be directly driven by a linear generator. The classifications of these devices based on wave direction and operation principle have been discussed. Furthermore, different types of power take-off systems have been introduced and

described. It is shown that development of linear machines to facilitate direct drive power take-off is advantageous but can only be achieved if machines optimised for low speed are developed.

The general layout of linear machines has been also explained in this Chapter. Details have been given of conventional linear induction machines, linear PM synchronous machines, linear variable reluctance PM machines and linear tubular PM machines, and a discussion outlining some of their benefits and drawbacks has taken place. The ease of manufacturing processes along with the rigidity of the translator have been considered. Finally, despite the intense competition between the members of the family of the variable reluctance PM machines, the double-sided linear Vernier hybrid machine has simple structure where both magnets and windings are mounted in the stator, while the robust translator consists of iron. Although this machine suffers from low power factor, the converter appears to be much cheaper than the low speed direct-drive machine. The flux concentration effect can be exploit to improve the no-load airgap flux density. Hence, this method has been shown to improve the power factor without increasing the magnet mass by adopting a topology that is capable of providing a flux concentration effect, i.e V-shape PM array. Therefore, it is worthwhile to investigate this topology further. Chapters 3 and 4 investigated this type of electrical machine for the purposes of improving the magnet utilisation and operating power factor.

In Chapter 3 the development of the linear Vernier hybrid machine including C-core and E-core structures has been detailed. The Chapter commenced with the description of the proposed C-core Inset Magnet Consequent Pole machine along with its operation principle. The implementation of the tapered ferromagnetic poles has been investigated and it has been shown that this technique is capable of reducing the pole-to-pole leakage flux and enhancing the main flux. Based on FEA the C-core Inset Magnet Consequent Pole machine has been optimised and analysed with the aim of improving the machine electromagnetic performance. It seems from the FEA simulations that the C-core Inset Magnet Consequent Pole machine can offer 50% higher thrust force, 37% higher power factor and exhibit 75.6% lower cogging force compared to the baseline Linear Vernier Hybrid Machine.

The C-core Inset Magnet Consequent pole machine has been further developed and converted to another version known as an E-core Inset Magnet Consequent Pole machine to facilitate the mechanical integrity by reducing the number of active parts, i.e. stator cores and shorten the active length. The results of the analysis show that the latter machine is

capable of delivering 23% higher force per machine mass owing to 18.5% saving in the overall mass, indicating that this machine is the most promising design.

The final Inset Magnet Consequent Pole design which has less number of components has been optimised and analysed for the purpose of further facilitating the manufacturing processes. The FEA simulations reveal that the proposed Inset Magnet Consequent Pole machine can offer a simple structure showing that this machine is suitable for low speed high force applications. This work provides a foundation for the investigation of modifications to the design and of new machines, which is the aim of the proceeding Chapter. Chapter 4 also introduced a further investigation on the Inset Magnet Consequent Pole machine including the force density, shear stress, attraction force and electrical efficiency. To facilitate ease of manufacturing and testing, a small prototype has been designed and built to validate the predicted results. A deeper discussion of the machine manufacturing and assembly processes as well as the experimental tests was presented in Chapters 5 and 6.

A second strand of the research work presented in this thesis focussed on extending the development of the Inset Magnet Consequent Pole machine introduced in Chapter 3. In Chapter 4, two novel topologies of the linear Vernier hybrid machine with different PM configurations known as the V-shape and V-shape Consequent Pole machines have been proposed, analysed and compared to the Inset Magnet Consequent Pole machine. The research initially looked at the optimisation of the new configurations and at how the electromagnetic performance and the electrical power factor could be improved without compromising the PM and overall machine volume. The flux concentration effect is the distinctive feature of the proposed topologies, in which 43.5% and 29.4% higher airgap flux density has been achieved by the V-shape and V-shape Consequent Pole machines respectively, compared to the Inset Magnet Consequent Pole machine, which resulted in power factor improvement of 40% and 28% for the former and latter machines, respectively.

A more in-depth comparison between these machines and the Inset Magnet Consequent Pole machine described in Chapter 3 has been made, based on the electromagnetic and electrical performances. The obtained results indicated that the V-shape topology is superior to the other machines in terms of no-load back EMF, force density and efficiency. However, this machine was shown to exhibit higher cogging force and require a double number of PMs and triangular iron spacers than that of the V-shape Consequent Pole machine, making the V-shape machine more complex in terms of manufacturing. This is due to the removal of the iron ribs which influences the triangular iron spacers to be constructed and assembled as individual parts.

Prototypes of the V-shape Consequent Pole and Inset Magnet Consequent Pole were built and demonstrated in the laboratory. Even though the V-shape machine has the superiority to the other machines, consideration has been given to the V-shape Consequent Pole Machine for the following reasons:

- The V-shape Consequent Pole machine has the advantage of a reduced number of components when building the prototype, i.e. a 50% less number of PMs and triangle iron spacers are required in the selected topology compared to its V-shape counterpart, which would therefore facilitate the complex manufacturing processes.
- The cogging force produced by the V-shape Consequent Pole machines is 32% lower than that of the V-shape machine.
- The closing airgap force felt by the translator of the V-shape Consequent Pole machine is 4.4% lower than that of the V-shape machine.
- The power factor achieved by this machine represents 93% of that obtained by the V-shape machine.
- The force density is only 8.8% lower than that of the V-shape machine.

A detailed description of the manufacturing and assembly processes of the prototype machines along with the development of the required test rig has been given in Chapter 5. An aluminium housing structure has been introduced, allowing the two prototypes to share the same stationary aluminium frame and translator. This contributed to a reduction in the materials required for construction and hence the associated costs. Another feature of the proposed aluminium housing is the possibility of adjusting the mechanical airgap by controlling the adjustable screws attached to the aluminium stator supports on both sides. The translator has been assembled using a non-magnetic material known as Tufnol along with a number of carbon fibre rods. The use of these materials resulted in a rigid and light supportive structure enabling the design of a thinner translator core back, which represents only 10% of that adopted in [2]. Two Linear guides and six carriages have been used offering smooth movement and are capable of reacting to any potential attraction forces without overloading the bearings set. Finally, each prototype has been connected to a ball screw actuator through a stainless steel shaft to form the complete test rig, which has been used in experimental validations covered in Chapter 6.

In Chapter 6, a series of experimental tests of the two prototypes is detailed and the results have been compared with the simulation data in order to complete the investigation.

The prototypes have been directly driven by a ball screw actuator with a limited maximum velocity of 0.3m/s, which in turn hindered the author from proving an accurate validity of these prototypes. The measured results have been used to verify the predicted results and a good correlation was established between both results. Errors of 7% and 6.5% have been shown between the measured and predicted back EMF for the inset magnet consequent pole and V-shape consequent pole machines, respectively. The discrepancy between simulation and measured results is potentially attributable to the end effect, material and mechanical errors. Both prototypes had the same volume and almost the same mass therefore the proposed V-shape consequent pole machine would have higher force density and higher force per active volume. In addition, due to the 30% reduction in the THD the proposed V-shape consequent pole machine has a very sinusoidal back EMF and exhibits 17.2% lower cogging force. The final results of the two proposed prototypes are shown in Table 8.1, which confirmed the superiority of the V-shape consequent pole prototype in terms of no-load back EMF, cogging force, static DC force, output power and power factor.

Table 8. 1: Summary of the performance comparison for IMCP and VCP machines

	IMCP			VCP		
	FEA	Exp.	Error[%]	FEA	Exp.	Error[%]
Peak back EMF [V]	15.3	14.2	7	18.2	17	6.6
pk-pk cogging force [N]	62	58	6.4	51	48	5.9
Peak DC force [N] at 10A	721	652	9.5	805	763	5.2
Output power at 0.3m/s	-	64	-	-	73	-
Power factor	0.5	0.5	-	0.65	0.63	3

Due to speed limitations of the actuator, the predicted electromagnetic performances discussed in Chapters 3 and 4 have not been achieved and not properly validated.

In Chapter 7, the intention of the author was to scale-up the V-shape consequent pole machine developed in Chapters 4 and validated in Chapter 6 to new designs, which can be used as alternative large scale machines for a 30kW generator was developed by Uppsala University. Different support structures and layouts have been proposed and assessed for the aim of reducing the translator mass and overall machine size. The estimated costs for the material required to build these designs have been provided. One design has been finally nominated as the most suitable option for this application, design E. The results show that

by employing the nominated configuration for use in the UU-WEC the following advantages can be obtained:

- The translator and stator vertical length can be reduced by 32% and 48%, respectively compared to the LPMG-UU, which in turn may lead to a significant reduction in the machine overall size and cost.
- The translator active mass represents only 16.2% of that used in LPMG-UU.
- The PMs are mounted on the stator hence the issue of mechanical integrity and thermal instability can be avoided.
- The proposed design requires only 33.6kg of PM to react the same force of that of the LPMG-UU.
- Small PM blocks can be used compared to that adopted in the LPMG-UU; they are much easier for manufacturing and handling.

8.3 Suggestions for Future Work

This thesis described the author's work in the continued development of the Linear Vernier Hybrid Machine. The machines investigated here are the subjects of continued research in this field. In this section, several potential ways for further work are concisely discussed under five headings. Firstly, further work concerning V-shape non-consequent pole machine is mentioned with particular reference to the direct drive wave energy converters. Secondly, further work concerning the proposed Inset Magnet Consequent Pole machine is discussed. Thirdly, further work focusing on the V-shape Consequent Pole machine is suggested. Finally, potential areas for extending the case study covered in Chapter 7 are provided.

8.3.1 The V-shape Machine

A number of potential avenues for further work related to the V-shape machine are summarised below:

1. An investigation looking at the possible improvement of manufacturing the V-shape machine presented in Chapter 4. This might be achieved by looking at different PM configurations, for example, by adopting a combination of V-shaped PM arrays with and without ribs. The result is half of the triangular-shaped segments can be attached to the stator tooth through the iron ribs, which in turn can improve the rigidity of the machine.
2. An investigation into the effect of the PM volume, i.e. re-optimising the PM dimensions and the V-angle of the V-shape PM arrays in the absence of the restrictions on PM

volume described in Chapter 4, allowing future authors to add more PM volume based on the expected optimal performance.

3. An investigation of cogging force and force ripple reduction which could be achieved by looking at the technique proposed in [97], or by re-optimising the C_{tip} and C_{root} , which identified in Chapter 3 to see the effect of the dimensions of the translator tooth.

8.3.2 The Inset Magnet Consequent Pole Machine

The work presented in Chapter 3 focused generally on the electromagnetic design of the Inset Magnet Consequent Pole machine. This is satisfactory because of the small size Inset Magnet Consequent Pole prototype. However, for a large scale Inset Magnet Consequent Pole machine, this is a need to develop a comprehensive mechanical design and optimisation methodology to further minimise structural material. This should include both the structural and thermal design of the Inset Magnet Consequent Pole machine, and should if possible, be incorporated with the electromagnetic design optimisation as is conducted in [133].

This machine has been proposed for the purpose of minimising the magnet mass without sacrificing the machine's electromagnetic performance. This goal has been successfully achieved by designing the machine using the FEA, and validating the predicted results by constructing the prototype. However, there is room for further analysis based on magnetic circuit in order to assess the effect of the tapered ferromagnetic poles in comparison to the rectangular ferromagnetic poles.

The thickness of the translator core back represents only 10% of that used in [2]. This indicates that there is a need to perform mechanical analysis investigating the effect of the translator thickness, for example, to evaluate the influence of the potential attraction force on the translator and deflection that might be caused using a general-purpose software package such as ANSYS. These investigations can be also applied to the mechanical bearings.

Further mechanical tests focusing on the machine assembly, including varying the airgap length to obtain unequal airgaps can be conducted. This would allow the researcher to experimentally investigate the effect of the attraction force either on the stator or stator structural support under different excitation currents, which can result in structural failures.

8.3.3 *The V-shape Consequent Pole Machine*

The work carried out on V-shape Consequent Pole machine can be extended in three areas:

1. Further investigation on PM volume which was held constant during the optimisation performed in Chapter 4 might result in a further improvement of the machine's electromagnetic performance and the airgap flux density and hence the power factor, for example, by increasing the PM width without considering its volume, this would allow more flux to be concentrated into the airgap.
2. Extending the optimisation of the translator parameters could lead to a further reduction of the unwanted cogging force.
3. An investigation of the cogging force and force ripple reduction which could be achieved by looking at the technique proposed in [97], or by re-optimising the C_{tip} and C_{root} , which identified in Chapter 3 to see the effect of the dimensions of the translator tooth.

8.3.4 *Case Study*

Further investigations can be carried out to extend the case study covered in Chapter 7, this may include:

1. A small scale of the optimal design with a multiple-sided structure described earlier in Chapter 7 is suggested to be simulated using FEA to predict the machine characteristics such as cogging force and static force. This would provide material for predicting the performance of the large scale machine.
2. Studies to investigate the mechanical structure that consider the rigidity and stiffness of the system and detailed mechanical analyses of the deflection using a software package such as ANSYS. The proposed designs should also be further investigated and compared when inactive material is included in the mechanical analysis.
3. Detailed analyses that consider the effects of different types of bearings and guides on machine behaviour.
4. Investigation into using the cable winding that was adopted in linear generator developed by Uppsala University on the proposed designs and the relative impact on the construction cost.
5. Further work should investigate which structures give the best stiffness/mass characteristics.

References

- [1] I. López, J. Andreu, S. Ceballos, I. M. de Alegría, and I. Kortabarria, "Review of wave energy technologies and the necessary power-equipment," *Renewable and sustainable energy reviews*, vol. 27, pp. 413-434, 2013.
- [2] M. A. Mueller and N. J. Baker, "Modelling the performance of the vernier hybrid machine," *IEE Proceedings-Electric Power Applications*, vol. 150, pp. 647-654, 2003.
- [3] F. d. O. Antonio, "Wave energy utilization: A review of the technologies," *Renewable and sustainable energy reviews*, vol. 14, pp. 899-918, 2010.
- [4] A. Vosough, "Wave energy," *International journal of multidisciplinary sciences and engineering*, vol. 2, pp. 60-63, 2011.
- [5] N. Delmonte, D. Barater, F. Giuliani, P. Cova, and G. Buticchi, "Review of oscillating water column converters," *IEEE Transactions on Industry Applications*, vol. 52, pp. 1698-1710, 2016.
- [6] A. Ahmed, Z. Saadatnia, I. Hassan, Y. Zi, Y. Xi, X. He, *et al.*, "Self-powered wireless sensor node enabled by a duck-shaped triboelectric nanogenerator for harvesting water wave energy," *Advanced Energy Materials*, vol. 7, p. 1601705, 2017.
- [7] J. Falnes, *Ocean waves and oscillating systems: linear interactions including wave-energy extraction*: Cambridge university press, 2002.
- [8] C. M. Johnstone, K. Nielsen, T. Lewis, A. Sarmento, and G. Lemonis, "EC FPVI coordinated action on ocean energy: A European platform for sharing technical information and research outcomes in wave and tidal energy systems," *Renewable Energy*, vol. 31, pp. 191-196, 2006.
- [9] R. M. D Magagna, A Uihlein, "2016 JRC Ocean Energy Status Report," *European Commission Joint Research Centre*, 2016.
- [10] D. Ross, *Power from the Waves*: Oxford University Press, USA, 1995.
- [11] J. Cruz, *Ocean wave energy: current status and future perspectives*: Springer Science & Business Media, 2007.
- [12] Z. Wu and A. Viola, "The challenge of wave energy: A review of the WECs state of the art developed in the world," in *OCEANS 2017-Aberdeen*, 2017, pp. 1-6.
- [13] A. Pecher and J. P. Kofoed, *Handbook of ocean wave energy*: Springer, 2017.
- [14] H. Jing, N. Maki, T. Ida, and M. Izumi, "Electromechanical Design of an MW Class Wave Energy Converter With an HTS Tubular Linear Generator," *IEEE Transactions on Applied Superconductivity*, vol. 28, pp. 1-4, 2018.
- [15] K. Gunn and C. Stock-Williams, "Quantifying the global wave power resource," *Renewable Energy*, vol. 44, pp. 296-304, 2012.
- [16] A. Stegman, A. de Andres, H. Jeffrey, L. Johanning, and S. Bradley, "Exploring Marine Energy Potential in the UK Using a Whole Systems Modelling Approach," *Energies*, vol. 10, p. 1251, 2017.
- [17] D. Magagna and A. Uihlein, "Ocean energy development in Europe: Current status and future perspectives," *International Journal of Marine Energy*, vol. 11, pp. 84-104, 2015.
- [18] Ocean Energy Systems (OES). Ocean Energy Systems: Annual Report, 2015. Available online: <https://www.ocean-energy-systems.org/library/annual-reports/> (accessed in July 2018).

References

- [19] S. Barstow, "World Waves: Integrated model, satellite and in-situ measurements providing quality wave and wind data anywhere, anytime," *Fugro OCEANOR, Norway* Apr. 2010.
- [20] J. Twidell and T. Weir, *Renewable energy resources*: Routledge, 2015.
- [21] B. Drew, A. R. Plummer, and M. N. Sahinkaya, "A review of wave energy converter technology," ed: Sage Publications Sage UK: London, England, 2009.
- [22] J. Falnes, "A review of wave-energy extraction," *Marine Structures*, vol. 20, pp. 185-201, 2007.
- [23] R. Gobato, A. Gobato, and D. F. G. Fedrigo, "Study Pelamis system to capture energy of ocean wave," *arXiv preprint arXiv:1508.01106*, 2015.
- [24] Ocean Power Technologies. Available at: <http://www.oceanpowertechnologies.com/> (accessed in August 2018).
- [25] J. Khan, G. Bhuyan, and A. Moshref, "Potential opportunities and differences associated with integration of ocean wave and marine current energy plants in comparison to wind energy," *Final Annex III Technical Report—2009-IEA-OES Document*, p. 64, 2009.
- [26] Aquamarine Power. Available at: <http://www.aquamarinepower.com/> (accessed in July 2018).
- [27] E. Lejerskog, H. Gravråkmø, A. Savin, E. Strömstedt, S. Tyrberg, K. Haikonen, *et al.*, "Lysekil research site, sweden: A status update," in *9th European Wave and Tidal Energy Conference, Southampton, UK, 5-9 September 2011*, 2011.
- [28] N. Hodgins, O. Keysan, A. McDonald, and M. Mueller, "Linear generator for direct drive wave energy applications," in *Electrical Machines (ICEM), 2010 XIX International Conference on*, 2010, pp. 1-6.
- [29] Z.-Q. Zheng, P. Huang, D.-X. Gao, and Z.-Y. Chang, "Analysis of electromagnetic force of the linear generator in point absorber wave energy converters," *Journal of Marine Science and Technology*, vol. 23, pp. 475-480, 2015.
- [30] F. Wu, P. Ju, X.-P. Zhang, C. Qin, G. J. Peng, H. Huang, *et al.*, "Modeling, control strategy, and power conditioning for direct-drive wave energy conversion to operate with power grid," *Proceedings of the IEEE*, vol. 101, pp. 925-941, 2013.
- [31] D. Valério, P. Beirão, and J. S. da Costa, "Optimisation of wave energy extraction with the Archimedes Wave Swing," *Ocean Engineering*, vol. 34, pp. 2330-2344, 2007.
- [32] Archimedes Wave Swing Ocean Energy, available online at <http://www.awsocan.com/> (accessed in August 2018).
- [33] A. Babarit, *Ocean Wave Energy Conversion: Resource, Technologies and Performance*: Elsevier, 2017.
- [34] N. Ahmadienia, "The linear induction motor (LIM) & single linear induction motor (SLIM)," *American Journal of Electrical Power and Energy Systems*, vol. 3, pp. 71-75, 2014.
- [35] R. Vermaak and M. J. Kamper, "Design aspects of a novel topology air-cored permanent magnet linear generator for direct drive wave energy converters," *IEEE Transactions on Industrial Electronics*, vol. 59, pp. 2104-2115, 2012.
- [36] C.-C. Hwang, P.-L. Li, and C.-T. Liu, "Optimal design of a permanent magnet linear synchronous motor with low cogging force," *IEEE Transactions on Magnetics*, vol. 48, pp. 1039-1042, 2012.

References

- [37] Q. Liu, H. Yu, M. Hu, C. Liu, J. Zhang, L. Huang, *et al.*, "Cogging force reduction of double-sided linear flux-switching permanent magnet machine for direct drives," *IEEE Transactions on Magnetics*, vol. 49, pp. 2275-2278, 2013.
- [38] A. Shiri and A. Shoulaie, "End effect braking force reduction in high-speed single-sided linear induction machine," *Energy Conversion and Management*, vol. 61, pp. 43-50, 2012.
- [39] M. H. Aliabadi, S. H. Hosseinian, S. J. Moghani, and M. Abedi, "Multisided linear induction generator, analytical modeling, 3-D finite element analysis and experimental test," *Elektronika ir Elektrotechnika*, vol. 19, pp. 8-15, 2013.
- [40] O. Danielsson, M. Eriksson, and M. Leijon, "Study of a longitudinal flux permanent magnet linear generator for wave energy converters," *International Journal of Energy Research*, vol. 30, pp. 1130-1145, 2006.
- [41] H. Polinder, M. A. Mueller, M. Scutto, and M. Goden de Sousa Prado, "Linear generator systems for wave energy conversion," in *Proceedings of the 7th European Wave and Tidal Energy Conference, Porto, Sept., 2007*.
- [42] D. Son and R. W. Yeung, "Optimizing ocean-wave energy extraction of a dual coaxial-cylinder WEC using nonlinear model predictive control," *Applied energy*, vol. 187, pp. 746-757, 2017.
- [43] M. Seal and M. Sengupta, "Design, analysis and fabrication of a linear permanent magnet synchronous machine," *Sādhanā*, vol. 42, pp. 1419-1429, 2017.
- [44] E. Spooner and L. Haydock, "Vernier hybrid machines," *IEE Proceedings-Electric Power Applications*, vol. 150, pp. 655-662, 2003.
- [45] M. A. Mueller, "Electrical generators for direct drive wave energy converters," *IEE Proceedings-generation, transmission and distribution*, vol. 149, pp. 446-456, 2002.
- [46] H. Polinder, B. C. Mecrow, A. G. Jack, P. G. Dickinson, and M. A. Mueller, "Conventional and TFPM linear generators for direct-drive wave energy conversion," *IEEE Transactions on Energy Conversion*, vol. 20, pp. 260-267, 2005.
- [47] Y. Huo, R. Qu, Y. Gao, S. Jia, and X. Fan, "Design of a linear vernier permanent magnet machine with high thrust force density and low thrust force ripple," in *Electric Machines and Drives Conference (IEMDC), 2017 IEEE International, 2017*, pp. 1-6.
- [48] D. Li, R. Qu, and T. A. Lipo, "High-power-factor vernier permanent-magnet machines," *IEEE Transactions on Industry Applications*, vol. 50, pp. 3664-3674, 2014.
- [49] Y. Du, M. Cheng, K. T. Chau, X. Liu, F. Xiao, and W. Zhao, "Linear primary permanent magnet vernier machine for wave energy conversion," *IET Electric Power Applications*, vol. 9, pp. 203-212, 2015.
- [50] J. Li, K. T. Chau, J. Z. Jiang, C. Liu, and W. Li, "A new efficient permanent-magnet vernier machine for wind power generation," *IEEE Transactions on Magnetics*, vol. 46, pp. 1475-1478, 2010.
- [51] A. A. Almoraya, N. J. Baker, K. J. Smith, and M. A. H. Raihan, "An investigation of a linear flux switching machine with tapered ferromagnetic poles," in *Electrical Machines and Systems (ICEMS), 2017 20th International Conference on, 2017*, pp. 1-5.
- [52] L. Huang, H. Yu, M. Hu, J. Zhao, and Z. Cheng, "A novel flux-switching permanent-magnet linear generator for wave energy extraction application," *IEEE Transactions on Magnetics*, vol. 47, pp. 1034-1037, 2011.

References

- [53] W. M. Arshad, T. Backstrom, and C. Sadarangani, "Analytical design and analysis procedure for a transverse flux machine," in *Electric Machines and Drives Conference, 2001. IEMDC 2001. IEEE International*, 2001, pp. 115-121.
- [54] D. Dong, W. Huang, F. Bu, Q. Wang, W. Jiang, and X. Lin, "Modeling and Static Analysis of Primary Consequent-Pole Tubular Transverse-Flux Flux-Reversal Linear Machine," *Energies*, vol. 10, p. 1479, 2017.
- [55] C. Rohrig, "Current waveform optimization for force ripple compensation of linear synchronous motors," in *Decision and Control, 2003. Proceedings. 42nd IEEE Conference on*, 2003, pp. 5891-5896.
- [56] A. Cosic, C. Sadarangani, and J. Timmerman, "Design and manufacturing of a linear transverse flux permanent magnet machines," in *Industry Applications Society Annual Meeting, 2008. IAS'08. IEEE*, 2008, pp. 1-5.
- [57] O. Dobzhanskyi, R. Gouws, and E. Amiri, "On the role of magnetic shunts for increasing performance of transverse flux machines," *IEEE Transactions on Magnetics*, vol. 53, pp. 1-8, 2017.
- [58] J. G. Washington, G. J. Atkinson, N. J. Baker, A. G. Jack, B. C. Mecrow, B. B. Jensen, *et al.*, "Three-phase modulated pole machine topologies utilizing mutual flux paths," *IEEE Transactions on Energy Conversion*, vol. 27, pp. 507-515, 2012.
- [59] M. R. Harris, G. H. Pajooman, and S. M. A. Sharkh, "The problem of power factor in VRPM (transverse-flux) machines," 1997.
- [60] F. Zhao, T. A. Lipo, and B.-i. Kwon, "Dual-stator interior permanent magnet vernier machine having torque density and power factor improvement," *Electric Power Components and Systems*, vol. 42, pp. 1717-1726, 2014.
- [61] T. W. Ching, K. T. Chau, and W. Li, "Power factor improvement of a linear vernier permanent-magnet machine using auxiliary DC field excitation," *IEEE Transactions on Magnetics*, vol. 52, pp. 1-4, 2016.
- [62] Y. Sui, Z. Yin, M. Wang, B. Yu, and P. Zheng, "A Tubular Staggered-Teeth Transverse-Flux PMLM with Circumferentially Distributed Three-Phase Windings," *IEEE Transactions on Industrial Electronics*, 2018.
- [63] A. Nematsaberi and J. Faiz, "A novel linear Stator-PM Vernier machine with spoke-type magnets," *IEEE Transactions on Magnetics*, pp. 1-5, 2018.
- [64] Y. Du, K. Chau, M. Cheng, Y. Fan, Y. Wang, W. Hua, *et al.*, "Design and analysis of linear stator permanent magnet vernier machines," *IEEE Transactions on Magnetics*, vol. 47, pp. 4219-4222, 2011.
- [65] Y. Du, M. Cheng, K. Chau, X. Liu, F. Xiao, W. Zhao, *et al.*, "Comparison of linear primary permanent magnet vernier machine and linear vernier hybrid machine," *IEEE Transactions on Magnetics*, vol. 50, pp. 1-4, 2014.
- [66] J. Li, K. Chau, J. Jiang, C. Liu, and W. Li, "A new efficient permanent-magnet vernier machine for wind power generation," *IEEE Transactions on Magnetics*, vol. 46, pp. 1475-1478, 2010.
- [67] M. Mueller and N. Baker, "Modelling the performance of the vernier hybrid machine," *IEE Proceedings-Electric Power Applications*, vol. 150, pp. 647-654, 2003.
- [68] Y. Du, K. Chau, M. Cheng, Y. Fan, W. Zhao, and F. Li, "A linear stator permanent magnet vernier HTS machine for wave energy conversion," *IEEE Transactions on Applied Superconductivity*, vol. 22, pp. 5202505-5202505, 2012.
- [69] A. Almoraya, N. Baker, K. Smith, and M. Raihan, "Development of a double-sided consequent pole linear vernier hybrid permanent-magnet machine for wave energy

References

- converters," in *Electric Machines and Drives Conference (IEMDC), 2017 IEEE International*, 2017, pp. 1-7.
- [70] J. K.-H. Shek, D. E. Macpherson, M. A. Mueller, and J. Xiang, "Reaction force control of a linear electrical generator for direct drive wave energy conversion," *IET renewable power generation*, vol. 1, pp. 17-24, 2007.
- [71] M. A. Mueller, J. Xiang, N. J. Baker, and P. R. M. Brooking, "Dynamic Modeling of a Linear Vernier Hybrid Permanent Magnet Machine Coupled to a Wave Energy Emulator Test Rig," in *Recent Developments of Electrical Drives*, ed: Springer, 2006, pp. 39-49.
- [72] N. J. Baker, M. A. H. Raihan, A. A. Almoraya, J. W. Burchell, and M. A. Mueller, "Evaluating Alternative Linear Vernier Hybrid Machine Topologies for Integration Into Wave Energy Converters," *IEEE Transactions on Energy Conversion*, vol. 33, pp. 2007-2017, 2018.
- [73] M. A. Mueller and N. J. Baker, "Direct drive electrical power take-off for offshore marine energy converters," *Proceedings of the Institution of Mechanical Engineers, Part A: Journal of Power and Energy*, vol. 219, pp. 223-234, 2005.
- [74] K. Nilsson, O. Danielsson, and M. Leijon, "Electromagnetic forces in the air gap of a permanent magnet linear generator at no load," *Journal of Applied Physics*, vol. 99, p. 034505, 2006.
- [75] I. A. Ivanova, O. Agren, H. Bernhoff, and M. Leijon, "Simulation of wave-energy converter with octagonal linear generator," *IEEE Journal of Oceanic Engineering*, vol. 30, pp. 619-629, 2005.
- [76] M.-J. Jin, C.-F. Wang, J.-X. Shen, and B. Xia, "A modular permanent-magnet flux-switching linear machine with fault-tolerant capability," *IEEE Transactions on Magnetics*, vol. 45, pp. 3179-3186, 2009.
- [77] L. Yan, W. Li, Z. Jiao, C.-Y. Chen, and I.-M. Chen, "Design and modeling of three-phase tubular linear flux-switching permanent magnet motor," in *Guidance, Navigation and Control Conference (CGNCC), 2014 IEEE Chinese*, 2014, pp. 2675-2680.
- [78] Q. Lu, Y. Yao, J. Shi, Y. Shen, X. Huang, and Y. Fang, "Design and performance investigation of novel linear switched flux pm machines," *IEEE Transactions on Industry Applications*, vol. 53, pp. 4590-4602, 2017.
- [79] W. Hao and Y. Wang, "Thrust Force Ripple Reduction of Two C-Core Linear Flux-Switching Permanent Magnet Machines of High Thrust Force Capability," *Energies*, vol. 10, p. 1608, 2017.
- [80] L. Huang, M. Hu, J. Liu, C. Liu, and W. Zhong, "Design and analysis of a linear hybrid excitation flux-switching generator for direct drive wave energy converters," *Advances in Mechanical Engineering*, vol. 5, p. 963093, 2013.
- [81] S. Zhou, H. Yu, M. Hu, C. Jiang, and L. Hao, "Reduction of cogging force in a linear flux-switching permanent-magnet brushless AC machine for direct-drive applications," *IEEE Transactions on Magnetics*, vol. 47, pp. 3252-3255, 2011.
- [82] V. DelliColli, P. Cancelliere, F. Marignetti, R. DiStefano, and M. Scarano, "A tubular-generator drive for wave energy conversion," *IEEE Transactions on Industrial Electronics*, vol. 53, pp. 1152-1159, 2006.
- [83] S. Niu, S. Ho, and W. Fu, "Performance analysis of a novel magnetic-g geared tubular linear permanent magnet machine," *IEEE transactions on magnetics*, vol. 47, pp. 3598-3601, 2011.

References

- [84] J. Zhang, H. Yu, Q. Chen, M. Hu, L. Huang, and Q. Liu, "Design and experimental analysis of AC linear generator with Halbach PM arrays for direct-drive wave energy conversion," *IEEE Transactions on applied superconductivity*, vol. 24, pp. 1-4, 2014.
- [85] L. Huang, M. Hu, Z. Chen, H. Yu, and C. Liu, "Research on a direct-drive wave energy converter using an outer-pm linear tubular generator," *IEEE Transactions on Magnetics*, vol. 53, pp. 1-4, 2017.
- [86] J.-M. Kim, M.-M. Koo, J.-H. Jeong, K. Hong, I.-H. Cho, and J.-Y. Choi, "Design and analysis of tubular permanent magnet linear generator for small-scale wave energy converter," *AIP Advances*, vol. 7, p. 056630, 2017.
- [87] T. Xia, H. Yu, Z. Chen, L. Huang, X. Liu, and M. Hu, "Design and analysis of a field-modulated tubular linear permanent magnet generator for direct-drive wave energy conversion," *IEEE Transactions on Magnetics*, vol. 53, pp. 1-4, 2017.
- [88] G. W. McLean, "Review of recent progress in linear motors," in *IEE Proceedings B (Electric Power Applications)*, 1988, pp. 380-416.
- [89] Z. Liu, W. Zhao, J. Ji, and Q. Chen, "A novel double-stator tubular vernier permanent-magnet motor with high thrust density and low cogging force," *IEEE Transactions on Magnetics*, vol. 51, pp. 1-7, 2015.
- [90] J. Wang and N. J. Baker, "A Linear Laminated Cylindrical Transverse Flux Machine for Use With a Free Piston Engine," *IEEE Transactions on Energy Conversion*, vol. 33, pp. 1988-1997, 2018.
- [91] N. P. Gargov and A. F. Zobaa, "Multi-phase air-cored tubular permanent magnet linear generator for wave energy converters," *IET Renewable Power Generation*, vol. 6, pp. 171-176, 2012.
- [92] C. Oprea, C. S. Martis, F. Jurca, D. Fodorean, L. Szabó, and L. Szabó, "Permanent magnet linear generator for renewable energy applications: Tubular vs. four-sided structures," in *Clean Electrical Power (ICCEP), 2011 International Conference on*, 2011, pp. 588-592.
- [93] A. S. McDonald, M. A. Mueller, and J. G. Jeffrey, "Development of a novel permanent magnet linear generator topology for direct-drive wave energy converters," in *Power Electronics, Machines and Drives, 2008. PEMD 2008. 4th IET Conference on*, 2008, pp. 81-85.
- [94] J. Faiz and A. Nematsaberi, "Linear electrical generator topologies for direct-drive marine wave energy conversion-an overview," *IET Renewable Power Generation*, vol. 11, pp. 1163-1176, 2017.
- [95] N. J. Baker, "Linear generators for direct drive marine renewable energy converters," *PhD thesis, Durham University*, 2003.
- [96] Y. Du, M. Cheng, K. T. Chau, X. Liu, F. Xiao, W. Zhao, *et al.*, "Comparison of linear primary permanent magnet vernier machine and linear vernier hybrid machine," *IEEE Transactions on Magnetics*, vol. 50, pp. 1-4, 2014.
- [97] X. Liu, C. Zou, Y. Du, and F. Xiao, "A linear consequent pole stator permanent magnet vernier machine," in *Electrical Machines and Systems (ICEMS), 2014 17th International Conference on*, 2014, pp. 1753-1756.
- [98] A. A. Almoraya, N. J. Baker, K. J. Smith, and M. A. H. Raihan, "Development of a double-sided consequent pole linear vernier hybrid permanent-magnet machine for wave energy converters," in *Electric Machines and Drives Conference (IEMDC), 2017 IEEE International*, 2017, pp. 1-7.

References

- [99] D. Li, R. Qu, J. Li, and W. Xu, "Consequent-pole toroidal-winding outer-rotor vernier permanent-magnet machines," *IEEE Transactions on Industry Applications*, vol. 51, pp. 4470-4481, 2015.
- [100] Y. Gao, R. Qu, D. Li, J. Li, and G. Zhou, "Consequent-pole flux-reversal permanent-magnet machine for electric vehicle propulsion," *IEEE Transactions on Applied Superconductivity*, vol. 26, pp. 1-5, 2016.
- [101] W. Li, T. W. Ching, and K. T. Chau, "Design and analysis of a new parallel-hybrid-excited linear vernier machine for oceanic wave power generation," *Applied Energy*, vol. 208, pp. 878-888, 2017.
- [102] W. Li, T. W. Ching, and K. T. Chau, "A new linear vernier permanent-magnet machine using high-temperature superconducting DC field excitation," *IEEE Transactions on Applied Superconductivity*, vol. 27, pp. 1-5, 2017.
- [103] S.-U. Chung, J.-W. Kim, B.-C. Woo, D.-K. Hong, J.-Y. Lee, and D.-H. Koo, "A novel design of modular three-phase permanent magnet vernier machine with consequent pole rotor," *IEEE Transactions on Magnetics*, vol. 47, pp. 4215-4218, 2011.
- [104] Z. Azar, Z. Q. Zhu, and G. Ombach, "Influence of electric loading and magnetic saturation on cogging torque, back-EMF and torque ripple of PM machines," *IEEE Transactions on Magnetics*, vol. 48, pp. 2650-2658, 2012.
- [105] N. Baloch, B.-i. Kwon, and Y. Gao, "Low-Cost High-Torque-Density Dual-Stator Consequent-Pole Permanent Magnet Vernier Machine," *IEEE Transactions on Magnetics*, pp. 1-5, 2018.
- [106] L. Xu, J. Ji, G. Liu, Y. Du, and H. Liu, "Design and analysis of linear fault-tolerant permanent-magnet vernier machines," *The Scientific World Journal*, vol. 2014, 2014.
- [107] M. A. H. Raihan, N. J. Baker, K. J. Smith, and A. A. Almoraya, "An E-core linear veriner hybrid permanent magnet machine with segmented translator for direct drive wave energy converter," in *Electric Machines and Drives Conference (IEMDC), 2017 IEEE International*, 2017, pp. 1-6.
- [108] N. J. Baker, M. A. H. Raihan, A. A. Almoraya, and J. Wang, "Electric Machine Design for Wave Energy Converters," in *European Wave and Tidal Energy Conference-EWTEC 2017*, 2017.
- [109] N. J. Baker, M. A. Mueller, and M. A. H. Raihan, "All electric drive train for wave energy power take off," *IET Renewable power generation*, vol. 10, 2016.
- [110] W. Li, K. T. Chau, T. W. Ching, and C. Liu, "A Phase-Decoupled Flux-Reversal Linear Generator for Low-Speed Oscillatory Energy Conversion Using Impedance Matching Strategy," *IEEE Transactions on Industrial Electronics*, vol. 65, pp. 7590-7599, 2018.
- [111] A. A. Almoraya, N. J. Baker, K. J. Smith, and M. A. H. Raihan, "A New Configuration of a Consequent Pole Linear Vernier Hybrid Machine with V-shape Magnets," in *2018 XIII International Conference on Electrical Machines (ICEM)*, 2018, pp. 2002-2008.
- [112] H. Y. Li, Z. Q. Zhu, "Investigation of stator slot/rotor pole combination of flux reversal permanent magnet machine with consequent-pole PM structure", *The 9th International Conference on Power Electronics, Machines and Drives, 2018. (PEMD2018)*, In press.
- [113] N. M. Kimoulakis, A. G. Kladas, and J. A. Tegopoulos, "Cogging force minimization in a coupled permanent magnet linear generator for sea wave energy extraction applications," *IEEE Transactions on Magnetics*, vol. 45, pp. 1246-1249, 2009.

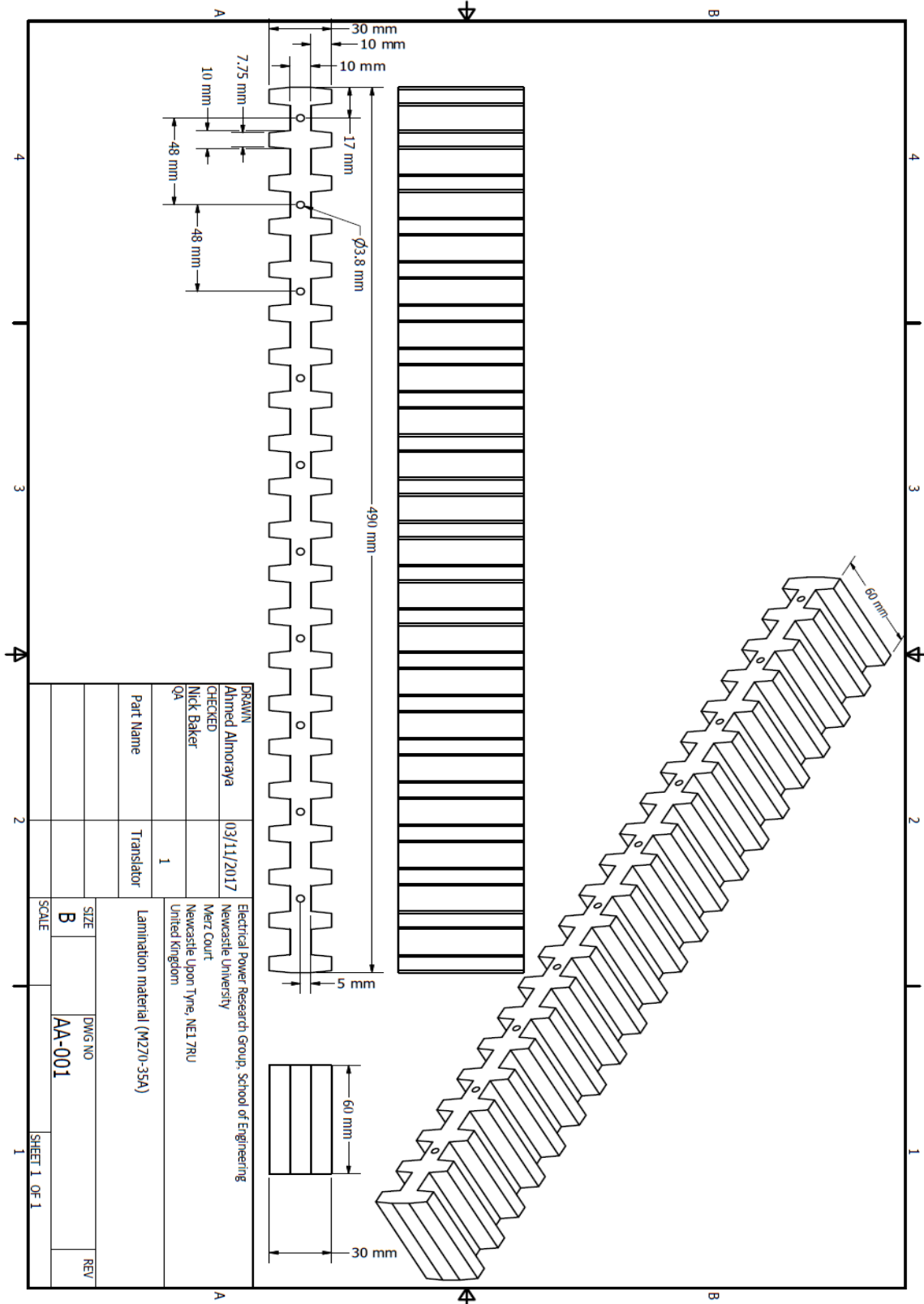
References

- [114] I. A. Ivanova, O. Agren, H. Bernhoff, and M. Leijon, "Simulation of cogging in a 100 kW permanent magnet octagonal linear generator for ocean wave conversion," in *Proceedings of the 2004 International Symposium on Underwater Technology (IEEE Cat. No. 04EX869)*, 2004, pp. 345-348.
- [115] L. Xu, G. Liu, W. Zhao, and J. Ji, "Hybrid Excited Vernier Machines with All Excitation Sources on the Stator for Electric Vehicles," *Progress In Electromagnetics Research M*, vol. 46, pp. 113-123, 2016.
- [116] G. Xu, L. Jian, W. Gong, and W. Zhao, "Quantitative comparison of flux-modulated interior permanent magnet machines with distributed windings and concentrated windings," *Progress In Electromagnetics Research*, vol. 129, pp. 109-123, 2012.
- [117] C. Shi, R. Qu, Y. Gao, D. Li, L. Jing, and Y. Zhou, "Design and Analysis of an Interior Permanent Magnet Linear Vernier Machine," *IEEE Transactions on Magnetics*, pp. 1-5, 2018.
- [118] N. Baloch, S. Khaliq, and B.-I. Kwon, "A high force density HTS tubular vernier machine," *IEEE Transactions on Magnetics*, vol. 53, pp. 1-5, 2017.
- [119] Y. Liu, H. Y. Li, and Z. Q. Zhu, "A High-Power Factor Vernier Machine With Coil Pitch of Two Slot Pitches," *IEEE Transactions on Magnetics*, pp. 1-5, 2018.
- [120] S. Yang, N. J. Baker, B. C. Mecrow, C. Hilton, G. Sooriyakumar, D. Kostic-Perovic, *et al.*, "Cost reduction of a permanent magnet in-wheel electric vehicle traction motor," in *Electrical Machines (ICEM), 2014 International Conference on*, 2014, pp. 443-449.
- [121] A. L. Shurajji, Z. Q. Zhu, and Q. F. Lu, "A novel partitioned stator flux reversal permanent magnet linear machine," in *Ecological Vehicles and Renewable Energies (EVER), 2015 Tenth International Conference on*, 2015, pp. 1-8.
- [122] S. Yang, I. Kakavas, N. J. Baker, B. C. Mecrow, C. Hilton, and D. K. Perovic, "The assembly of a V shape in-wheel motor with reduced mechanical support," 2016.
- [123] E. Hultman, B. Ekergård, T. Kamf, D. Salar, and M. Leijon, "Preparing the Uppsala University wave energy converter generator for large-scale production," in *Proceedings of the 5th International Conference on Ocean Energy, Halifax, NS, Canada*, 2014, pp. 4-6.
- [124] E. Hultman and M. Leijon, "Six-degrees-of-freedom (6-DOF) work object positional calibration using a robot-held proximity sensor," *Machines*, vol. 1, pp. 63-80, 2013.
- [125] E. Hultman, D. Salar, and M. Leijon, "Robotized surface mounting of permanent magnets," *Machines*, vol. 2, pp. 219-232, 2014.
- [126] E. Hultman and M. Leijon, "Automated cable preparation for robotized stator cable winding," *Machines*, vol. 5, p. 14, 2017.
- [127] Seabased AB, available online at: <https://www.seabased.com/>, (accessed in November 2018).
- [128] I. A. Ivanova, O. Agren, H. Bernhoff, and M. Leijon, "Simulation of cogging in a 100 kW permanent magnet octagonal linear generator for ocean wave conversion," in *Underwater Technology, 2004. UT'04. 2004 International Symposium on*, 2004, pp. 345-348.
- [129] Development of a Novel Air-Cored Permanent Magnet Linear Generator for Direct Drive Ocean Wave Energy Converters, PhD thesis, Stellenbosch University, 2013.
- [130] R. Vermaak and M. J. Kamper, "Experimental evaluation and predictive control of an air-cored linear generator for direct-drive wave energy converters," *IEEE Transactions on Industry Applications*, vol. 48, pp. 1817-1826, 2012.

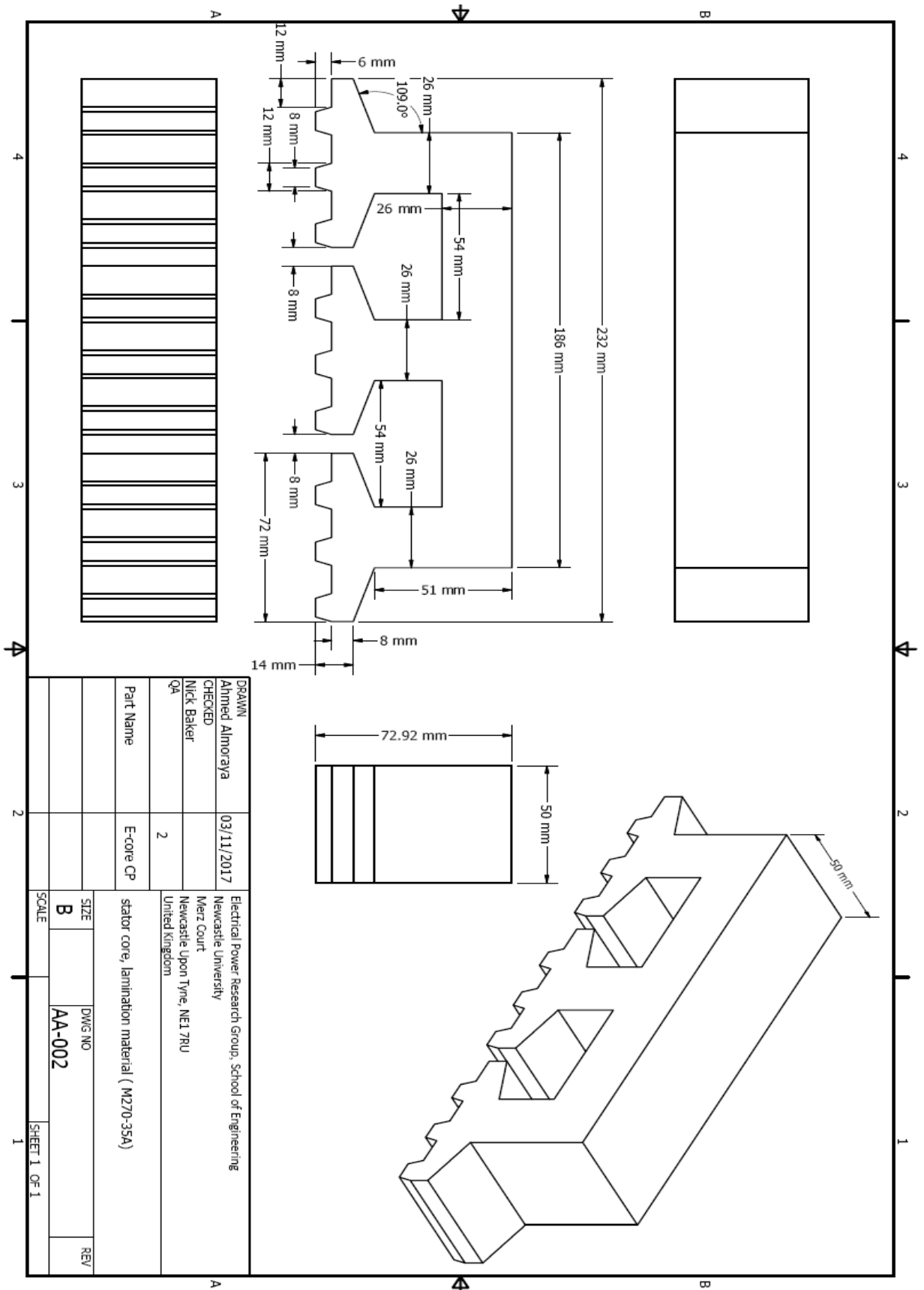
References

- [131] London Metal Exchange (LME), available online at: <https://www.lme.com>, (accessed in December 2018).
- [132] Magnet Applications, available online at: <http://webcache.googleusercontent.com>, (accessed: December 2018).
- [133] N. Hodgins, O. Keysan, A. S. McDonald, and M. A. Mueller, "Design and testing of a linear generator for wave-energy applications," *IEEE Transactions on Industrial Electronics*, vol. 59, pp. 2094-2103, 2012.

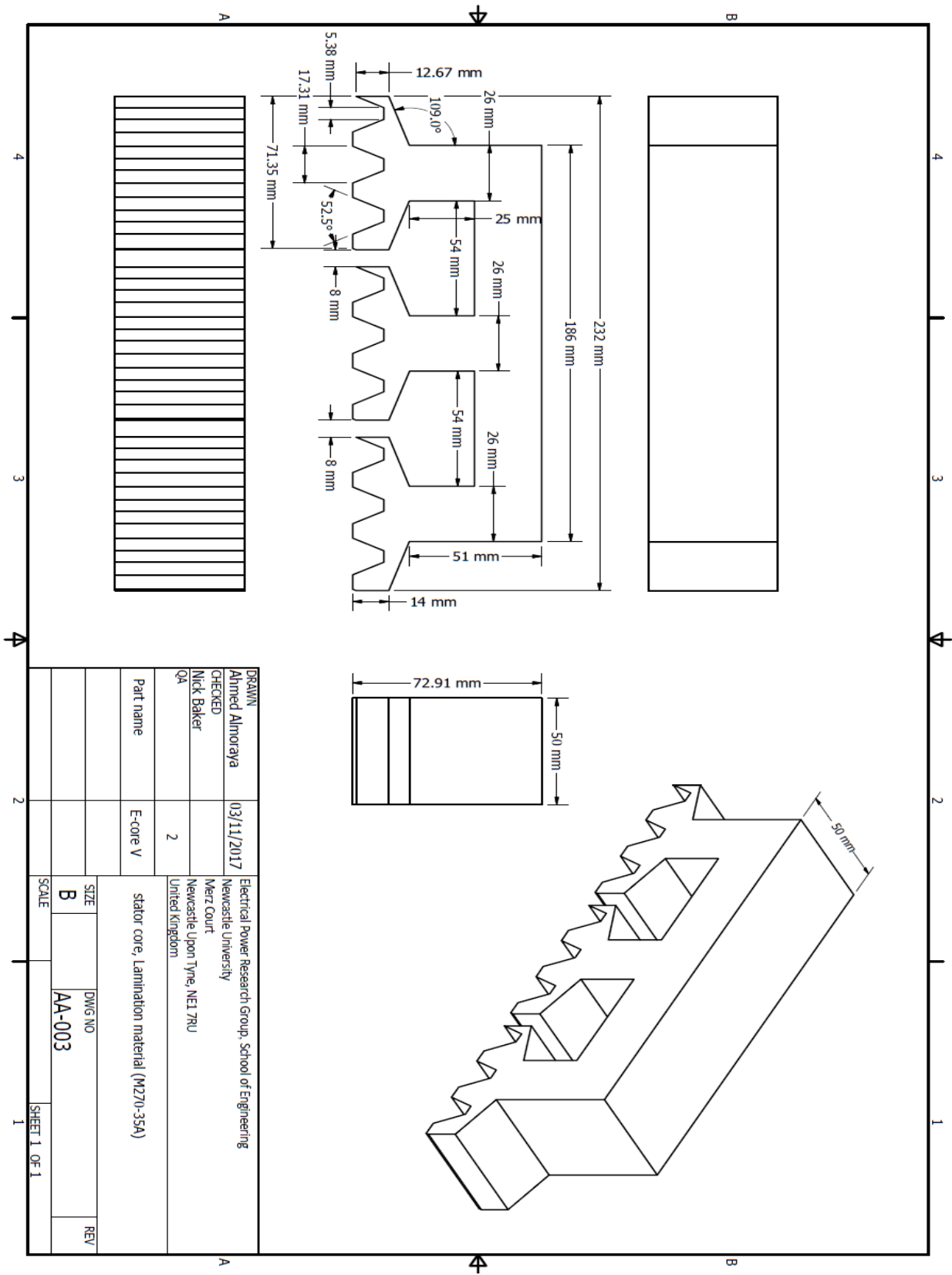
Appendix A: CAD Drawings



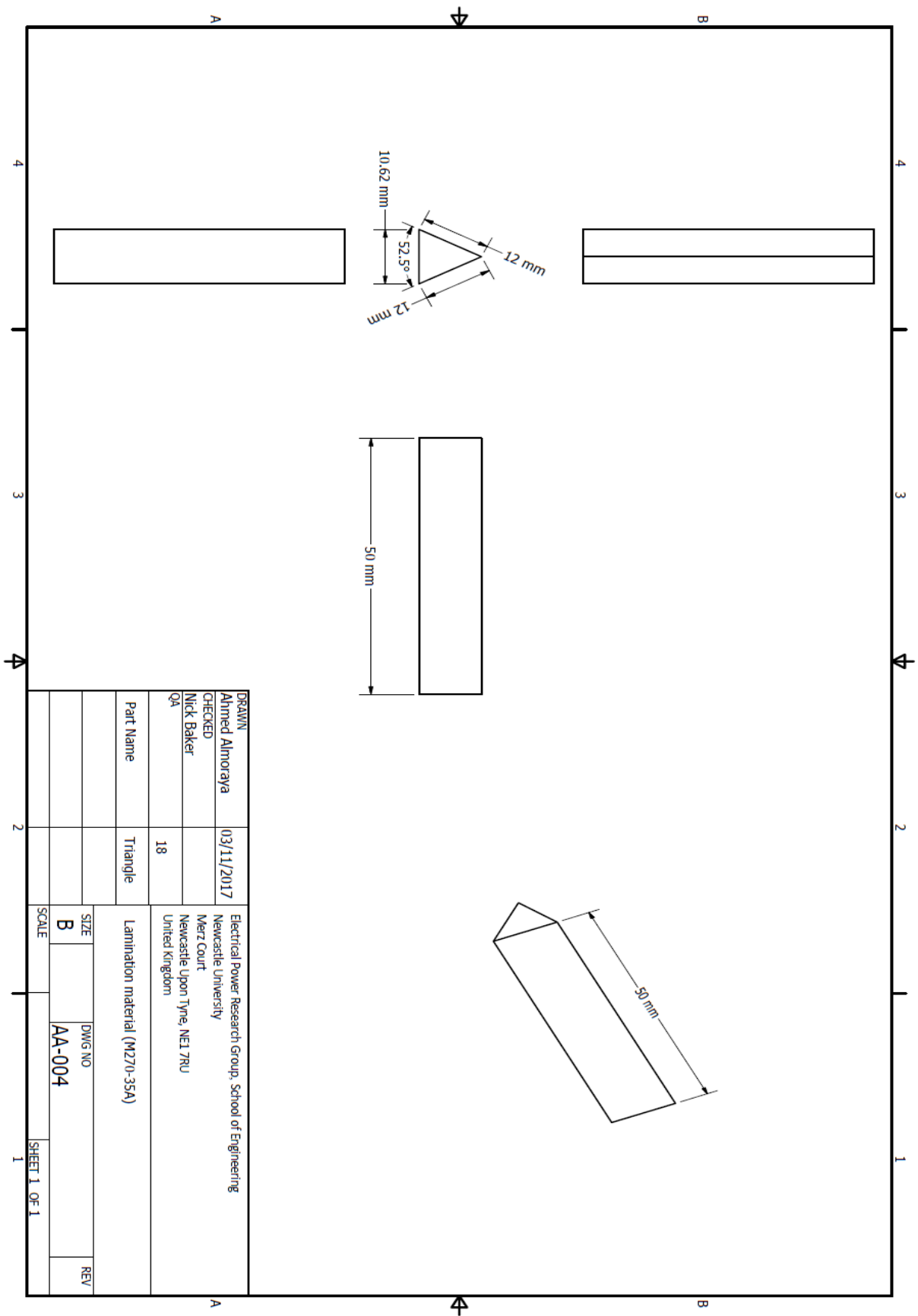
Appendix A: CAD Drawings



Appendix A: CAD Drawings

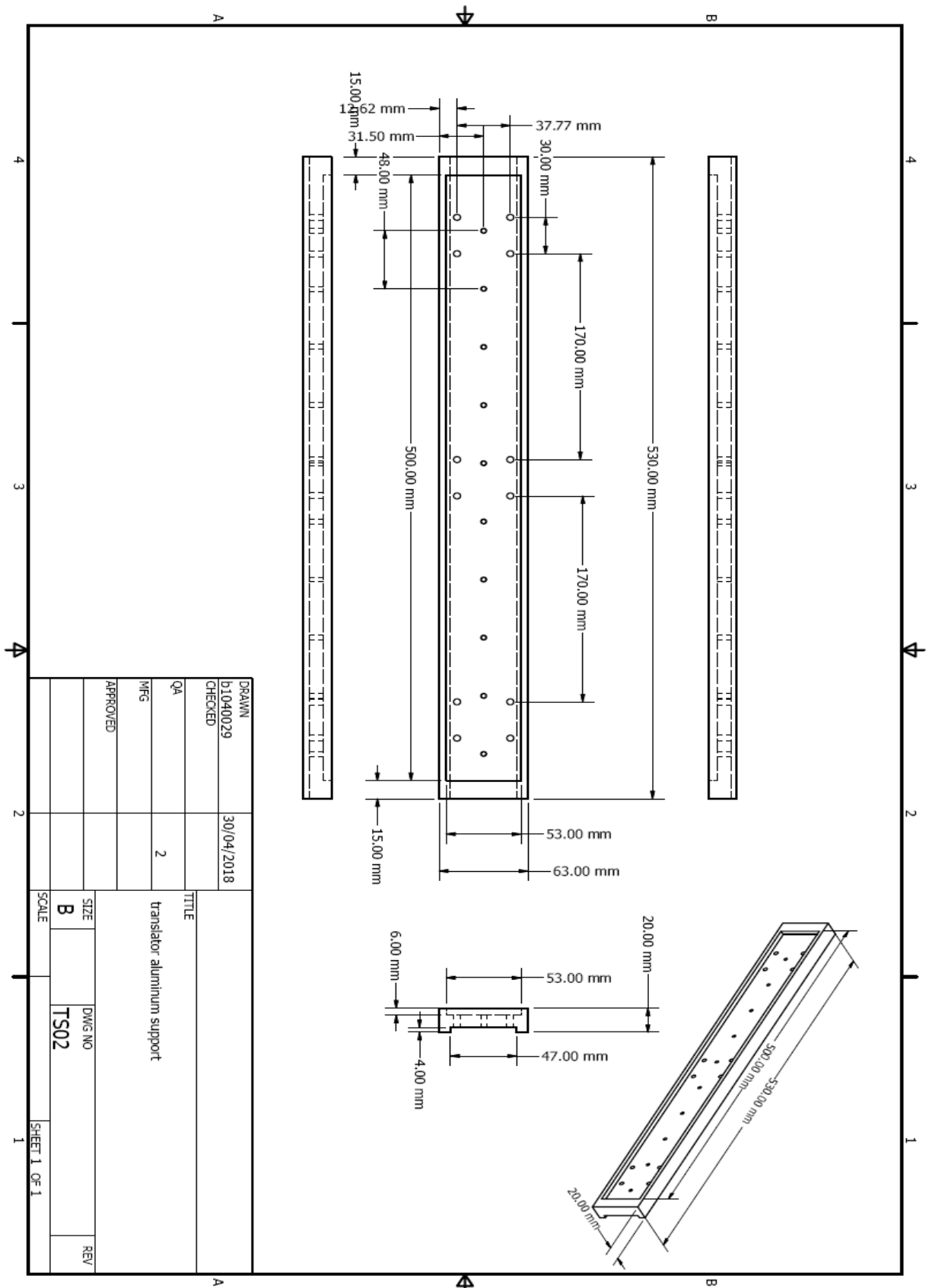


Appendix A: CAD Drawings

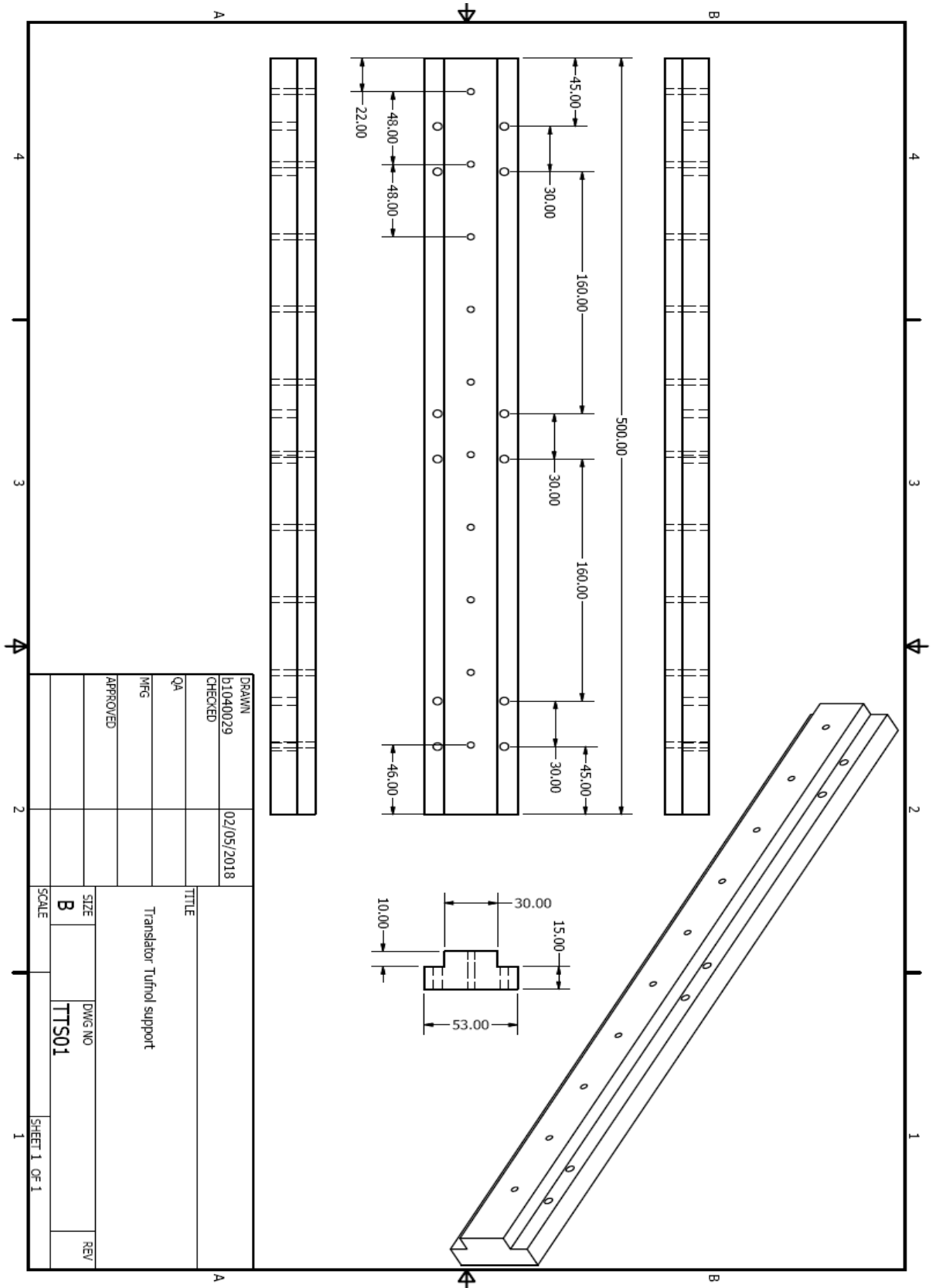


DRAWN		Ahmed Almoraya		03/11/2017		Electrical Power Research Group, School of Engineering Newcastle University	
CHECKED		Nick Baker				Menz Court Newcastle Upon Tyne, NE1 7RU United Kingdom	
QA				18			
Part Name		Triangle		Lamination material (M270-35A)			
SIZE		B		AA-004		REV	
SCALE						SHEET 1 OF 1	

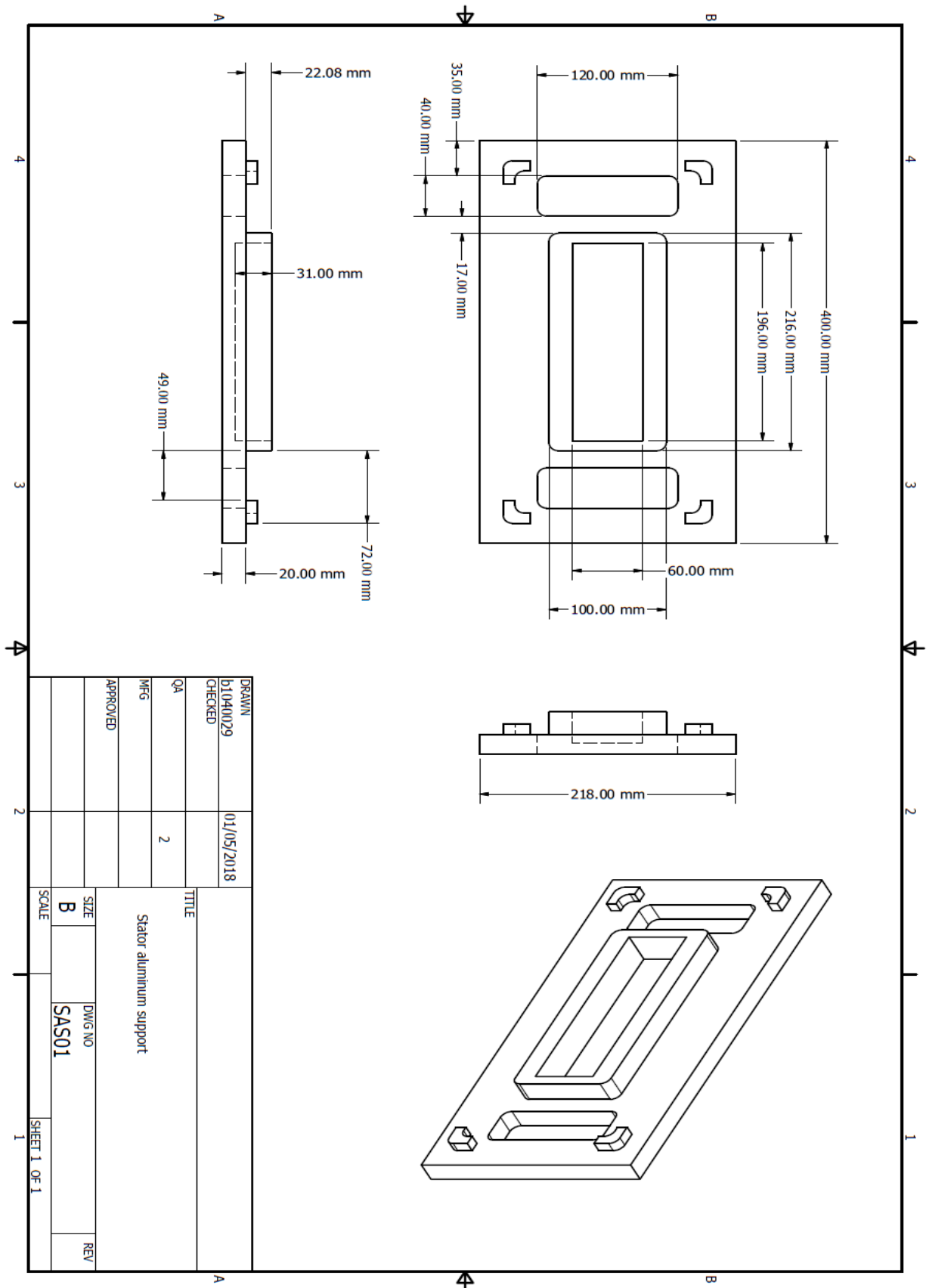
Appendix A: CAD Drawings



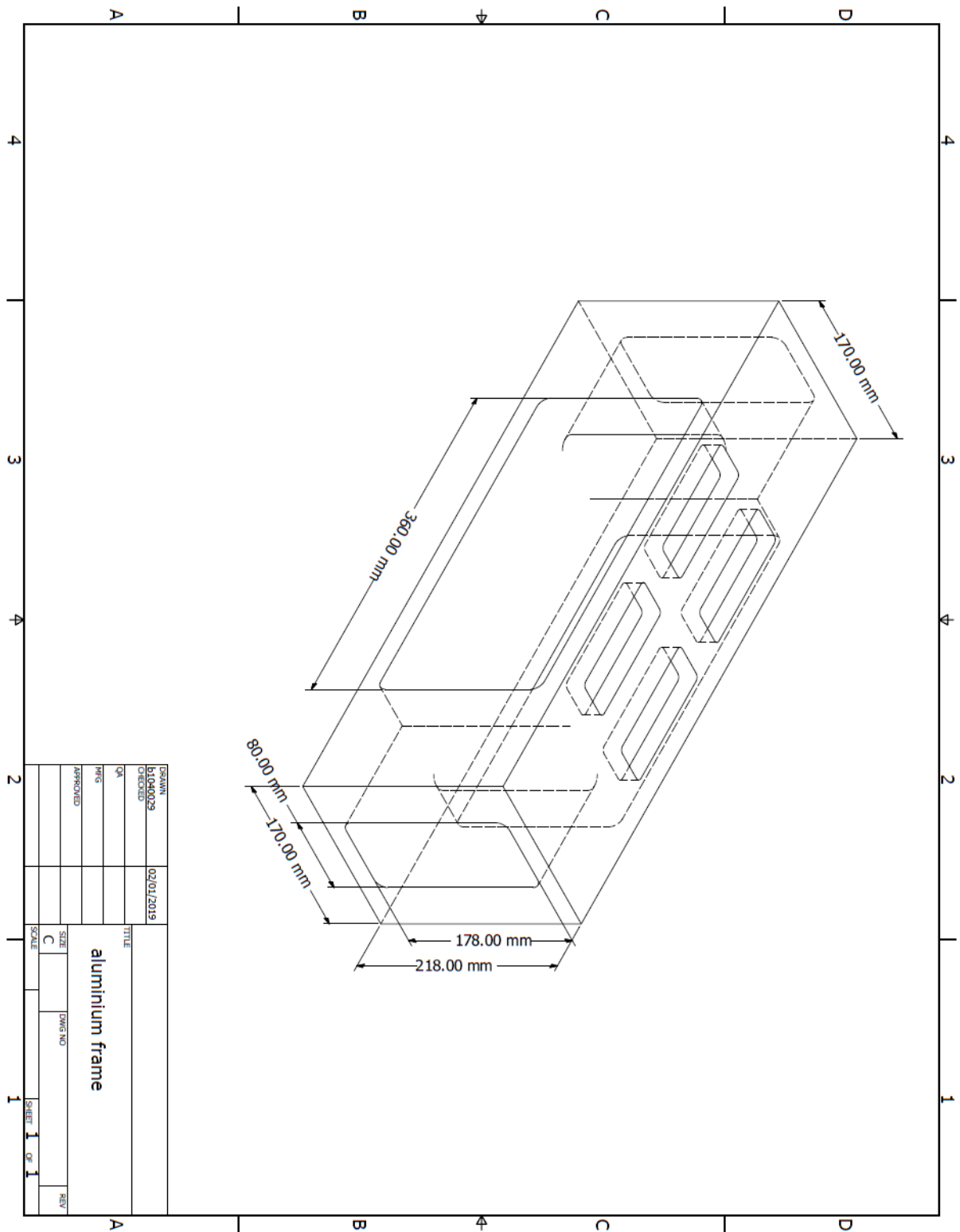
Appendix A: CAD Drawings



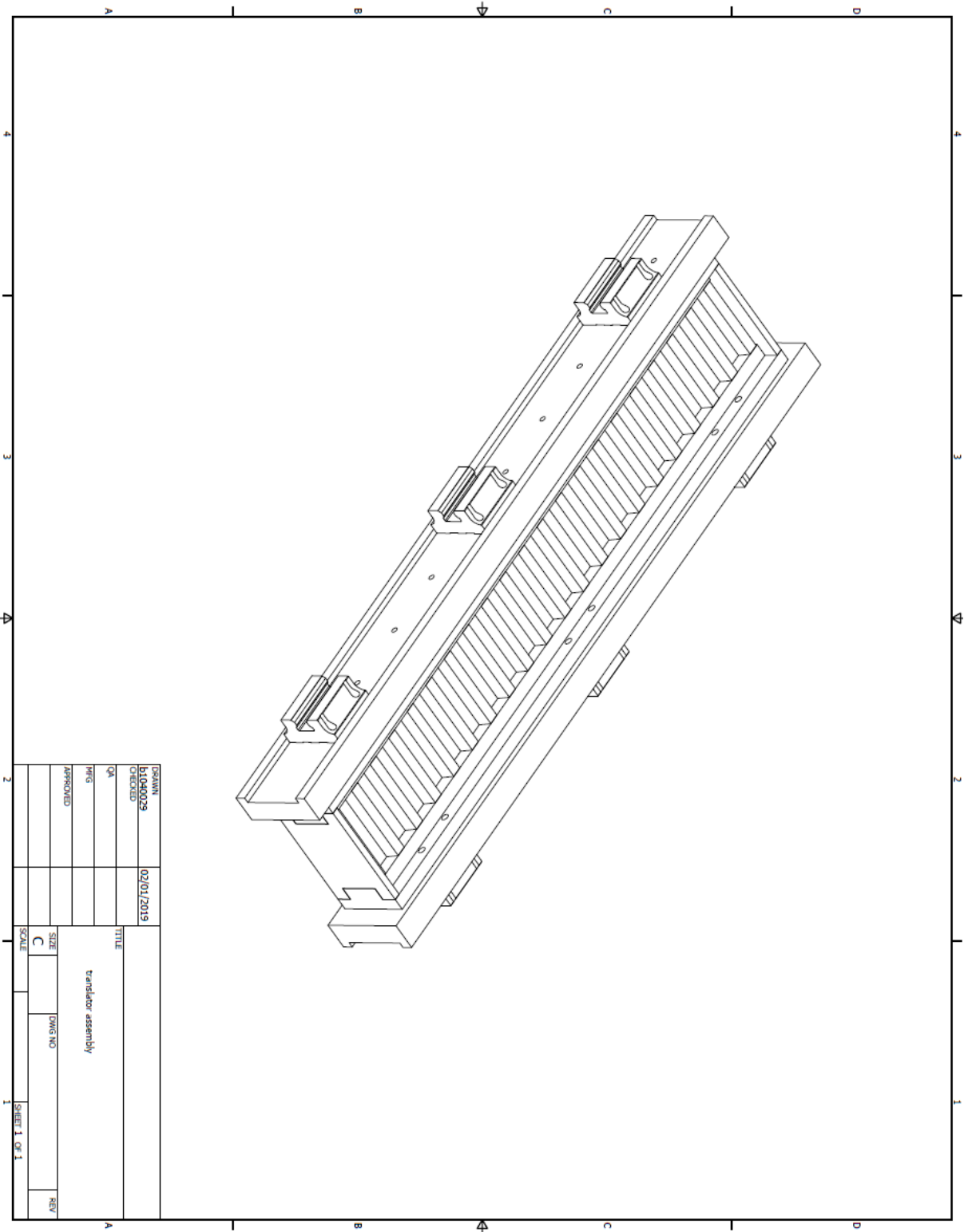
Appendix A: CAD Drawings



Appendix A: CAD Drawings



Appendix A: CAD Drawings



DESIGN	02/01/2019	TITLE	
BLANK/029		translator assembly	
CREATED		SIZE	DWG NO.
QA		C	
MFG		SCALE	REV
APPROVED			
		SHEET 1 OF 1	

Appendix B: Glue Datasheet

HUNTSMAN

Enriching lives through innovation

Advanced Materials

Araldite® LY 5052 / Aradur® 5052*

COLD CURING EPOXY SYSTEMS

Araldite® LY 5052 is a low viscosity epoxy resin

Aradur® 5052 is a mixture of polyamines

APPLICATIONS	Aerospace and industrial composites, tooling, aircraft repair.		
PROPERTIES	<ul style="list-style-type: none"> • Low viscosity, easy impregnation of reinforcement materials. • Long potlife (2 hours for 100 ml at ambient), ample processing time allows production of big objects. • High temperature resistance (glass transition temperature) after ambient cure: 60 °C, after post-cure at 100:120 °C. • Excellent mechanical and dynamic properties after ambient cure with potential for even higher properties after post-cure at elevated temperatures. • Also laminates show outstanding mechanical and dynamic properties. This system is qualified by the Luftfahrtbundesamt (German Aircraft Authority) for the production of gliders. <p>Adequate skin protection is indispensable.</p>		
PROCESSING	<ul style="list-style-type: none"> • Wet lay-up • Resin Transfer Moulding (RTM) • Pressure Moulding • Filament Winding 		
PRODUCT DATA	Araldite® LY 5052		
	Aspect (visual)	clear liquid	
	Viscosity at 25 °C (ISO 12058-1)	1000 – 1500 **	[mPa s]
	Density at 25 °C (ISO 1675)	1.17	[g/cm ³]
	Epoxide index (ISO 3001)	6.65 – 6.85 **	[Eq/kg]
	Aradur® 5052		
	Aspect (visual)	clear liquid	
	Viscosity at 25 °C (ISO 12058-1)	40 – 60 **	[mPa s]
	Density at 25 °C (ISO 1675)	0.94	[g/cm ³]
	Amine value (ISO 9702)	9.55 – 9.75 **	[Eq/kg]

** Specified data are on a regular basis analysed. Data which is described in this document as "typical" is not analysed on a regular basis and is given for information purposes only. Data values are not guaranteed or warranted unless if specifically mentioned.

STORAGE	<p>Provided that the products described above are stored in a dry place in their original, properly closed containers at the above mentioned storage temperatures they will have the shelf lives indicated on the labels.</p> <p>Partly emptied containers should be closed immediately after use.</p>
----------------	--

Appendix B: Glue Datasheet

HUNTSMAN

Enriching lives through innovation

PROPERTIES OF THE CURED, NEAT FORMULATION					
GLASS TRANSITION TEMPERATURE (ISO 11357-2, DSC, 10 K/MIN)	<i>Cure:</i>		$T_{g \text{ onset}} / ^\circ\text{C}$	$T_g / ^\circ\text{C}$	
	2 days 25 °C		50 - 52	52 - 55	
	8 days 25 °C		60 - 64	62 - 66	
	4 month 23 °C		64 - 68	67 - 71	
	1 day 23 °C + 10 h 40 °C		68 - 72	70 - 76	
	1 day 23 °C + 20 h 40 °C		72 - 76	74 - 80	
	1 day 23 °C + 10 h 50 °C		78 - 82	80 - 85	
	1 day 23 °C + 15 h 50 °C		81 - 85	82 - 88	
	1 day 23 °C + 10 h 60 °C		92 - 96	94 - 104	
	1 day 23 °C + 15 h 60 °C		94 - 98	96 - 106	
	1 day 23 °C + 2 h 80 °C		106 - 110	108 - 114	
	1 day 23 °C + 8 h 80 °C		112 - 116	114 - 122	
	1 day 23 °C + 1 h 90 °C		104 - 108	108 - 118	
	1 day 23 °C + 4 h 90 °C		112 - 116	116 - 126	
	1 day 23 °C + 1 h 100 °C		116 - 120	118 - 130	
	1 day 23 °C + 4 h 100 °C		118 - 124	120 - 134	
Even if post-cured at elevated temperature <u>after</u> a prolonged cure at ambient, a good increase of the glass transition temperature is obtained as follows :					
	4 months 23 °C + 4 h 130 °C		106 - 112	120 - 132	
TENSILE TEST (ISO 527)	<i>Cure:</i>		7 days RT	15 h 50 °C	8 h 80 °C
	Tensile strength	[MPa]	49 - 71	82 - 86	84 - 86
	Elongation at tensile strength	(%)	1.5 - 2.5	3.1 - 3.7	5.7 - 5.9
	Ultimate strength	[MPa]	49 - 71	80 - 83	80 - 84
	Ultimate elongation	(%)	1.5 - 2.5	3.5 - 5.5	7.0 - 8.5
	Tensile modulus	[MPa]	3350 - 3550	3450 - 3650	3000 - 3200
FLEXURAL TEST (ISO 178)	<i>Cure:</i>		15 h 50 °C	8 h 80 °C	
	Flexural strength	[MPa]		130 - 140	116 - 122
	Elongation at flexural strength	(%)		5.8 - 6.3	6.5 - 7.2
	Ultimate strength	[MPa]		90 - 115	87 - 113
	Ultimate elongation	(%)		8.0 - 9.5	8.5 - 13.4
	Flexural modulus	[MPa]		3000 - 3300	2700 - 3000
FRACTURE PROPERTIES BEND NOTCH TEST (ISO 13586)	<i>Cure:</i>		8 h 80 °C		
	Fracture toughness K_{1C}	MPa√m	0.77-0.83		
	Fracture energy G_{1C}	[J/m ²]	192 - 212		
WATER ABSORPTION (ISO 62)	<i>Immersion:</i>		7 days RT	8 h 80 °C	
	4 days H ₂ O 23 °C	(%)	0.45 - 0.50	0.40 - 0.45	
	10 days H ₂ O 23 °C	(%)	0.70 - 0.80	0.65 - 0.70	
	30 min H ₂ O 100 °C	(%)	0.55 - 0.60	0.45 - 0.50	
	60 min H ₂ O 100 °C	(%)	0.70 - 0.80	0.60 - 0.70	
COEFFICIENT OF LINEAR THERMAL EXPANSION (ISO 11359-2)	<i>Mean value:</i>		7 d RT	15 h 50 °C	8 h 80 °C
	α from 20 - 50 °C	[10 ⁻⁶ /K]	97	-	-
	α from 20 - 90 °C	[10 ⁻⁶ /K]	-	71	-
	α from 20 - 120 °C	[10 ⁻⁶ /K]	-	-	71
POISSON'S RATIO		(ν)	0.35		

Appendix C: Tufnol Datasheet



Tufnol Whale

SRBF - Synthetic resin Bonded Fabric
 Medium weave cotton/phenolic resin laminate
 Colour: Natural (brown)
 Density: 1.36(sheet) 1.35(rod)/cm³

Material Data Sheet

Mechanical Properties	Value	Unit
Cross breaking strength	130	MPa
Charpy impact strength (notched)	11.5	kJ/m ²
Compressive strength (flatwise)	310	MPa
Compressive strength (edgewise)	200	MPa
Shear strength (flatwise)	90	MPa
Tensile strength	68	MPa
Young's modulus	6.3	GPa

Thermal Properties	Value	Unit
Maximum working temperature – continuous	120	°C
Maximum working temperature – intermittent	130	°C
Thermal classification	E	
Thermal conductivity through laminae	0.32	W/(mK)
Thermal expansion in plane of laminae	2.2	X10 ⁻⁵ /K
Specific heat	1.5	kJ/(kgK)

Electrical properties	Value	Unit
Insulation resistance after immersion in water	1 x 10 ⁸	Ω (ohms)
Electric strength (edgewise in oil @ 90°C)	12	kV
Electric strength (flatwise in oil @ 90°C) 1.6mm thk.	4.5	MV/m
Electric strength (flatwise in oil @ 90°C) 3mm thk.	2.6	MV/m
Electric strength (flatwise in oil @ 90°C) 6mm thk.	2.0	MV/m


Other Properties	Value	Unit
Water absorption 1.6mm thk.	90	Mg
Water absorption 3mm thk.	105	Mg
Water absorption 6mm thk.	130	Mg
Water absorption 12mm thk.	160	Mg
Water absorption (rod)	3.3	Mg/cm ²

Sheet - BS EN 60893-3-4 Type PF CC 203	
Rod - BS EN 61212-3-3 Type PF CC 42	

Direct Plastics Ltd. Unit 14 Portland Business Park, Richmond Park Road, Sheffield, S13 8HS

The following information corresponds with our current knowledge and indicates our products and possible applications. We cannot give a legally binding guarantee of certain properties or the suitability for a specific application. Existing commercial patents must be observed. A definitive quality guarantee is given in our general conditions of sales. Unless otherwise stated, these values represent averages taken from injection moulding samples. We reserve the right of technical alterations.

Appendix D: Carbon Fibre Rod Datasheet



Description

4.0 mm diameter high modulus carbon fiber rod available in various lengths. These pultruded carbon fiber composite rods have a high fibre content of high modulus carbon in an epoxy matrix, making them extremely rigid and strong.

Select the required length using the radio buttons below the price.

4.0 mm Carbon Fiber Rod Specification	
Diameter	4.0 mm
Weight per m	18 g per meter
Length	See the options below the price
Structural material	T300 carbon fibers
Matrix	Epoxy resin
Carbon content	Approx. 60%
Youngs Modulus	230 GPa
Ultimate tensile strength	1600-2300 mPa
Fibre density	1.4 - 1.8 g/cm ³
Resin glass transition Tg	170° C
Packing type	Rigid-usually sent in a postal tube

Appendix E: Linear Guideway Datasheet

Unflanged Carriages - Low

with retained ball cage

Linear Guideways

Order No.	d ₁	d ₂	d ₃	d ₄	Dynamic load C KN	Static load C _{0rad + ax} kN	M _x Nm	M _y Nm	M _z Nm
L1016.UL30	M 8	9,0	14,0	M6x1,0	37,33	55,50	719	560	560
L1016.UL30-L	M 8	9,0	14,0	M6x1,0	48,35	71,88	931	836	836
L1016.UL30-XL	M 8	9,0	14,0	M6x1,0	53,83	88,18	1142	1361	1361
L1016.UL35-S	M 8	9,0	14,0	M6x1,0	26,72	41,43	655	275	275
L1016.UL35	M 8	9,0	14,0	M6x1,0	53,31	82,66	1307	991	991
L1016.UL35-L	M 8	9,0	14,0	M6x1,0	66,61	103,29	1633	1424	1424
L1016.UL35-XL	M 8	9,0	14,0	M6x1,0	73,29	127,68	2020	2330	2330
L1016.UL45	M10	14,0	20,0	M8x1,25	73,14	111,30	2353	1559	1559
L1016.UL45-L	M10	14,0	20,0	M8x1,25	86,99	132,39	2798	2170	2170
L1016.UL45-XL	M10	14,0	20,0	M8x1,25	100,52	166,87	3527	3455	3455
L1016.UL55	M12	16,0	23,0	M8x1,25	88,26	136,62	3385	2361	2361
L1016.UL55-L	M12	16,0	23,0	M8x1,25	119,10	183,14	4538	4202	4202
L1016.UL55-XL	M12	16,0	23,0	M8x1,25	161,43	259,71	6430	6617	6617

Tel: 01483 26 67 74
Fax: 01483 26 67 75

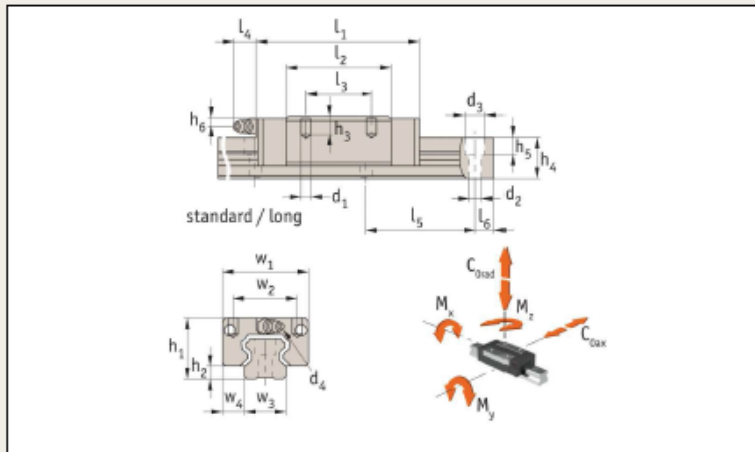
Email: info@automotioncomponents.co.uk
Web: automotioncomponents.co.uk

AUTOMOTION[®]
COMPONENTS

Unflanged Carriages - Low

with retained ball cage

Linear Guideways



L1016.UL

Material

Hardened and ground steel.

Technical notes

Select the size and number of carriages to suit the required load then select the required rail length, (see part nos. L1016.15 through to L1016.55).

Standard preload carriages are K_0 (no preload) or K_1 ($0.02 \times$ dynamic load capacity). Other preloads available on request.

Order No.	Rail size	h_1	w_1	l_1	h_2	h_3	h_4	h_5	h_6	w_2	w_3	w_4	l_2	l_3	l_4	l_5	l_6	δ_{max} Kg
L1016.UL15-S	15	24	34	40,6	3,3	4,8	13,0	6,0	5,5	26	15	9,5	22,2	-	5,0	60	20,0	0,10
L1016.UL15	15	24	34	58,6	3,3	4,8	13,0	6,0	5,5	26	15	9,5	40,2	26	5,0	60	20,0	0,17
L1016.UL15-L	15	24	34	66,1	3,0	4,8	13,0	6,0	5,5	26	15	9,5	47,7	26	5,0	60	20,0	0,18
L1016.UL20-S	20	28	42	48,3	4,5	5,5	16,3	8,5	5,1	32	20	11,0	27,5	-	15,6	60	20,0	0,17
L1016.UL20	20	28	42	69,3	4,5	5,5	16,3	8,5	7,1	32	20	11,0	48,5	32	15,6	60	20,0	0,26
L1016.UL25-S	25	33	48	54,0	5,8	6,8	19,2	9,0	7,2	35	23	12,5	32,3	-	15,6	60	20,0	0,21
L1016.UL25	25	33	48	79,2	5,8	6,8	19,2	9,0	7,2	35	23	12,5	57,5	35	15,6	60	20,0	0,38
L1016.UL30-S	30	42	60	64,2	7,0	10,0	22,8	12,0	10,0	40	28	16,0	37,2	-	15,6	80	20,0	0,50
L1016.UL30	30	42	60	94,8	7,0	10,0	22,8	12,0	10,0	40	28	16,0	67,8	40	15,6	80	20,0	0,80
L1016.UL30-L	30	42	60	105,0	7,0	10,0	22,8	12,0	10,0	40	28	16,0	78,0	40	15,6	80	20,0	0,94
L1016.UL30-XL	30	42	60	130,5	7,0	10,0	22,8	12,0	10,0	40	28	16,0	103,5	60	15,6	80	20,0	1,16
L1016.UL35-S	35	48	70	75,5	7,5	10,0	26,0	12,0	11,5	50	34	18,0	44,5	-	16,0	80	20,0	0,80
L1016.UL35	35	48	70	111,5	7,5	10,0	26,0	12,0	11,5	50	34	18,0	80,5	50	16,0	80	20,0	1,20
L1016.UL35-L	35	48	70	123,5	7,5	10,0	26,0	12,0	11,5	50	34	18,0	92,5	50	16,0	80	20,0	1,40
L1016.UL35-XL	35	48	70	153,5	7,5	10,0	26,0	12,0	11,5	50	34	18,0	122,5	72	16,0	80	20,0	1,84
L1016.UL45	45	60	86	129,0	8,9	15,5	31,1	17,0	14,4	60	45	20,5	94,0	60	16,0	105	22,5	1,64
L1016.UL45-L	45	60	86	145,0	8,9	15,5	31,1	17,0	14,4	60	45	20,5	110,0	60	16,0	105	22,5	1,93
L1016.UL45-XL	45	60	86	174,0	8,9	15,5	31,1	17,0	14,4	60	45	20,5	139,0	80	16,0	105	22,5	2,42
L1016.UL55	55	70	100	155,0	12,7	18,0	38,0	20,0	14,0	75	53	23,5	116,0	75	16,0	120	30,0	2,67
L1016.UL55-L	55	70	100	193,0	12,7	18,0	38,0	20,0	14,0	75	53	23,5	154,0	75	16,0	120	30,0	3,57
L1016.UL55-XL	55	70	100	210,0	12,7	18,0	38,0	20,0	14,0	75	53	23,5	171,0	95	16,0	120	30,0	3,97

Order No.	d_1	d_2	d_3	d_4	Dynamic load C kN	Static load $C_{\text{load} + \text{ax}}$ kN	M_x Nm	M_y Nm	M_z Nm
L1016.UL15-S	M 4	4,5	7,5	M3x0,5	5,81	9,90	69	32	32
L1016.UL15	M 4	4,5	7,5	M3x0,5	11,67	19,90	137	120	120
L1016.UL15-L	M 4	4,5	7,5	M3x0,5	14,12	24,05	166	171	171
L1016.UL20-S	M 5	6,0	9,5	M6x1,0	9,25	15,93	148	66	66
L1016.UL20	M 5	6,0	9,5	M6x1,0	17,98	30,96	289	224	224
L1016.UL25-S	M 6	7,0	11,0	M6x1,0	12,87	21,34	230	103	103
L1016.UL25	M 6	7,0	11,0	M6x1,0	25,25	41,73	447	358	358
L1016.UL30-S	M 8	9,0	14,0	M6x1,0	18,50	27,51	356	153	153

Tel: 01483 26 67 74 Email: info@automotioncomponents.co.uk
 Fax: 01483 26 67 75 Web: automotioncomponents.co.uk

AUTOMOTION[®]
COMPONENTS

Appendix F: IMCP Machine Integrated with a Full Test Rig

